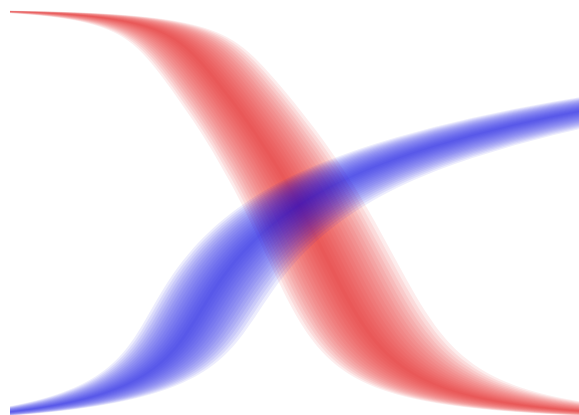
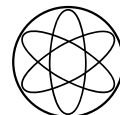
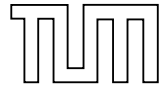

Axial Anomaly and Vector Interactions in the Polyakov–Nambu–Jona-Lasinio Model

Nino Maria Bratovic



Technische Universität München
Physik-Department





TECHNISCHE UNIVERSITÄT MÜNCHEN
Institut für Theoretische Physik T39

Axial Anomaly and Vector Interactions in the Polyakov–Nambu–Jona-Lasinio Model

Nino Maria Bratovic

Vollständiger Abdruck der von der Fakultät für Physik der Technischen Universität München zur Erlangung des akademischen Grades eines

Doktors der Naturwissenschaften (Dr. rer. nat.)

genehmigten Dissertation.

Vorsitzender: Univ.-Prof. Dr. Stephan Paul
Prüfer der Dissertation: 1. Univ.-Prof. Dr. Wolfram Weise (em.)
2. Univ.-Prof. Dr. Alejandro Ibarra

Die Dissertation wurde am 19.11.2012 bei der Technischen Universität München eingereicht und durch die Fakultät für Physik am 30.11.2012 angenommen.

Abstract

The Polyakov–Nambu–Jona-Lasinio (PNJL) model is used to investigate properties of strongly interacting matter in the non-perturbative regime. It features both spontaneous chiral symmetry breaking and statistical color confinement, i. e. the suppression of color non-singlets. A consistent cutoff scheme for the $2 + 1$ flavor PNJL model is introduced and shown to be superior to previously existing schemes: it ensures both the propagation of quarks as free particles at high temperatures as well as the correct treatment of thermodynamics.

The main points of interest of this work are the location, and conditions for the existence, of a critical point in the phase diagram of Quantum Chromodynamics (QCD), according to the PNJL model. Particular emphasis is put on the influence of two important parameters: first, the axial U(1) breaking Kobayashi-Maskawa-'t Hooft interaction strength K . Second, the repulsive vector interaction coupling g_v . We discuss state-of-the-art knowledge about these parameters and give our own estimate of g_v , based on a comparison to recent lattice QCD data for the curvature of the chiral crossover. We find that a reasonable choice of parameters results, by a large margin, in a phase diagram without a critical point or a first-order chiral phase transition.

Zusammenfassung

Wir verwenden das Polyakov–Nambu–Jona-Lasinio–(PNJL–)Modell, um die Eigenschaften stark wechselwirkender Materie im nicht-perturbativen Bereich zu untersuchen. In diesem Modell ist sowohl die spontane Brechung der chiralen Symmetrie realisiert, als auch eine statistische Beschreibung des Farb-Confinements möglich, d.h. die Unterdrückung von Objekten, die keine Farb-Singulets sind. Wir führen ein selbstkonsistentes Regularisierungsschema für das $2 + 1$ -dimensionale PNJL-Modell ein und zeigen, dass es gegenwärtigen Schemata überlegen ist: es stellt sicher, dass sowohl Quarks bei hohen Temperaturen wie freie Teilchen propagieren, als auch thermodynamische Größen korrekt behandelt werden.

Der hauptsächliche Fokus dieser Arbeit liegt auf der Bestimmung der Position, und Bedingungen für die Existenz, eines kritischen Punktes im Phasendiagramm der Quantenchromodynamik (QCD), basierend auf dem PNJL-Modell. Besonderes Augenmerk gilt dabei dem Einfluss zweier wichtiger Parameter: erstens der Kobayashi–Maskawa–'t Hooft– Wechselwirkungsstärke K , und zweitens der repulsiven Vektorwechselwirkungsstärke g_v . Wir diskutieren den aktuellen Forschungsstand zu diesen Parametern und geben eine eigene Abschätzung von g_v an. Diese beruht auf dem Vergleich der Krümmung des chiralen Crossovers zu jüngsten Gitter-QCD-Ergebnissen. Es zeigt sich, dass für eine sinnvolle Wahl von Parametern das Phasendiagramm weder einen kritischen Punkt noch einen Phasenübergang erster Ordnung enthält.

Contents

1	Introduction	1
2	The QCD phase diagram	5
2.1	Introduction	5
2.2	Chiral symmetry and the chiral condensate	6
2.3	Color confinement and the Polyakov loop	7
2.4	Lattice QCD	8
2.5	Experimental and empirical information	10
2.6	Model calculations	11
3	The three-flavor Polyakov–Nambu–Jona-Lasinio model	13
3.1	Introduction	13
3.2	Lagrangian	13
3.3	Bosonization for three quark flavors	15
3.4	NJL parameter sets	20
3.5	Polyakov loop dynamics	22
3.6	Thermodynamic potential and quasiparticle energy eigenvalues	23
4	Cutoff schemes	27
4.1	Introduction	27
4.2	High temperature limit in the two-flavor NJL model	27
4.3	High temperature limit in the 2 + 1 flavor NJL model	31
4.4	PNJL model results for 2 flavors	32
4.5	PNJL model results for 2 + 1 flavors	34
4.6	Summary	39
5	Axial anomaly and Columbia plot	41
5.1	Introduction	41
5.2	Kobayashi–Maskawa–’t Hooft interaction strength K	41
5.3	Dependence of the critical point on the current quark masses	43
5.4	Chiral limit and degenerate quark masses	44
5.5	Curvature of the phase transition line	46
5.6	Type of the phase transition at $\mu = 0$	50
5.7	Transition systematics in m_u – m_s – μ space	51
5.8	Summary	55
6	Parameters of the Polyakov loop effective potential	57
6.1	Introduction	57
6.2	Fukushima Potential	59
6.2.1	Preliminary Remarks	59
6.2.2	Variation of the parameter a	60
6.2.3	Variation of the parameter b	60

6.3	Effective potential used in this work	61
6.3.1	Preliminary Remarks	61
6.3.2	Variation of the parameter c	62
6.3.3	Variation of the parameter d	63
6.3.4	Variation of parameter T_0	63
6.3.5	Fit to lattice QCD results and discussion	63
6.3.6	Influence of cutoff schemes	65
6.3.7	Freeze-out curve and μ -dependent T_0	67
6.4	Summary	67
7	Vector Interactions	71
7.1	Introduction	71
7.2	Reduced vector interaction	73
7.3	Baryon number density and chiral condensate	77
7.3.1	Baryon number density as a function of temperature	78
7.3.2	Baryon number density as a function of chemical potential	78
7.3.3	Chiral condensates as functions of density	80
7.4	Location of the critical point	81
7.5	First-order transition in the temperature–density plane	83
7.5.1	RKH parameter set	85
7.5.2	HK parameter set	86
7.5.3	LKW parameter set	87
7.5.4	Change of g_v for non-standard values of K	87
7.6	Phase diagram in the temperature–density plane	90
7.7	Transition line curvature as a function of g_v	93
7.8	Complete vector interaction	95
7.8.1	Comparison between reduced and complete vector interaction	95
7.8.2	Fixed density ratios	98
7.9	Summary	100
8	Summary and outlook	101
8.1	Summary	101
8.2	Discussion	101
8.3	Outlook	102
A	Appendix	105
A.1	Intermediate calculations in the bosonization procedure	105
A.1.1	Transformation of $\det J_{\pm}$	105
A.1.2	Symmetry properties of products of Gell-Mann matrices	107
A.2	Influence of parameters on the crossover bands	108
	Bibliography	118
	Acknowledgements	119

Chapter 1

Introduction

Quantum chromodynamics (QCD), the theory of strong interactions, has been studied for decades. It has played a major role in three research areas awarded with Nobel Prizes in Physics so far¹ and still continues to offer plenty of challenges and puzzles. Many open questions relate to the search for the phase diagram of QCD, which shows how strongly interacting matter behaves under different thermodynamic conditions. Depending on parameters such as temperature, chemical potential and density, one maps out regions (phases) where matter is characterized by common properties and specific symmetry patterns. The implications of the phase diagram reach from physics shortly after the big bang to the structure and composition of dense astronomical objects like neutron stars. Our work contributes to the study of important aspects of this hotly discussed topic, combining model calculations with input from other sources, both experimental and theoretical.

QCD is characterized by the deceptively simple Lagrangian

$$\mathcal{L}_{\text{QCD}} = \sum_f \bar{\psi}_f (i\gamma^\mu D_\mu - m_f) \psi_f - \frac{1}{2} \text{tr} [G_{\mu\nu} G^{\mu\nu}]. \quad (1.1)$$

The ψ_f are the quark fields, fundamental fermions of flavors species f . They carry $\text{SU}(3)_c$ color charges and are therefore subject to the strong interaction; effects of the other interactions are comparably weak and neglected in this work. We also include only the three quark flavors with the smallest bare masses m_f : the u-quark (“up”), the d-quark (“down”) and the s-quark (“strange”) in our considerations; the three heavy quarks do not contribute at scales relevant for our study. Additional ingredients of the Lagrangian are the gluonic field strength tensor $G^{\mu\nu} := \frac{i}{g} [D^\mu, D^\nu]$ and the covariant derivative $D_\mu := \partial_\mu - i g \frac{\lambda_a}{2} A_\mu^a$, with the eight gluon fields A_μ^a , eight Gell-Mann matrices λ^a , $a \in \{1, \dots, 8\}$, and the coupling strength g .

The Lagrangian in eq. (1.1) respects several symmetries on the classical level. In nature, a complex symmetry pattern emerges, with some symmetries conserved, some explicitly broken, some spontaneously broken and one anomalously broken. Among these effects, two can be considered the most important: on the one hand, the spontaneous breaking of the so-called chiral symmetry governs physics at low energy and density. On the other hand, the spontaneous breaking of the $\text{SU}(3)_c$ center symmetry $\text{Z}(3)$ is related to color confinement: only color-neutral objects are observed as free particles. Studying the interplay between these effects is complicated by the non-Abelian nature of QCD: its coupling strength is small at high energy (“asymptotic freedom”) but becomes large with decreasing energy so that perturbative methods, based on an expansion in the coupling, break down. This rich structure is one of the features that make QCD a very challenging, but equally fascinating subject of study. The model we use in this work mimics the observed symmetry pattern which is a crucial condition for calculations of the phase diagram.

¹Murray Gell-Mann in 1969, Gross, Politzer and Wilczek in 2004 and Nambu in 2008

One of the most frequently discussed possible features of the phase diagram is the existence and location of a critical end point². At such a point, a first-order transition line between two phases, characterized by a discontinuous order parameter, turns into a crossover, where thermodynamical observables undergo a rapid change. The most common example is the critical point at the end of the liquid/gas transition in the pressure–temperature phase diagram of water. Beyond that point, it is impossible to distinguish clearly between the two states of matter.

The notion of a critical point of QCD is in large parts based on models like the one we are using in this work. It has long been known, however, that its location is strongly dependent on the parameters of the model. Our goal in this work is to investigate how likely the existence of a critical point is when state-of-the-art results from many different approaches are considered. The method is characterized by two simple steps: First, we systematically study the robustness of the critical point under a change of model parameters that are not yet under strong constraints. Second, we discuss the implications of the most probable values of these parameters for the critical point.

This thesis is organized as follows. First, in Chapter 2, we give a brief overview over known as well as commonly expected features of the QCD phase diagram. The main methods of determining its properties are listed and some advantages and disadvantages presented.

Chapter 3 introduces the Polyakov–Nambu–Jona-Lasinio (PNJL) model. We start from the underlying effective Lagrangian mimicking the symmetry patterns of the QCD Lagrangian and show the important steps and approximations in the calculation of the thermodynamic potential Ω . The used input parameters are listed and their origins discussed.

The PNJL model is non-renormalizable so that a cutoff has to be applied. In Chapter 4, we discuss three different cutoff schemes. We show that the “soft” cutoff scheme we are using has distinct advantages over the commonly used methods. In the second half of that chapter, we show our standard results for the phase diagram and thermodynamic quantities in the $2 + 1$ flavor case. That diagram will be the baseline of comparison throughout the thesis. Some results in the two flavor scenario are given for reference. We also compare to recent results from lattice QCD calculations.

Chapter 5 continues the discussion of lattice QCD results, especially of the so-called “Columbia plot” and its continuation to finite chemical potential, the “critical surface”. Special emphasis is put on the influence of the strength of the axial $U(1)$ anomaly, in the model given by the Kobayashi–Maskawa–’t Hooft coupling strength K . We discuss some experimental as well as theoretical indications for its possible dependence on temperature and chemical potential. It is seen that the critical surface can change considerably with K . Interestingly, the main differences appear in μ – T regions that lattice QCD calculations will have considerable difficulty reaching. In the context of the curvature κ of the chiral crossover determined, again, from lattice QCD, we discuss the influence of several likely functional forms of $K(T, \mu)$ on the curvature result from our model. We find that none of these forms yields a small enough curvature.

In chapter 6 we focus on the Polyakov loop effective potential \mathcal{U} . Two popular forms are presented and the role of its parameters investigated. Since recent lattice QCD results show the Polyakov loop crossover to be very smooth, it is one goal of this chapter to study which modifications of \mathcal{U} would be necessary to achieve this effect. We show how such changes would impact pure glue calculations. The last part of the chapter presents the strong influence of cutoff schemes on the interplay between the chiral and the (de-)confinement crossovers. In this context, we also show the results of allowing the pure glue transition temperature T_0 to run with μ .

Chapter 7 introduces a vector-type interaction into the model. It consists of two parts: in the first, a relatively simple interaction Lagrangian is studied that is common in the literature. The second part treats a more complex vector interaction term that does not mix flavors. We discuss

²Usually it is just called “the critical point” for convenience. However, in some works it is speculated that more than one critical point could exist.

differences between the two interaction variants; where they are identical, we use the simpler one. The dependence of the critical point on the vector interaction strength g_v is studied in detail, especially in combination with a change in the strength of the axial anomaly. The chiral first-order transition is presented in the T - ρ_B plane with ρ_B the net baryon density. Constraints from the phase transition of nuclear matter are used to infer likely values for K and g_v . Finally, we find our own estimate of g_v by again calculating the crossover curvature κ .

We give a summary, our conclusions and an outlook for the future in chapter 8.

Chapter 2

The QCD phase diagram

2.1 Introduction

The thermodynamic properties of matter under the influence of quantum chromodynamics are described by the QCD phase diagram. It is usually displayed with temperature T and quark chemical potential μ as the axes, corresponding to the independent variables of a grand canonical ensemble¹. The phase diagram, though a subject of studios research since the 70s [27], is still largely a matter of conjecture.

In this chapter, we give a brief overview of its expected features and the main research approaches, as far as relevant to our work: computational approximations of QCD on a grid (so-called "lattice QCD", section 2.4), information gleaned from experiments and astrophysical observation (section 2.5), and model calculations (section 2.6). For more information, we refer to some of the excellent reviews on this topic, e. g. [122, 54].

A commonly used sketch of expectations about the phase diagram is shown in Fig. 2.1. The most striking, and most debated, feature is certainly the critical point: it is speculated that the smooth chiral crossover (see section 2.2) becomes a first-order transition with increasing μ ; indications of this stem mostly from predictions of chiral models (section 2.6). However, firmly known facts are rather scarce; we discuss them in the following. Theoretical arguments

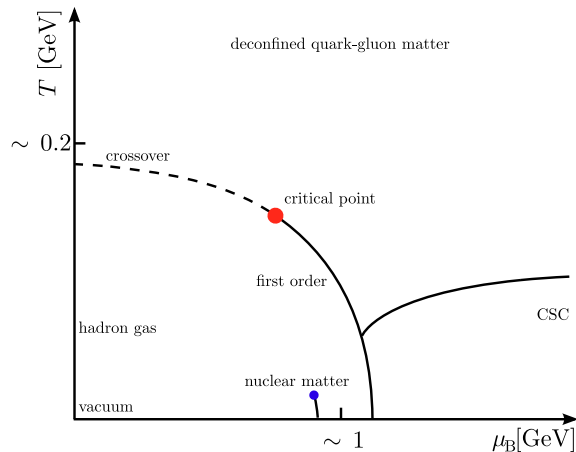


Fig. 2.1: Common basic expectations about the QCD phase diagram. Dashed: chiral crossover, see sections 2.2 and 2.4. Beyond the critical point (red), the transition is first-order (solid line). Line to the right: separation of color-superconducting (CSC) matter from quark-gluon matter.

¹In chapter 7 we will discuss the benefits of switching μ for the net baryon density ρ_B . They are related by $\rho_B = -\frac{1}{3} \frac{\partial \Omega}{\partial \mu}$, where Ω is the grand canonical potential.

determine what to expect at large T and large μ : At high temperatures $T \gtrsim \Lambda_{\text{QCD}}$, in accordance with the QCD property of asymptotic freedom [59, 60, 107, 108], the ground state is expected to be a so-called quark-gluon plasma (QGP), i. e. deconfined “partonic” matter with quarks and gluons as active degrees of freedom. The scale parameter Λ_{QCD} is, apart from the current quark masses, the only free parameter in QCD. Its numerical value varies with the renormalization scheme used to connect to experimental values; it is about $\Lambda_{\text{QCD}} \gtrsim 200$ MeV.

For large chemical potentials, on the other hand, it was found that the gap energy of a color superconducting state is of the order of Λ_{QCD} [4]. The ground state at asymptotically high densities is expected to be the color-superconducting color-flavor locked (CFL) phase: quark-quark Cooper pairs (“diquark condensates”) break the (approximate) $SU(3)_c \times SU(3)_L \times SU(3)_R$ symmetry down to the diagonal subgroup $SU(3)_{c+L+R}$, where even the baryon number is not conserved [4]. At low temperature and intermediate μ , a plethora of diverse color superconducting phases with non-vanishing diquark condensates, e. g. a crystalline phase, is being discussed [3]. In this work, we will not include diquark degrees of freedom; this remains as an objective of future work. Instead, we focus on the region of intermediate temperatures and chemical potentials.

That region is governed by the interplay of two important properties of QCD: the first is the spontaneous breaking of chiral symmetry, and the second is color confinement.

2.2 Chiral symmetry and the chiral condensate

The QCD vacuum at $T = 0$ and $\mu = 0$ is a much more interesting phase than the completely symmetric system that was initially expected (Wigner-Weyl realization). Although a symmetry of the QCD Lagrangian, chiral symmetry is spontaneously broken² in nature (Nambu-Goldstone realization of the vacuum). It is defined by invariance under the transformation of quark fields as

$$\psi \longrightarrow \exp [i\lambda_a \theta^a] \psi, \quad (2.2.1)$$

with the Gell-Mann matrices in flavor space λ_a , $a = 1 \dots 8$ and parameters θ^b , $b = 1 \dots 8$. One empirical proof is that the pseudoscalar mesons are much lighter³ than their scalar counterparts. For example the pseudoscalar neutral pion π_0 with quantum numbers $I^G J^{PC} = 1^- 0^{-+}$ has a mass of about 135 MeV, while the scalar a_0 meson with $I^G J^{PC} = 1^- 0^{++}$ has a mass of 980 ± 20 MeV [16]. The most common measure of chiral symmetry breaking is the so-called “chiral condensate” or “quark condensate”,

$$\langle \bar{\psi}\psi \rangle = \langle 0 | \bar{\psi}\psi | 0 \rangle = \langle 0 | \bar{u}u | 0 \rangle + \langle 0 | \bar{d}d | 0 \rangle + \langle 0 | \bar{s}s | 0 \rangle \quad (2.2.2)$$

for the three lightest quark flavors. With $\psi_L := 1/2(1 - \gamma_5)\psi$ and $\psi_R := 1/2(1 + \gamma_5)\psi$, with the definition, based on the Dirac gamma matrices, $\gamma_5 := i\gamma_0\gamma_1\gamma_2\gamma_3$, we have

$$\bar{\psi}\psi = \bar{\psi}_R\psi_L + \bar{\psi}_L\psi_R. \quad (2.2.3)$$

This operator is clearly not invariant under separate chiral $SU(3)_L$ and $SU(3)_R$ transformations with

$$\psi_{L/R} \xrightarrow{SU(3)_{L/R}} \exp \left[i\theta_a^{L/R} \lambda^a \right] \psi_{L/R}. \quad (2.2.4)$$

Consequently, the mass term in the QCD Lagrangian, $m\bar{\psi}\psi$, breaks chiral symmetry explicitly, and from a non-vanishing expectation value of $\langle \bar{\psi}\psi \rangle$ follows a ground state with broken chiral symmetry (Nambu-Goldstone phase).

²For this discovery, Yoichiro Nambu was awarded one half of the Nobel Prize in Physics in 2008.

³Although they are the Goldstone bosons of a broken continuous gauge symmetry, they are not exactly massless because of the non-vanishing current quark masses. These masses are comparatively small, however, so that the mechanism of spontaneous symmetry breaking is still a good description of physics.

The Gell-Mann–Oakes–Renner relation [56] based on the symmetries of QCD and their breaking patterns connects the the chiral condensate $\langle \bar{\psi}\psi \rangle$ to the pion mass m_π . In two flavors, it reads, with the pion decay constant f_π and the up- and down quark current masses m_u and m_d , respectively,

$$m_\pi^2 f_\pi^2 = -(m_u + m_d) \langle \bar{u}u + \bar{d}d \rangle. \quad (2.2.5)$$

It follows that the chiral condensate has a finite value in the vacuum⁴. On the other hand, for $T \rightarrow \infty$ (Stefan–Boltzmann limit), a gas of free quarks and gluons should be a good description of the system. The pressure P_q for each quark flavor q can be calculated as

$$P_q(T; m_q) \approx 4 N_c \frac{7}{8} \left[\frac{\pi^2}{90} T^4 - \frac{1}{42} m_q^2 T^2 + \mathcal{O}(m_q^4) \right] \quad (2.2.6)$$

and, since one can easily show that

$$\langle \bar{\psi}\psi \rangle = -\frac{\partial P(T, \mu)}{\partial m_q}, \quad (2.2.7)$$

the condensate vanishes at high temperature in the chiral limit $m_q \rightarrow 0$ [141]. Therefore, a phase transition must occur somewhere at intermediate temperatures. For the study of this region, lattice QCD calculations have proved an invaluable tool (see section 2.4).

2.3 Color confinement and the Polyakov loop

Close to the vacuum, matter is in the hadronic phase. Hadrons like pions or nucleons are colorless; $SU(3)_c$ colored objects like the constituent quarks or gluons are confined and not observed freely. For asymptotically high temperatures, the quark kinetic energy becomes large with respect to the confining potential (strongly coupled quark gluon plasma, sQGP) and matter is deconfined. Similarly, for very large densities, mean free distances between the quarks become small and color confinement ceases.

In a system without *dynamical* quark degrees of freedom (the heavy quark limit), the expectation value $\langle \Phi \rangle$ of the renormalized Polyakov loop is an order parameter for the confinement/deconfinement transition. The Polyakov loop L itself is a Wilson loop winding around the periodic imaginary time direction,

$$L(\vec{x}) = \mathcal{P} \exp \left\{ i \int_0^\beta d\tau A_4(\vec{x}, \tau) \right\} \quad (2.3.1)$$

and the order parameter is

$$\langle \Phi(\vec{x}) \rangle = \left\langle \frac{1}{N_c} \text{tr} [L(\vec{x})] \right\rangle. \quad (2.3.2)$$

In the confined phase, the $SU(3)$ center symmetry $Z(3)$ for the elements of $SU(3)_c$ under periodic boundary conditions in the inverse temperature direction is exact; in the deconfined phase, it is spontaneously broken. This symmetry is also explicitly broken by the presence of dynamical quarks: their antiperiodicity in imaginary time requires fermionic fields to transform trivially under $Z(3)$. For $\langle \Phi \rangle$, one finds the transformation pattern

$$\langle \Phi \rangle \xrightarrow{Z(3)} z \langle \Phi \rangle \quad \text{with} \quad z \in \left\{ e^{\frac{2n\pi i}{3}} \mid n = 0, 1, 2 \right\}. \quad (2.3.3)$$

If $\langle \Phi \rangle = 0$, it is trivially invariant and the symmetry is intact. For $\langle \Phi \rangle \neq 0$, only $z = 1$ is allowed, and the symmetry is broken. A simple but intuitive interpretation of the Polyakov loop

⁴This is also true in the chiral limit, where $m_\pi = m_u = m_d = 0$.

was worked out in [94, 95]. They showed for the thermal expectation value of the correlation of two Polyakov loops:

$$e^{-\beta F_{\bar{q}q}(\vec{x}-\vec{y}, T)} = \left\langle \Phi(\vec{x}) \Phi^\dagger(\vec{y}) \right\rangle, \quad (2.3.4)$$

where $F_{\bar{q}q}(\vec{x}-\vec{y}, T)$ is the free energy of two static color sources at \vec{x} and \vec{y} . It was then argued, using the cluster decomposition theorem, that one can write

$$\langle \Phi \rangle = e^{-\frac{1}{2}\beta F_q^\infty} \quad (2.3.5)$$

for the asymptotic free energy of a hypothetical “single” quark⁵. Clearly, when $Z(3)$ symmetry is intact and $\langle \Phi \rangle = 0$, it takes infinite free energy F_q^∞ to liberate the quark – it is confined. If the symmetry is broken and $\langle \Phi \rangle \rightarrow 1$, then $F_q^\infty \rightarrow 0$, signalling deconfinement. In the following, in accordance with the usage in the literature, we drop the braces and denote the expectation value $\langle \Phi \rangle$ from now on simply as “the Polyakov loop” Φ .

Lattice QCD calculations are very well suited to calculate the Polyakov loop at $\mu = 0$, both in the pure glue scenario and with dynamical quarks. Recent results are presented in Fig. 6.1 and Fig. 6.2 in section 6.1.

2.4 Lattice QCD

The lattice approach to study non-perturbative QCD physics was proposed by Wilson in 1974 [139]: the functional integration in the QCD partition function is carried out by importance sampling on a discrete (usually Euclidean) space time grid with a lattice spacing a and real time extent N_τ . The smallest describable wavelength on a lattice extends over two units of a , so that momenta are restricted to $|k| \leq \pi/a$, giving a natural ultraviolet cutoff scale. For the transcription of QCD onto the lattice, statistical mechanics methods can be used.

The definition of the action is, however, highly non-trivial. The discretization of the theory leads naturally to errors in powers of the lattice spacing, in addition to effects from the finite volume and the continuum extrapolation $a \rightarrow 0$. Depending on the formulation of the action and the inclusion of terms that do not contribute in the continuum limit, these discretization errors can be reduced. A multitude of techniques has been developed that we cannot cover in any detail in this work (for an introduction, see e. g. [62]). For our purposes it is important to note that the common lattice actions like Wilson or staggered fermions break chiral symmetry to some degree. However, it can still be mimicked and studied approximately and relations like the Gell-Mann–Oakes–Renner relation, eq. (2.2.5), have been reproduced. In principle, the overlap fermion formulation [100] or an approximation, domain wall fermions, are able to describe (almost) chirally invariant fermions. The downside is the enormous amount of computing power required, even compared to the other actions that already necessitate the use of large computer clusters. Nevertheless, quite recently calculations at finite temperature from this approach have been forthcoming [74, 36]. First results indicate that findings with dynamical overlap fermions [17] and domain wall fermions [11] are compatible with those from the other actions.

Regardless of the formalism, lattice QCD calculations usually show a smooth *crossover* of the chiral condensate at $\mu = 0$. The study of the order of this transition, i. e. first or second order, or crossover, is depicted in the so-called Columbia plot as a function of the current quark masses. Reasonable estimates then put the physical point in the crossover region. We discuss the Columbia plot, and our result for it, in more detail in chapter 5.

Two major collaborations, the hotQCD collaboration [10] (mainly based in Bielefeld and Brookhaven) and the Budapest–Wuppertal group [19] using different fermion realizations, have found results for the chiral transition at $\mu = 0$ that essentially agree with each other after

⁵For antiquarks, the relation is, analogously, $\langle \Phi^\dagger \rangle = e^{-\frac{1}{2}\beta F_{\bar{q}}^\infty}$.

careful treatment of discretization errors and extrapolations to the continuum limit⁶ and physical current quark masses [10], see black diamonds and green triangles in Fig. 2.3. We cannot cover these procedures in detail, for which we refer to the respective publications, but it should be kept in mind that there is still some freedom in determining what exactly is the “physical” extrapolation. We show results for the chiral condensate⁷ in Figs. 2.2 and 2.3.

It should be noted that the transition occurs at lower temperatures than in our calculations in the following chapters; this is a known problem of the PNJL model that is remedied to some degree by its nonlocal extension (see section 2.6). We will see that our framework nevertheless achieves good agreement with lattice QCD results when they are normalized to the critical temperature, see e.g. the comparison of the results seen in Fig. 2.3 to ours, presented in Fig. 4.5. Lattice QCD groups provide us also with information about the order parameter

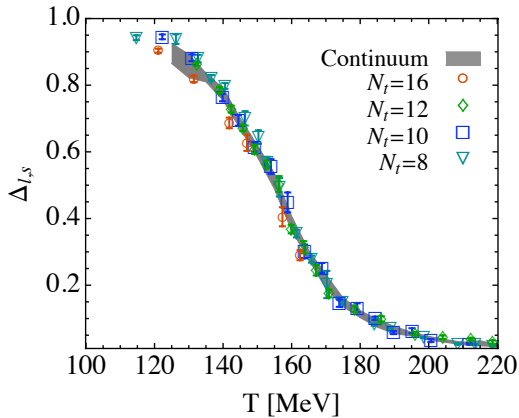


Fig. 2.2: Collection results for $\Delta_{I,S}$ from [19], see def. (4.5.2).

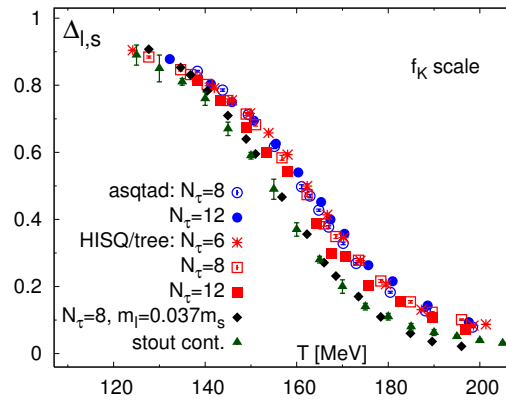


Fig. 2.3: Collection results for $\Delta_{I,S}$ from [10], see def. (4.5.2).

of deconfinement, the Polyakov loop Φ (definition in 3.5, results in Fig. 6.1 and Fig. 6.2). It is a subject of ongoing research what the relation between the chiral, and the Polyakov loop (de-)confinement transition is. Lattice QCD results tend to show two essentially coinciding crossovers (“entanglement”); no fundamental reason is known for this effect. Casher [29] and ’t Hooft [124] have argued that confinement implies chiral symmetry [50]. Then, deconfinement should, as a tendency, set in earlier than chiral restoration. This scenario will be evident in our version of the phase diagram, see e.g. Fig. 4.6b. We comment on the degree of entanglement and its dependence on model settings in sections 4.5, 6.3.6 and 6.3.7.

So far, we have restricted the discussion along the T axis to $\mu = 0$. The extension of lattice calculations to finite chemical potentials suffers from the notorious “fermion sign problem”: in the “quenched” evaluation of the partition function, quark fields are integrated out to give

$$Z = \int \mathcal{D}U e^{-S_g[U]} \prod_f \det M(m_f, \mu_f), \quad (2.4.1)$$

where $\det M$ is the fermion determinant for the flavor f and S_g the pure gauge action. Since for the Dirac operator the hermiticity relation $\mathcal{D}(\mu)^\dagger = \gamma_5 \mathcal{D}(-\mu^*) \gamma_5$ holds, the fermion determinant is complex for color group SU(3) and real chemical potential. This prohibits its use as a probability weight in the Monte-Carlo algorithms (see e.g. review [106]). The problem itself remains unsolved, but there exist several ways of circumventing it: these include, among others,

⁶In addition, the kaon decay constant f_K instead of the more common Sommerfeld scale was used to produce physical temperature values.

⁷The quantity $\Delta_{I,S}$ is a combination the chiral condensates for different flavors, see def. (4.5.2) and the following discussion.

reweighting, calculations with imaginary chemical potential ($\mu^* = -\mu$ then makes the fermion determinant real) and a Taylor expansion around μ/T . So far, no direct evidence for a change of the crossover at $\mu = 0$ into a first-order transition was found for $\mu/T \lesssim 1$. Extrapolations of the curvature of the “critical surface” in the Columbia plot could be expected to give indication of such a change. We discuss this practice in chapter 5 and show that one has to be careful not to infer too much from the small μ/T region to the domain of intermediate μ .

Therefore, although lattice QCD is immensely useful for small fractions μ/T , one needs additional input to complete the phase diagram.

2.5 Experimental and empirical information

The region at low temperature and small but finite densities is the domain of nuclear matter (NM). It is known to exhibit no indications of chiral symmetry restoration or deconfinement; its successful description is realized on the level of mesonic and hadronic degrees of freedom. It exists in a gaseous and a liquid phase, separated by a first-order phase transition. At $T = 0$, nuclear matter net baryon density starts to form around⁸ $\mu_B = \mu_{\text{NM}} \approx 924$ MeV. Multi-fragmentation experiments suggest that the first-order transition ends in a critical end point with $\mu \approx \mu_{\text{NM}}$ and $T = 15 \sim 20$ MeV [77, 78]. Calculations with state-of-the-art in-medium chiral perturbation theory yield very similar results [46]. We will use this accurate information in chapter 7, arguing that the nuclear matter liquid/gas coexistence region should not overlap with a phase of (even partially) restored chiral symmetry. This constraint allows us to determine limiting values for model input parameters (section 7.5.4).

So far, no direct⁹ indications of a first-order transition in the phase diagram other than the NM transition have been found in experiments. Indeed, it is still an open question which observables might be best suited for the search for a first-order phase transition and a possible critical point. Lattice QCD calculations at vanishing μ suggest that the fluctuations of conserved quantities as a function of μ are sensitive to the correlation length ξ which diverges¹⁰ at a critical temperature. The sensitivity is increased for cumulant ratios of these fluctuations in baryon number, charge or strangeness [102, 34]. However, a recent publication [103]¹¹ reports that first results from the RHIC beam energy scan (BES) program “did not confirm any of the suggested [critical point] signals” in the “most ‘suspected’ area of the QCD phase diagram”. The lack of signals is rendered more significant by the fact that the hypothetical critical point is expected to be an “attractor of isentropic trajectories” [101]. As a consequence, it is believed that it should be enough to create a thermalized medium with initial conditions *close* to the critical point [2]. It is then not possible to “narrowly miss” the critical point in an experiment and the lack of signals must be taken seriously. Data analysis will probably continue for some time; an update on results should be given soon.

We will not go further into details of this expansive and hotly debated topic on the experimental side of physics; for a list and discussion of proposed measurements, see e. g. [2].

Apart from experiments, empirical findings from astrophysics recently advanced the quest for the phase diagram and sparked a lot of renewed discussion. The mass of the neutron star “PSR-J1614-2230” was measured with extraordinary precision [41] as $M = (1.97 \pm 0.04) M_\odot$ with M_\odot the mass of our sun. The strong requirements this entails for the “stiffness” of the equation of state, i.e., the large increase of pressure with energy density, eliminates several more “exotic” phases from the phase diagram [64, 89, 88, 137] at low temperature and moderate

⁸The nucleon mass is about 939 MeV and the binding energy in isospin-symmetric nuclear matter around 16 MeV.

⁹In section 6.3.7 and the following summary, we discuss cautious claims of an indirect observation of the phase transition.

¹⁰In collision experiments with a “fireball” of finite size, this quantity is necessarily finite as well.

¹¹It might be worth noting that this work was published only by a member of the STAR collaboration and not by the STAR collaboration as a whole.

density. We do not make use of these constraints in this work but they certainly suggest further studies in this direction in the future.

2.6 Model calculations

After the discussion in the foregoing, it is clear that only the edges of the phase diagram in Fig. 2.1 are known with some certainty. The situation is still unclear in the middle of the phase diagram, where the first-order phase transition and the critical point are conjectured. Non-perturbative approaches that – in principle – take full QCD into account, like functional renormalization group [138, 105] and Dyson–Schwinger techniques [114, 5, 47, 113], are being rapidly developed. So far they have not arrived at a level that allows reliable calculations of the area in the middle of the phase diagram by themselves. Thus, that region can presently only be investigated with nonperturbative *models* that do not suffer from the fermion sign problem. Results from the mentioned “full QCD” approaches is often used as fruitful input. Probably most prominent among models are the Polyakov–Quark–Meson (PQM) model [119, 69] and the Polyakov-extended Nambu–Jona-Lasinio model which we will present in the next chapter.

There exists an updated version of the usual local PNJL model, namely a nonlocal approach [57, 68, 67]. In that framework, no artificial cutoff (cf. chapter 4) is necessary and the running of the QCD coupling strength is incorporated in a natural and consistent way. The disadvantage of such a model closer to physical reality is the added complexity of its equations. This translates directly into computational costs that are higher by a factor of ~ 100 . Our work in the local model may therefore serve as a trailblazer for later studies with the nonlocal formalism: the relatively cheap calculations allow us to scan large parameter spaces and thus identify important aspects and interesting phenomena of the QCD phase diagram.

Chapter 3

The three-flavor Polyakov–Nambu–Jona-Lasinio model

3.1 Introduction

In this chapter we give an overview over the three-flavor PNJL model. We follow largely the exposition in [21], in particular in terms of nomenclature and definitions. Several detailed introductory works are available, e. g. [26, 81, 82, 134].

The NJL model was invented by Nambu and Jona-Lasinio in 1961 [98, 99] to describe the nucleon mass as stemming mostly from the “self-energy of some primary fermion field” and physical nucleons as quasi-particle excitations. It was conceived in analogy to the formation of an energy gap in the Bardeen–Cooper–Schrieffer (BCS) theory of superconductivity [8] with the pion playing the role of the phonon. After the development of quantum chromodynamics, the NJL model was re-interpreted with quarks instead of nucleons as the basic fermionic degrees of freedom [24]. In analogy to the electron-electron pairing in the BCS theory, it features the spontaneous formation of quark-antiquark pairs $\langle \bar{\psi}\psi \rangle$, the chiral condensate (see section 2.2), if an attractive interaction with a certain minimum strength is given¹. Thus, NJL-type models are a successful framework for the study of QCD properties related strongly to chiral symmetry and its breaking pattern.

3.2 Lagrangian

The original NJL Lagrangian for two flavors in Minkowski space-time is

$$\mathcal{L}_{\text{NJL}} = \bar{\psi} (i\cancel{\partial} - \hat{m}_0) \psi + \frac{G}{2} \left[(\bar{\psi}\psi)^2 + (\bar{\psi}i\gamma_5\vec{\tau}\psi)^2 \right]. \quad (3.2.1)$$

with the Pauli matrices $\vec{\tau} = (\tau_1, \tau_2, \tau_3)^\top$ in flavor space and $\hat{m}_0 = \text{diag}(m_u, m_d)$. This Lagrangian displays exact chiral symmetry in the limit $m_0 = 0$. For three flavors, a natural generalization is the sum of a kinetic term

$$\mathcal{L}_{\text{kin}} = \bar{\psi} (i\cancel{\partial} - \hat{m}_0) \psi \quad (3.2.2)$$

with $\psi = (u, d, s)^\top$ and $\hat{m}_0 = \text{diag}(m_u, m_d, m_s)$, and an interaction term

$$\mathcal{L}_{\text{int}} = \frac{G}{2} \sum_{a=0}^{N_f^2-1} \left[(\bar{\psi}\lambda_a\psi)^2 + (\bar{\psi}\lambda_a i\gamma_5\psi)^2 \right], \quad (3.2.3)$$

¹With the strongly attractive color singlet channel, this is certainly true for QCD.

where the λ_i , $i = 1 \dots 8$, are the eight Gell-Mann matrices in flavor space and $\lambda_0 := \sqrt{2/3} \mathbf{1}$. In the chiral limit $m_u = m_d = m_s = 0$ it respects, like the QCD Lagrangian, the full symmetry structure of

$$\mathrm{SU}(3)_{\mathrm{color}} \times \mathrm{SU}(3)_{\mathrm{L}} \times \mathrm{SU}(3)_{\mathrm{R}} \times \mathrm{U}(1)_{\mathrm{V}} \times \mathrm{U}(1)_{\mathrm{A}}. \quad (3.2.4)$$

A non-vanishing chiral quark condensate $\langle \bar{\psi}\psi \rangle$ implies that chiral symmetry is spontaneously broken² and we remain with

$$\mathrm{SU}(3)_{\mathrm{color}} \times \mathrm{SU}(3)_{\mathrm{V}} \times \mathrm{U}(1)_{\mathrm{V}} \times \mathrm{U}(1)_{\mathrm{A}}. \quad (3.2.5)$$

in the case of degenerate current quark masses³. However, we know that the classical axial $\mathrm{U}(1)$ symmetry is broken by quantum effects, which constitutes the so-called ‘‘axial anomaly’’⁴: the four-dimensional axial vector current is not conserved, as one finds, even for vanishing current quark masses,

$$\partial_\mu j^{\mu 5} = \partial_\mu \bar{\psi} \gamma_\mu \gamma_5 \psi = -\frac{g^2 N_f}{32\pi^2} \epsilon^{\mu\nu\lambda\sigma} G_{\mu\nu}^a G_{\lambda\sigma}^a \quad (3.2.6)$$

with the gluonic field strength tensor $G_{\mu\nu}^a$ and the four-dimensional totally antisymmetric Levi-Civita symbol $\epsilon^{\mu\nu\lambda\sigma}$ [1, 15]. In the NJL model the anomaly is realized by the inclusion of the following term that conserves chiral symmetry but breaks $\mathrm{U}(1)_{\mathrm{A}}$:

$$\mathcal{L}_{\mathrm{KMT}} = K \left[\det_f \left(\bar{\psi} \frac{1 + \gamma_5}{2} \psi \right) + \det_f \left(\bar{\psi} \frac{1 - \gamma_5}{2} \psi \right) \right]. \quad (3.2.7)$$

Interactions of the type (3.2.7) have been first considered by Kobayashi and Maskawa [84, 83] and further developed by ’t Hooft [125, 126]. In that work it was also shown that the term arises naturally from instanton interactions which solves the so-called ‘‘ $\mathrm{U}_{\mathrm{A}}(1)$ puzzle’’: before, it was unknown why the empirical mass of the η' meson, the $\mathrm{SU}(3)$ singlet, is more than twice as large as that of its octet counterpart, the η meson, see Fig. 3.1 and Table 3.1. The Kobayashi–Maskawa–’t Hooft (KMT) term is repulsive in the η' channel so that $m_{\eta'}$ is lifted away from the Goldstone sector. The KMT coupling strength K is equivalent to the strength of the axial anomaly in the model.

Following these considerations we use the following Lagrangian in the calculation:

$$\mathcal{L} = \mathcal{L}_{\mathrm{kin}} + \mathcal{L}_{\mathrm{int}} + \mathcal{L}_{\mathrm{KMT}}. \quad (3.2.8)$$

In chapter 7, it will be augmented by a vector interaction term. This combination, plus an axial vector term, is a natural result if one Fierz transforms a color current-current interaction motivated by QCD, and then drops color non-singlet channel terms [135].

For our calculations, we construct an effective thermodynamic potential⁵ Ω , which is defined by

$$\mathcal{Z} =: \exp^{-\Omega V/T} \quad \text{or, equivalently,} \quad \Omega = -\frac{\ln \mathcal{Z}}{V^{(4)}}, \quad (3.2.9)$$

where $V^{(4)} = \beta V$ is the 4-dimensional volume and \mathcal{Z} is the partition function

$$\mathcal{Z} = \int \mathcal{D}\bar{\psi} \mathcal{D}\psi e^{-S_{\mathrm{E}}}. \quad (3.2.10)$$

with the Euclidean action $S_{\mathrm{E}} = \int d^4 x_{\mathrm{E}} \mathcal{L}_{\mathrm{E}}$ and $\mathcal{L}_{\mathrm{E}} = -\mathcal{L}$. In the following the subscript ‘‘E’’ for the Euclidean formulation will be dropped. Details about these definitions as well as the

²as well as explicitly by the nonvanishing current quark masses to a small degree

³The flavor symmetry $\mathrm{SU}(3)_{\mathrm{V}}$ is then broken by non-degenerate current quark masses with $m_s > m_u \approx m_d$.

⁴also called Adler-Bell-Jackiw anomaly [1, 15]

⁵More precisely, it is the thermodynamic potential *density*, i.e. the thermodynamic potential per volume V . This designation is usually omitted.

Wick rotation from real to imaginary time, which is then identified with the inverse temperature dimension, the evaluation of thermal propagators and Matsubara sums etc. are part of standard thermal field theory textbook knowledge so that we will not elaborate them here. The goal of this chapter is to give an understanding of the necessary steps taken and the approximations that were used to arrive at the effective thermodynamic potential Ω .

3.3 Bosonization for three quark flavors

We proceed by ‘bosonizing’ the Lagrangian, by which fermionic degrees of freedom are replaced by effective bosonic degrees of freedom. In the two-flavor case, this procedure is easily done with a Hubbard-Stratonovich transformation [70, 123]. For three flavors, the process is more involved. It is instructive to follow the process to some degree, in particular to see where various approximations are applied. We outline here the major steps and refer for details to [21] based on work from [80, 111, 118], or to [67], where the framework is generalized to non-local interactions.

Our first goal is to re-write the KMT interaction term (3.2.7) into a more suitable form. For this, we define

$$(J_{\pm}(x))_{fg} = \bar{\psi}_f(x) \frac{1}{2} (1 \mp \gamma_5) \psi_g(x) \quad (3.3.1)$$

with flavor indices f and g so that

$$\mathcal{L}_{\text{KMT}} = K (\det_f J_+ + \det_f J_-). \quad (3.3.2)$$

The flavor structure of the matrices J_{\pm} can be expressed in terms of the Gell-Mann matrices,

$$J_{\pm} = \sum_{a=0}^8 c_a^{\pm} \lambda^a \quad \text{with 18 coefficients} \quad c_a^{\pm} = \frac{1}{2} \text{tr} [\lambda^a J_{\pm}], \quad (3.3.3)$$

where we have used $\text{tr} [\lambda^a \lambda^b] = 2\delta_{ab}$. Applying the Newton-Girard formulae, the determinant of any 3×3 matrix can be written as

$$\det A = \frac{1}{6} (\text{tr} [A])^3 - \frac{1}{2} \text{tr} [A] \text{tr} [A^2] + \frac{1}{3} \text{tr} [A^3]. \quad (3.3.4)$$

We then have

$$\det J_{\pm} = \left(\sqrt{\frac{2}{3}} \right)^3 (c_0^{\pm})^3 - \sqrt{\frac{2}{3}} \sum_{m=1}^8 c_0^{\pm} (c_m^{\pm})^2 + \frac{2}{3} \sum_{l,m,n=1}^8 d^{lmn} c_l^{\pm} c_m^{\pm} c_n^{\pm} \quad (3.3.5)$$

with the totally symmetric anticommutator structure constants d^{lmn} of SU(3) (see appendix A.1.1).

The interaction term \mathcal{L}_{int} in (3.2.3) can also be expressed in term of c_a^{\pm} . The generators $t^m = \frac{1}{2} \lambda^m$ of SU(N) in the fundamental representation fulfill the relation

$$(t^m)_{ij} (t^m)_{kl} = \frac{1}{2} \left(\delta_{il} \delta_{kj} - \frac{1}{N} \delta_{ij} \delta_{kl} \right) \quad (3.3.6)$$

with a summation over $m = 1, \dots, 8$. From this we derive, with the λ^a instead of the t^m and an $a = 0$ term included:

$$\sum_{a=0}^8 (\lambda^a)_{ij} (\lambda^a)_{kl} = 2 \left(\delta_{il} \delta_{kj} - \frac{1}{3} \delta_{ij} \delta_{kl} \right) + \frac{2}{3} \delta_{ij} \delta_{kl} = 2\delta_{il} \delta_{kj}. \quad (3.3.7)$$

Using $(J^{\pm})_{ij} = \frac{1}{2} (\bar{\psi}_i \psi_j \pm \bar{\psi}_i \gamma_5 \psi_j)$, we then find

$$\begin{aligned} c_a^+ c_a^- &= \frac{1}{4} \text{tr} [\lambda^a J^+] \text{tr} [\lambda^a J^-] = \frac{1}{4} \lambda_{ij}^a J_{ji}^+ \lambda_{kl}^a J_{lk}^- = \frac{1}{2} \delta_{il} \delta_{jk} J_{ji}^+ J_{lk}^- = \frac{1}{2} J_{ji}^+ J_{ij}^- \\ &= \frac{1}{8} (\bar{\psi}_i \psi_j - \bar{\psi}_i \gamma_5 \psi_j) (\bar{\psi}_j \psi_i - \bar{\psi}_j \gamma_5 \psi_i) = \frac{1}{8} [(\bar{\psi}_i \psi_j) (\bar{\psi}_j \psi_i) - (\bar{\psi}_i \gamma_5 \psi_j) (\bar{\psi}_j \gamma_5 \psi_i)]. \end{aligned} \quad (3.3.8)$$

Again with the help of relation (3.3.7) we write

$$(\bar{\psi}\lambda^a\psi)^2 = \bar{\psi}_i\lambda_{ij}^a\psi_j\bar{\psi}_k\lambda_{kl}^a\psi_l = 2\bar{\psi}_i\psi_j\bar{\psi}_j\psi_i \quad (3.3.9)$$

and then, combining eqs. (3.3.8) and (3.3.9), obtain

$$16c_a^+c_a^- = (\bar{\psi}\lambda^a\psi)^2 + (\bar{\psi}i\lambda^a\gamma_5\psi)^2. \quad (3.3.10)$$

Finally, \mathcal{L}_{int} can be expressed as

$$\mathcal{L}_{\text{int}} = \frac{G}{2} \sum_{a=0}^8 \left[(\bar{\psi}\lambda^a\psi)^2 + (\bar{\psi}\lambda^a i\gamma_5\psi)^2 \right] = 8G \sum_{a=0}^8 c_a^+c_a^-. \quad (3.3.11)$$

We now introduce 18 bosonic fields M_a^+ , M_a^- as well as 18 auxiliary fields ξ_a^+ , ξ_a^- by inserting into the Euclidean partition function

$$\mathcal{Z} = \int \mathcal{D}\psi\mathcal{D}\bar{\psi} \exp \left\{ \int d^4x (\mathcal{L}_{\text{kin}} + \mathcal{L}_{\text{3-flavor}} + \mathcal{L}_{\text{KMT}}) \right\}, \quad (3.3.12)$$

unity in the form (in Euclidean formulation):

$$\begin{aligned} 1 &= \int \prod_a \mathcal{D}\xi_a^+ \int \prod_a \mathcal{D}\xi_a^- \delta(\xi_a^+ - c_a^+) \delta(\xi_a^- - c_a^-) \\ &= \int \prod_a \mathcal{D}\xi_a^+ \prod_a \mathcal{D}\xi_a^- \prod_a \mathcal{D}M_a^+ \prod_a \mathcal{D}M_a^- \exp \left\{ \int d^4x [M_a^+ (\xi_a^+ - Kc_a^+) + M_a^- (\xi_a^- - Kc_a^-)] \right\}. \end{aligned} \quad (3.3.13)$$

The integration over the fermionic fields $\bar{\psi}$ and ψ is performed first; the relevant parts have been collected in

$$\tilde{\mathcal{Z}}_\psi = \int \mathcal{D}\psi\mathcal{D}\bar{\psi} \exp \left\{ \int d^4x [\bar{\psi}_f (i\hat{\not{\partial}} - \hat{m}_0) \psi_f - KM_a^+c_a^+ - KM_a^-c_a^-] \right\}. \quad (3.3.14)$$

Note that the c_a^\pm are functions of those fields, see eqs. (3.3.1) and (3.3.3). With the definition of the c_a^\pm in eq. (3.3.3), we find

$$\sum_a M_a^\pm c_a^\pm = \frac{1}{2} \sum_a M_a^\pm \sum_{f,g} (\lambda^a)_{fg} J_{gf}^\pm(x) = \bar{\psi}_g(x) \sum_a \left[\frac{1}{2} M_a^\pm(x) \lambda^a \left(\frac{1 \pm \gamma_5}{2} \right) \right] \psi_f(x). \quad (3.3.15)$$

Using this relation and $\int \mathcal{D}\eta \int \mathcal{D}\bar{\eta} \exp(-\bar{\eta}\hat{\mathcal{O}}\eta) = \det \hat{\mathcal{O}}$ for a matrix (operator) $\hat{\mathcal{O}}$, we evaluate the integration in eq. (3.3.14) to

$$\tilde{\mathcal{Z}}_\psi = \exp(\log \det X), \quad (3.3.16)$$

where we have defined the matrix X implicitly by

$$\log \det X = \text{tr} \log \left[i\hat{\not{\partial}} - \hat{m}_0 - \frac{K}{2} \sum_a M_a^-(x) \left(\frac{1 + \gamma_5}{2} \right) \lambda_a - \frac{K}{2} \sum_a M_a^+(x) \left(\frac{1 - \gamma_5}{2} \right) \lambda_a \right]. \quad (3.3.17)$$

Integrations over the ξ_a^\pm and the M_a^\pm remain. A possible next step would be the integration over the fields ξ_a^\pm ,

$$\tilde{\mathcal{Z}}_\xi = \int \prod_a (\mathcal{D}\xi_a^- \mathcal{D}\xi_a^+) \exp \left\{ \int d^4x \left[\frac{8G}{K^2} \xi_a^+ \xi_a^- + K \det J_+ + K \det J_- + iM_a^+ \xi_a^+ + iM_a^- \xi_a^- \right] \right\}. \quad (3.3.18)$$

Instead, it is more convenient to change the auxiliary fields here. Looking at the comparatively simple interaction term (3.2.3), we define, inspired by the treatment of the pure 4-point interaction formalism, scalar and pseudoscalar fields:

$$S_a = \bar{\psi} \lambda^a \psi, \quad (3.3.19)$$

$$P_a = \bar{\psi} i \gamma_5 \lambda^a \psi, \quad (3.3.20)$$

with $a = 0, \dots, 8$. Comparing with eq. (3.3.10), we find

$$16 c_a^+ c_a^- = S_a^2 + P_a^2. \quad (3.3.21)$$

Moreover,

$$c_a^\pm = \frac{1}{2} \text{tr} [\lambda^a J_\pm] = \frac{1}{4} (\lambda^a \bar{\psi} (1 \mp \gamma_5) \psi) = \frac{1}{4} (\bar{\psi} (\lambda^a)^\top (1 \mp \gamma_5) \psi). \quad (3.3.22)$$

Because of the structure of the Gell-Mann matrices we have

$$(\lambda^a)^\top = (\lambda^a)^* = v_a \lambda^a, \quad (3.3.23)$$

where we have defined

$$v_a = \begin{cases} -1, & a \in \{2, 5, 7\}, \\ +1, & a \in \{0, 1, 3, 4, 6, 8\}, \end{cases} \quad (3.3.24)$$

discerning between the symmetric and the antisymmetric λ^a . Inserting this into eq. (3.3.22), we write

$$c_a^\pm = v_a \frac{1}{4} (\bar{\psi} \lambda^a (1 \mp \gamma_5) \psi) = v_a \frac{1}{4} [(\bar{\psi} \lambda^a \psi) \pm i (\bar{\psi} i \gamma_5 \lambda^a \psi)] = v_a \frac{1}{4} [S_a \pm i P_a]. \quad (3.3.25)$$

To stay consistent, we also have to introduce new auxiliary fields ρ_a and π_a instead of M_a^\pm :

$$\rho_a = \frac{K}{4} (M_a^+ + M_a^-), \quad (3.3.26)$$

$$\pi_a = i \frac{K}{4} (M_a^+ - M_a^-), \quad (3.3.27)$$

and conversely

$$M_a^\pm = \frac{2}{K} (\rho_a \mp i \pi_a). \quad (3.3.28)$$

The relation $\xi_a^\pm = K c_a^\pm$ is enforced by the delta distributions in eq. (3.3.13). Together with eq. (3.3.5) we have all necessary pieces to rewrite $\tilde{\mathcal{Z}}_\xi \mapsto \tilde{\mathcal{Z}}_{S,P}$:

$$\begin{aligned} \tilde{\mathcal{Z}}_{S,P} = & \int \prod_a (\mathcal{D}S_a \mathcal{D}P_a) \exp \left\{ \int d^4x \frac{K}{64} \left[\frac{4}{3} \sqrt{\frac{2}{3}} (S_0^3 - 3S_0 P_0^2) - \right. \right. \\ & \left. \left. - 2\sqrt{\frac{2}{3}} \sum_{m=1}^8 (S_0 S_m^2 - S_0 P_m^2 - 2S_m P_0 P_m) + \frac{4}{3} \sum_{l,m,n=1}^8 d^{lmn} (S_l S_m S_n - 3S_l P_m P_n) \right] + \right. \\ & \left. + \sum_{a=0}^8 (\rho_a S_a + \pi_a P_a) + \sum_{a=0}^8 \frac{G}{2} (S_a^2 + P_a^2) \right\}. \quad (3.3.29) \end{aligned}$$

We have used $v_a^2 = 1$ for all a and $v_0 = +1$. The only other place where the v_a still occurred was in front of the the totally symmetric d^{lmn} . It can, however, be shown (see appendix A.1.2) that

$$v_l v_m v_n d^{lmn} = d^{lmn} \quad (3.3.30)$$

so that all v_a are eliminated from the calculation. The result in eq. (3.3.29) can be displayed in an elegant compact form by defining

$$A_{abc} := \frac{1}{3!} \epsilon_{ijk} \epsilon_{mnl} \lambda_{im}^a \lambda_{jn}^b \lambda_{kl}^c, \quad (3.3.31)$$

with $a, b, c = 0, \dots, 8$. Then, $\tilde{Z}_{S,P}$ is written more neatly as

$$\tilde{Z}_{S,P} = \int \prod_a (\mathcal{D}S_a \mathcal{D}P_a) \exp \left[\int d^4x \sum_{a=0}^8 \left\{ \rho_a S_a + \pi_a P_a + \frac{G}{2} [S_a^2 + P_a^2] + \frac{K}{4} A_{abc} [S_a S_b S_c - 3S_a P_b P_c] \right\} \right] \quad (3.3.32)$$

after a tedious but straight-forward calculation, where an overall constant has been neglected. The same variable change in the fermion determinant (3.3.17) results in

$$\log \det X = \text{tr} \log \left[i\not{\partial} - \hat{m}_0 - \sum_a \lambda^a \rho_a - i\gamma_5 \sum_a \lambda^a \pi_a \right]. \quad (3.3.33)$$

The integral in eq. (3.3.32) is not analytically solvable because of the cubic term. We therefore proceed by applying the stationary phase approximation, where the integral over the exponential function is assumed to be dominated by the extremal configuration of the exponent. The minimizing values $\tilde{S}_a(\rho_b, \pi_c)$ and $\tilde{P}_a(\rho_b, \pi_c)$ are given implicitly by the conditions

$$\rho_a + G\tilde{S}_a + \frac{3K}{4} A_{abc} [\tilde{S}_b \tilde{S}_c - \tilde{P}_b \tilde{P}_c] = 0 \quad (3.3.34)$$

and

$$\pi_a + G\tilde{P}_a - \frac{3H}{2} A_{abc} \tilde{S}_b \tilde{P}_c = 0. \quad (3.3.35)$$

We then have

$$\mathcal{Z} = \int \prod_a (\mathcal{D}\rho_a \mathcal{D}\pi_a) e^{-S^{\text{bos}}}, \quad (3.3.36)$$

where

$$S^{\text{bos}} = -\log \det X - \int d^4x \left\{ \rho_a \tilde{S}_a + \pi_a \tilde{P}_a + \frac{G}{2} [\tilde{S}_a^2 + \tilde{P}_a^2] + \frac{K}{4} A_{abc} [\tilde{S}_a \tilde{S}_b \tilde{S}_c - 3\tilde{S}_a \tilde{P}_b \tilde{P}_c] \right\}. \quad (3.3.37)$$

In this work, we consider only the mean field scenario. In this approximation, we assume non-vanishing global mean field values $\bar{\rho}_a$ for the scalar⁶ fields ρ_a and zero mean field values of the pseudoscalar fields π_a as follows:

$$\begin{aligned} \rho_a(x) &= \bar{\rho}_a + \delta\rho_a(x), \\ \pi_a(x) &= \delta\pi_a(x). \end{aligned} \quad (3.3.38)$$

Fluctuation terms $\delta\rho_a$ and $\delta\pi_a$ will be dropped in this expansion. Further, only fields invariant under the charge conjugation operation \mathcal{C} can be non-vanishing. From the infinitesimal transformation law

$$\psi \xrightarrow{\mathcal{C}} \bar{\psi} \lambda^a \psi + \bar{\psi} i\alpha [\lambda^a, \hat{Q}] \psi + \mathcal{O}(\alpha^2) \quad (3.3.39)$$

⁶The symmetry properties of these auxiliary fields can be inferred from eqs. (3.3.13), (3.3.26) and (3.3.27).

it follows that only the expectation values $\bar{\rho}_0$, $\bar{\rho}_3$ and $\bar{\rho}_8$ remain in the physical realm. The same is true for the fields $\bar{S}_a := \tilde{S}_a(\bar{\rho}_b, 0)$. For them and for the $\bar{\rho}_a$ it is then convenient to switch to the physical quark flavor basis by defining

$$\begin{aligned}\bar{S}_u &:= \sqrt{\frac{2}{3}}\bar{S}_0 + \bar{S}_3 + \frac{1}{\sqrt{3}}\bar{S}_8, \\ \bar{S}_d &:= \sqrt{\frac{2}{3}}\bar{S}_0 - \bar{S}_3 + \frac{1}{\sqrt{3}}\bar{S}_8, \\ \bar{S}_s &:= \sqrt{\frac{2}{3}}\bar{S}_0 - \frac{2}{\sqrt{3}}\bar{S}_8,\end{aligned}\tag{3.3.40}$$

and the same for the $\bar{\rho}_a$. The following steps are lengthy but straight-forward textbook calculations and we arrive at the bosonized Euclidean mean field action

$$\frac{S^{\text{MFA}}}{V^{(4)}} = -2 \int \frac{d^4p}{(2\pi)^4} \text{Tr}_f \text{Tr}_c \log \left[p^2 \mathbf{1}_{3 \times 3} + \hat{M}^2 \right] - \frac{1}{2} \left[\sum_i \left(\bar{\rho}_i \bar{S}_i + \frac{G}{2} \bar{S}_i \bar{S}_i \right) + \frac{K}{2} \bar{S}_u \bar{S}_d \bar{S}_s \right].\tag{3.3.41}$$

The fermion determinant was transformed to momentum space and we left unevaluated the traces in flavor space, Tr_f , and in color space, Tr_c . We have defined a preliminary effective mass matrix, $\hat{M} = \text{diag}(M_u, M_d, M_s)$, with effective quark masses $M_i = m_i + \bar{\rho}_i$. In order to be consistent with previous work, we redefine at this point

$$\sigma_a := G \bar{S}_a \quad \text{and} \quad K \rightarrow -2K.\tag{3.3.42}$$

The sign change in K renders this important quantity positive. It amounts to a definition of

$$\mathcal{L}_{\text{KMT}} = -K \left[\det_f (\bar{\psi} (1 + \gamma_5) \psi) + \det_f (\bar{\psi} (1 - \gamma_5) \psi) \right].\tag{3.3.43}$$

The fields σ_u , σ_d and σ_s are the mean field chiral condensates. In our convention they are given by

$$\sigma_q = 2G \langle \bar{q}q \rangle\tag{3.3.44}$$

for each quark flavor q and turn out negative in the calculations⁷. Evaluating the equations self-consistently in the flavor basis, we arrive at the final effective quark masses

$$\begin{aligned}M_u &= m_u - \sigma_u + \frac{K}{2G^2} \sigma_d \sigma_s, \\ M_d &= m_d - \sigma_d + \frac{K}{2G^2} \sigma_s \sigma_u, \\ M_s &= m_s - \sigma_s + \frac{K}{2G^2} \sigma_u \sigma_d.\end{aligned}\tag{3.3.45}$$

With these definitions, we find for the effective thermodynamic potential defined in eq. (3.2.9):

$$\Omega = \Omega_{\text{fermion}} + \frac{\sigma_u^2}{4G} + \frac{\sigma_d^2}{4G} + \frac{\sigma_s^2}{4G} - \frac{K}{2G^3} \sigma_u \sigma_d \sigma_s,\tag{3.3.46}$$

where Ω_{fermion} is from the evaluation of the fermion determinant. For that part, we can apply standard thermal field theory methods, as the differences to the free fermion case so far can be absorbed in to the effective mass definitions as above. So far, we have then

$$\Omega_{\text{fermion}}^{(1)} = -T \sum_n \int \frac{d^3p}{(2\pi)^3} \text{Tr} \log \left[\beta \left(i\omega_n \gamma_0 + \vec{\gamma} \cdot \vec{p} + \hat{M} \right) \right].\tag{3.3.47}$$

⁷Provided a consistent cutoff scheme is used with the effective thermodynamic potential, see chapter 4.

For details on fermionic Matsubara propagator and frequencies $\omega_n = (2n + 1)\pi T$, see [75]. For calculations at finite quark chemical potentials, one has to replace

$$\omega_n \longrightarrow \begin{cases} \omega_n - i\hat{\mu} & \text{for quarks,} \\ \omega_n + i\hat{\mu} & \text{for antiquarks,} \end{cases} \quad (3.3.48)$$

with the flavor chemical potential matrix $\hat{\mu} = \text{diag}(\mu_u, \mu_d, \mu_s)$. For the different treatment of quarks and antiquarks, we use the Nambu-Gor'kov representation [58, 97] of the inverse propagator:

$$S^{-1}(\omega_n, \vec{p}) = \frac{1}{2} \begin{pmatrix} (i\omega_n + \hat{\mu})\gamma_0 + \vec{\gamma} \cdot \vec{p} + \hat{M} & 0 \\ 0 & (i\omega_n - \hat{\mu})\gamma_0 + \vec{\gamma} \cdot \vec{p} + \hat{M} \end{pmatrix}. \quad (3.3.49)$$

The trace in

$$\Omega_{\text{fermion}}^{(2)} = -T \sum_n \int \frac{d^3p}{(2\pi)^3} \text{Tr} \log [\beta S^{-1}(\omega_n, \vec{p})]. \quad (3.3.50)$$

then includes the trace over the Nambu-Gor'kov space

In this work, we will for the most part use a flavor-independent chemical potential $\mu := \mu_u = \mu_d = \mu_s$. In chapter 7, we will discuss consequences of $\mu_u = \mu_d \neq \mu_s$ and conduct some exploratory studies for three independent flavor chemical potentials.

3.4 NJL parameter sets

The model has several parameters: the four-fermion coupling strength G , the KMT coupling strength K , the cutoff scale Λ (see chapter 4) and the current quark masses m_u , m_d and m_s . We have not produced our own parameter set, but use numbers available in the literature that fit the vacuum masses of the pseudoscalar meson octet and singlet (see Fig. 3.1 and Table 3.1) well.

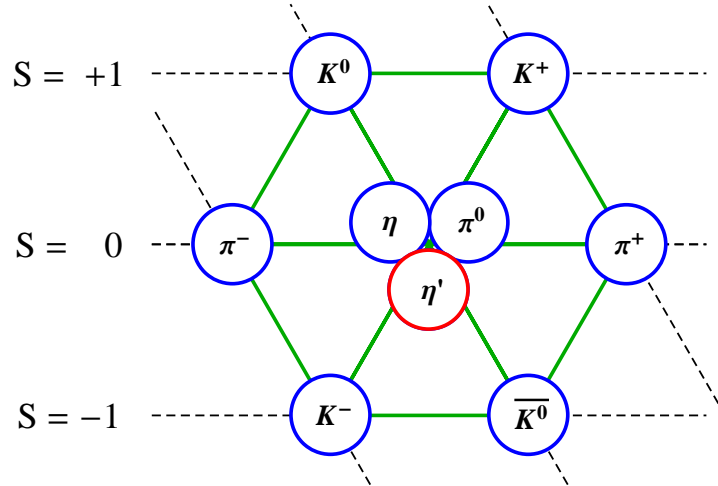


Fig. 3.1: Pseudoscalar meson nonet. The observed particles η and η' are products of the mixing between the singlet η_1 particle and the octet η_8 particle. Approximately, the η' is a singlet (red) whereas the η meson belongs to the octet (blue). Plot from [21].

Several input parameter sets for the NJL model with 2+1 flavors are available, see Table 3.2. Differences between the “HK” set from [63] and the “RKH” set from [110] stem from the different treatment of the η' mass. Since it is larger than the $\bar{q}q$ decay threshold, an imaginary part appears in the $\bar{q}q$ polarization diagram [26] that has to be dealt with to find a physical, real-valued mass. The “LKW” set from [92] has been determined with an extended Lagrangian including vector

particle	π^\pm [MeV]	π^0 [MeV]	K^\pm [MeV]	K^0 [MeV]	η [MeV]	η' [MeV]
mass	140	135	494	498	548	958

Table 3.1: Masses of the light pseudoscalar mesons [16]

and axial-vector interaction terms. Despite the apparent differences, all sets produce very good fits to the empirically determined mass spectrum in Table 3.1. In this work, we will mostly use the RKH parameter set for easier comparison with earlier work [127, 26, 21]. Results for the particle masses from this set are shown in Table 3.3.

For chapter 7, we examine all three sets in calculations including vector interaction terms. We find that the ‘‘RKH’’ parameter set produces results notably different from those of the other two sets. For that reason, we will switch to the ‘‘LKW’’ set as a standard set in that chapter. Results for the physical quantities from that set are presented in Table 3.4. Note that, because of the inclusion of vector and axial vector interactions, they also produce numbers for $m_{\rho,\omega}$, m_{K^*} and m_ϕ .

acronym	Λ [MeV]	$G\Lambda^2$	$K\Lambda^5$	$m_{u,d}$ [MeV]	m_s [MeV]	reference
RKH	602.3	3.67	12.36	5.5	140.7	[110]
HK	631.4	3.67	9.29	5.5	135.7	[63]
LKW	750	3.64	8.9	3.6	87	[92]

Table 3.2: Selection of different three-flavor NJL parameter sets with their respective sources

f_π [MeV]	m_π [MeV]	m_K [MeV]	m_η [MeV]	$m_{\eta'}$ [MeV]
92.4	135	479.7	514.8	957.8
$M_{u,d}$ [MeV]	M_s [MeV]	$ \langle\bar{\psi}_u\psi_u\rangle ^{1/3}$ [MeV]	$ \langle\bar{\psi}_s\psi_s\rangle ^{1/3}$ [MeV]	
367.7	549.5	-241.9	-257.7	

Table 3.3: Physical quantities resulting from the ‘‘RKH’’ parameter values from [110], see Table 3.2

f_π [MeV]	m_π [MeV]	m_K [MeV]	m_η [MeV]	$m_{\eta'}$ [MeV]	$M_{u,d}$ [MeV]
93	139	498	519	963	361
M_s [MeV]	$ \langle\bar{\psi}_u\psi_u\rangle ^{1/3}$ [MeV]	$ \langle\bar{\psi}_s\psi_s\rangle ^{1/3}$ [MeV]	$m_{\rho,\omega}$ [MeV]	m_{K^*} [MeV]	m_ϕ [MeV]
501	-287	-306	765	864	997

Table 3.4: Physical quantities resulting from the ‘‘LKW’’ parameter values from [63], see Table 3.2

3.5 Polyakov loop dynamics

As the NJL model was originally developed to describe nucleon dynamics, it has no notion of confinement. Color confinement is, however, a feature of prime importance for the QCD phase diagram. We have discussed in section 2.3 that the Polyakov loop, defined in eq. (2.3.2), is an order parameter of the associated symmetry.

It was mainly Fukushima’s idea⁸ that an effective potential, determined from pure glue results, could be used to govern the behavior of the Polyakov loop as a function of temperature, while connecting it to the quarks (implemented in the NJL formalism) via the gluonic background [50]. Interestingly, the two notions, conceived at different ends of the mass spectrum, namely the heavy quark limit for the Polyakov loop, and the chiral limit for the NJL model, could be meaningfully combined in a single model. In this so-called Polyakov–Nambu–Jona-Lasinio, or PNJL, model, both Polyakov loop and chiral condensate retained their status as order parameters⁹.

Requiring little computational power compared to lattice QCD (see section 2.4), the model is well suited to reproduce its results, as well as extend calculations to finite chemical potentials. In particular, the “locking” of the chiral transition and the Polyakov loop, i.e. (de-)confinement, transition is considered a great success.

In the model, spontaneous $Z(3)$ symmetry breaking is enforced by means of an effective Polyakov loop potential \mathcal{U} . Assuming a constant, purely temporal gluonic background field (working in the Polyakov gauge), the Polyakov loop is expressed solely by the diagonal Gell-Mann matrices λ_3 and λ_8 :

$$\Phi = \frac{1}{3} \text{tr} \left[e^{i(\phi_3 \lambda_3 + \phi_8 \lambda_8)} \right], \quad (3.5.1)$$

where we have defined $\phi_a := A_4^a/T$. Nondiagonal matrices can be integrated out from the gluonic partition function [50]; their influence is contained in the group structure, i.e. in the Haare measure, expressed in terms of the Polyakov loop:

$$J(\Phi, \Phi^*) = \frac{9}{8\pi^2} \left(1 - 6\Phi\Phi^* + 4(\Phi^3 + \Phi^{*3}) - 3(\Phi\Phi^*)^2 \right). \quad (3.5.2)$$

This piece is included in the Polyakov loop effective potential $\mathcal{U}(T, \Phi, \Phi^*)$. The most common ansatz is the phenomenological one from [117] that we will also use in this work:

$$\frac{\mathcal{U}(T, \Phi, \Phi^*)}{T^4} = -\frac{1}{2}b_2(T)\Phi\Phi^* + b_3 \left(\frac{T_0}{T} \right)^3 \ln \left[1 - 6\Phi\Phi^* + 4(\Phi^3 + \Phi^{*3}) - 3(\Phi\Phi^*)^2 \right] \quad (3.5.3)$$

with

$$b_2(T) = a_0 + a_1 \left(\frac{T_0}{T} \right) + a_2 \left(\frac{T_0}{T} \right)^2. \quad (3.5.4)$$

Its construction is based on the notion that the potential should first reproduce lattice QCD results in the pure glue system. Results for the parameters are listed in Table 3.5.

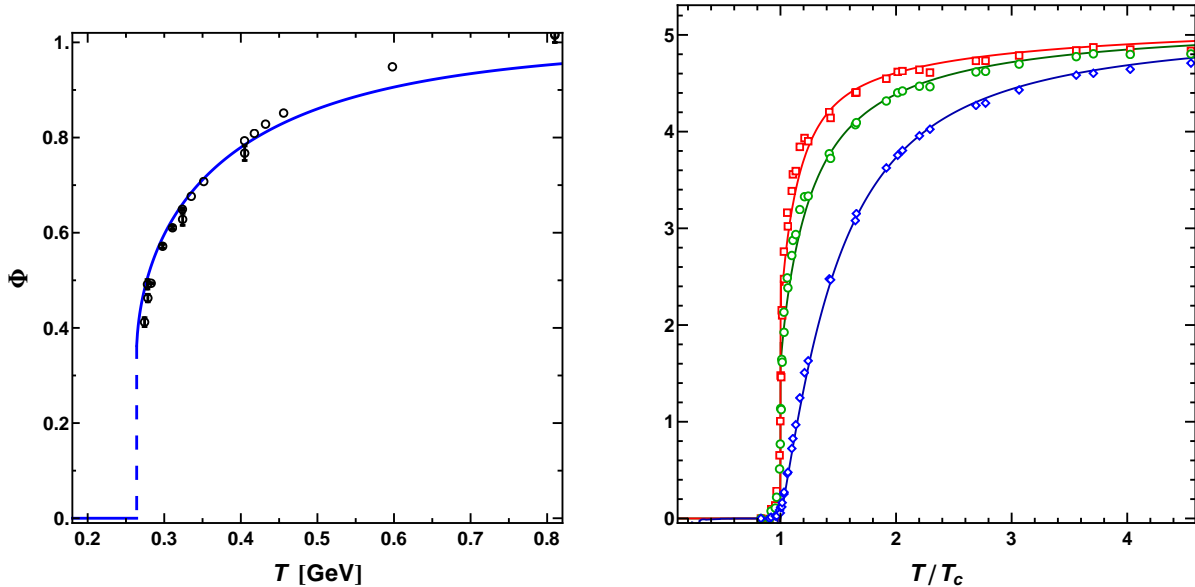
T_0	a_0	a_1	a_2	b_3
270 MeV	3.51	-2.47	15.2	-1.7

Table 3.5: Parameters for the Polyakov loop effective potential in (3.5.3), from [117].

⁸Based on an earlier suggestion by Meisinger and Ogilvie [96]

⁹More precisely: *approximate* order parameters, as both pertinent symmetries are in addition explicitly broken by the non-vanishing, non-infinite current quark masses. The effects are small.

The fits are presented in Figures 3.2a (Polyakov loop Φ) and 3.2b (pressure p , energy density ϵ and entropy density s). The potential \mathcal{U} is then added unchanged to the effective thermodynamic



(a) Fit to the Polyakov loop

(b) From top to bottom: fit to normalized energy density ϵ/T^4 (red), entropy density $3/4 s/T^4$ (green) and pressure $3p/T^4$ (blue)

Fig. 3.2: Simultaneous fit of Polyakov loop effective potential parameters in (3.5.3) to lattice QCD data. Polyakov loop from [73], thermodynamic quantities from [20].

potential from the NJL part of the model. We discuss this ansatz and the effects of variations of \mathcal{U} on the 2+1 flavor calculations in more detail in chapter 6. The rescaled potential $\mathcal{U}(T, \Phi, \Phi^*)/T^4$ is plotted in Fig. 3.3 for a series of ratios T/T_0 for illustration, with $\Phi = \Phi^* \in \mathbb{R}$. Indeed, in the mean field scenario we can, without loss of generality, set $\phi_8 \equiv 0$ from which $\Phi = \Phi^*$ follows [115].

There is an ongoing effort to develop a Polyakov loop effective potential from underlying principles, e. g. [23, 55]. Kondo has shown that the nonlocal version of the PNJL model [57, 68, 67] can be deduced from first principles QCD [85]. The local variant used in this work is then just another simplifying assumption.

The fermionic propagator is minimally coupled to the gluonic background with the additional replacement rule

$$\omega_n \longrightarrow \begin{cases} \omega_n + A_4 & \text{for quarks} \\ \omega_n - A_4 & \text{for antiquarks.} \end{cases} \quad (3.5.5)$$

in the fermionic propagator matrix S^{-1} in def. (3.3.49).

3.6 Thermodynamic potential and quasiparticle energy eigenvalues

The thermodynamic potential in def. 3.3.50 is then evaluated by performing the Matsubara summation (see e. g. [75]) and we find:

$$\begin{aligned} \Omega' = & -\frac{1}{2} \int \frac{d^3p}{(2\pi)^3} E_p - T \int \frac{d^3p}{(2\pi)^3} \log \left[1 + e^{-E_p/T} \right] \\ & + \frac{\sigma_u^2}{4G} + \frac{\sigma_d^2}{4G} + \frac{\sigma_s^2}{4G} - \frac{K}{2G^3} \sigma_u \sigma_d \sigma_s + \mathcal{U}(\Phi, \Phi^*, T). \end{aligned} \quad (3.6.1)$$

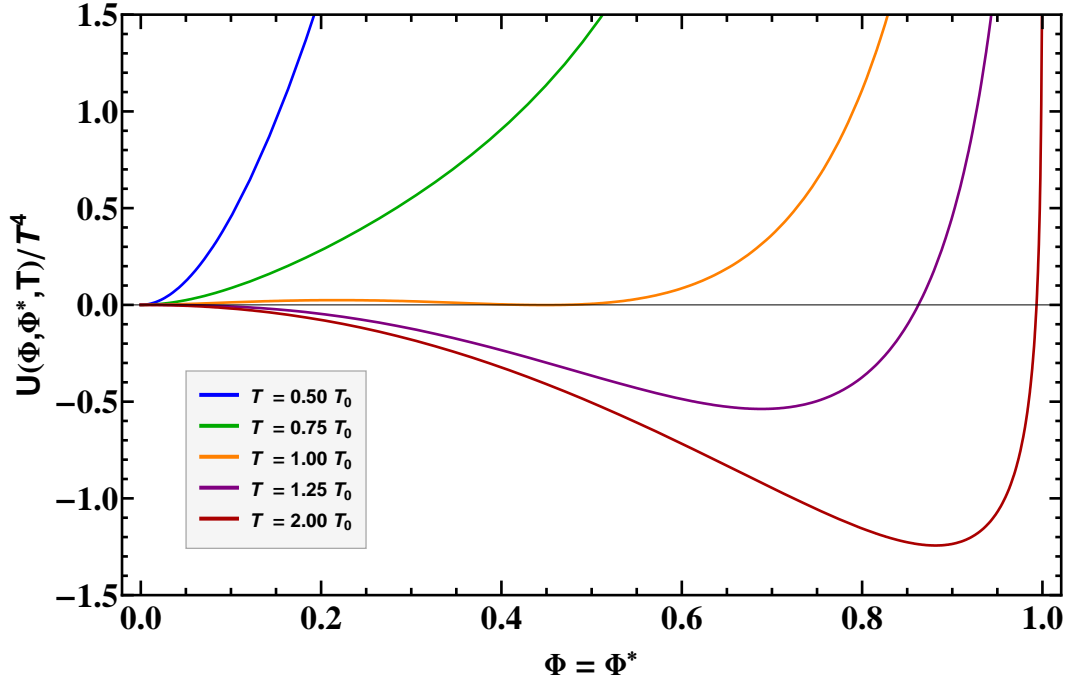


Fig. 3.3: Pure gauge Polyakov loop effective potential \mathcal{U} according to def. (3.5.3) as a function of $\Phi = \Phi^*$ at different temperatures, expressed in relation to $T_0 = 270$ MeV

The designation Ω' is given because this is still a preliminary result: as a consequence of the non-renormalizability of NJL models, a cutoff has to be applied. We will discuss our choice and alternatives in detail in chapter 4. The E_p are the positive quasiparticle energy eigenvalues of the fermionic propagator matrix. They are given in Table 3.6, where we have used the definitions:

$$\begin{aligned}\mu_r &= \mu + i\frac{\phi_8}{\sqrt{3}}T, \\ \mu_b &= \mu - i\frac{2\phi_8}{\sqrt{3}}T.\end{aligned}\tag{3.6.2}$$

With the exception of Chapter 7, we work in the isospin symmetric case and therefore treat “up” and “down” quarks as indistinguishable. The E_p from Table 3.6 then reduce to the eigenvalues given in Table 3.7 for the 2 + 1 flavor case. Finally, our calculations are performed by evaluating the mean field equations

$$\frac{\partial\Omega}{\partial\sigma_u} = \frac{\partial\Omega}{\partial\sigma_s} = \frac{\partial\Omega}{\partial\phi_3} = 0\tag{3.6.3}$$

for each choice of T and μ .

Name	Number	Formula
$E_{u,r}^{+,+}$	E_1	$\sqrt{M_u^2 + p^2} + \mu_r + i\phi_3 T$
$E_{d,r}^{+,+}$	E_2	$\sqrt{M_d^2 + p^2} + \mu_r + i\phi_3 T$
$E_{s,r}^{+,+}$	E_3	$\sqrt{M_s^2 + p^2} + \mu_r + i\phi_3 T$
$E_{u,r}^{+,-}$	E_4	$\sqrt{M_u^2 + p^2} + \mu_r - i\phi_3 T$
$E_{d,r}^{+,-}$	E_5	$\sqrt{M_d^2 + p^2} + \mu_r - i\phi_3 T$
$E_{s,r}^{+,-}$	E_6	$\sqrt{M_s^2 + p^2} + \mu_r - i\phi_3 T$
$E_{u,r}^{-,+}$	E_7	$\sqrt{M_u^2 + p^2} - \mu_r + i\phi_3 T$
$E_{d,r}^{-,+}$	E_8	$\sqrt{M_d^2 + p^2} - \mu_r + i\phi_3 T$
$E_{s,r}^{-,+}$	E_9	$\sqrt{M_s^2 + p^2} - \mu_r + i\phi_3 T$
$E_{u,r}^{-,-}$	E_{10}	$\sqrt{M_u^2 + p^2} - \mu_r - i\phi_3 T$
$E_{d,r}^{-,-}$	E_{11}	$\sqrt{M_d^2 + p^2} - \mu_r - i\phi_3 T$
$E_{s,r}^{-,-}$	E_{12}	$\sqrt{M_s^2 + p^2} - \mu_r - i\phi_3 T$
$E_{u,b}^+$	E_{13}	$\sqrt{M_u^2 + p^2} + \mu_b$
$E_{d,b}^+$	E_{15}	$\sqrt{M_d^2 + p^2} + \mu_b$
$E_{s,b}^+$	E_{14}	$\sqrt{M_s^2 + p^2} + \mu_b$
$E_{u,b}^-$	E_{16}	$\sqrt{M_u^2 + p^2} + \mu_b$
$E_{d,b}^-$	E_{17}	$\sqrt{M_d^2 + p^2} + \mu_b$
$E_{s,b}^-$	E_{18}	$\sqrt{M_s^2 + p^2} + \mu_b$

Table 3.6: Quasiparticle energy eigenvalues, each with multiplicity 2, in the scenario of three distinct quark flavors.

Name	Number	Formula	Multiplicity
$E_{u,r}^{+,+}$	E_1	$\sqrt{M_u^2 + p^2} + \mu_r + i\phi_3 T$	4
$E_{s,r}^{+,+}$	E_5	$\sqrt{M_s^2 + p^2} + \mu_r + i\phi_3 T$	2
$E_{u,r}^{+,-}$	E_2	$\sqrt{M_u^2 + p^2} + \mu_r - i\phi_3 T$	4
$E_{s,r}^{+,-}$	E_6	$\sqrt{M_s^2 + p^2} + \mu_r - i\phi_3 T$	2
$E_{u,r}^{-,+}$	E_3	$\sqrt{M_u^2 + p^2} - \mu_r + i\phi_3 T$	4
$E_{s,r}^{-,+}$	E_7	$\sqrt{M_s^2 + p^2} - \mu_r + i\phi_3 T$	2
$E_{u,r}^{-,-}$	E_4	$\sqrt{M_u^2 + p^2} - \mu_r - i\phi_3 T$	4
$E_{s,r}^{-,-}$	E_8	$\sqrt{M_s^2 + p^2} - \mu_r - i\phi_3 T$	2
$E_{u,b}^+$	E_9	$\sqrt{M_u^2 + p^2} + \mu_b$	4
$E_{s,b}^+$	E_{11}	$\sqrt{M_s^2 + p^2} + \mu_b$	2
$E_{u,b}^-$	E_{10}	$\sqrt{M_u^2 + p^2} + \mu_b$	4
$E_{s,b}^-$	E_{12}	$\sqrt{M_s^2 + p^2} + \mu_b$	2
			36

Table 3.7: Quasiparticle energy eigenvalues in a 2 + 1 flavor scenario

Chapter 4

Cutoff schemes

4.1 Introduction

The contact interactions in the Lagrangian render the (P)NJL model non-renormalizable. Several regularization methods are available, both Lorentz covariant and non-covariant. The most prominent covariant methods are the Euclidean four-momentum cutoff, the Pauli-Villars scheme, and regularization in proper time [81]. Most widely used are, however, non-covariant three-momentum cutoff schemes that are less involved. In these schemes, momentum space integrals are only carried out for $|\vec{p}|^2 < \Lambda^2$. Lorentz symmetry is broken in the system by finite temperatures and chemical potentials so that the additional breaking by the cutoff scheme is of no relevance. The three-momentum cutoff can be performed in several ways. In this chapter, we will investigate three different prescriptions to apply a three-momentum cutoff. It will be evident that the commonly used “minimal” cutoff prescription suffers from inconsistencies. A new “soft” cutoff prescription is the better choice.

First, in section 4.2, we study the high temperature limit where the differences between the cutoff schemes can be calculated analytically. For simplification, we perform the calculations first for two degenerate quark flavors in the NJL model in its basic version with chiral scalar and pseudoscalar four-quark couplings. The inclusion of Polyakov loop dynamics into the system does not affect the discussion, because the Polyakov loop (expectation value) Φ behaves as

$$\Phi \longrightarrow 1 \quad \text{for} \quad T \longrightarrow \infty \quad (4.1.1)$$

and drops out of the equations in the high-temperature limit. Following the two-flavor calculations, we discuss the case of 2 + 1 flavors in the NJL model in section 4.3. We then show results for the condensates and the QCD phase diagram in the two-flavor PNJL model in section 4.4. Results for 2 + 1 flavors are presented in section 4.5.

4.2 High temperature limit in the two-flavor NJL model

The NJL thermodynamic potential in the two-flavor scenario (in analogy to the three-flavor thermodynamic potential in def. 3.6.1), before the application of any cutoff, is

$$\Omega = -4N_c N_f \frac{1}{2} \int_0^\infty \frac{d^3 p}{(2\pi)^3} E_p - 4N_c N_f T \int_0^\infty \frac{d^3 p}{(2\pi)^3} \log \left[1 + e^{-E_p/T} \right] + \frac{\sigma^2}{2G} \quad (4.2.1)$$

with

$$E_p = \sqrt{p^2 + M^2} \quad \text{and} \quad M = m - \sigma, \quad (4.2.2)$$

so that we can already note for later use

$$\frac{\partial E_p}{\partial \sigma} = -\frac{M}{E_p}. \quad (4.2.3)$$

The first term of (4.2.1) diverges and has to be regularized, whereas the other two terms are well behaved.

Using the terminology from [52], we identify terms of (4.2.1) as follows: The second term is the temperature-dependent *thermal quark energy*. It describes the contributions due to the quark quasiparticles at non-vanishing temperatures. The last term is the *condensation energy*. The three cutoff schemes that we discuss in this section are:

1. **Maximal cutoff:** all integrals are integrated only up to the cutoff Λ , so that

$$\Omega^{\max} = -12 \int_0^{\Lambda} \frac{d^3p}{(2\pi)^3} E_p - 24T \int_0^{\Lambda} \frac{d^3p}{(2\pi)^3} \log [1 + e^{-E_p/T}] + \frac{\sigma^2}{2G} \quad (4.2.4)$$

This is the original NJL cutoff scheme. It turns out, however, that this prescription fails to produce the correct thermodynamics, primarily the important Stefan-Boltzmann limit. To remedy this, the “minimal“ cutoff scheme was introduced [109].

2. **Minimal cutoff:** only the divergent first term of (4.2.1) is cut off, the converging thermal quark energy integral is integrated to infinity.

$$\Omega^{\min} = -12 \int_0^{\Lambda} \frac{d^3p}{(2\pi)^3} E_p - 24T \int_0^{\infty} \frac{d^3p}{(2\pi)^3} \log [1 + e^{-E_p/T}] + \frac{\sigma^2}{2G} \quad (4.2.5)$$

This scheme takes the high momentum modes into account, so that the Stefan-Boltzmann limit of the pressure at high temperatures is reproduced. It is, however, conceptually inconsistent, since it includes fermionic interactions at momenta beyond the cutoff. In addition, there is no reason to treat the two terms differently since they stem from the same source. For calculations in the chiral limit, where there is no explicit chiral symmetry breaking, the condensates die off so rapidly that this inconsistency does not cause problems. With finite current quark masses and the resulting explicit chiral symmetry breaking, this scheme has flaws that we will show in this section. They are taken care of with the following new cutoff scheme which will be seen to be superior to the previous two.

3. **New, “soft” cutoff:** the divergent term is cut off, and the thermal quark energy term is modified such that for momenta $p > \Lambda$, all quark condensates are set to zero¹:

$$\begin{aligned} \Omega^{\text{soft}} = & -12 \int_0^{\Lambda} \frac{d^3p}{(2\pi)^3} E_p - 24T \int_0^{\Lambda} \frac{d^3p}{(2\pi)^3} \log [1 + e^{-E_p/T}] \\ & - 24T \int_{\Lambda}^{\infty} \frac{d^3p}{(2\pi)^3} \log [1 + e^{-E_p|_{\sigma=0}/T}] + \frac{\sigma^2}{2G} \end{aligned} \quad (4.2.6)$$

This cutoff scheme captures the correct high temperature limit by including high momentum modes. It adheres strictly to the NJL prescription that, for momenta $p > \Lambda$, the 4-fermion interaction is turned off². Note that in the PNJL model case the quasi particle energy eigenvalues E_p depend on the Polyakov loop variables. Quasi particles still feel the Polyakov loop Φ even for $p > \Lambda$. It is natural that Polyakov loop dynamics, defined

¹More precisely, the coupling strength G should be set to zero. In our formulation, it is equivalent and numerically easier to instead set $\sigma_q = 0$ for all q . Such a prescription has already been discussed but not applied in [117].

²All other fermionic couplings, e.g. the 6-fermion KMT coupling strength K appearing in the three flavor calculations or the vector interaction coupling strength g_v (see section 7.1), are turned off as well.

independently of the chiral symmetry breaking scenario, are not affected by the NJL cutoff discussion. At very high temperatures, the Polyakov loop expectation value becomes 1 so that the Stefan-Boltzmann limit is unaffected.

The self-consistent gap equation $\frac{\partial\Omega}{\partial\sigma} = 0$ derived from (4.2.1) for the chiral condensate σ reads

$$\frac{\partial\Omega}{\partial\sigma} = 12 \int_0^\infty \frac{d^3p}{(2\pi)^3} \frac{M}{E_p} - 24 \int_0^\infty \frac{d^3p}{(2\pi)^3} \frac{M}{E_p (e^{E_p/T} + 1)} + \frac{\sigma}{G} = 0. \quad (4.2.7)$$

To study the consequences of different cutoff schemes, we split this expression into four terms:

$$\frac{\partial\Omega}{\partial\sigma} = 12 \int_0^\Lambda \frac{d^3p}{(2\pi)^3} \frac{M}{E_p} - 24 \int_0^\Lambda \frac{d^3p}{(2\pi)^3} \frac{M}{E_p (e^{E_p/T} + 1)} - 24 \int_\Lambda^\infty \frac{d^3p}{(2\pi)^3} \frac{M}{E_p (e^{E_p/T} + 1)} + \frac{\sigma}{G}, \quad (4.2.8)$$

where we have already applied the cutoff to the divergent term which all three cutoff schemes demand.

With the maximal cutoff, the third term is missing, since no integration is carried out beyond the cutoff Λ . The gap equation then becomes

$$\frac{\partial\Omega}{\partial\sigma} = 12 \int_0^\Lambda \frac{d^3p}{(2\pi)^3} \frac{M}{E_p} - 24 \int_0^\Lambda \frac{d^3p}{(2\pi)^3} \frac{M}{E_p (e^{E_p/T} + 1)} + \frac{\sigma}{G} = 0 \quad (4.2.9)$$

Because of the strict cutoff, the E_p from eq. (4.2.2) are bounded as

$$E_p \leq \sqrt{M^2 + \Lambda^2} = \sqrt{(m - \sigma)^2 + \Lambda^2} \leq \sqrt{(m - \sigma|_{T=0})^2 + \Lambda^2}. \quad (4.2.10)$$

Since therefore $e^{E_p/T} \leq e^{\sqrt{\Lambda^2 + M^2}/T}$, we have

$$-24 \int_0^\Lambda \frac{dp}{2\pi^2} \frac{p^2 M}{E_p (e^{E_p/T} + 1)} \rightarrow -12 \int_0^\Lambda \frac{dp}{2\pi^2} \frac{p^2 M}{E_p} \quad \text{for } T \rightarrow \infty, \quad (4.2.11)$$

so that the second and first term in (4.2.9) cancel. In the case of the maximal cutoff, we are then only left with the equation

$$\frac{\partial\Omega}{\partial\sigma} = \frac{\sigma}{G} = 0, \quad (4.2.12)$$

so that

$$\sigma = 0 \quad (4.2.13)$$

is the only solution. According to formula (4.2.2), this means that the effective quark mass is reduced to the current quark mass at extremely high temperatures, which is the physically correct limit:

$$M = m - \sigma \longrightarrow m \quad \text{for } T \longrightarrow \infty. \quad (4.2.14)$$

However, as mentioned, the correct Stefan-Boltzmann limit is not reached in this scheme (see Fig. 4.8). In the case of the “soft” cutoff, where the condensates are set to zero for $p > \Lambda$, the result is exactly the same, because the σ -independent part for $p > \Lambda$ of the fermionic integral of Ω does not survive the derivative $\partial/\partial\sigma$. Accordingly, the third term in (4.2.8), in the following called the “extra term”, is not present, and $\sigma = 0$ is again the asymptotic solution.

However, in the case of the minimal cutoff, we have to take the extra term into account. Because the momentum is integrated to infinity there, the exponential in the denominator can no longer be easily evaluated in the high temperature limit, and no obvious expansion suggests itself. We introduce the substitution

$$x \equiv E_p/T = \frac{\sqrt{M^2 + p^2}}{T}, \quad \text{so that} \quad E_p = xT. \quad (4.2.15)$$

Then

$$p^2 = (xT)^2 - M^2 \quad \text{and} \quad dp = \frac{xT^2}{\sqrt{(xT)^2 - M^2}} dx. \quad (4.2.16)$$

The lower integration limit is now determined by

$$p = \Lambda \quad \Leftrightarrow \quad x = \frac{\sqrt{M^2 + \Lambda^2}}{T} \rightarrow 0 \quad \text{for} \quad T \rightarrow \infty \quad (4.2.17)$$

and the upper limit by

$$p \rightarrow \infty \quad \Leftrightarrow \quad x \rightarrow \infty \quad (4.2.18)$$

for any given, arbitrarily high value of T . The substitution then gives for the extra term

$$-24 \int_{\Lambda}^{\infty} \frac{dp}{2\pi^2} \frac{p^2 M}{E_p (e^{E_p/T} + 1)} \quad \rightarrow \quad -\frac{12}{\pi^2} \int_0^{\infty} dx \frac{TM \sqrt{(xT)^2 - M^2}}{e^x + 1}. \quad (4.2.19)$$

This evaluates to³

$$-\frac{12}{\pi^2} \int_0^{\infty} dx \frac{T^2 M \sqrt{x^2 - \left(\frac{M}{T}\right)^2}}{e^x + 1} \quad \rightarrow \quad -\frac{12}{\pi^2} \int_0^{\infty} dx \frac{xT^2 M}{e^x + 1} \quad \text{for} \quad T \rightarrow \infty \quad (4.2.20)$$

and finally we get

$$-12 M \frac{T^2}{\pi^2} \int_0^{\infty} dx \frac{x}{e^x + 1} = -2 MT^2, \quad (4.2.21)$$

where in the last step we have used that the integral is simply the *Riemann zeta function* $\zeta(2) = \frac{\pi^2}{6}$. In contrast to (4.2.12), the gap equation for the minimal cutoff is then

$$\frac{\partial \Omega}{\partial \sigma} = -2 MT^2 + \frac{\sigma}{G} = 0, \quad (4.2.22)$$

which yields⁴

$$M = \frac{\sigma}{2T^2 G} \rightarrow 0 \quad \text{for} \quad T \rightarrow \infty. \quad (4.2.23)$$

In the calculation, this shows up directly by a sign change in the chiral condensate: since $M = m - \sigma$ at $T = 0$ with $\sigma < 0$, it would appear that $\sigma > 0$ as $T \rightarrow \infty$. Note that this unphysical sign change happens already at finite temperatures of around $1.5 T_c$, with T_c the chiral transition temperature. For two flavors, the sign change effect itself is negligible [109] because of the small light quark current mass m . However, there are large differences in the phase diagram, see section 4.4. In summary, the new ‘‘soft’’ cutoff scheme is the only one that establishes the correct thermodynamics in the high- T limit. This cutoff will primarily be pursued for the remainder of this work.

³Note that $x = \frac{E_p}{T} > 0$ always, because E_p is by definition always positive.

⁴The condition that σ is finite for high temperatures is trivially the case for a physical system.

4.3 High temperature limit in the 2 + 1 flavor NJL model

In the 2 + 1 flavor scenario, the sign change effect just mentioned is more pronounced, as the strange-quark current mass is of the order of 100 MeV. The calculation goes essentially in analogy with the two-flavor case; it is only slightly more involved because of the flavor mixing KMT determinant. We will see in the end that its effects on the high T limit are negligible. For a three-flavor NJL model including the KMT interaction we have

$$\Omega = -6 \sum_q \int_0^\infty \frac{d^3p}{(2\pi)^3} E_p^q - 12T \sum_q \int_0^\infty \frac{d^3p}{(2\pi)^3} \log [1 + e^{-E_p^q/T}] + \frac{\sigma_u^2 + \sigma_d^2 + \sigma_s^2}{4G} - \frac{K}{2G^3} \sigma_u \sigma_d \sigma_s \quad (4.3.1)$$

with $q = u, d, s$ and

$$E_p^q = \sqrt{p^2 + M_q^2} \quad \text{and} \quad M_q = m_q - \sigma_q + \frac{K}{4G^2} h_{qjk} \sigma_j \sigma_k. \quad (4.3.2)$$

We have defined

$$h_{qjk} = \begin{cases} 1/2 & \text{if } \{q, j, k\} = \{u, d, s\} \text{ or any permutation thereof} \\ 0 & \text{if } q = j, q = k \text{ or } j = k. \end{cases} \quad (4.3.3)$$

Then

$$\frac{\partial E_p^q}{\partial \sigma_r} = -\frac{M_q}{E_p^q} \Gamma_{qr} \quad (4.3.4)$$

with

$$\Gamma_{qr} = \delta_{qr} - \frac{K}{4G^2} h_{qjk} (\sigma_j \delta_{kr} + \delta_{jr} \sigma_k). \quad (4.3.5)$$

In the case of the new cutoff (the analogue of (4.2.6)) as well as for the maximal cutoff (analogous to (4.2.4)), we have, for $T \rightarrow \infty$, the same cancellation of terms as in the two-flavor case. We therefore, in analogy to (4.2.22), end up with the following gap equations purely from the condensation energy terms:

$$\frac{\partial \Omega}{\partial \sigma_r} = \frac{\sigma_r}{2G} - \frac{K}{2G^3} h_{rjk} \sigma_j \sigma_k = 0. \quad (4.3.6)$$

The three coupled gap equations (4.3.6) have the five solutions presented in Table 4.1, where $a = \frac{G^2}{K} \approx 660$ MeV. The only physically sensible solution is the first one with

$$\sigma_u = \sigma_d = \sigma_s \equiv 0 \quad \text{at} \quad T \rightarrow \infty \quad (4.3.7)$$

As in the two-flavor case, this means that

$$M_q \longrightarrow m_q \quad \text{for all flavors as} \quad T \longrightarrow \infty, \quad (4.3.8)$$

which agrees with our physical understanding.

solution no.	1	2	3	4	5
σ_u	0	-a	-a	a	a
σ_d	0	-a	a	-a	a
σ_s	0	a	-a	-a	a

Table 4.1: Solutions of the three coupled gap equations (4.3.6), with $a = \frac{G^2}{K} \approx 660$ MeV.

In the case of the widely used minimal cutoff, we have to consider the “extra term” again, i. e. the remaining integration in the second term of (4.3.1) from Λ to infinity. The three-flavor analogue to eq. (4.2.22) is

$$\frac{\partial \Omega}{\partial \sigma_r} = -2M_q T^2 \Gamma_{qr} + \frac{\sigma_r}{2G} - \frac{K}{2G^3} h_{rjk} \sigma_j \sigma_k = 0. \quad (4.3.9)$$

The physically correct high-temperature result $\sigma_q \rightarrow 0$ for all flavors is *not* a solution of this equation: setting $\sigma_q = 0$ for all q would yield $-2m_q T^2 \Gamma_{qr} = 0$. For finite quark masses, this equation is false, as $\Gamma_{qr} \neq 0$ always, see eq. (4.3.3) and eq. (4.3.5).

4.4 PNJL model results for 2 flavors

Although the unphysical sign change effect in two flavors is marginal, it has a strong effect on the QCD phase diagram. Fig. 4.1 shows the normalized chiral condensate σ as a function of T at $\mu = 0$ for two degenerate flavors $m_u = m_d$, using both the minimal and the new cutoff scheme. The σ from the minimal cutoff changes its sign at $T = 381$ MeV, or $T = 1.7 T_c$. Fig. 4.2a shows the two-flavor phase diagram calculated with the minimal cutoff; Fig. 4.2b the same, but calculated with the new cutoff scheme. For the two-flavor scenario, we use the same values for NJL and Polyakov loop effective potential input parameters as in [117], where a minimal cutoff scheme was used.

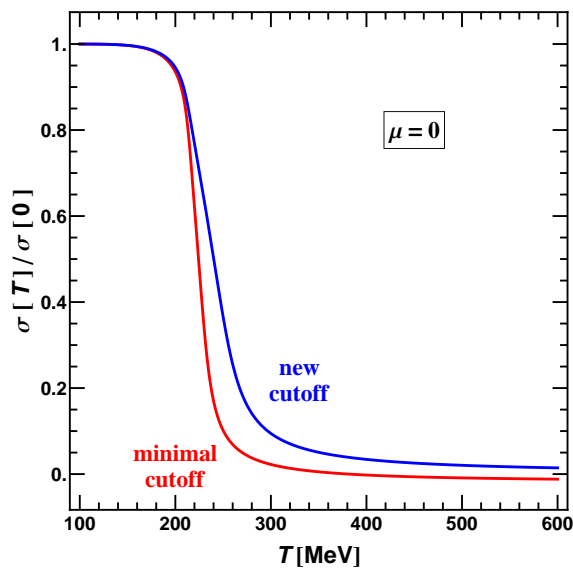


Fig. 4.1: Comparison of normalized chiral condensate σ for two degenerate flavors as a function of T at $\mu = 0$ for two different cutoff schemes. Left curve (red) from the minimal cutoff prescription in eq. (4.2.5), right curve (blue) from the new cutoff prescription in eq. (4.2.6).

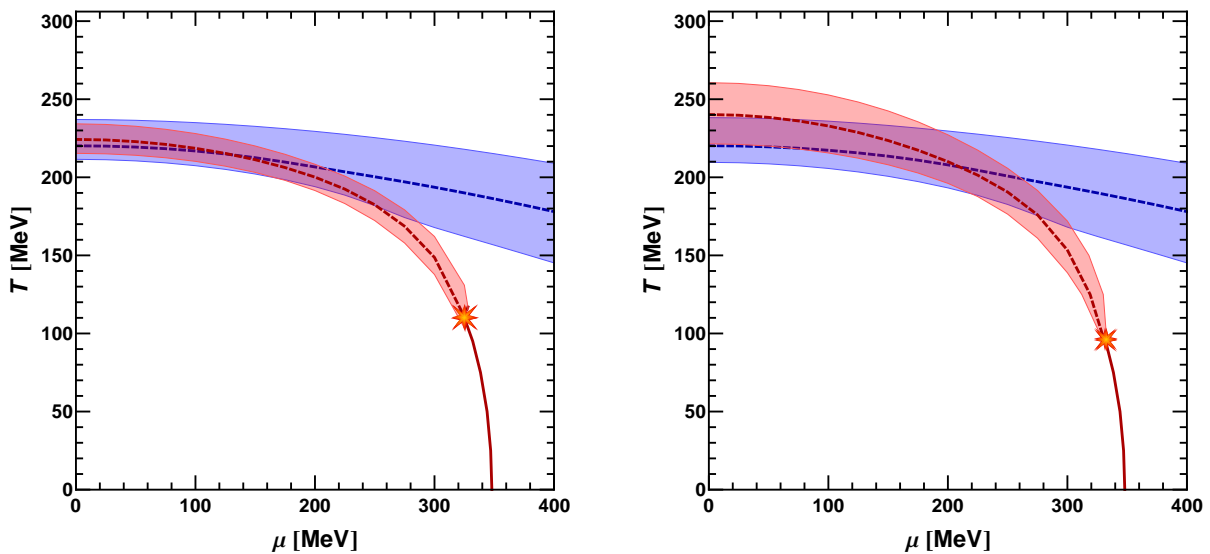
Next, we present the QCD phase diagram. It is shown in a format that we will keep throughout this work. Instead of giving transition lines for crossovers, we show transition bands. In this way, the smooth nature of the crossovers is evident. For the chiral transition, we determine the lower bound, central value and upper bound by the values at which σ_u has decreased from its vacuum value at $T = 0$ and $\mu = 0$ to 75%, 50% and 25% of that value, respectively. The first-order transition is naturally given by the gap at the critical temperature T_c . For the confinement/deconfinement transition we determine lower bound, central value and upper bound by the temperatures where the Polyakov loop has reached values of 0.2, 0.35 and 0.5, respectively.

These choices are basically equivalent to schemes based on the slopes of the curves but they are numerically more stable.

In the phase diagrams, we show the chiral crossover as a red band and the Polyakov loop crossover as a blue band. When we normalize temperatures to a “critical” temperature T_c at $\mu = 0$, in the case of a crossover we use for T_c the center T_{cross}^X of the chiral crossover band, defined by

$$\frac{\sigma_u(T_{\text{cross}}^X, \mu = 0)}{\sigma_u(0, 0)} = 0.5. \quad (4.4.1)$$

Fig. 4.2a and Fig. 4.2b demonstrate that there the cutoff scheme has considerable effect on the QCD phase diagram even in two flavors. The main consequences of the new cutoff are a smoother transition (broader crossover band) and a shift of the band towards slightly higher temperatures. In the chiral limit, $m \equiv m_u = m_d \equiv 0$, the high temperature limit of the chiral

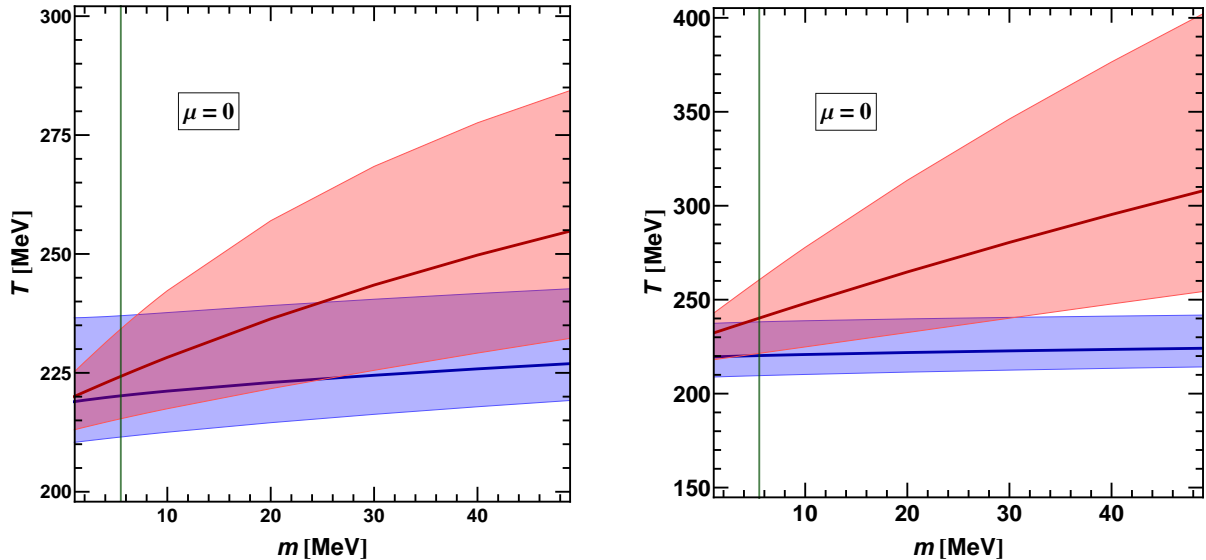


(a) Minimal cutoff, see (4.2.5).

(b) New “soft” cutoff, see (4.2.6).

Fig. 4.2: Two-flavor QCD phase diagrams resulting from two different cutoff prescriptions. The (de-) confinement crossover band is shown in blue (dashed), the chiral crossover band in red (dashed). The critical point is marked by a star and the chiral first order transition by a solid red line.

condensate is 0 for all cutoff schemes. However, considerable differences between the cutoff prescriptions remain: Fig. 4.3a and Fig. 4.3b show location and width of the crossover bands for chiral and Polyakov loop transition at $\mu = 0$ as a function of the light quark current mass m . Fig. 4.3a gives the result of the maximal cutoff prescription and Fig. 4.3b that of our new cutoff scheme.



(a) Minimal cutoff, see (4.2.5).

(b) “Soft” cutoff, see (4.2.6).

Fig. 4.3: Crossover band of chiral (red) and Polyakov loop (blue) crossover at $\mu = 0$ as a function of the light current quark mass $m \equiv m_u = m_d$. Calculated for two different cutoff prescriptions. Vertical line marks value from standard parameter set.

4.5 PNJL model results for 2 + 1 flavors

Next, we turn to the 2 + 1 flavor case, where we treat up and down quarks as equal (“2”) and include the strange quark (“+1”). The thermodynamic potential Ω with the “soft” cutoff scheme is now

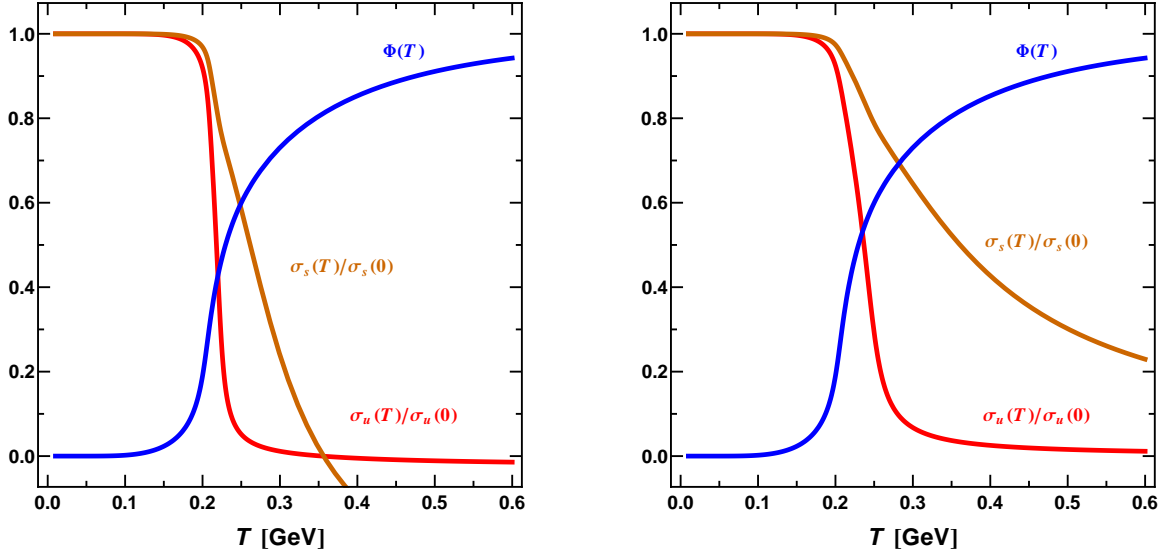
$$\begin{aligned} \Omega^{\text{soft}} = & -\frac{1}{2} \int_0^\Lambda \frac{d^3p}{(2\pi)^3} E_p - T \int_0^\Lambda \frac{d^3p}{(2\pi)^3} \log \left[1 + e^{-E_p/T} \right] - T \int_\Lambda^\infty \frac{d^3p}{(2\pi)^3} \log \left[1 + e^{-E_p^{\text{free}}/T} \right] \\ & + \frac{\sigma_u^2}{2G} + \frac{\sigma_s^2}{4G} - \frac{K}{2G^3} \sigma_u^2 \sigma_s + \mathcal{U}(\Phi, \Phi^*, T), \end{aligned} \quad (4.5.1)$$

where the quasi particle energy eigenvalues E_p are given in Table 3.7 and the E_p^{free} are obtained from the E_p by setting $G = K = 0$, or, equivalently, $\sigma_u = \sigma_s = 0$. The “minimal” cutoff for 2 + 1 flavors is given simply by replacing the E_p^{free} with the E_p in eq. (4.5.1).

We present light quark (σ_u) and strange quark (σ_s) condensate and Polyakov loop as a function of T at $\mu = 0$ in Fig. 4.4a (minimal cutoff) and Fig. 4.4b (new cutoff). The high temperature limits of vanishing condensates (new cutoff) and finite values for the minimal cutoff are clearly visible. In [52], where a minimal cutoff is used, it is argued that the “s-quark sector behaves unnaturally at extremely high temperatures” and that this is “of no importance practically”. At this point we disagree: the observed “unnatural” behavior is just the consequence of a physically inconsistent cutoff scheme. The unphysical sign change of the s-quark condensate appears already at $T \sim 350 \text{ MeV} \sim \Lambda/2$, below twice the transition temperature T_c , and renders conclusions based on the minimal cutoff prescription questionable.

In lattice QCD publications, instead of the individual condensates σ_u and σ_s at $\mu = 0$, usually the “subtracted chiral condensate” introduced in [31] is given. It is defined by

$$\Delta_{\text{ls}} := \left. \frac{\sigma_u(T) - \frac{m_u}{m_s} \sigma_s(T)}{\sigma_u(0) - \frac{m_u}{m_s} \sigma_s(0)} \right|_{\mu=0}. \quad (4.5.2)$$



(a) Minimal cutoff, cf. (4.2.5).

(b) “Soft” cutoff, see (4.5.1).

Fig. 4.4: Normalized chiral condensates and Polyakov loop as a function of the temperature at $\mu = 0$ for two different cutoff schemes.

This definition removes “unphysical, quadratically divergent, additive” contributions that “show no finite temperature effects and obscure the physically important contribution from vacuum chiral symmetry breaking” [31].

In Fig. 4.5, we show our results for Δ_{ls} as a function of T/T_c and compare to two different sets of lattice QCD results from the hotQCD collaboration [10]. We chose the HISQ/tree points with f_K as the scale to convert raw results into physical values for the temperature. With this prescription, points from calculations with various lattice actions and temporal extents N_τ collapse into a narrow band [10]. In Fig. 4.5a, we compare to $N_\tau = 12$ results with $m_s/m_u = 20$. Fig. 4.5b shows an interpolation (based on $N_\tau = 8$ results) to the physical light quark mass with $m_s/m_u \approx 27$. This ratio is close to our ratio from the RKH parameter set of $m_{s,0}/m_{u,0} \approx 26$. The latter results also overlap with continuum extrapolated results with physical pion masses, $m_\pi = 135$ MeV, calculated with staggered fermions and one-link stout improvement [19]. It is evident that in Fig. 4.5b the subtracted chiral condensate is steeper and reproduced well by our results, depicted by the red band. The band represents that there is no single clearly determined T_c but a broad crossover range. The center curve is given by T_{cross}^X from def. (4.4.1).

The effects on the 2 + 1 flavor QCD phase diagram are shown in Fig. 4.6a (minimal cutoff) and Fig. 4.6b (new cutoff). This comparison shows the sensitivity of the phase diagram on the cutoff scheme: the crossover bands are considerable broader with our new prescription. These smooth transitions are also seen in recent lattice QCD results [13], in particular for the Polyakov loop (see chapter 6.)

The entanglement between the chiral and the (de-)confinement crossover is stronger with the “minimal” cutoff. The explanation is straight-forward: in the second term of def. (4.2.5), Polyakov loop and chiral condensates influence each other over the whole momentum range from $p = 0$ to $p = \infty$. Lattice QCD data indeed show notable entanglement of the transitions [13]. However, the “minimal” cutoff with its unphysical foundation and consequences cannot be the correct mechanism to model this feature. In chapter 6 we investigate the relationship between Polyakov loop and chiral condensates in more detail; particular emphasis is placed on the cutoff prescriptions as well as the Polyakov loop effective potential. Fig. 4.8 presents the total pressure p/T^4 in the 2 + 1 flavor PNJL model at $\mu = 0$ as a function of T/T_c .

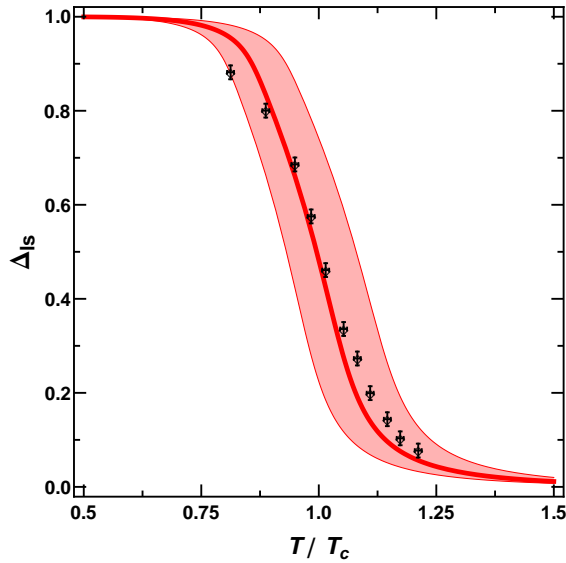
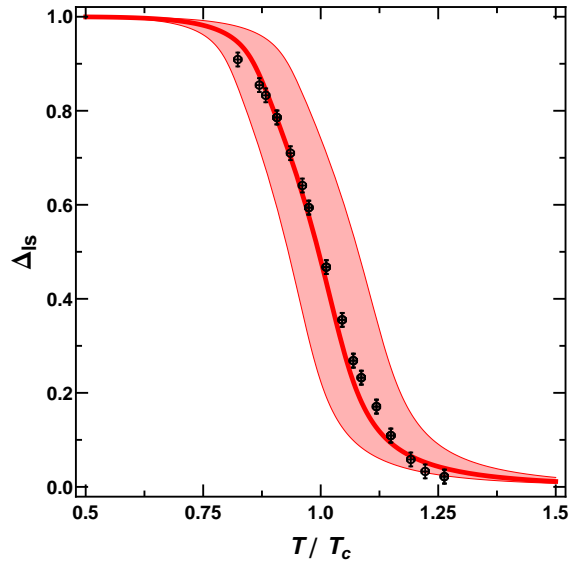
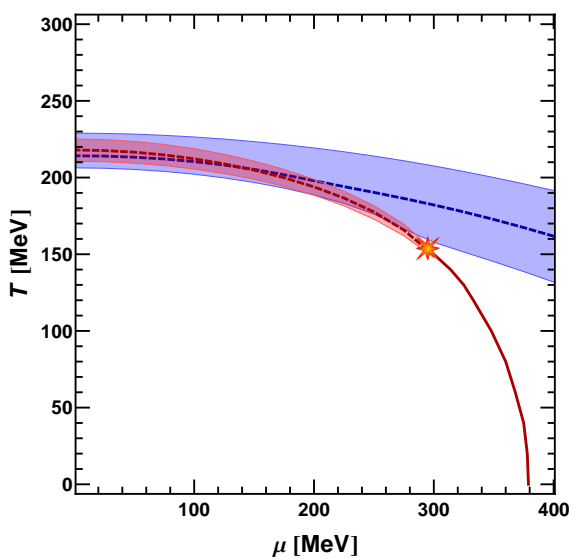
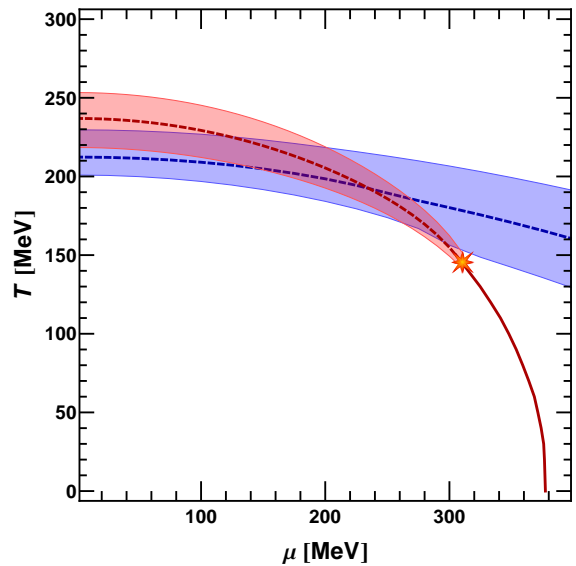
(a) Result with $N_\tau = 12$ and $m_s/m_u = 20$.(b) Result with $N_\tau = 8$, interpolated to the physical light quark mass with $m_s/m_u \approx 27$.

Fig. 4.5: Comparison of our results (red band) for Δ_{ls} with $m_{s,0}/m_{u,0} \approx 26$ (see eq. (4.5.2)) as a function of T/T_c with two different sets of lattice QCD results from [10].



(a) Minimal cutoff, cf. (4.2.5).



(b) New “soft” cutoff, see (4.5.1).

Fig. 4.6: 2 + 1 flavor QCD phase diagrams resulting from two different cutoff prescriptions. The (de-) confinement crossover band is shown in blue (dashed), the chiral crossover band in red (dashed). The critical point is marked by a star and the chiral first order transition by a solid red line.

The pressure is simply the negative thermodynamic potential (density),

$$p = -\Omega, \quad (4.5.3)$$

normalized such that $p(T = 0, \mu = 0) \equiv 0$. The lower, dark green curve in Fig. 4.8 is the result from the “maximal” cutoff scheme used e.g. in [26]. The omission of higher momentum modes in the thermodynamic potential (4.2.4) leads to the wrong high temperature limit for the pressure. It is evident that the “maximal” cutoff prescription cannot yield physical results for the thermodynamic quantities. By contrast, the red curve with an orange band in Fig. 4.8 is the result from the soft cutoff scheme. The band is again a consequence of the width of the crossover band at $\mu = 0$, cf. Fig. 4.6b. This curve features the correct high temperature limit.

Establishing the correct behavior of the pressure p allows us to display the phase diagram from Fig. 4.6b accurately in the p - T plane. This is useful for comparing to known phase diagrams such as those of water or liquid Helium [136]. Our result is presented in Fig. 4.7. The liquid/gas phase transition is calculated using in-medium chiral perturbation theory [46].

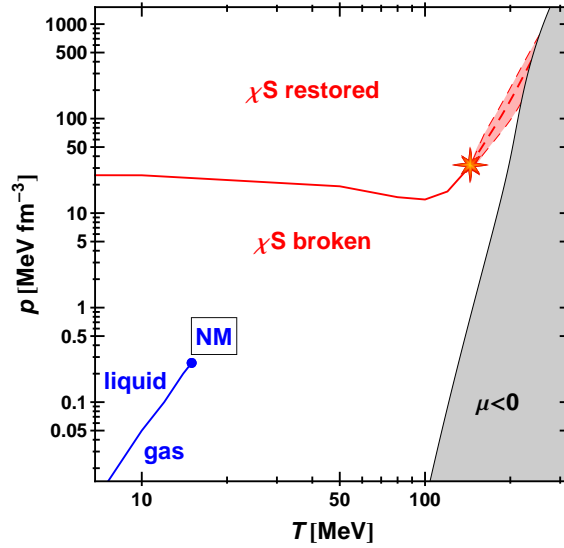


Fig. 4.7: Double-logarithmic phase diagram of QCD with pressure p and temperature T as external parameters. Chiral first order transition in solid red, crossover band dashed, critical point denoted by a star. Results for the nuclear matter (NM) liquid/gas transition from [46].

From the pressure we calculate the energy density ϵ and the entropy density⁵ s via the standard thermodynamic relations at $\mu = 0$

$$s = \frac{\partial p}{\partial T} \quad \text{and} \quad \epsilon = Ts - p. \quad (4.5.4)$$

Figures 4.9, 4.10 and 4.11 present the energy density ϵ , entropy density s and the trace anomaly $\epsilon - 3p$ as functions of T/T_c at $\mu = 0$. For each curve, a band has been added that stems from the choice of T_c within the chiral crossover bands (see Fig. 4.6b). Lattice QCD results from [33] and [12] have been added for comparison. Our curves describe the data quite well.

⁵The source of the discrepancy between upper points peaking at $6 \sim 7$ [32] and lower points peaking around 4 [18] is at present unknown.

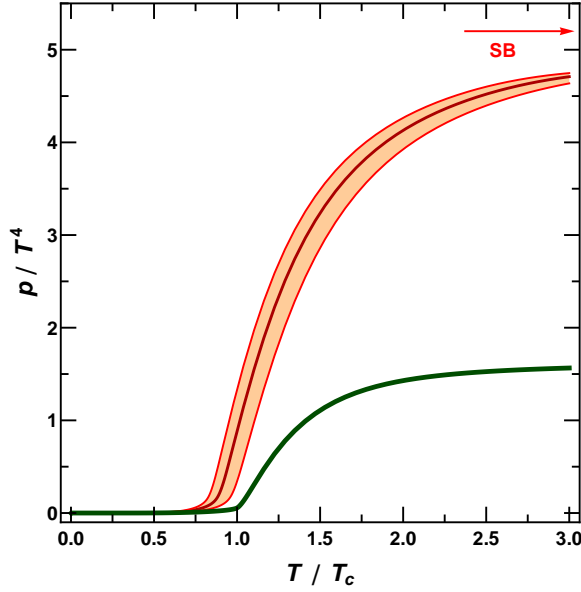


Fig. 4.8: Normalized total pressure p/T^4 as a function of T/T_c at $\mu = 0$ in the 2 + 1 flavor PNJL model. Red with orange band: result from *soft cutoff* prescription (4.5.1). Dark green: result from *maximal* cutoff prescription (4.2.4). “SB” marks the correct Stefan–Boltzmann limit.

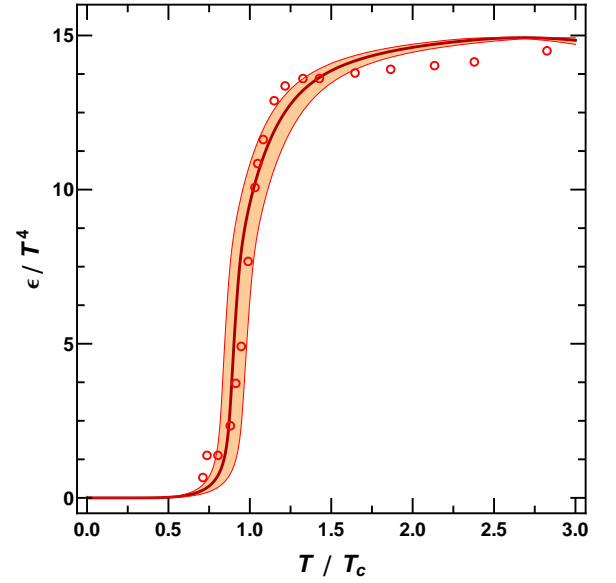


Fig. 4.9: Normalized energy density ϵ/T^4 as a function of T/T_c at $\mu = 0$ in the 2 + 1 flavor PNJL model, calculated with the *soft cutoff* prescription (4.5.1). Orange band corresponds to the crossover band. Circles are lattice QCD results from [33].

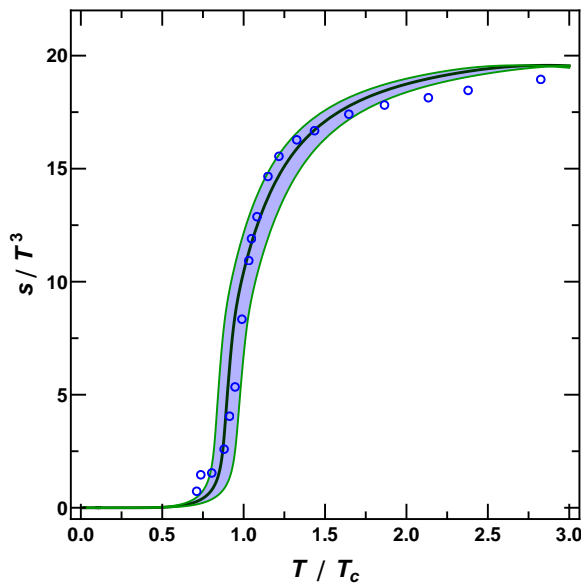


Fig. 4.10: Normalized entropy density s/T^3 as a function of T/T_c at $\mu = 0$ in the 2 + 1 flavor PNJL model, calculated with the *soft cutoff* prescription (4.5.1). Blue band corresponds to the crossover band. Circles are lattice QCD results from [33].

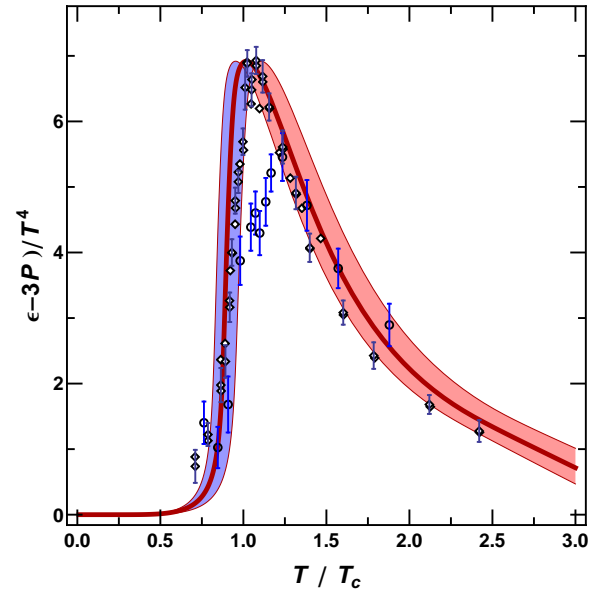


Fig. 4.11: Normalized trace anomaly $(\epsilon - 3p)/T^4$ as a function of T/T_c at $\mu = 0$ in the 2 + 1 flavor PNJL model, calculated with the *soft cutoff* prescription (4.5.1). Band corresponds to the crossover band. Points with error bars from collection in [12].

4.6 Summary

We have shown in this chapter that the violation of chiral symmetry by the “minimal” cutoff is well understood. It is quite strong and its consequences should not be dismissed as negligible, even in a two-flavor scenario. The “soft” cutoff (4.2.6) eliminates the unphysical sign change of the chiral condensates that appears when using a “minimal” cutoff prescription. Calculations with this scheme are numerically only slightly more expensive and easily implemented. In addition, results for thermodynamic quantities are in good agreement with lattice QCD results. We conclude that there is a strong preference for the new “soft” cutoff.

Chapter 5

Axial anomaly and Columbia plot

5.1 Introduction

The $2 + 1$ flavor PNJL model introduces two new features not present in the two-flavor model: the first is the increased explicit chiral symmetry breaking by the large strange-quark mass m_s . The second is the Kobayashi-Maskawa-'t Hooft (KMT) interaction. One of its effects is the coupling of the effective mass of the light quarks also to the strange quark condensate and vice versa, cf. (3.3.45). Consequently, the influence of the strange current quark mass is not restricted to the chiral transition of the strange-quark condensate alone; this transition is very slow in any case and therefore not a good indicator of chiral restoration. More importantly, it also affects the transition of the light quark condensate σ_u which is used to determine the location of the critical point in both the two- and $2 + 1$ flavor models.

By varying the quantities which govern these two new features, i.e. the strange-quark current mass m_s and the KMT coupling strength K , we gain deeper insight into the nature of their effects on the critical point.

Our procedure is, at this level, straightforward: We change the value of the parameter under consideration while keeping all others fixed. Then we calculate the phase diagram with each of these changed parameter sets. To distinguish between the parameter used in a calculation and the standard value from the parameter fixing to vacuum properties, we denote the latter with the subscript “0”. Thus, the standard values are K_0 , $m_{u,0}$, $m_{d,0}$ and $m_{s,0}$. It should be noted that by changing one parameter independently of the others, the meson spectrum is no longer reproduced: in the case of the coupling strength K , the η' mass $m_{\eta'}$ is changed predominantly, while changing the strange quark m_s affects primarily the kaon mass.

This chapter is organized as follows: First, in section 5.2 we investigate some consequences of a change in the KMT coupling K . We briefly discuss available information about its possible dependence on T and μ . In sections 5.3 and 5.4 we extend the study to variations in the current quark masses, including the chiral limit and a scenario of three degenerate flavors.

Changes in the transition lines under a variation of K prompts us to calculate the curvature of those lines and compare them to recent lattice results in section 5.5.

We then move on to produce the lower part of the so-called Columbia plot in section 5.6. It is a concise way of displaying possible phase transition orders at $\mu = 0$ as a function of the current quark masses [87] and a subject of intense interest by lattice communities.

5.2 Kobayashi–Maskawa–'t Hooft interaction strength K

As stated in 3.2, the KMT coupling strength K governs the axial anomaly in the PNJL model. It also determines, as the solution of the “U(1) puzzle”, the main mechanism behind the large mass of the η' meson. This is shown in Fig. 5.1, where we display the η' meson mass in the vacuum as a function of K/K_0 with K_0 being the “standard” value from the parameter fixing

to vacuum properties. The other meson masses are affected only very little by this change.

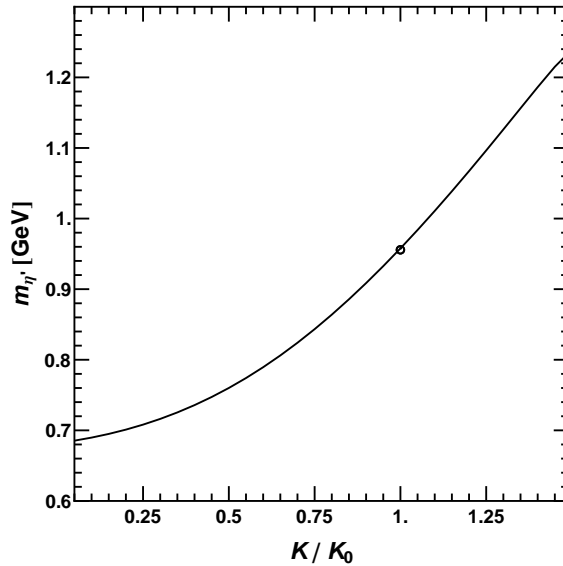


Fig. 5.1: Mass of the pseudoscalar η' meson as a function of the KMT coupling strength K/K_0 . Circle marks standard result at $K = K_0$.

Why is the variation of K interesting to us when we know how strong it must be to generate the large $m_{\eta'}$ in the vacuum? It is by no means obvious that the couplings of the PNJL model are constants with T and μ . For the four fermion scalar coupling G this is almost universally assumed in models. The KMT interaction, on the other hand, is based on instanton dynamics [126]. Therefore, finite temperature and finite chemical potential effects might be gauged by properties of instanton ensembles, e. g. the instanton density and size scale. There are several theoretical attempts to determine these properties, e. g. [30, 61]. It is believed that at finite temperature and density the η' mass is reduced [76].

Experimental indications have been reported in [38, 131, 133, 132], based on two pion Bose-Einstein correlations measured in $\sqrt{s} = 200$ GeV Au+Au collisions at RHIC. An η' mass reduction from 958 MeV in the vacuum to, according to them, $340_{-60}^{+50} \pm 280_{-140} \pm 42$ in medium, would certainly indicate a large reduction of K (cf. Fig. 5.1). A finite temperature generalization [86] of the Witten-Veneziano formula [130, 140] comes to quantitatively similar conclusions. Recently, lattice QCD calculations using the chiral symmetry respecting, but very expensive “overlap fermion” discretization have been performed [74, 36]. They find, close to the chiral limit, first indications of $U(1)_A$ restoration for $T \gtrsim 192$ MeV.

The reduction of K as a function of μ and T is one way of modeling such effects in our framework. In section 5.5 we briefly describe some forms of K as a function of temperature or chemical condensate based on instanton dynamics and explore their effect on the curvature of the chiral transition line. Recently, an ansatz for the combined dependence $K(T, \mu)$ has been proposed [37], but its complex form and additional momentum-dependence put it beyond the scope of this thesis. As the simplest possible choice, for the most parts of our work we study variations of a globally constant K that does depend on neither temperature nor chemical potential.

The trajectory of the critical point resulting from a change in K for a PNJL model has been studied first in [52]. After verification, we want to expand on these results. Fig. 5.2 shows the dependence of the critical point location on this quantity. It is evident that the influence of this coupling constant is significant. Increasing K – and with it the strength of the axial anomaly –

shifts the critical point towards lower chemical potential¹ and enlarges the range of the first-order phase transition. Conversely, lowering K drives the critical point down in the phase diagram, shortening the first-order phase transition line. By changing K substantially, it is even possible to eliminate the critical point completely. In chapter 7, we combine this effect with the inclusion of vector-type interactions in the PNJL model and draw important conclusions for the QCD phase diagram.

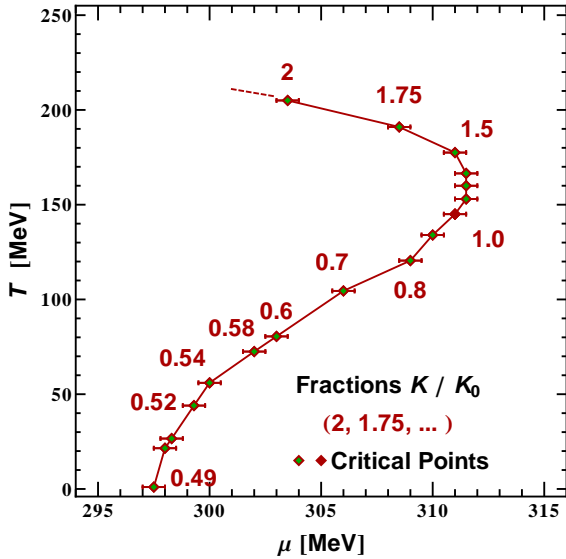


Fig. 5.2: Trajectory of the critical point for different fraction of K/K_0 in our model. Note the vast difference in scales between the T and the μ axis. Some of the corresponding phase diagrams are displayed in Fig. 5.3.

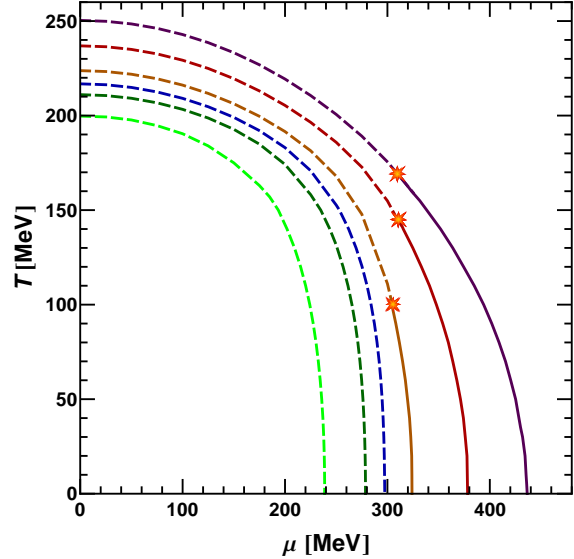


Fig. 5.3: Phase diagrams resulting from different choices for K/K_0 . From innermost to outermost: $K/K_0 = 0, 1/3, 1/2, 2/3, 1, 4/3$. Solid lines are first-order transitions, dashed lines denote crossovers. The critical points (stars) are located along the trajectory shown in Fig. 5.2. For this plot, we have left out crossover bands for the sake of lucidity.

Fig. 5.2 reproduces some findings of [52], where a different parameter set [63] and the “minimal” cutoff prescription 4.2.5 was used. Both approaches give in this respect equivalent qualitative results, although they differ quantitatively for thermodynamic quantities and the chiral condensates. There is, however, a clear difference in comparison with the same plot calculated in a nonlocal PNJL model (cf. Fig. 11 in [67]). This comparison indicates that the existence of the cutoff itself influences the behavior of this trajectory tremendously, while the specifics of the cutoff procedure have relatively little influence.

5.3 Dependence of the critical point on the current quark masses

In this section and the next one we perform critical point trajectory studies as in Fig. 5.2, but as functions of a change in the current quark masses. This is a preparation for the determination of the Columbia plot in this chapter; it is also instructive to see the relative influence of the different parameters on this elusive point.

In Fig. 5.4 we show the dependence of the location of the critical point in the phase diagram on the strange-quark current mass m_s . One solid marker denotes the starting point,

¹after an intermediate range from $1 \lesssim K/K_0 \lesssim 1.5$

i.e. the unchanged value which results from the parameter fit to the meson spectrum. This is $m_{s,0} = 140.7$ MeV for the RKH parameter set [110]. The left solid marker corresponds to the case of three degenerate quark masses with $m_u = m_d = m_s = 5.5$ MeV. As can be seen, the location of the critical point depends sensitively on the value of the strange quark mass for small m_s . The cross at the left end of the trajectory is the value for $m_s = 0$; the dashed line at the right end is an extrapolation.

Interestingly, the location of the critical point does not vary greatly when m_s stays in the relatively wide range between 70 and 280 MeV. We recall that most parameter sets give values of m_s between 120 and 150 MeV. Evidently, the location of the critical point is quite stable with respect to a change in m_s alone. This is not surprising, as it is associated with the light quark transition that is influenced only slightly by the strange quark sector, at least as long as we confine ourselves to a flavor-independent chemical potential $\mu \equiv \mu_u = \mu_d = \mu_s$ (cf. section 7.8.2). Now that we have information about the impact of the large strange current quark mass,

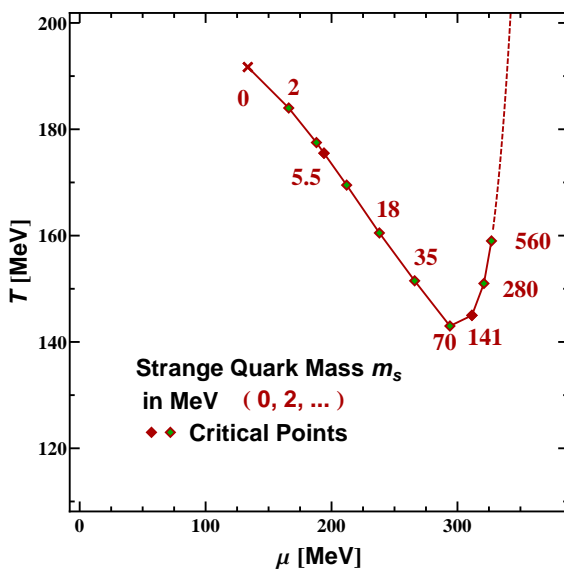


Fig. 5.4: Trajectory of the location of the critical point as a function of the strange quark current mass m_s .

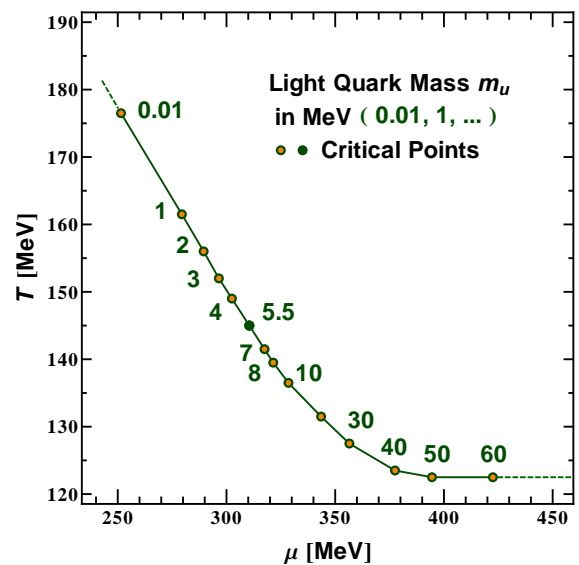


Fig. 5.5: Trajectory of the location of the critical point as a function of the light quark current mass $m_u = m_d$.

we can ask how the light quark mass, one order of magnitude smaller than the strange-quark mass, influences our model. The results are shown in Fig. 5.5. The standard parameter set value is again denoted by the solid plot marker. At the left end of the curve we have added a short dashed line, because we cannot determine the end point here exactly: for $m_u \approx 0$ it is numerically expensive to determine the order of the transition.

Regarding the question of its existence, it is clear that *ceteris paribus* there will always be a critical point in the phase diagram for reasonable choices of the masses. In section 5.7 we will see how large current quark masses would have to be in order to smoothen the first-order transition line into a crossover altogether. The result depends strongly on K .

5.4 Chiral limit and degenerate quark masses

After having considered the impact of $m_u = m_d$ and m_s , varied separately, on the critical point, we proceed to change both parameters simultaneously. The first step in this direction is to check effects of degenerate quark masses, starting with the chiral limit, i. e. $m_u = m_d = m_s = 0$.

With no explicit chiral symmetry breaking in the model any more, the influence of the KMT interaction strength K is more evident. In Fig. 5.6 we show the transition lines in the phase diagram for different values of K . A stronger $U(1)_A$ symmetry breaking term delays the restoration of chiral symmetry, visible in the increased areas under the curves.

The rate of increase of the transition parameters is examined in more detail in Fig. 5.7. With red diamonds, we have plotted the relative change of $T_{\text{trans}}(\mu = 0)$ as a function of K/K_0 . The relative change of $\mu_{\text{trans}}(T = 0)$ as a function of K/K_0 is shown with blue circles. Because of the large change in μ and the comparatively small change in T , the relative change in the area under the curves is almost identical to the μ_{trans} curve for $K \leq K_0$ and is therefore not explicitly shown.

Since the effects in the μ -direction are significantly larger, increasing K/K_0 means decreasing the curvature of the phase transition line. In the following section 5.5 we will compare this quantity to some recent lattice QCD results to check if a preference for a certain value of K can be determined. We continue with a scenario with three quark flavors of degenerate masses

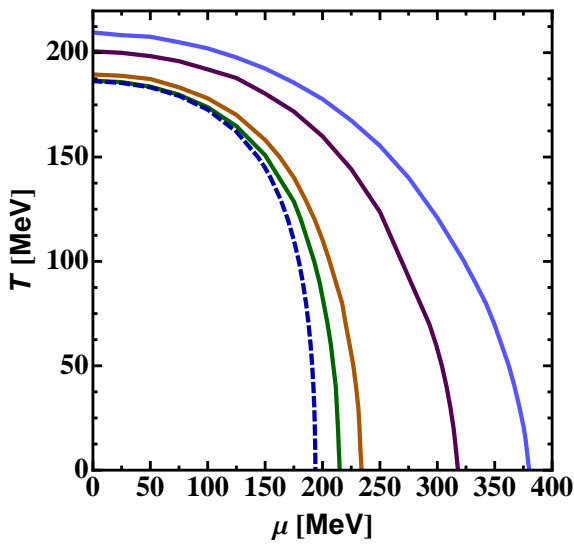


Fig. 5.6: Transition lines in the phase diagram for different values for the KMT interaction strength K in the chiral limit. From innermost to outermost: $K/K_0 = 0, 1/3, 1/2, 1, 4/3$. Solid lines are first-order transitions, the dashed line is the second order transition for $K = 0$. There is no crossover anywhere for any value of K .

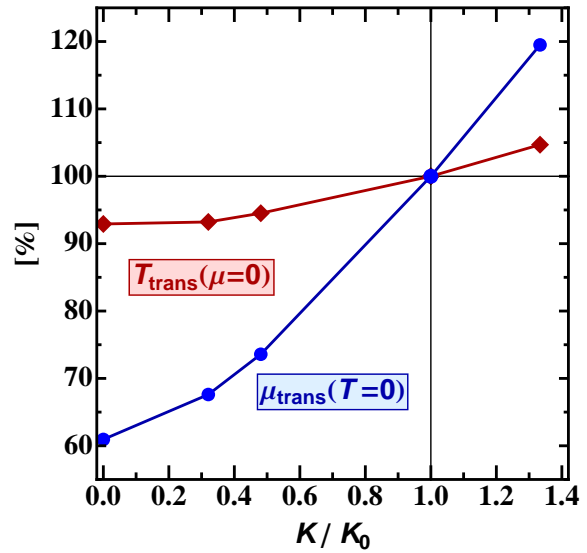


Fig. 5.7: Diamonds: relative change of $T_{\text{trans}}(\mu = 0)$ as a function of K/K_0 in the chiral limit. Circles: relative change of $\mu_{\text{trans}}(T = 0)$ as a function of K/K_0 in the chiral limit.

($m_q \equiv m_u = m_d = m_s$). In Fig. 5.8 we have plotted the chiral condensate, $-\sigma_q$ at $\mu = 0$ as a function of temperature, for different values of m_q . Curves on the left-hand side result from lower values of m_q (starting from $m_q = 1$ MeV), curves on the right-hand side from higher values (up to $m_q = 3$ MeV). It is clearly visible how the first-order transition in the chiral limit (not depicted) is weakened with increasing current quark mass until, at a critical point with $m_q = 2.43(1)$, it becomes second-order. From there on, it turns into a crossover. As a consequence, a critical point appears in the phase diagram. The trajectory of the critical point with increasing current quark mass is shown in Fig. 5.9. Further studies of this subject could be compared to e.g. lattice calculations within the imaginary chemical potential approach [40], where two tricritical points in the T - m_q -phase diagram are found.

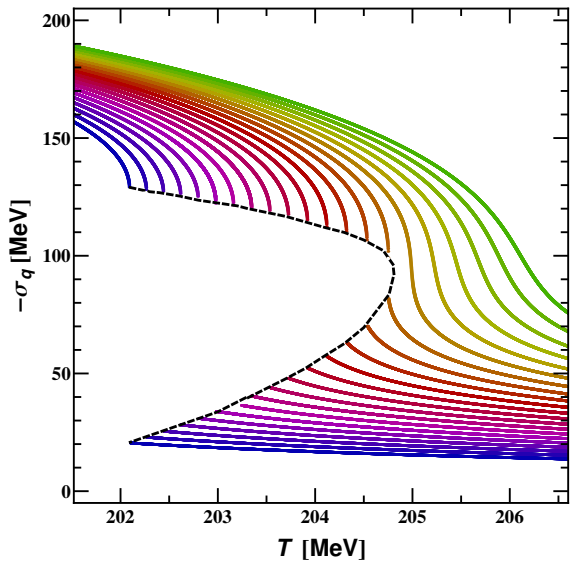


Fig. 5.8: Chiral condensate at $\mu = 0$ as a function of T for different (but equal) current quark masses, $m_q \equiv m_u = m_d = m_s$; masses increase from left (1.0 MeV) to right (3.0 MeV) in steps of 0.1 MeV.

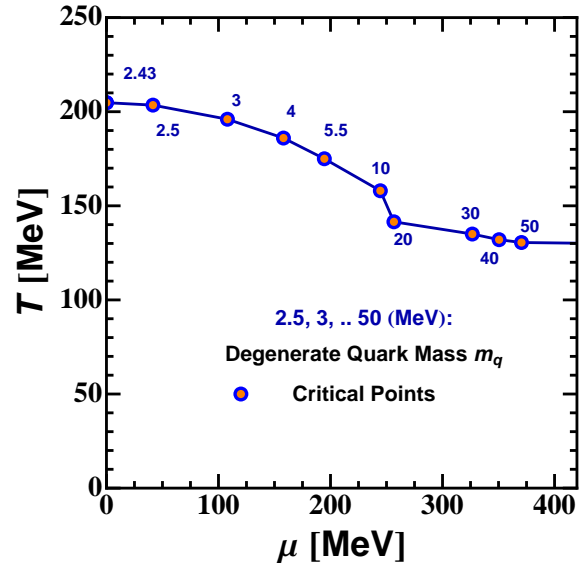


Fig. 5.9: Trajectory of critical points in a scenario with three degenerate current quark masses $m_q \equiv m_u = m_d = m_s$.

5.5 Curvature of the phase transition line

We have seen in the last section how changing K influences the curvature of the chiral transition line. In the chiral limit $m_u = m_d = m_s = 0$, we had plotted the termination points of the transition lines at the $T = 0$ and $\mu = 0$ axes in Fig. 5.7. The different rate of increase leads to a changing curvature of the transition line as a whole. The same behavior is found in the case of $m_u = m_{u,0}$ and $m_s = m_{s,0}$.

For the curvature of the transition line, recent lattice QCD results [72, 43] are available. Although lattice calculations cannot, because of the fermion sign problem, be extended to large values of μ/T , the curvature can be determined by Taylor expansion to the leading (second) order in μ/T .

In the chiral limit the transition is first-order at $\mu = 0$ and the determination of the curvature is straight-forward. For a crossover we calculate the curvature of the line of constant $\sigma_u(T_{\text{cross}}^X, \mu) / \sigma_u(T = 0, \mu = 0) = 0.5$. Characterizing crossovers by a band means that we should take the whole band into account also when we are interested in κ . By determining the curvatures of the line of constant $\sigma_u(T_{\text{low}}, \mu) / \sigma_u(T = 0, \mu = 0) = 0.75$ as well as of the line of constant $\sigma_u(T_{\text{high}}, \mu) / \sigma_u(T = 0, \mu = 0) = 0.25$, we specify error bands for the curvature.

The curvature κ of the transition is defined by

$$\frac{T_c(\mu)}{T_c(0)} = 1 - \kappa \left(\frac{\mu^2}{T_c^2} \right), \text{ or equivalently, } \kappa = -T_c \left. \frac{dT_c(\mu)}{d\mu^2} \right|_{\mu^2=0} \quad (5.5.1)$$

with T_c denoting the critical temperature in the chiral limit, or either T_{trans} , T_{low} , or T_{high} in the case of a crossover. Two independent lattice calculations [72, 43] give $\kappa \simeq 0.06$ with comparatively small errors.

We show the curvature κ as a function of K/K_0 in Fig. 5.10. Chiral limit results are marked by orange crosses (no errors given), physical quark mass results (crossovers) by blue dots with error bars according to the transition bands. Lattice results are added as solid lines with gray

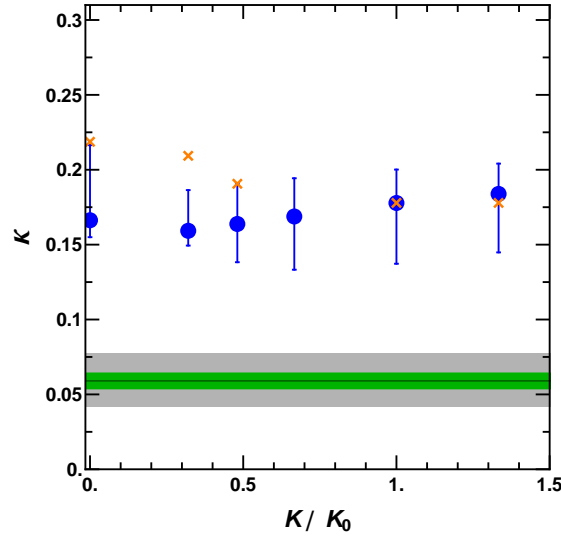


Fig. 5.10: Curvature κ - given by (5.5.1) - as a function of K/K_0 in the chiral limit (red crosses) and for physical quark masses (blue circles). The error bars show the range of κ corresponding to the crossover width at $\mu = 0$. The thick green line shows a result from lattice calculations [72]. The slim gray line and shaded area are lattice results from [43].

and green error ranges. The plot has two main messages. First, κ is quite insensitive to a globally constant K . Chiral limit values range between $0.18 \lesssim \kappa \lesssim 0.22$. For finite current quark masses, κ is for all error bars consistent with $0.15 \lesssim \kappa \lesssim 0.19$. Second, all values are far from the lattice QCD values $\kappa \simeq 0.05 \sim 0.07$.

In principle, we imagine K “in nature” to be some function $K_{\text{phys}}(T, \mu)$, see section 5.2. The next simplest assumption after a globally constant K as in Fig. 5.10 is a coupling that depends only on temperature *or* chemical potential.

We start with the temperature dependence of K . One possible estimate for $K(T)$ is based on the semi-classical instanton tunneling amplitude $n(T, \xi)$ [121]:

$$K(T)/K_0 \sim n(T, \xi) \sim \exp\left[-\frac{8}{3}(\pi \xi T)^2\right], \quad (5.5.2)$$

where ξ is the instanton size. Its average is usually estimated as $\xi \approx 1/3$ fm. In Fig. 5.11 we show K as a function of T based on (5.5.2) for this, as well as some other choices of ξ . Already for $\xi \gtrsim 1/6$ the restoration of $U(1)_A$ is very quick and takes place at $T \lesssim T_c$. Recent lattice QCD results show no indication of a restoration of $U(1)_A$ below or around T_c . We present results² for the curvature κ as a function of the instanton size ξ in Fig. 5.12. The influence of the T -dependence of K on κ is evidently small. This goes especially for the low values of ξ which, according to Fig. 5.11, seem to be the more reasonable ones.

Next, we study K as a function of μ . The effect on the curvature at $\mu = 0$ of a μ -dependent K is expected to be small as well. It is instructive to see the quantitative effect of even extreme assumptions for $K(\mu)$. Let us first assume a linear decrease of K with μ of the form

$$K(\mu) = K_0 - \frac{\mu}{\Lambda} (K_0 - K_{\text{min}}^\Lambda), \quad (5.5.3)$$

²The early restoration of $U(1)_A$ has strong effects on the chiral condensates. For this plot only, we determined the crossover boundary by $\sigma_u(T)/\sigma_u(0) = 0.6, 0.4$ and 0.2 instead of the usual $0.75, 0.5$ and 0.25 .

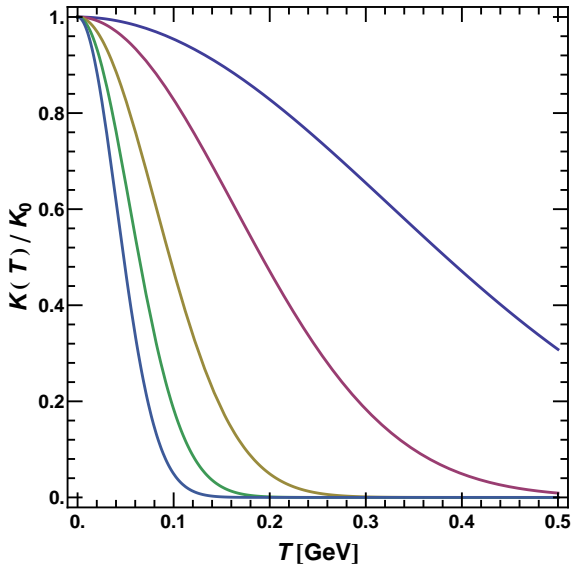


Fig. 5.11: Normalized KMT coupling $K(T)/K_0$ as a function of the temperature for different values of the instanton size ξ according to eq. (5.5.2). From right to left: $\xi = 1/12, 1/6, 1/3, 1/2$ and $2/3$.

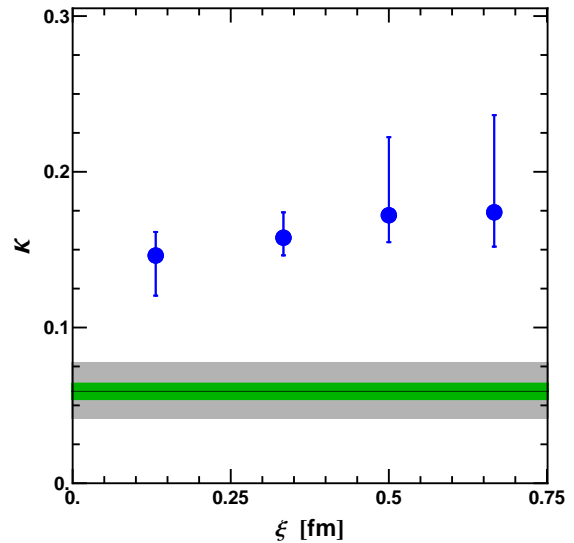


Fig. 5.12: Curvature κ of the crossover boundary near T_c as a function of the instanton size ξ , see eq. (5.5.2) and Fig. 5.11. Lattice data and error bars as in Fig. 5.10.

so that $K(\mu)$ decreases linearly from $K = K_0$ at $\mu = 0$ to $K = K_{\min}^\Lambda$ at $\mu = \Lambda$ as depicted in Fig. 5.13. Fig. 5.14 then shows the curvature κ as a function of the minimal value $K_{\min}^\Lambda \equiv K(\mu = \Lambda)$. Evidently the effect is so weak that within error bars it is negligible.

As an alternative to the linear form, we have also investigated the effects of an exponentially decreasing $K(\mu)$ of the form

$$K(\mu) = K_0 e^{-(\mu^2/\mu_0^2)} \quad (5.5.4)$$

with a free scale parameter μ_0 . This Gaussian ansatz is motivated by the suppression of the instanton density due to Debye screening [30].

Fig. 5.15 shows the functions $K(\mu)$ for some choices of μ_0 . The impact on the curvature is then depicted in Fig. 5.16. Only for $\mu \lesssim 0.375 \Lambda$ (second point from the left) do the error bars for κ move away from the standard result ($K = K_0$) significantly. This choice corresponds to the second curve from the bottom in Fig. 5.15, which already shows a drastic decrease of K with μ . In this scenario, the axial anomaly would have almost completely disappeared already within the hadronic phase and far below the cutoff, which is very unlikely.

Physically reasonable choices of $K(\mu)$ are therefore seen to have little impact on κ . The case of $K_{\text{phys}}(T, \mu)$ may then be decently approximated by our studies for a globally changed K , under the assumption that the degrees of susceptibility of K to T and μ are not extraordinarily skewed.

In conclusion, we notice a discrepancy between results of our model at this stage and results of lattice QCD calculations for the phase transition curvature κ . Neither global changes of K nor sensible choices for K as a function of T or μ were able to improve matters in this respect. A solution is found in the inclusion of a repulsive vector type interaction with a large coupling g_v (see section 7.7, especially Fig. 7.36).

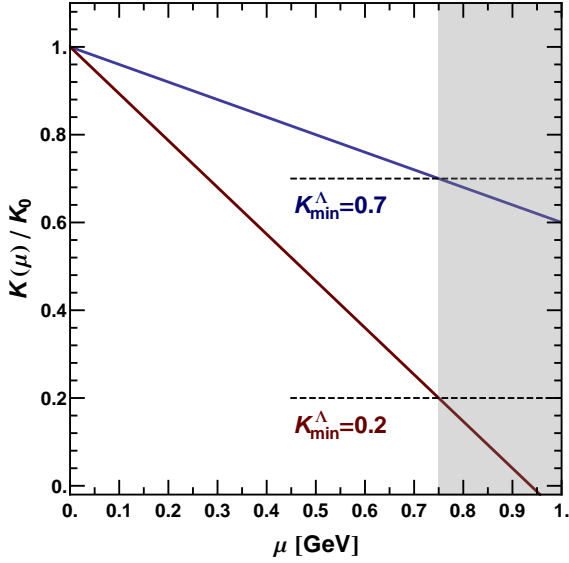


Fig. 5.13: Normalized, linearly running KMT coupling $K(\mu)/K_0$ as a function of the chemical potential for different values of K_{\min}^Λ according to eq. (5.5.3). The gray area marks chemical potential beyond the cutoff Λ .

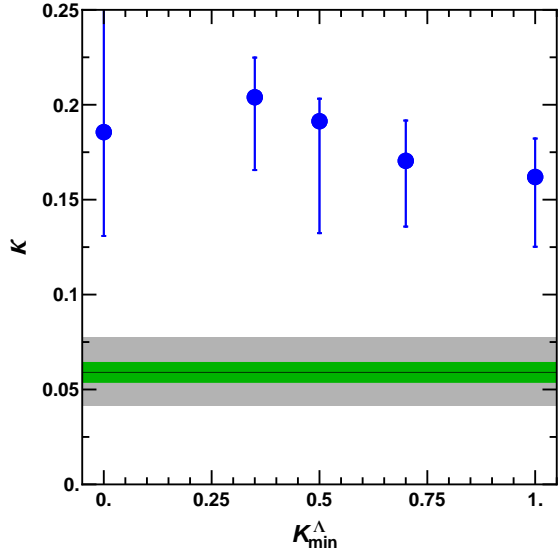


Fig. 5.14: Curvature κ of the crossover boundary near T_c as a function of K_{\min}^Λ , see eq. (5.5.3) and Fig. 5.13. Lattice data and error bars as in Fig. 5.10.

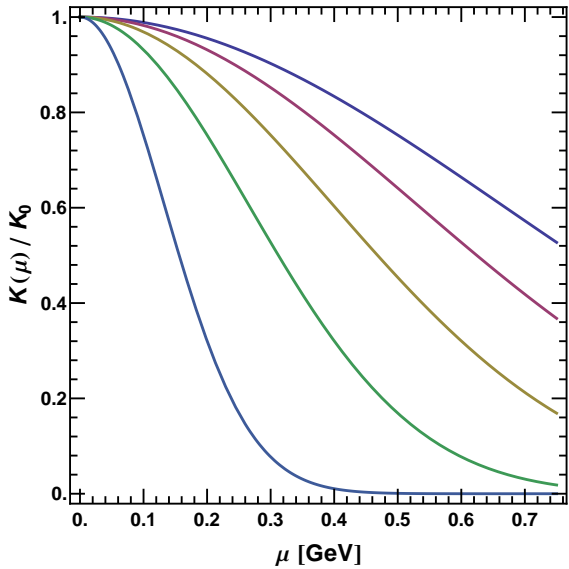


Fig. 5.15: Normalized, exponentially decreasing KMT coupling $K(\mu)/K_0$ as a function of the chemical potential for different values of μ_0/Λ according to eq. (5.5.4). From left to right: $\mu_0/\Lambda = 1/4, 3/8, 1/2, 3/4, 1$ and $5/4$.

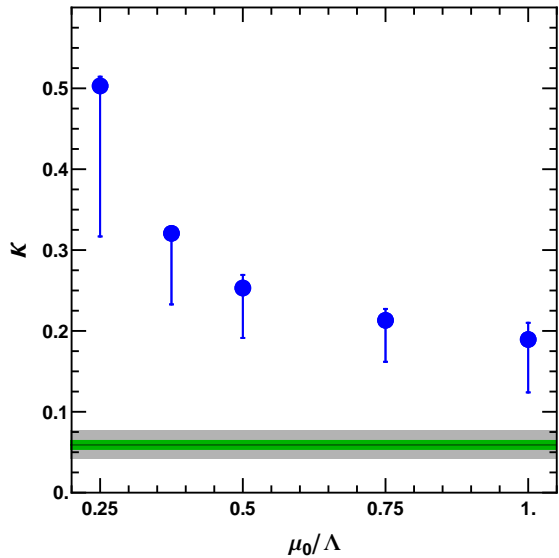


Fig. 5.16: Curvature κ of the crossover boundary near T_c as function of K_{\min}^Λ , see eq. (5.5.3) and Fig. 5.13. Lattice data and error bars as in Fig. 5.10.

5.6 Type of the phase transition at $\mu = 0$

A concise way to display the information about different classes of phase transitions at $\mu = 0$ in the m_u - m_s -plane is the so-called ‘‘Columbia plot’’ [25, 71, 87]. In section 5.4 we have already calculated one line in this plane. In the following, we present a number of Columbia Plots for different scenarios. For some of these scenarios, similar calculations done with the unphysical ‘‘minimal’’ cutoff scheme and different parameter set can be found in [52].

The first plot, shown in Fig. 5.17, is the standard case, as calculated in our model with all input values (except the current quark masses) according to the parameter fit. The plotted curve is the line of second-order phase transitions. Mass combinations between this curve and the origin (chiral limit) result in a first-order transition along the temperature axis in the phase diagram. Mass combinations beyond the line signify a crossover at $\mu = 0$. For very heavy quark masses the system is dominated by gluon dynamics. In the upper right corner of the Columbia plot another first-order transition region is expected [87]. The lower dashed line marks the case of three degenerate flavors $m_u = m_d = m_s$. The evolution of the chiral condensate along this line was shown in Fig. 5.8. The trajectory of critical points in the first-order region was presented in Fig. 5.9.

Our result for the form of the second-order curve with its smooth convergence toward to the m_u and m_s axes compares well with qualitative results from chiral random matrix calculations [49]. This close correspondence confirms that the Columbia plot, at least for $\mu = 0$, is almost exclusively determined by chiral dynamics³.

Our finding also compare quite well with lattice QCD results. In [42], the authors estimate upper bounds for a specific point on the second order line, namely the point where the m_s/m_u ratio equals the ratio in their input parameter set. Their ratio of about 27.3 is well comparable with ours of about 25. As it turns out, our point with $m_s/m_u=27.3$ on the second-order line lies at ($m_u = 0.36$ MeV, $m_s = 9.9$ MeV). Expressed as a fraction of the m_u input parameter $m_{u,0} = 5.5$ MeV, the coordinates of this point are ($m_u = 0.066 m_{u,0}$, $m_s = 1.8 m_{s,0}$). The value of $0.066 m_{u,0}$ is in good agreement with the upper limit of about $0.07 m_{u,0}$ found for $N_T = 4$ in [42]. However, at this point the predictive power of these lattice data is still somewhat uncertain, since the authors state that their upper boundary estimate increases by about 50% (to $0.12 m_{u,0}$) when increasing N_T by 50% (from $N_T = 4$ to $N_T = 6$): the continuum limit has obviously not yet been reached.

Fig. 5.18 investigates the very low m_u region of the Columbia plot. The horizontal axis now shows $m_u^{2/5}$ so that the resulting curve is a straight line, as it should be according to a generic Landau-Ginzburg analysis [71, 141, 49]. We extrapolate and find that the tri-critical point lies at about $m_s = 18.4$ MeV. For all higher values of m_s with $m_u = 0$, the transitions are expected⁴ to be second-order [87].

Next, we examine the influence of the KMT interaction on the Columbia plot. The results of this study are collected in Fig. 5.20a. The area under the curve in each case represents a region of a first-order transitions, the curve itself is second-order and the area above the curve implies crossovers. The $K = K_0 = 156$ GeV⁻⁵ curve is the same as in Fig. 5.17. For $K = 0$ there is only a single point of second-order transition at $m_u = m_s = 0$ and crossovers everywhere else.

The growing areas under the curves in Fig. 5.17 show that at $\mu = 0$ an increasing KMT interaction strength K influences the phase transition in the *opposite* way of an increase in the bare quark masses. From the quark mass gap equations (3.3.45) we would intuitively expect that the KMT term effectively increases the quark mass and thus a change in K acts in the *same*

³In this context it might be important to keep in mind that, with the exception of the overlap fermion discretization [74], chiral symmetry is broken to some extent by all lattice formulations of QCD.

⁴Determining the difference between a first and a second order transition is not possible with our numerical setup.

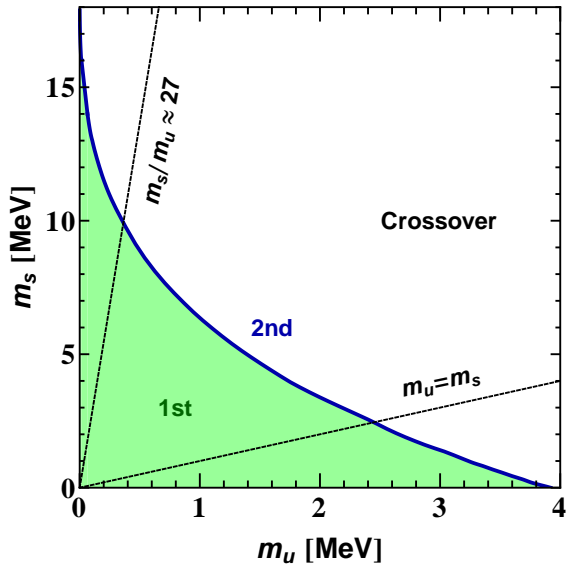


Fig. 5.17: Classification of the transition of the (light quark) chiral condensate at the temperature axis ($\mu = 0$), depending on $m_u = m_d$ and m_s (Columbia plot). The $m_s/m_u \approx 27$ line has been included to compare the absolute values to results in [42] (see text above).

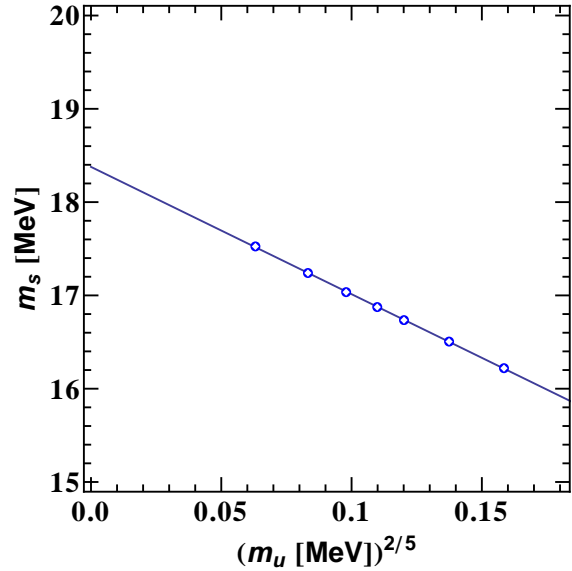


Fig. 5.18: Classification of the transition of the (light quark) chiral condensate at the temperature axis ($\mu = 0$), depending on $m_u^{2/5}$ and m_s (Columbia plot), detail.

direction as a change in the bare masses. However, in the self-consistent calculation, this term is overpowered by the condensation term (last term in 4.2.6) and the relationship is reversed.

Note that combinations of current quark mass that result in a first-order transition in our Columbia plot of Fig. 5.17 are far below the parameter values of $m_{u,0} = 5.5$ MeV and $m_{s,0} = 141$ MeV. It is evident that for all studied values of K , there is a crossover at $\mu = 0$ for our standard parameter values.

5.7 Transition systematics in m_u - m_s - μ space

Calculating ‘‘Columbia’’ curves as in Fig. 5.20a for different chemical potentials, one constructs the so-called ‘‘critical surface’’. In the literature, the curvature of this sheet of critical points is still under discussion. Even just for the low μ/T scenario, arguments for curvatures of both signs can be found [39, 106]. In this context, a negative curvature means a shrinking first-order transition region when μ is increased. The notion of back-bending has also been brought up, where the critical surface first curves away from the physical point, then turns around and hits it at higher chemical potentials [51, 30].

In our model we can construct the full three-dimensional ‘‘Columbia’’ structure in μ - m_u - m_s -space. In contrast to lattice QCD groups, we do not have to extrapolate and can therefore check explicitly the curvature and signs of back-bending. For our standard parameter set with $K_0 = 156$ GeV $^{-5}$, we get the picture shown in Fig. 5.19. With these settings we find a monotonous bending of this second order transition surface towards the ‘‘physical’’ (or model parameter) combination of m_u and m_s . This is the expected result of a positive curvature for all μ . Next, we look into the effects on the standard Columbia plot when varying the $U(1)_A$. In Fig. 5.20 we have collected results for four different values of K , namely $K = 50$ GeV $^{-5}$, $K = 100$ GeV $^{-5}$, $K = K_0 = 156$ GeV $^{-5}$ and $K = 200$ GeV $^{-5}$, or, in relative terms, $K = 0.32 K_0$, $K = 0.64 K_0$, $K = K_0$ and $K = 1.28 K_0$. Fig. 5.20a shows the patterns at $\mu = 0$ and Fig. 5.20b

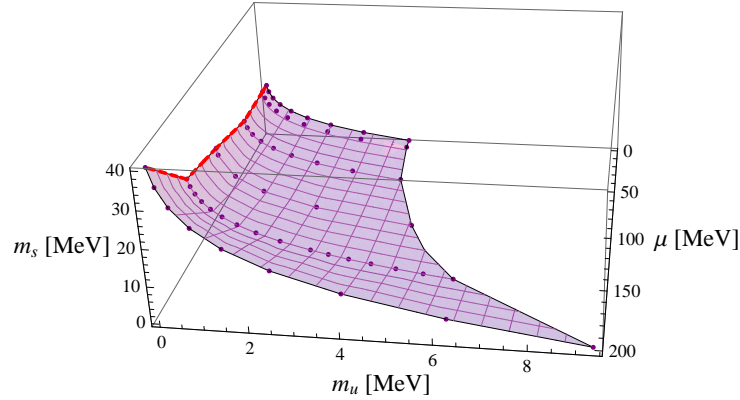
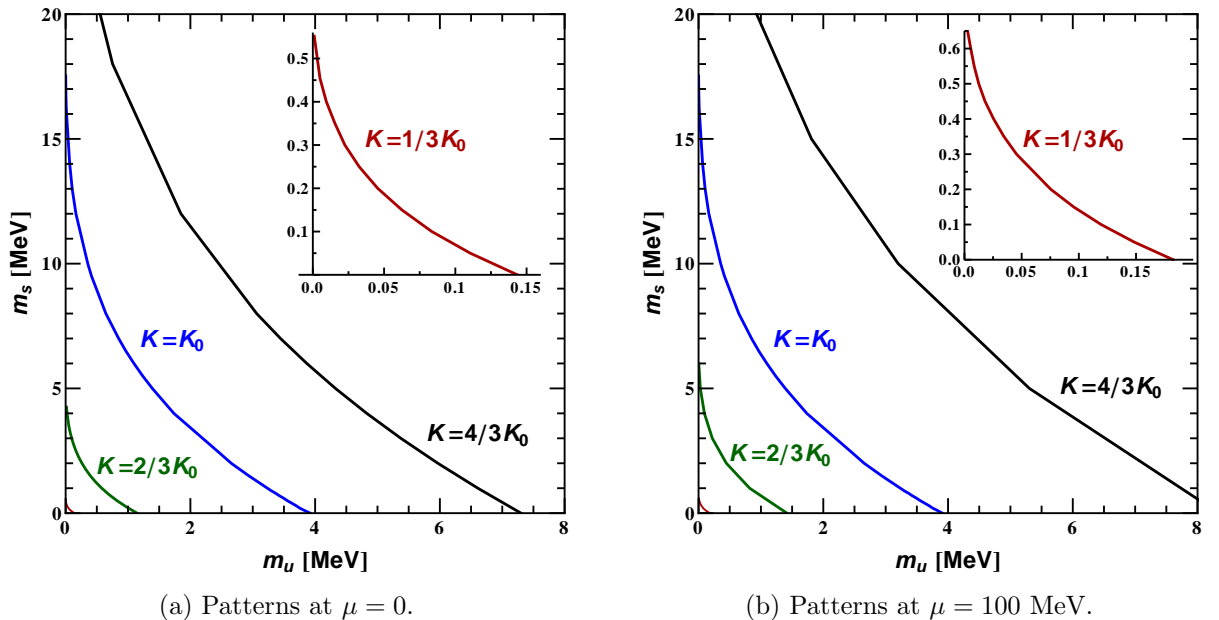


Fig. 5.19: Columbia plots (second order transition lines as functions of m_u and m_s) as a function of μ for $K = K_0$. The surface terminates at the border on the right and the one in the rear, but continues on the left and in front. The dashed red lines therefore denote where we stopped the calculations, while the solid black lines are the physical boundaries for $\mu \geq 0$ and $m_u \geq 0$.

at $\mu = 100$ MeV. Evidently, the first-order phase transition regions expand with increasing μ for all studied values of K . Accordingly, the curvature of the critical surface is always positive in these scenarios. Fig. 5.21 presents the analogue of Fig. 5.19 for a smaller K of $K = 1/3K_0$. In



(a) Patterns at $\mu = 0$.

(b) Patterns at $\mu = 100$ MeV.

Fig. 5.20: “Columbia Plot” describing the transition orders for different values of K at two different chemical potentials μ . Areas left of the curves denote first-order transitions, areas right of the curves crossovers. The curve itself indicates second order transitions, i. e. critical points.

this scenario, there is no longer a first-order transition in the phase diagram for physical quark masses, see Fig. 5.2 and Fig. 5.3. The critical surface ends at about $\mu \sim 250$ MeV, where the

transition temperature has decreased to $T = 0$ (Fig. 5.3). A third interesting scenario, between

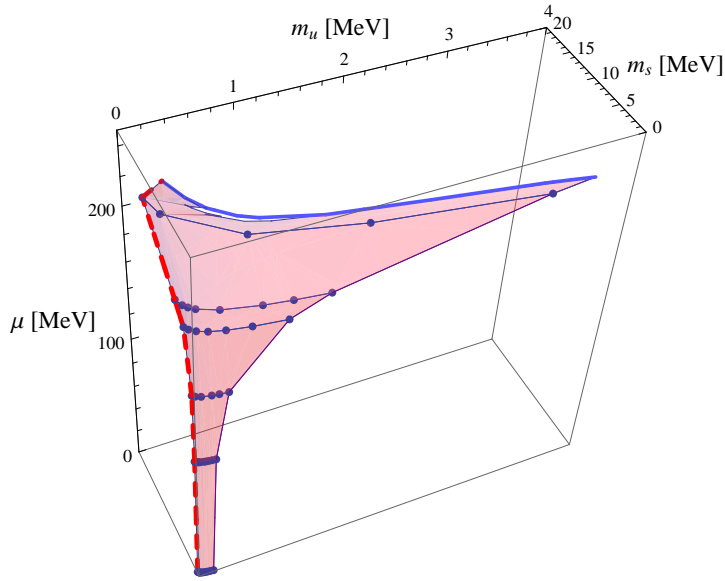


Fig. 5.21: Columbia plots (second order transition lines as functions of m_u and m_s) as a function of μ for $K = \frac{1}{3}K_0$. The surface terminates at the border on the right and in front (blue, black), but continues on the left and in the rear (dashed red). From the spectators point of view, the first-order transition volume lies before the surface and the crossover region beyond.

the standard scenario with a critical point ($K = K_0$) and a scenario with a pure crossover ($K = K_0/3$) is the setting of $K = K_0/2$. According to Fig. 5.2 that is the value at which the critical point vanishes from the phase diagram. The m_u - m_s - μ space “Columbia” plot in this case is somewhat involved. We present it in 5.22 for comparison but will not go into a detailed description.

The comparison of Figs. 5.19, 5.21 and 5.22 sends a message of caution: in all cases, the curvature of the critical surface is small until about $\mu \sim 150$ MeV. From then on, it increases considerably, and the surface is changed also qualitatively. It is evident from the comparison of these three plots that one has to be extremely careful in extrapolating lattice QCD data for small μ in order to determine the existence of a critical point. In order to stress this point, we show the “Columbia” plot for $K = K_0/2$ at $\mu = 270$ MeV in Fig. 5.23. For low current masses, a phase of restored chiral symmetry (χ SR) has appeared. The first-order transition region has split up into two separate areas. It should be noted that these effects are far from the physical point, as $m_s \ll m_s^0$. In addition, the choice of $T \sim 0$ and $\mu \sim 250$ MeV puts them deep into the domain of nuclear physics. The plot is simply a demonstration that increasing μ in the Columbia plot can lead to complex scenarios that are not evident from the low μ behavior – compare Fig. 5.20 and Fig. 5.23. The phase of restored chiral symmetry (χ SR) is the large μ boundary of the critical surface. Its shape can be partially seen from Figs. 5.24 and 5.25. They show a slice at $m_s = 0$ through the three-dimensional plots in Fig. 5.22 and Fig. 5.19, respectively. The χ SR phase trivially intersects with the critical surface at $T = 0$. The plots confirm again that the curvature of the critical surface is strongly sensitive to μ and K . In addition, e.g. for $K = K_0$ the curvature at $m_s = 0$ in Fig. 5.25 is almost constant, in contrast to the situation at $m_s > 0$ and $m_u = 0$, visible in Fig. 5.19. These effects are another factor in the challenges when extrapolating from small to large chemical potentials.

In section 2.4 we mentioned that, for lattice QCD calculations at finite μ , approximations

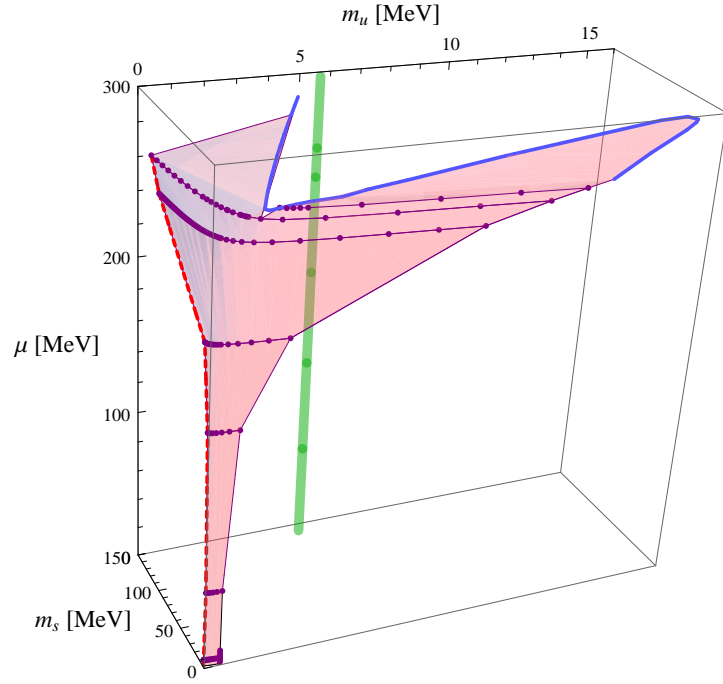


Fig. 5.22: Columbia plots (second order transition lines as functions of m_u and m_s) as a function of μ for $K \approx \frac{1}{2}K_0$. The surface terminates at the border on the right and in front, but continues on the left and in the rear. The green bar represents the “physical point” line that the right hand border of the Columbia surface will hit eventually.

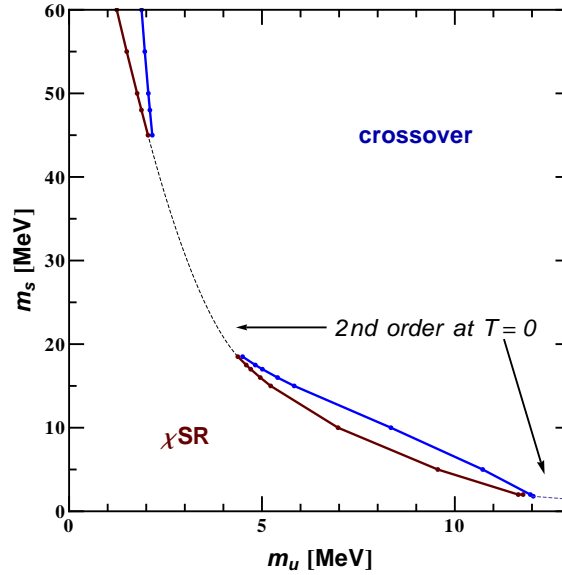


Fig. 5.23: Columbia plot at $\mu = 270$ MeV for $K \approx \frac{1}{2}K_0$. In the two areas between the bold lines, there is a first-order transition. Dashed line between the crossover region and the region with restored chiral symmetry (“ χ SR”) marks second order transitions at $T = 0$.

have to be made that have limited ranges of applicability (“fermion sign problem”). The reweighting and Taylor expansion techniques are limited to $\mu/T \lesssim 1$, while the imaginary chemical potential approach breaks down at $\mu_B \approx 500$ MeV, or $\mu \approx 183$ MeV [106]. Fig. 5.26 gives

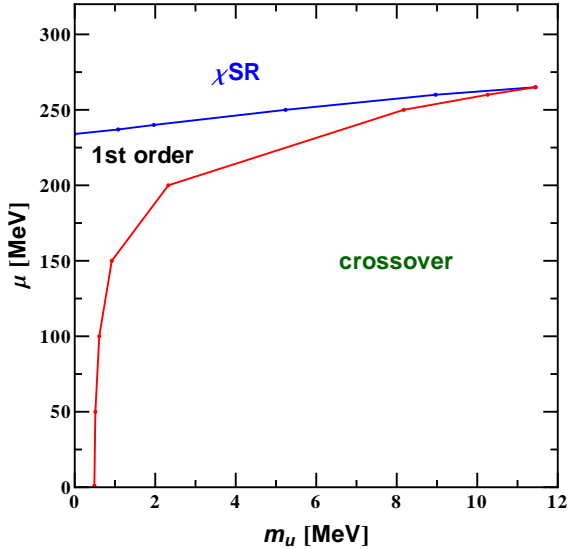


Fig. 5.24: Slice through Fig. 5.22 at $m_s = 0$ for $K \approx \frac{1}{2}K_0$, including the upper boundary determined by the $T = 0$ condition (upper solid line). The lower solid line is the second order transition line.

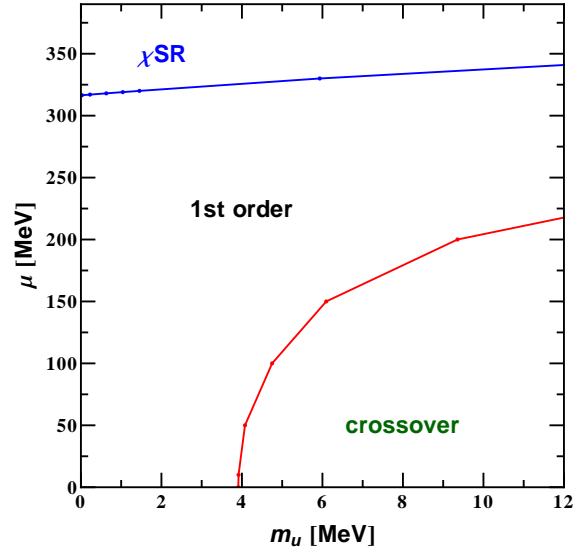


Fig. 5.25: Slice through Fig. 5.19 at $m_s = 0$ for $K = K_0$, including the upper boundary determined by the $T = 0$ condition (upper solid line). The lower solid line is the second order transition line.

an impression how far lattice QCD can (at most) determine the critical surface. We present the ratios μ/T for the critical points at $\mu_s = 0$ and varying μ_u at $K = K_0/2$ and $K = K_0$, corresponding to the red lines in Fig. 5.24 and Fig. 5.25, respectively. We have shaded the regions inaccessible to the lattice in gray. Interestingly, all three techniques seem to be limited to $\mu \lesssim 150$ MeV: up to this chemical potential, results for all values of K were qualitatively similar, with major differences occurring only for higher μ . However, one should keep in mind that the curvature of the chiral transition in lattice QCD results is smaller than in our calculation (without vector interaction).

We conclude this chapter with a short study of the $T = 0$ curves of the critical surface, presented in Fig. 5.27. They mark the boundary between the crossover, first-order transition, and χ SR regions in the μ - m_u - m_s space. Even for the small range of K from $0.32K_0 \sim 0.51K_0$, there are large qualitative as well as quantitative differences. Note that at $\mu = 0$ the respective Columbia plots would be qualitatively identical (cf. Fig. 5.20a), with no indication of the enormous differences at large μ and small T .

5.8 Summary

We have performed extensive studies of the transition patterns of the chiral condensate, starting from $\mu = 0$ (Columbia plot) and extending to finite chemical potentials. As one result, we have shown that certain areas in $\mu - m_u - m_s$ space, especially for $\mu \leq 150$ MeV, have the same Columbia plot structure for all values of the axial $U(1)$ symmetry breaking interaction $K > 0$ and that other areas are strongly influenced by changes of this quantity. We have provided several examples for this fact, which serve to underline an important message: the curvature of the critical surface at small chemical potential μ is not necessarily a good indication of physics at large μ , especially regarding the existence of the critical point. Our work shows that the axial anomaly is of paramount importance and can influence high density physics.

At this point, further input about the critical surface and the Columbia plot from lattice QCD is necessary. Even more important would be a better theoretical understanding of the μ

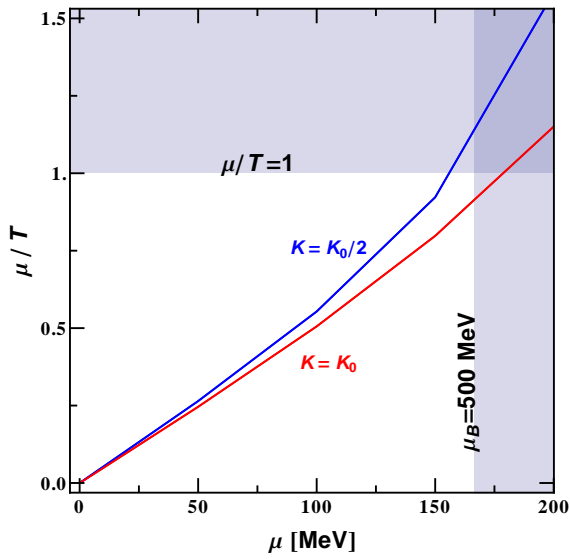


Fig. 5.26: Ratio μ/T as a function of quark chemical potential μ along the $m_s = 0$ critical line. Upper curve (blue) corresponds to red line in Fig. 5.24, i. e. $K = K_0/2$. Lower curve (red) corresponds to red line in Fig. 5.25, i. e. $K = K_0$. Shaded areas show regions probably inaccessible by lattice calculations, see foregoing discussion.

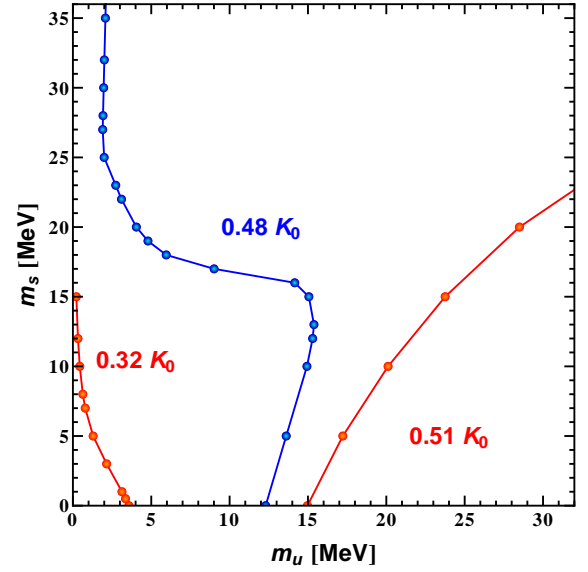


Fig. 5.27: “Columbia Plot” describing the transition orders at $T \approx 0$ for different values of K . Areas left of the curves denote first-order transitions, areas right of the curves crossovers. The curve itself indicates second order transitions, i. e. critical points.

and T dependence of K . In [51], some exploration of the critical surface under the influence of an exponentially decreasing K was performed; while promising, the assumed functional form is only one option out of many.

We also studied the curvature of the chiral phase transition line κ for a large variety of T - or μ -dependent forms for the KMT interaction strength K . In all cases the results were incompatible with recent, very precise lattice QCD results. For one possible solution, we refer to section 7.7.

Chapter 6

Parameters of the Polyakov loop effective potential

6.1 Introduction

In the last few years, lattice QCD has made significant progress in determining the chiral condensate and the Polyakov loop as functions of T at $\mu = 0$. In Fig. 6.1 we show lattice QCD results for the renormalized Polyakov loop at $\mu = 0$ as a function of T/T_c , collected in [13]. A recent update by the same group, the hotQCD collaboration, is found in [9]. Results by the independent Budapest-Wuppertal group are very close [19]. Fig. 6.2 shows results from both groups combined as a function of absolute values of T . It is remarkable how close all the curves

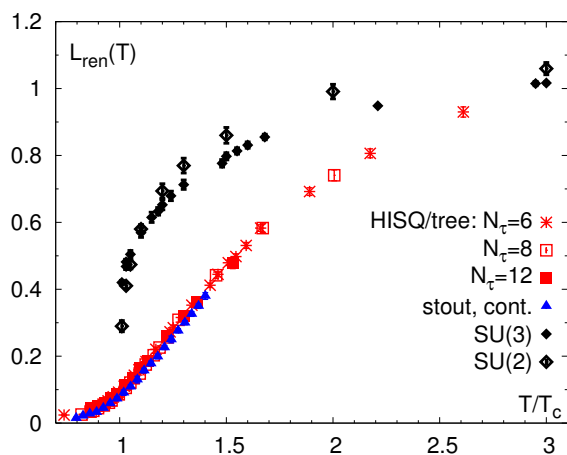


Fig. 6.1: Renormalized Polyakov loop L_{ren} as a function of T/T_c at $\mu = 0$ with $T_c = 157$ MeV. Pure gauge results in black, 2 + 1 flavor results in color. Plot taken from [13].

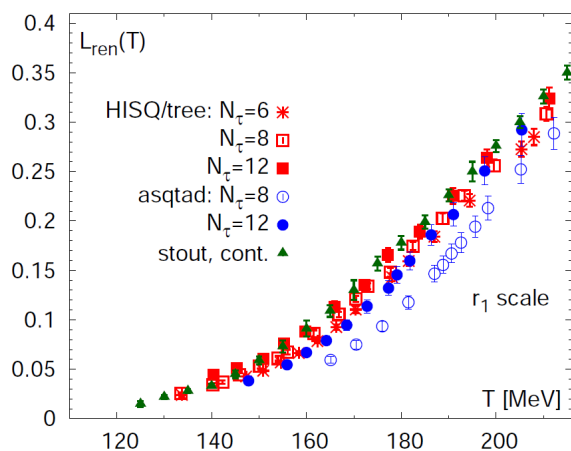


Fig. 6.2: Low temperature region of the renormalized Polyakov loop L_{ren} as a function of T at $\mu = 0$, showing detailed results from both the hotQCD and the Wuppertal-Budapest collaborations. Plot taken from [10].

are to one another, especially taking into account the different lattice QCD actions and spacings used. All data sets apart from the $N_\tau = 8$ asqtad set are reported to be insensitive to cutoff effects [10] so that the convergence of the calculations appears to be well under control. This motivates our strong focus on the Polyakov loop in this chapter. The main goal is to find a mechanism that produces a Polyakov loop crossover as shown in Fig. 6.1. The second objective is to determine the influence that cutoff schemes (see chapter 4) have on the interplay between chiral and Polyakov loop dynamics. The behavior of the Polyakov loop is determined by the Polyakov

loop effective potential $\mathcal{U}(\Phi)$, see section 3.5. Our potential is designed [109, 117] by fitting to pure glue lattice results [20, 73]. It is then added unchanged to the effective thermodynamic potential (density) Ω . The assumption that this is a good approximation to real physics is not trivial. In fact, recently the discussion of matter back-reactions from quark loops onto Polyakov loop dynamics has gained a lot of momentum. The standard PNJL model is incomplete in this regard. One of the simplest proposed back-reaction mechanisms is a reduction of T_0 , depending on the number of flavors [119, 120]. A more involved ansatz [53] is motivated by the chemical freeze-out curve derived from experimental data and combined with an interpretation based on the Statistical Model [6, 14, 35]. It sets T_0 as function of μ and fits the parameters of the function according to the freeze-out points. We will examine both of these ideas in section 6.3.4 and section 6.3.7, respectively.

In principle, there are two main methods for modeling¹ a pure glue quantity such as the Polyakov loop effective potential. One can either adhere strictly to the information from pure glue theory, as described in 3.5. Or one can determine $\mathcal{U}(\Phi)$ in such a way as to reproduce $2 + 1$ flavor lattice QCD results. Having set the former method as our standard, we will in this chapter vary the parameters of $\mathcal{U}(\Phi)$ and investigate the consequences this has on the final results.

If a Polyakov loop effective potential is supposed to reproduce pure glue lattice results for the Polyakov loop and thermodynamic quantities, there are two main requirements: First, the *location* of the minimum of the curve $\mathcal{U}_T(\Phi)$ for a given temperature T determines $\Phi(T)$. Therefore, the requirement of a good fit to Polyakov loop lattice data makes strong demands on the location of the minima of $\mathcal{U}_T(\Phi)$ as a function of T . Secondly, thermodynamic quantities are calculated from the pressure $p = -\mathcal{U}(T)$, where $\mathcal{U}(T)$ is determined via $\mathcal{U}(\Phi)$ and $\Phi(T)$. Consequently, the *depth* of the minimum as a function of T determines pure glue thermodynamics. Given these two facts and the boundary conditions, there is almost no freedom to tune the Polyakov loop effective potential.

In this chapter we investigate two different potentials $\mathcal{U}(\Phi)$. Section 6.2 will deal with the comparatively simple Fukushima potential (6.2.1), an instructive model due to its clear structure. In section 6.3 we treat our own potential, the Rößner–Ratti–Weise ansatz [117]. Keeping the functional forms, we will vary the respective parameters. The first step is to understand the effects of parameter choices for $\mathcal{U}(\Phi)$ on results both in pure glue calculations as well as in scenarios including quark degrees of freedom. In a second step we will find a parameter combination that reproduces $2 + 1$ flavor lattice results well and investigate what the consequences are for pure glue results. Results are presented and discussed in section 6.3.5.

In section 6.3.6, we investigate the strong influence of the cutoff procedure on the interplay between chiral condensate and Polyakov loop. The variation of the pure gauge transition temperature T_0 proves useful for this. Section 6.3.7 follows the recent suggestion [53] to orient PNJL type calculations of the QCD phase diagrams more towards the freeze-out curve determined by the “Statistical Model” from experimental data [6, 14, 35]. We discuss the utility of this approach, in particular in connection with the choice of the cutoff prescription. A summary of the chapter is given in section 6.4.

¹Apart from semi-phenomenologic modeling, there are also attempts at determination from underlying principles, e. g. [23, 85, 55].

6.2 Fukushima Potential

6.2.1 Preliminary Remarks

The potential suggested by Fukushima in [52] involves only two parameters:

$$\mathcal{U}_{\text{Fuku}} = -bT \left[54e^{-a/T} \Phi^* \Phi + J(\Phi, \Phi^*) \right]. \quad (6.2.1)$$

The piece

$$J(\Phi, \Phi^*) = \log \left(1 - 6\Phi^* \Phi - 3(\Phi^* \Phi)^2 + 4(\Phi^3 + \Phi^{*3}) \right) \quad (6.2.2)$$

is the Haar measure term from integrating out the non-diagonal group elements in color space [50, 65]. In the original paper, the author chose

$$a = 664 \text{ MeV} \quad \text{and} \quad b\Lambda^{-3} = 0.03 \quad (6.2.3)$$

with $\Lambda = 602.3 \text{ MeV}$ (this and the other NJL parameters stem from [63]) such that the pure glue transition occurs at $T_0 = 270 \text{ MeV}$ and the transition region in the 2+1 flavor scenario including quarks is around $T \approx 200 \text{ MeV}$. We denote this parameter set in the following as a_0 and b_0 . The ansatz (6.2.1, 6.2.3), motivated by the strong-coupling limit, does not reproduce pure glue thermodynamics accurately. It does not include dynamical transverse gluons which dominate the pressure at high temperature. It is now understood [53] that transverse gluon dynamics are also controlled by the Polyakov loop and their effects can be incorporated in $\mathcal{U}(\Phi)$. The potential $\mathcal{U}_T(\Phi)$ with input values from [52] for the parameters a_0 and b_0 at different temperatures is shown in Fig. 6.3. Compared to the same figure with our standard choice, Fig. 3.3 in section 3.5, it is notably shallower.

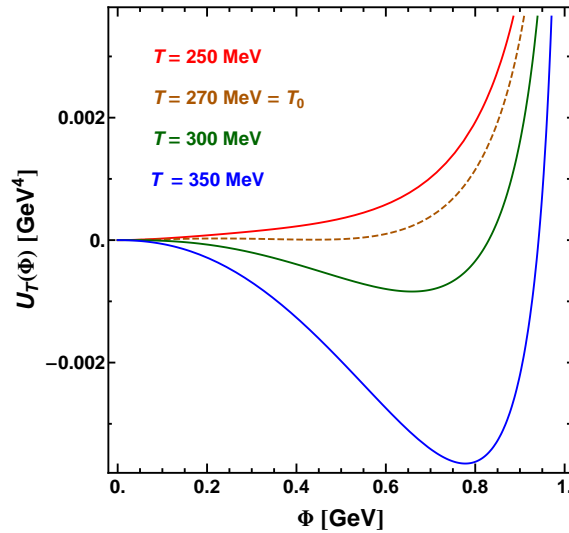


Fig. 6.3: Polyakov loop effective potential from eq. (6.2.1) as a function of the Polyakov loop Φ with the original choices for $a = a_0$ and $b = b_0$ at different temperatures. From top to bottom: $T = 250 \text{ MeV}$, $T = 270 \text{ MeV} = T_0$ (critical), $T = 300 \text{ MeV}$ and $T = 350 \text{ MeV}$.

6.2.2 Variation of the parameter a

From the ansatz (6.2.1) it is evident that the parameter a sets a temperature scale. In Fig. 6.4 we show \mathcal{U} as a function of Φ at a fixed temperature of $T = 300$ MeV for three different values of a . The minima as a function of Φ are shifted and their depth is changed when varying a . The physical implications are evident when one compares the curves at different temperatures, chosen such that the minima coincide. We have plotted this in Fig. 6.5. For each temperature, the Polyakov loop takes the value at which the minimum is localized.

Next, in Figs. 6.6 and 6.7, we compare the pure glue quantities to lattice QCD calculations. Fig. 6.6 shows the Polyakov loop as a function of T for three different choices of a . Its shape fits lattice results reasonably well for $a \lesssim 700$ MeV, at least up to $2T_c$. Changes in the parameter a systematically shift the curves as expected. A reduced pure glue critical temperature T_0 of 190 MeV as suggested by [119, 120] corresponds to a choice of $a \approx 500$ MeV.

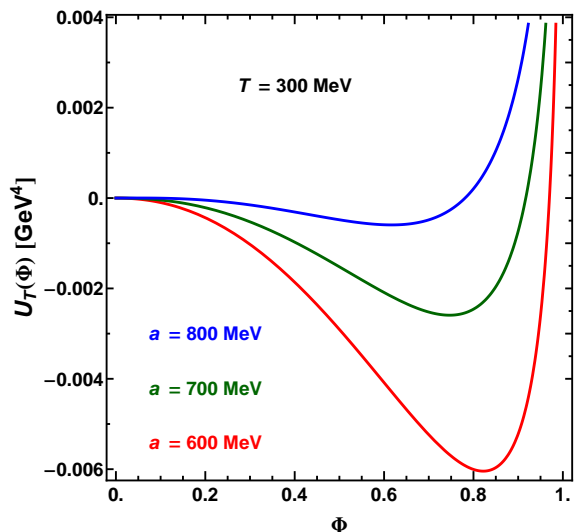


Fig. 6.4: Comparison of the Polyakov loop effective Potential $\mathcal{U}_T(\Phi)$ at fixed temperature $T = 300$ MeV as a function of Φ in a pure glue scenario for to different values of a in the potential (6.2.1).

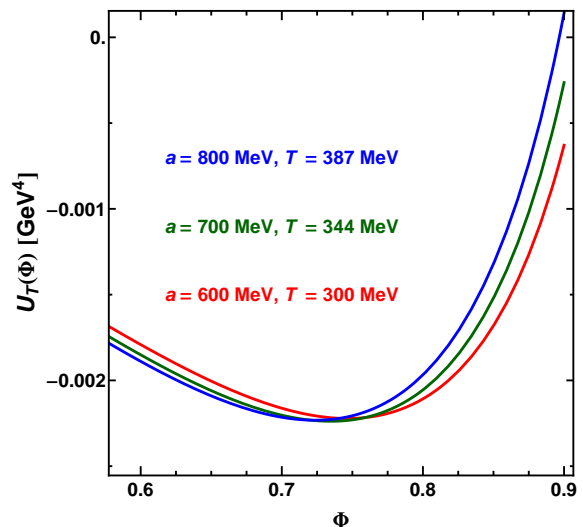


Fig. 6.5: Comparison of the Polyakov loop effective Potential $\mathcal{U}_T(\Phi)$ as a function of Φ in a pure glue scenario for different values of a in the potential (6.2.1), each curve at a different temperature. The temperature is determined such that the minima roughly coincide. From top to bottom: $a = 600$ MeV and $T = 300$ MeV, $a = 700$ MeV and $T = 344$ MeV, and $a = 800$ MeV and $T = 387$ MeV.

In Fig. 6.7 we compare the pure glue pressure derived from the potential (6.2.1) to lattice QCD results. All curves are significantly too low and fail to match the lattice QCD points. This can be traced back to the shallowness of \mathcal{U} in Fig. 6.3. For other thermodynamic quantities such as the entropy density s and the energy density ϵ , the situation is essentially the same.

6.2.3 Variation of the parameter b

The parameter b determines the overall depth of the Polyakov loop effective potential. In the pure glue scenario, Φ as a function of T is therefore not affected by a change of b . The strong influence on pure glue thermodynamic properties is seen in Fig. 6.8. It shows the pure glue system pressure as a function of T for different values of b . Lattice results are reproduced best with $b \approx b_2 = 2.7 b_0$, at least up to $T \sim 1.5T_c$.

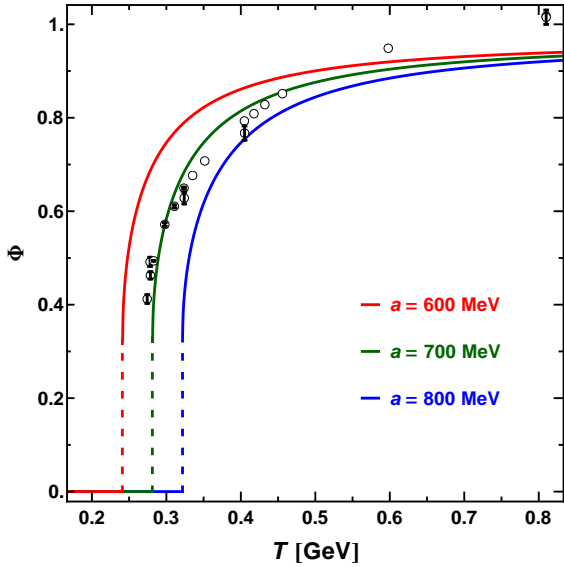


Fig. 6.6: Comparison of the Polyakov loop as a function of T in the pure glue scenario for different values of a in the potential (6.2.1). From left to right, result from the choices of $a = 600$ GeV, $a = 700$ GeV and $a = 800$ GeV, respectively. Circles with error bars are lattice results of [73].

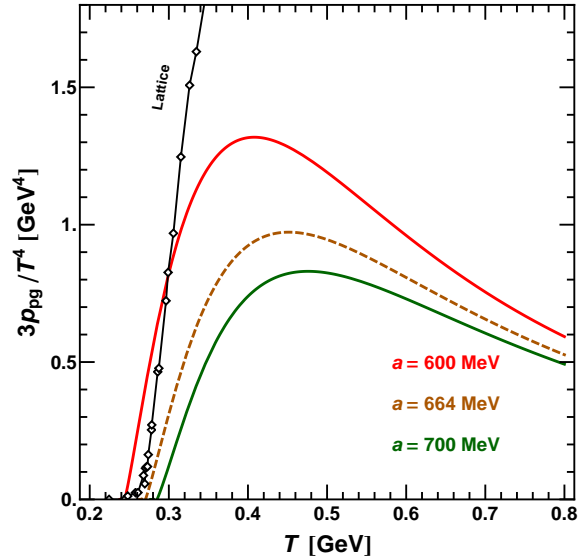


Fig. 6.7: Pure glue system pressure as a function of T for different values of a in the potential (6.2.1), compared to lattice QCD results (black diamonds) [20]. Pressure curves, from top to bottom, correspond to $a = 600$ MeV, $a = a_0 = 664$ MeV (dashed) and $a = 700$ MeV.

In the full calculation, the gluon contribution to the pressure is even less than Fig. 6.8 suggests. Fig. 6.9 shows the pressure of the full system (gluons and quarks) as a function of T . Already at $T \sim \Lambda/2$ there is virtually no difference between the curves for different values of b .

6.3 Effective potential used in this work

6.3.1 Preliminary Remarks

In the previous section we have seen that the potential from (6.2.1) is conceptually interesting but falls short in several respects. The reproduction of pure glue data is still the most reliable foundation to construct a physically meaningful Polyakov loop effective potential. The potential that we use in our work (see section 3.5) is the one developed in [116] and [117]:

$$\mathcal{U}(\Phi, \Phi^*, T) = -\frac{1}{2}b_2(T)\Phi^*\Phi + b_4(T) \log [J(\Phi, \Phi^*)] \quad (6.3.1)$$

with

$$b_2(T) = a_0 + a_1 \left(\frac{T_0}{T}\right) + a_2 \left(\frac{T_0}{T}\right)^2 \quad (6.3.2)$$

and

$$b_4(T) = b_4 \left(\frac{T_0}{T}\right)^3 \quad (6.3.3)$$

with the values for a_0 , a_1 , a_2 and b_4 given in Table 3.5 in section 3.5. The Haar measure term $J(\Phi, \Phi^*)$ is the same as in (6.2.2). In the following study we permit two variations: an overall re-scaling of the potential by a factor c ; and a relative re-weighting of the b_2 and b_4 terms by

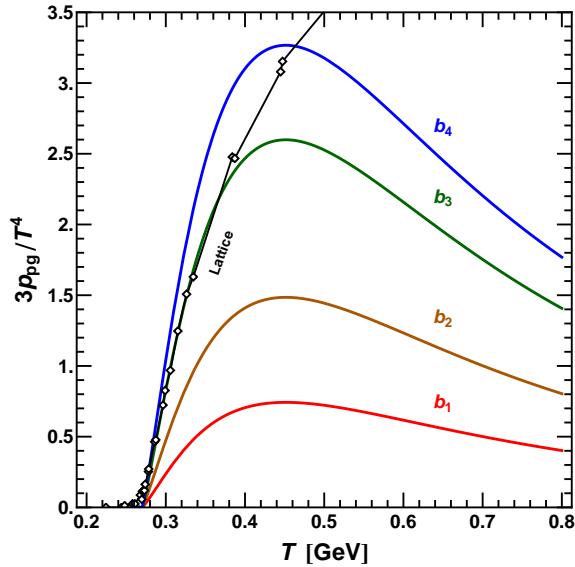


Fig. 6.8: Pure gauge system pressure p_{pg} as a function of T for different values of b in the potential (6.2.1), compared to lattice results (black diamonds) from [33]. Pressure curves, from bottom to top, correspond to b_0 , $b_1 = 1.5 b_0$, $b_2 = 2.7 b_0$ and $b_3 = 3.3 b_0$.

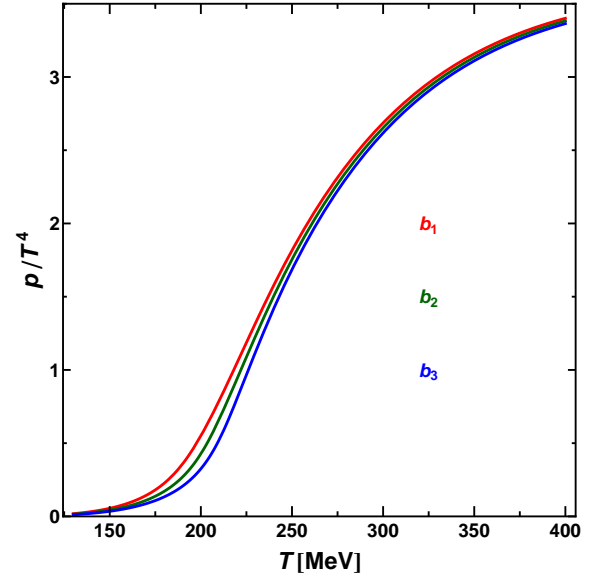


Fig. 6.9: Full system pressure normalized by T^4 as a function of T for different values of b . From top to bottom: b_0 , $b_1 = 1.5 b_0$ and $b_2 = 2.7 b_0$.

re-scaling $\bar{b}_2(T) = d b_2(T)$:

$$\mathcal{U}(\Phi, \Phi^*, T) = c \left\{ -\frac{1}{2} \bar{b}_2(T) \Phi^* \Phi + b_4(T) \log [J(\Phi, \Phi^*)] \right\}. \quad (6.3.4)$$

The parameter c controls the total magnitude of the potential and corresponds to b in the Fukushima potential 6.2.1. The parameter d controls the weight of the $\Phi\Phi^*$ term independent of the Haar measure term.

6.3.2 Variation of the parameter c

In analogy to the parameter b in section 6.2.3, the Polyakov loop in the pure glue scenario is not affected by a change in c . In Fig. 6.10 we present the pure glue pressure as a function of T for different values of c . The choice of $c = 1$ reproduces our standard settings which by construction result in the perfect fit to lattice QCD data from [33] and the Stefan–Boltzmann limit. Changes of the order of 20% make the curve deviate considerably. It was seen in Figs. 6.8 and 6.9 that large differences in the pure glue pressure do not necessarily carry over into the full system. In contrast to the Fukushima potential, the high temperature limit of the pressure is finite with our ansatz but depends strongly on c . This has significant effects on the thermodynamics of the full quark-gluon system. As an example, we show the normalized energy density ϵ/T^4 as a function of T/T_{cross}^X for the same three values of c as in Fig. 6.10. As a reminder, T_{cross}^X is the center of the chiral crossover band at $\mu = 0$. The red circles are lattice QCD results from [33].

In the full 2 + 1 flavor calculation, increase of c leads to a stronger degree of entanglement between chiral and Polyakov loop transition. This effect is evident e. g. in [55].

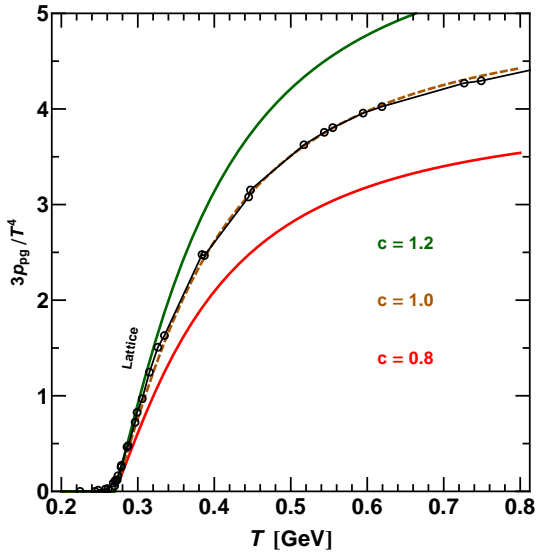


Fig. 6.10: Pure gauge system pressure as a function of T for different values of c in the potential (6.3.4), compared to lattice results (black circles) from [20]. Pressure curves, from top to bottom, correspond to $c = 1.2$, $c = 1.0$ and $c = 0.8$.

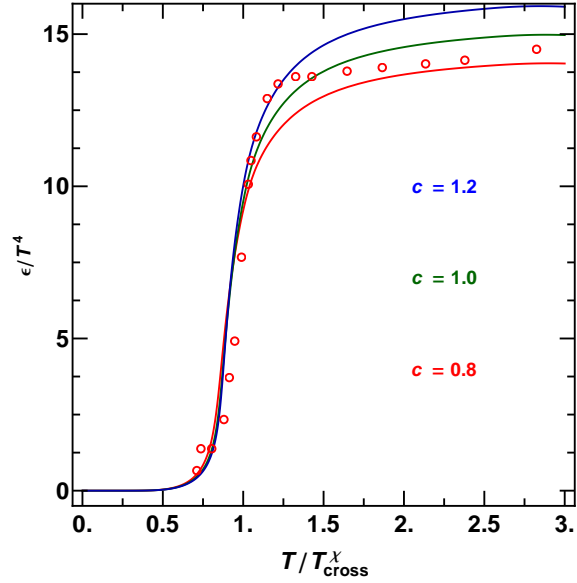


Fig. 6.11: Rescaled energy density ϵ/T^4 at $\mu = 0$ as a function of T/T_{cross}^X for $c = 0.8$, $c = 1.0$ and $c = 1.2$ from bottom to top. T_{cross}^X is defined in eq. (4.4.1). Red circles are lattice QCD results from [33].

6.3.3 Variation of the parameter d

The parameter d in (6.3.4) is the equivalent of the parameter a in (6.2.1) so that we expect similar results upon variation of d . Fig. 6.12 shows the shift of the Polyakov loop in the pure glue system for several values of d . In the pure glue pressure, even small changes in d lead to considerable differences already at $T \gtrsim 1.5 T_0$. (Fig. 6.13).

In the full 2 + 1 flavor calculation, the pressure is affected to a lesser degree, as shown in Fig. 6.14. The Polyakov loop crossover tends to become smoother with decreasing d . At the same time, the transitions are shifted towards higher T and their degree of entanglement increases.

6.3.4 Variation of parameter T_0

The third parameter in our potential (6.3.4) is the pure glue transition temperature T_0 . In contrast to the Fukushima potential parameter a in the Fukushima potential, it shifts the pure gluonic quantities on the T axis entirely. For 2 + 1 flavors we present as an example the rescaled energy density ϵ/T^4 in Fig. 6.15. The chiral condensate and Polyakov loop crossover widths at $\mu = 0$ are collected in Fig. 6.16. Lowering T_0 to about 190 MeV as suggested in [119, 120] makes the Polyakov loop crossover step and separates it from the chiral transition, features that are not present in 2 + 1 flavor lattice QCD results. For very small $T_0 \lesssim 150$ MeV the Polyakov loop transition turns into a crossover.

6.3.5 Fit to lattice QCD results and discussion

The most efficient way to broaden the Polyakov loop transition was found to be a reduction of the parameter d . The same effect was achieved with an increase in a in the Fukushima potential (see 6.2.2). At the same time, lowering d also raises the transition temperatures considerably. The best way to lower them is a reduction of T_0 , as suggested in [119, 120]. In the interplay

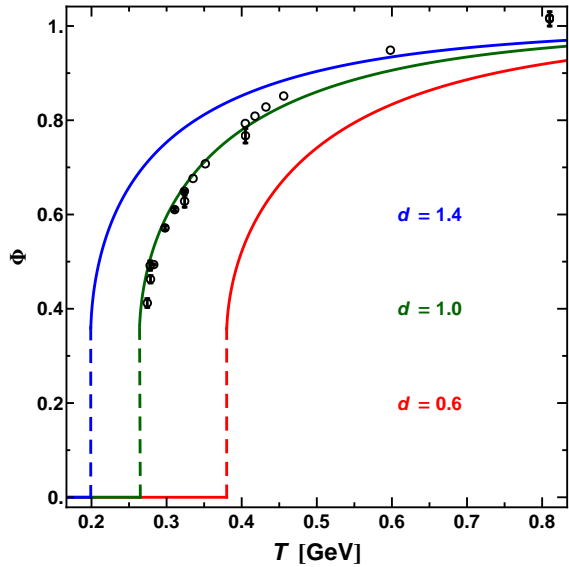


Fig. 6.12: Polyakov loop as a function of T for a selection of values for d . From left to right: $d = 1.4$, $d = 1.0$, $d = 0.6$. Circles with error bars are lattice results of [73].

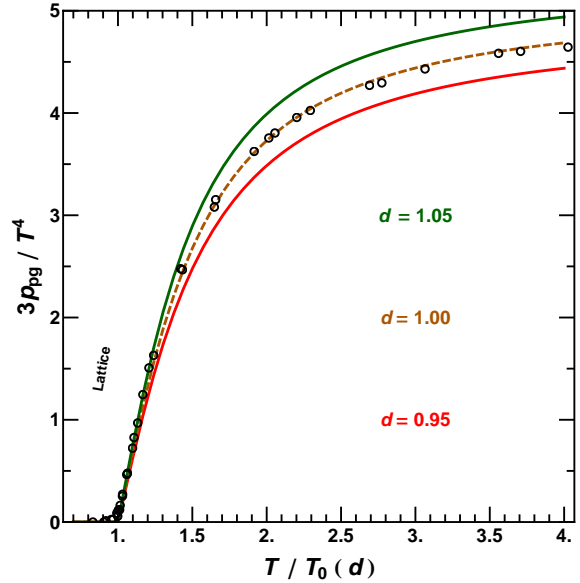


Fig. 6.13: Pure glue system pressure as a function of $T/T_0(d)$ for a selection of values for d . From top to bottom: $d = 1.05$, $d = 1.00$ (dashed), $d = 0.95$. Black circles correspond to lattice results from [20].

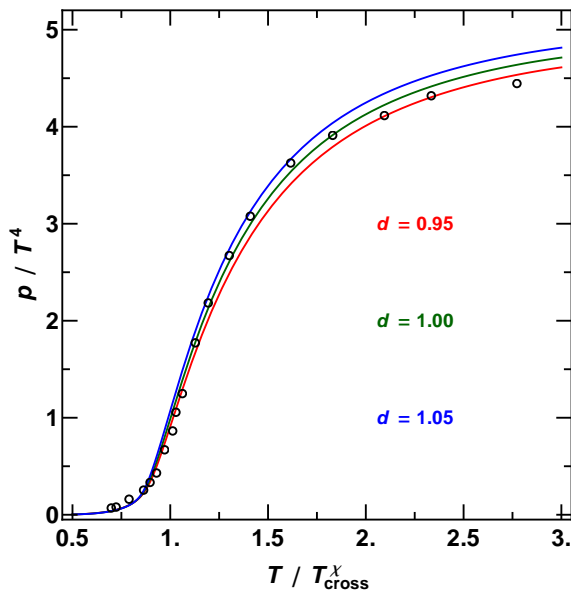


Fig. 6.14: Rescaled pressure p/T^4 as a function of T/T_{cross}^X for a selection of values for d . From bottom to top: $d = 0.95$, $d = 1.00$ and $d = 1.05$. Circles correspond to lattice results from [33].

between these two effects, we fit the results from [13] best by choosing

$$T_0 = 190 \text{ MeV} \quad \text{and} \quad d = 0.25 \quad (6.3.5)$$

in the potential (6.3.4). This means that the high-pressure limit in the pure glue scenario is only a quarter of its physical value. Polyakov loop and normalized chiral condensate with this choice

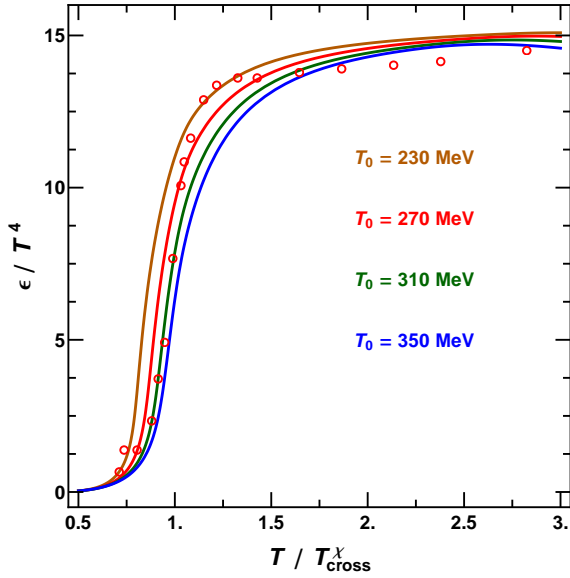


Fig. 6.15: Rescaled energy density ϵ/T^4 as a function of T/T_{cross}^X for different values of T_0 in (6.3.1). From top to bottom: $T_0 = 230$ MeV, $T_0 = 270$ MeV, $T_0 = 310$ MeV and $T_0 = 350$ MeV. Red circles are lattice results from [33].

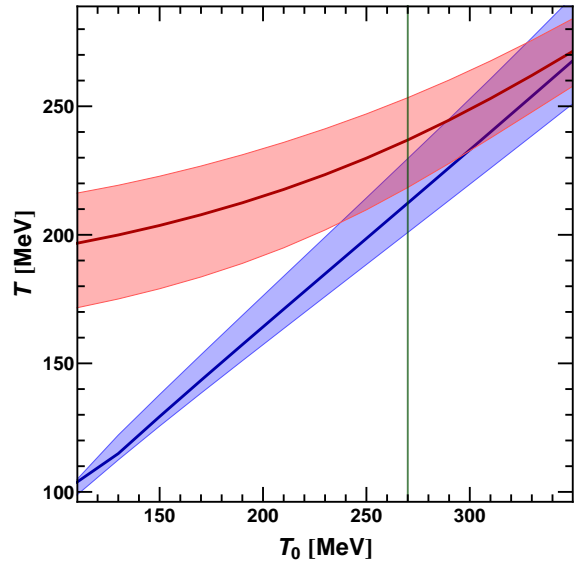


Fig. 6.16: Transition bands for the chiral condensate (upper band, red) and the Polyakov loop (lower band, blue) at $\mu = 0$ as a function of T_0 in (6.3.1).

are presented in Fig. 6.17 as a function of T . The gray band represents lattice QCD results collected in [13]. The chiral transition takes place at too high temperature T_{cross}^X in comparison to the lattice – a known issue with standard PNJL type models. However, it should be noted that T_{cross}^X is essentially unchanged with respect to our standard parameter choice of $T_0 = 270$ MeV and $d = 1$. The phase diagram resulting from the settings (6.3.5) is shown in Fig. 6.18. In comparison to our “standard” phase diagram (Fig. 4.6b in section 4.5), the temperature T_{cp} of the critical point is lowered² from around 150 MeV to about 125 MeV, mostly as a consequence of the reduced T_0 . Its chemical potential μ_{cp} is unaltered.

6.3.6 Influence of cutoff schemes

In sections 4.4 and 4.5, we mentioned that the degree of entanglement between the chiral and the Polyakov loop transition is strongly affected by the cutoff procedure. It is instructive to study the analogue of Fig. 6.16 for the other two cutoff procedures described, namely (4.2.4) and (4.2.5) in section 4.2, as they are the most widely used ones.

In the case of the minimal cutoff (4.2.5), the crossover bands are entangled to the highest degree (Fig. 6.19). The complete overlap at $T_0 = 270$ MeV is remarkable, but the bands are too narrow, i. e. the transitions too fast, in comparison to the lattice QCD results. This is true especially for the chiral transition, and at all values of T_0 .

For the maximal cutoff (4.2.4), the chiral transition is about as wide as with our new cutoff scheme. Remember, however, that $2 + 1$ flavor thermodynamics cannot be reproduced with the maximal cutoff (cf. section 4.5).

²We show in chapters 5 and 7 that the existence, let alone the location of the critical point is strongly dependent on a several parameters. It is interesting to note that already this result suggests a shorter chiral first-order transition line. Additional findings to this effect will be forthcoming in the cited chapters.

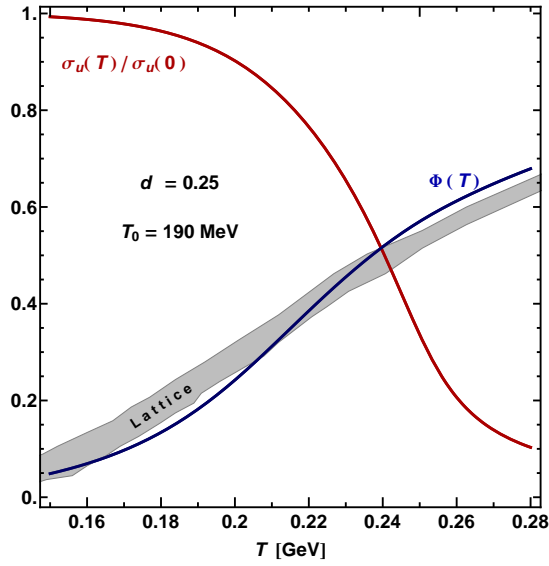


Fig. 6.17: Normalized chiral condensate $\sigma_u(T)/\sigma_u(0)$ and Polyakov loop $\Phi(T)$ with the parameter choices of $d = 0.25$ and $T_0 = 190$ MeV in (6.3.4). For the Polyakov loop, lattice results from [13] have been added as a gray band.

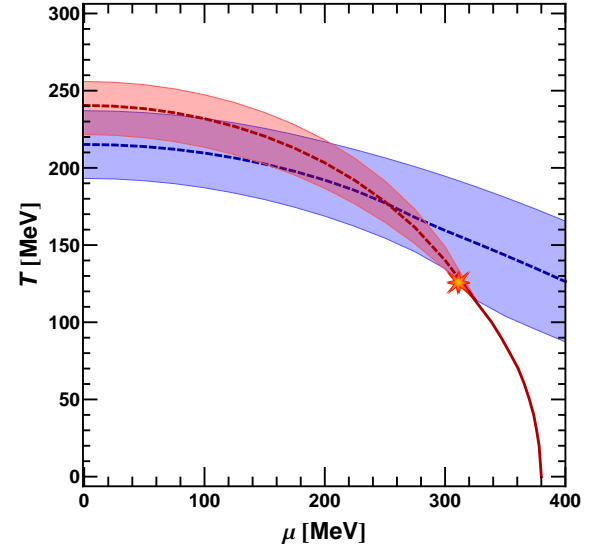


Fig. 6.18: QCD phase diagram resulting from the parameter choices of $d = 0.25$ and $T_0 = 190$ MeV in ansatz (6.3.4). The (de-)confinement crossover band is shown in blue (dashed), the chiral crossover band in red (dashd). The critical point is marked by a star and the chiral first-order transition by a solid red line.

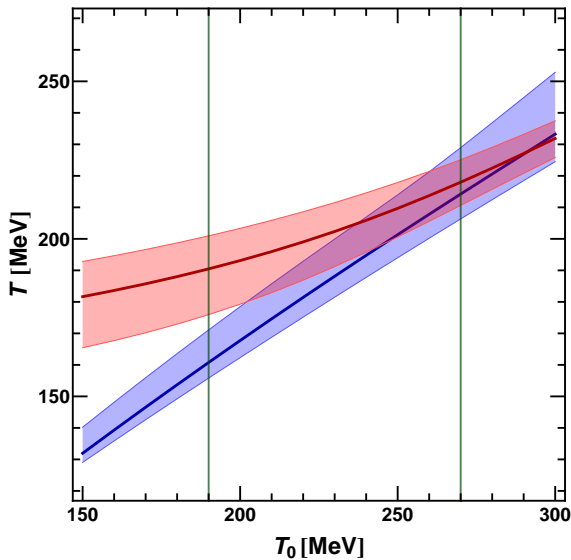


Fig. 6.19: Transition bands for the chiral condensate (upper band, red) and the Polyakov loop (lower band, blue) at $\mu = 0$ as a function of T_0 in (6.3.1), calculated with the "minimal" cutoff (4.2.5).

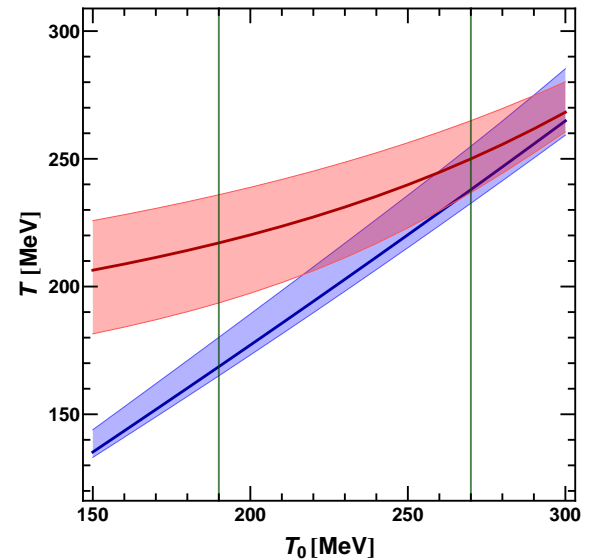


Fig. 6.20: Transition bands for the chiral condensate (upper band, red) and the Polyakov loop (lower band, blue) at $\mu = 0$ as a function of T_0 in (6.3.1), calculated with the "maximal" cutoff (4.2.4).

6.3.7 Freeze-out curve and μ -dependent T_0

The ‘‘Statistical Model’’ [6, 14, 35] works remarkably well reproducing particle ratios at chemical freeze-out in heavy-ion collisions, using just temperature and chemical potential as input. In [53], it is suggested to bring PNJL model results phenomenologically in agreement with the freeze-out curve. To this end, a μ -dependent T_0 is proposed³. The main argument is that the entropy density s counts the effective degrees of freedom and therefore its increase should be connected to deconfinement. In the PNJL model results, s is connected more strongly to the chiral transition, so that it seems natural to attempt to bring the two transitions closer together.

The freeze-out curve is parametrized in [35]. The assumed correlation between the freeze-out curve and the running of T_0 with μ motivates the use of the same curvature:

$$\frac{T_0(\mu)}{T_0(\mu=0)} = 1 - \kappa_f \frac{\mu^2}{T_0(\mu=0)^2} \quad (6.3.6)$$

with $\kappa_f = 0.238$. For easier comparison, we use in this section the same parameter set⁴ as in [53], namely the Hatsuda–Kunihiro set [63].

Again, we find that the choice of a cutoff scheme is crucial. The following figures show the QCD phase diagram resulting from a running T_0 according to (6.3.6). Figs. 6.21a and 6.21b show the case of an initial $T_0(\mu=0) = 270$ MeV with the new cutoff (left, Fig. 6.21a) and the minimal cutoff (right, Fig. 6.21b). Figs. 6.22a and 6.22b show the analogue for an initial $T_0(\mu=0) = 190$ MeV. This value was again motivated by the renormalization group arguments in [119, 120] and is close to the choice of $T_0(\mu=0) = 200$ MeV used in [53]. Fig. 6.21a presents the result with the new cutoff and Fig. 6.21b the result with the minimal cutoff. In black, with error bars, are the ‘‘Statistical Model’’ freeze-out points. As always, dashed lines with bands are crossovers, solid lines denote first-order transitions. Note that in all of the four diagrams, for chemical potentials larger than that of the critical point, μ_{cp} , the Polyakov loop transition becomes first-order. We have encountered this effect already for low, but fixed T_0 in section 6.3.4. The unusual behavior of the Polyakov loop at $T \lesssim 25$ MeV has numerical causes and carries no physical meaning.

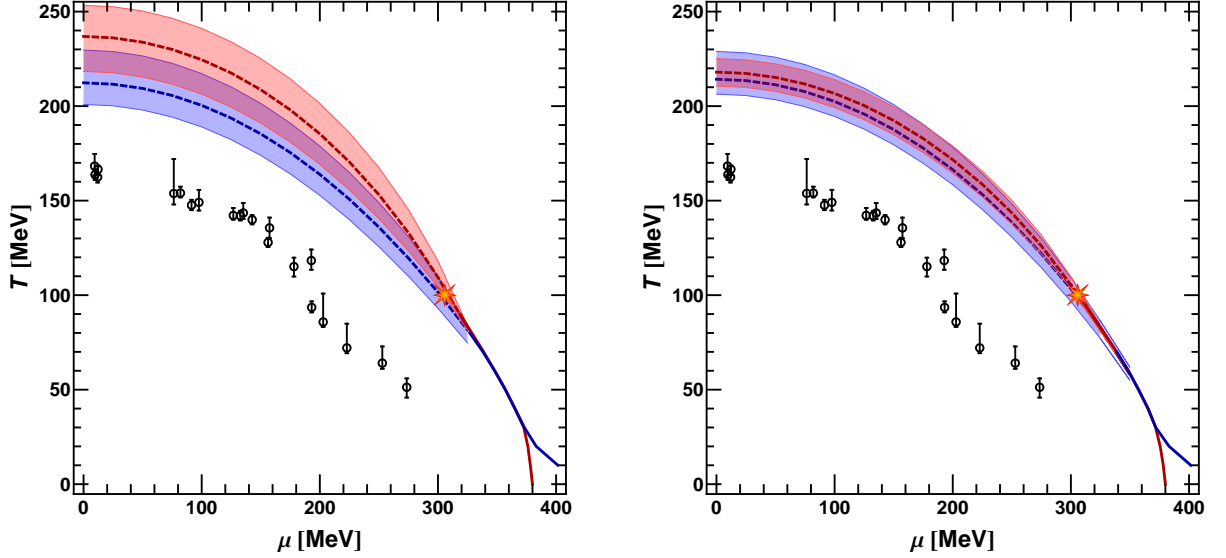
Both transitions, in particular the Polyakov loop transition, come only close to the freeze-out points when the initial $T_0(\mu=0) \sim 190$ MeV. The effect that all transitions/crossovers become very close and parallel as described in [53] is only true in the case of the minimal cutoff scheme. We already saw in the last section, especially Fig. 6.19, that this prescription tends to put the transitions close to each other. Because of its clearly unphysical properties (see chapter 4), results based on it should be treated with caution. It is obvious that, if the chiral condensates go to the wrong high temperature limit (namely towards negative current quark masses instead of vanishing), then their melting must happen faster and earlier. Thus the minimal cutoff puts the chiral transition closer to the Polyakov loop transition band in Fig. 6.22b than in Fig. 6.22a, but for reasons that are unphysical.

6.4 Summary

In this chapter, we have investigated systematic connections between the Polyakov loop effective potential $\mathcal{U}(\Phi)$ and $2+1$ flavor lattice QCD results. They have been verified with two different potential forms separately, namely the Fukushima potential (6.2.1) and our potential (6.3.1). We have found that the smooth transition of the Polyakov loop indicated by recent lattice QCD results [13, 10, 19] can be reproduced in our calculation with the parameter choices of

³An explicit μ dependence of the Polyakov loop effective potential, based on renormalization group arguments, is also suggested in [119]. This is a very promising approach to include effects of a matter back-reaction to the Polyakov loop.

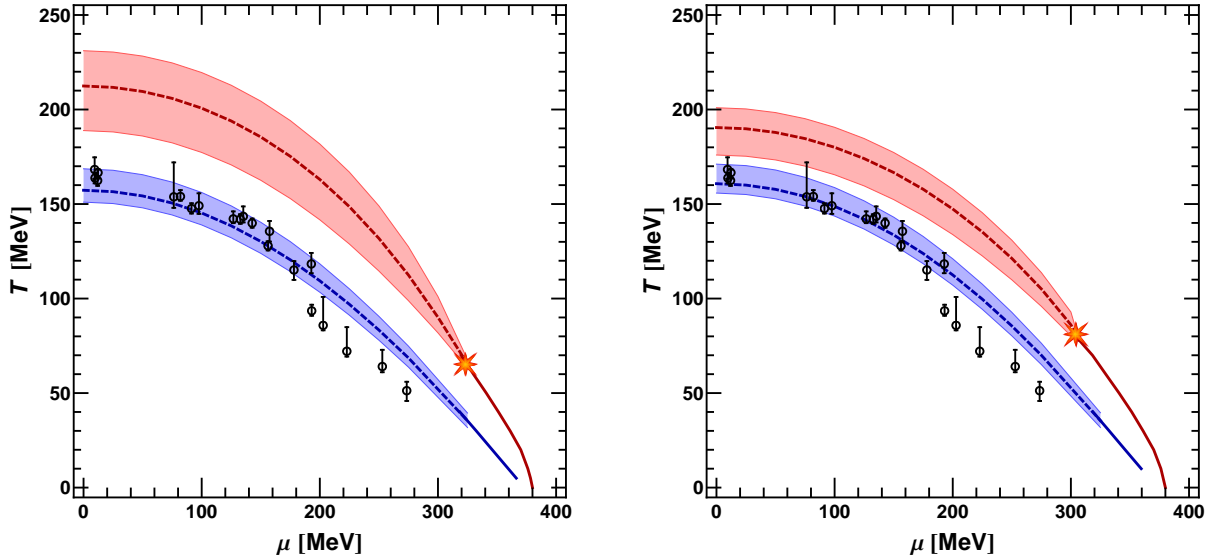
⁴The differences are negligible for this study; they consist mainly in a slightly shifted critical point.



(a) New "soft" cutoff from (4.2.6).

(b) Minimal cutoff from (4.2.5).

Fig. 6.21: QCD phase diagram with running T_0 according to (6.3.6). Black circles with error bars from the "Statistical model". Polyakov loop transition in blue, chiral transition in red. Dashed lines are crossovers, solid lines first-order transitions. Here, we have used $T_0(\mu = 0) = 270$ MeV.



(a) New "soft" cutoff from (4.2.6).

(b) Minimal cutoff from (4.2.5).

Fig. 6.22: QCD phase diagram with running T_0 according to (6.3.6). Black circles with error bars from the "Statistical model". Polyakov loop transition in blue, chiral transition in red. Dashed lines are crossovers, solid lines first-order transitions. Here, we have used $T_0(\mu = 0) = 190$ MeV.

(6.3.5) in (6.3.4). Doing so, one gives up the primary fit of the effective potential to pure glue lattice results. The phase diagram resulting from this choice (Fig. 6.18) is very similar to our standard phase diagram (Fig. 4.6b). For the remainder of this work, we will, however, stick to our original prescription for $\mathcal{U}(\Phi)$ found in section 3.5, which is based on reproducing pure glue lattice results.

We have also shown, by varying T_0 in section 6.3.6, that the degree of entanglement between the chiral and the Polyakov loop crossover is strongly sensitive to the combination of the cutoff scheme and the choice of T_0 .

In section 6.3.7, we have followed a recent suggestion [53] to model $T_0(\mu)$ such that PNJL model results for the chiral transition come closer to the freeze-out points indicated by the Statistical Model [6, 14, 35]. We have found that the effects shown in that work are mostly due to the use of the unphysical “minimal” cutoff. In addition, by comparing to the lattice QCD data presented in the introduction (section 6.1) it is clear that the assumption of a close relation between the freeze-out points and the Polyakov loop is not supported by the lattice QCD results. Regarding the possible connection between the freeze-out curve and the chiral phase transition, a recent study with a linear nuclear-meson model shows that the freeze-out curve reflects neither a phase transition nor a rapid crossover line [48].

Chapter 7

Vector Interactions

7.1 Introduction

In PNJL type models, a vector current interaction can appear together with a corresponding axial vector current interaction, with each of the terms separately invariant under chiral $SU(3)_L \times SU(3)_R$ transformations:

$$\delta\mathcal{L} = -\frac{G_V}{2} \sum_{a=0}^8 \left[(\bar{\psi}\gamma_\mu\lambda^a\psi)^2 + \frac{G_A}{G_V} (\bar{\psi}\gamma_\mu\gamma_5\lambda^a\psi)^2 \right]. \quad (7.1.1)$$

A simple schematic vector interaction

$$\delta\mathcal{L}_v = -\frac{g_v}{2} (\bar{\psi}\gamma^\mu\psi)^2 \quad (7.1.2)$$

is also used. This “reduced” interaction is quite common in current research [52, 93, 142, 143]. Its use is motivated by the simpler case of two degenerate flavors. There, the two vector interaction types described above differ only by a factor. One of the major aims of this chapter is to investigate the differences between these two interactions in the 2 + 1 flavor scenario. Further goals are the investigation of the influence of the vector interaction on the QCD phase diagram, as well as of the interplay between the KMT interaction strength K and the vector coupling strength g_v .

The inclusion of $\delta\mathcal{L}$ or $\delta\mathcal{L}_v$ adds the vector interaction coupling strength g_v to the set of input parameters. Constraining its value range is part of an ongoing effort. We collect here a few numbers from different approaches as a guideline for our work, all of which turn out to paint a quite consistent picture.

One of the simplest systems motivated by QCD is a color-current interaction:

$$\mathcal{L}_{\text{int}}^c = -G_c \sum_{a=1}^8 (\bar{\psi}\gamma_\mu t^a\psi)^2 \quad (7.1.3)$$

with the $SU(3)_c$ generators t^a and a coupling strength G_c . The color singlet part of its Fierz transform [135] is then

$$\mathcal{L}_{\text{int}}^{c,\text{singlet}} = G_S \sum_{i=0}^8 \left[\left(\bar{\psi} \frac{\lambda^i}{2} \psi \right)^2 + \left(\bar{\psi} \gamma_5 \frac{\lambda^i}{2} \psi \right)^2 \right] - G_V \sum_{i=0}^8 \left[\left(\bar{\psi} \gamma_\mu \frac{\lambda^i}{2} \psi \right)^2 + \left(\bar{\psi} \gamma_\mu \gamma_5 \frac{\lambda^i}{2} \psi \right)^2 \right] \quad (7.1.4)$$

with

$$G_S = 2G_V = \frac{8}{9}G_c, \quad \text{so that} \quad G_V = \frac{1}{2}G_S \quad (7.1.5)$$

which would point towards $g_v = 0.5G$ in our convention.

In [79] the authors explore a two-flavor nonlocal PNJL model at imaginary chemical potentials. It reproduces the $2\pi/3$ periodicity of the QCD partition function, called Roberge-Weiss (RW) periodicity and the RW transition [112]. For the best fit, the value $g_v = 0.4G$ is given. In the three-flavor model, K influences the pion vacuum masses only slightly. The role of G in two- and three-flavor models is therefore very similar. Accordingly, we expect g_v/G to be roughly comparable in the two scenarios¹.

In this chapter we use as a standard the parameter set from [92]. The authors include a vector interaction of the type shown in eq. (7.1.1). By fitting to the vector meson spectrum, they arrive at a value of $g_v \approx 1.1G$ in our notation.

The study [93] investigates so-called “hybrid stars” which are neutron stars with an exotic core. Based on a number of assumptions about a crossover from hadronic matter with hyperons to a quark matter core with strangeness, they calculate mass–radius ratios for these hybrid stars using the Tolman–Oppenheimer–Volkoff equation [128, 129, 104]. It is shown that values of $g_v/G \sim 1$ produce results compatible with the recently found two solar mass neutron star PSR J1614-2230 [41].

For the sake of completeness, we mention two other promising approaches that, at the present stage, only give rough estimates but continue to be improved. The first is described in [91]. In this very recent work, two flavor PNJL model results and relativistic mean field hadronic model results [90] are matched. The vector interaction in the former is intended as the counterpart of the nucleon–nucleon interaction in the latter framework. Their current level of precision allows only to deduce $0.8 < g_v/G < 3$.

The second is an example of an attempt to extract numbers from lattice QCD calculations. In [44] a two flavor mean field model is used to extrapolate vector coupling strengths from flavor diagonal and off-diagonal susceptibilities of light quarks at vanishing chemical potential. The results indicate absolute values of g_v between 4 GeV^{-2} and 19 GeV^{-2} . Given the usual values of G between 6 GeV^{-2} and 12 GeV^{-2} , one finds a range of about $0.3 < g_v/G < 3$.

In conclusion, the range indicated by all these sources is roughly

$$0.4 \lesssim g_v/G \lesssim 1.1 \tag{7.1.6}$$

with a tendency towards larger g_v . For now, we treat g_v as a free parameter and vary it mostly between $g_v = 0$ and $g_v = G$.

We start our investigations by using the “reduced” vector interaction of eq. (7.1.2) in section 7.2. Our consistent cutoff scheme (4.5.1), described in chapter 4, is again shown to be important for the model to agree with physical constraints. In particular, switching off g_v for $p > \Lambda$ turns out to be crucial.

The goal of section 7.3 is to show the consistency of our model setup with physical constraints. In sections 7.3.1 and 7.3.2 the baryon number density ρ_B as a function of temperature and chemical potential is studied. We then move on to the object of prime interest throughout this thesis, the light quark chiral condensate. Its behavior as a function of the total baryon density ρ_B is explored in 7.3.3.

The location of the critical point and its trajectory under a change of g_v are investigated in section 7.4. We compare results of four different parameter choices: three NJL parameter sets [92, 63, 110], one of which calculated with both of the two different Polyakov loop effective potentials expounded in chapter 6. From the comparison a clear preference for one of the models emerges which is used throughout this chapter as a standard choice.

Section 7.5 contains a systematic study of the first-order transition in the temperature–density plane. We explain the phenomenon of the *chiral coexistence region* and discuss its overlap with a domain that is dominated by well known nuclear physics. Using our knowledge

¹It is important to note that this does not mean that the numbers of flavors is of little consequence for the results. In section 7.8.2 we discuss differences between the two- and the three-flavor case due to the influence of the strange quark chiral condensate when a vector interaction like (7.1.1) is included.

about this field we put constraints on our parameter choices for the vector interaction strength g_v as well as the Kobayashi–Maskawa–’t Hooft coupling K .

The complete phase diagram in the T – μ –plane is discussed in section 7.6, both in the chiral limit and for physical quark masses.

In section 7.7 we show that with an appropriate choice of g_v , lattice QCD results for the chiral transition line curvature κ (see also section 5.5) are reproduced remarkably well.

The vector part of $\delta\mathcal{L}$ of eq. (7.1.1) is studied in section 7.8. We show the differences in the results from this interaction and the “reduced” version $\delta\mathcal{L}_v$ of (7.1.2) in section 7.8.1. We then investigate scenarios of fixed ratios of the different flavor densities ρ_u , ρ_d and ρ_s . As an application of this, we present results for the order of the chiral transition at $T \approx 0$ as a function of different, but fixed flavor density ratios.

Our findings are summarized in section 7.9.

7.2 Reduced vector interaction

We write the reduced interaction $\delta\mathcal{L}_v$ of (7.1.2) without its prefactor out as

$$(\bar{\psi}\gamma^\mu\psi)^2 = \left(\sum_{q \in \{u, d, s\}} \bar{q}\gamma^\mu q \right)^2. \quad (7.2.1)$$

Here ψ denotes the column vector $(u, d, s)^\top$ in flavor space, whereas q designates any one of its components. Note that $(\bar{\psi}\gamma^\mu\psi)^2 = \frac{3}{2}(\bar{\psi}\gamma^\mu\lambda^0\psi)^2$, with $\lambda^0 := \sqrt{\frac{2}{3}}\mathbf{1}$. The terms are now expressed as expectation values and fluctuations:

$$\bar{q}\gamma^\mu q = \langle \bar{q}\gamma^\mu q \rangle + (\bar{q}\gamma^\mu q - \langle \bar{q}\gamma^\mu q \rangle), \quad (7.2.2)$$

where the second term on the right hand side is the fluctuation term, which we take to be small in the mean field approach. Let us first look at the spatial components γ^i with $i \in \{1, 2, 3\}$. In that case, the expectation value

$$\langle \bar{q}\gamma^i q \rangle \equiv 0 \quad (7.2.3)$$

because of spatial isotropy. Only the γ^0 terms remain at mean field level. Defining the single flavor density \hat{n}_q , its expectation value ρ_q and the fluctuation $\delta\hat{n}_q$ as their difference,

$$\hat{n}_q := q^\dagger q, \quad \rho_q = \langle \hat{n}_q \rangle \quad \text{and} \quad \delta\hat{n}_q = \hat{n}_q - \rho_q \quad \text{for} \quad q \in \{u, d, s\}, \quad (7.2.4)$$

we have

$$\bar{q}\gamma^0 q = q^\dagger q = \hat{n}_q = \rho_q + (\hat{n}_q - \rho_q) = \rho_q + \delta\hat{n}_q. \quad (7.2.5)$$

This means

$$\hat{n}_q^2 = (\rho_q + \delta\hat{n}_q)^2 = \rho_q^2 + 2\rho_q\delta\hat{n}_q + \delta\hat{n}_q^2 \approx \rho_q^2 + 2\rho_q(\hat{n}_q - \rho_q) = 2\hat{n}_q\rho_q - \rho_q^2, \quad (7.2.6)$$

where in the second step we have neglected the squared fluctuation term $\delta\hat{n}_q^2$. From the expression (7.2.1) we then have

$$\begin{aligned} (\bar{\psi}\gamma^0\psi)^2 &\longrightarrow 2\hat{n}_u\rho_u - \rho_u^2 + 2\hat{n}_d\rho_d - \rho_d^2 + 2\hat{n}_s\rho_s - \rho_s^2 + 2(\rho_u + \delta\hat{n}_u)(\rho_d + \delta\hat{n}_d) \\ &\quad + 2(\rho_u + \delta\hat{n}_u)(\rho_s + \delta\hat{n}_s) + 2(\rho_d + \delta\hat{n}_d)(\rho_s + \delta\hat{n}_s). \end{aligned} \quad (7.2.7)$$

After simplifications and omitting products of fluctuation terms, we have

$$\mathcal{L}_v^{\text{red}} = -\frac{g_v}{2} \left[2(\rho_u + \rho_d + \rho_s)(\hat{n}_u + \hat{n}_d + \hat{n}_s) - (\rho_u + \rho_d + \rho_s)^2 \right]. \quad (7.2.8)$$

$$= -\frac{g_v}{2} \left[2\rho_{uds}\hat{n}_{uds} - \rho_{uds}^2 \right] \quad (7.2.9)$$

with

$$\hat{n}_{\text{uds}} = \hat{n}_{\text{u}} + \hat{n}_{\text{d}} + \hat{n}_{\text{s}} \quad \text{and} \quad \rho_{\text{uds}} = \rho_{\text{u}} + \rho_{\text{d}} + \rho_{\text{s}} \equiv \langle \hat{n}_{\text{uds}} \rangle. \quad (7.2.10)$$

We elucidate in the following the effects of including the vector interaction from a thermodynamics viewpoint. The fermionic grand canonical partition function \mathcal{Z} can be defined [142] by

$$\mathcal{Z} = \int \mathcal{D}\bar{\psi} \mathcal{D}\psi e^{i \int d^4x (\mathcal{L} + \psi^\dagger \hat{\mu} \psi)}. \quad (7.2.11)$$

For a flavor-diagonal chemical potential matrix $\hat{\mu} = \text{diag}(\mu_{\text{u}}, \mu_{\text{d}}, \mu_{\text{s}})$ we have

$$\psi^\dagger \hat{\mu} \psi = \sum_q \mu_q \hat{n}_q, \quad (7.2.12)$$

where μ_q is the chemical potential for a specific quark flavor q . Following basic statistical physics techniques, we find that the (grand canonical) thermodynamic potential (density) Ω in the mean field approximation is only slightly changed by the addition of $\delta\mathcal{L}_{\text{v}}$:

$$\Omega(T, V, \mu_q) \rightarrow \Omega'(T, V, \mu_q) = \Omega(T, V, \mu_q - g_{\text{v}} \rho_{\text{uds}}) - \frac{g_{\text{v}}}{2} \rho_{\text{uds}}^2 \quad (7.2.13)$$

with $q = \text{u, d, s}$. In the literature [7, 52] the shifted chemical potential is often denoted as:

$$\mu_q^{\text{r}} := \mu_q - g_{\text{v}} \rho_{\text{uds}} \quad (7.2.14)$$

and

$$\Omega' = \Omega(T, V, \mu_q^{\text{r}}) - \frac{g_{\text{v}}}{2} \rho_{\text{uds}}^2. \quad (7.2.15)$$

The state variables remain, however, the unshifted chemical potentials μ_q .

Evidently we retrieve the quark number density via the usual thermodynamic formula

$$\frac{\partial \Omega'}{\partial \mu_q} = -\rho_q. \quad (7.2.16)$$

It is interesting to note that the last term in (7.2.13) acts in favor of an unbounded increase of ρ_{uds} , whereas the effective shift $\mu_q \rightarrow \mu_q^{\text{r}}$ suppresses the total quark density. Already in [52] it has been stated that the latter effect prevails, as we expect from a repulsive interaction.

This general form for Ω can be further simplified to study specific scenarios. We will explore two variants: First, the case where all μ_q are increased equally. This has been done in a large number of 2+1 flavor (P)NJL calculations as well as in all of the previous chapters of this work. The second variant sets $\mu_{\text{u}} = \mu_{\text{d}}$ but $\mu_{\text{s}} = 0$ so that there is zero net strangeness: fermionic occupation number functions of flavor q are identical at $\mu_q = 0$ for particles and antiparticles. Strangeness, or net strange quark number density, as the difference of strange quark and anti-quark numbers must then vanish. This situation is relevant, for example, for standard nuclear matter. We will see that for effects concerning the light quark chiral transition the difference between $\mu_{\text{s}} = \mu_{\text{u}}$ and $\mu_{\text{s}} = 0$ scenarios is negligible; this is a consequence of the relatively large strange quark current mass. Therefore, after having verified this, we will mostly work with degenerate chemical potentials $\mu_{\text{u}} = \mu_{\text{d}} = \mu_{\text{s}}$.

Let us see how the equations turn out in these two scenarios. For identical chemical potentials $\mu := \mu_{\text{u}} = \mu_{\text{d}} = \mu_{\text{s}}$, the term (7.2.12) turns into

$$\psi^\dagger \hat{\mu} \psi = \mu \sum_q \hat{n}_q = \mu \hat{n}_{\text{uds}}, \quad (7.2.17)$$

and eq. (7.2.13) reduces to

$$\Omega'(T, V, \mu) = \Omega(T, V, \mu - g_{\text{v}} \rho_{\text{uds}}) - \frac{g_{\text{v}}}{2} \rho_{\text{uds}}^2. \quad (7.2.18)$$

The condition of a minimized Ω as a function of the quark number densities ρ_q then reads

$$0 = \frac{\partial\Omega'}{\partial\rho_q} = \frac{\partial\Omega'}{\partial\mu} (-g_v) - g_v\rho_{uds} = \frac{\partial\Omega'}{\partial\mu} + \rho_{uds} \quad (7.2.19)$$

so that we retrieve

$$\frac{\partial\Omega'}{\partial\mu} = -\rho_{uds}. \quad (7.2.20)$$

The situation is very similar when we set $\mu_{ud} := \mu_u = \mu_d$ and $\mu_s = 0$, i. e. with vanishing net strange quark number density, $\rho_s = 0$. Using isospin invariance we also know that $\rho_u = \rho_d =: 1/2\rho_{ud}$. The only difference to the previous case is then the formal substitution

$$\rho_{uds} \rightarrow \rho_{ud} \quad \text{with} \quad \rho_{ud} = \rho_u + \rho_d = \langle \hat{n}_{ud} \rangle. \quad (7.2.21)$$

The differences between scenarios with symmetric chemical potentials on the one hand and vanishing strange quark chemical potential on the other hand are explored in Figs. 7.1 and 7.2. In both cases, the temperature is set to 10 MeV. We choose $g_v = 0$ and plot functions of $\mu_{ud} = \mu_u = \mu_d$.

In Fig. 7.1 we show the total baryon number densities in the two scenarios. The baryon number density is defined as

$$\rho_B = \frac{1}{3} (\rho_u + \rho_d + \rho_s). \quad (7.2.22)$$

For the lower curve, $\mu_s \equiv 0$ so that $\rho_s \equiv 0$ for all μ_{ud} and $\rho_B = \rho_u + \rho_d$. For the upper curve, μ_s is set equal to μ_{ud} . Note that symmetric chemical potentials do not mean flavor-symmetric matter because the current quark masses are different; this is only the case if in addition we have degenerate quark masses, $m_u = m_d = m_s$. Evidently, net baryon strangeness starts to contribute around $\mu_{ud} \approx 440$ MeV. The discontinuity in the light quark density is unaffected by the strange quark chemical potential choices. This continues to be true for all temperatures and values of g_v in our studies. It follows that as long as we restrict ourselves to the chiral transition in the light quark sector, we do not have to distinguish between $\mu_s = 0$ and $\mu_s = \mu_{ud}$.

Fig. 7.2 shows the chiral condensates for the same parameters as in Fig. 7.1. The two upper curves on top of each other show the light quark condensates, unaffected by μ_s . The two lower curves are the strange quark condensates for $\mu_s = \mu_{ud}$ in the middle and for $\mu_s = 0$ on the bottom. Around 380 MeV the light quark condensate transition effects a small discontinuity in σ_s . The important thing this figure helps to keep in mind is the following: if the strange quark chemical potential μ_s is fixed at a small value $\mu_s \lesssim 440$ MeV, the strange quark chiral condensate does not undergo the chiral transition.

Fig. 7.1 prompts us to show another instructive curve: the net strangeness fraction of the total quark number density ρ_{uds} for all flavors. It is depicted in Fig. 7.3 as a function of μ , where $\mu = \mu_u = \mu_d = \mu_s$. In the case of $\mu_s = 0$ the fraction is trivially zero. The strangeness fraction rises, over a range of only about 150 MeV, quickly from zero to the proximity of the perturbative limit of $1/3$ (dashed line), as the influence of the different current quark masses dwindles. In section 7.8.2 of this chapter we will investigate, using the complete vector interaction (7.1.1), different relative abundances of the quark flavors by allowing for independent flavor-specific chemical potentials.

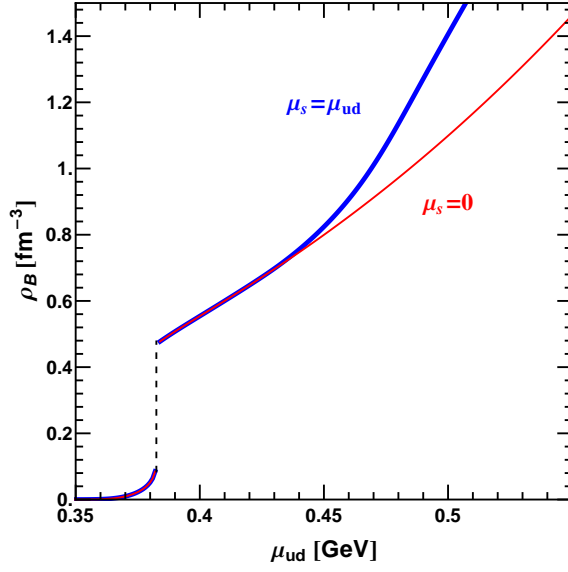


Fig. 7.1: Comparison of the total baryon number densities as a function of $\mu_u = \mu_d$ at $T = 10$ MeV and for $g_v = 0$ in two cases: i) $\mu_s = \mu_{ud}$ (in thick blue on top) and ii) $\mu_s = 0$ (in slim red on the bottom).

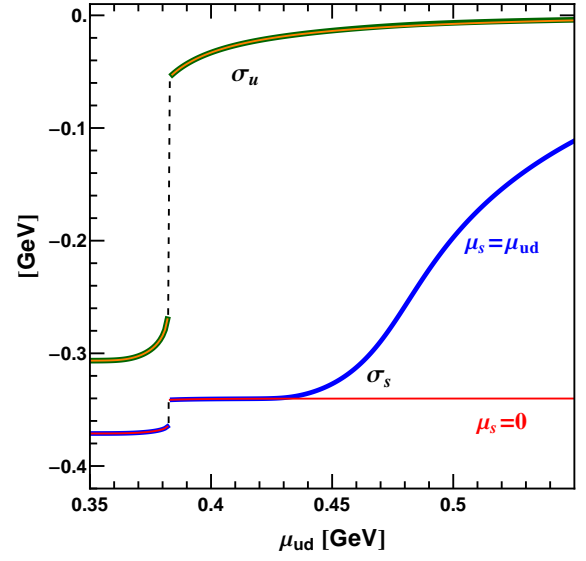


Fig. 7.2: Light quark (σ_u , curve(s) on top) and strange quark (σ_s , two lower curves) chiral condensates at $T = 10$ MeV and $g_v = 0$ as a function of μ_{ud} . For vanishing strange quark chemical potential, σ_s does not die out, whereas σ_u is unaffected.

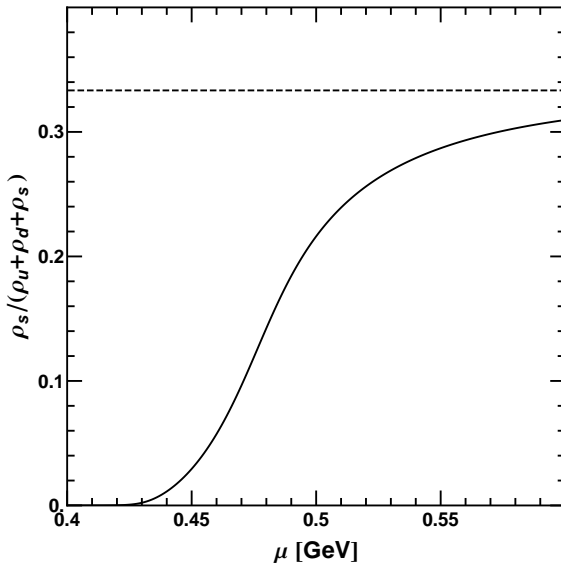


Fig. 7.3: Fraction of net strangeness with respect to the total density of all flavors as a function of $\mu \equiv \mu_u = \mu_d = \mu_s$. The dashed line is the perturbative limit of $1/3$.

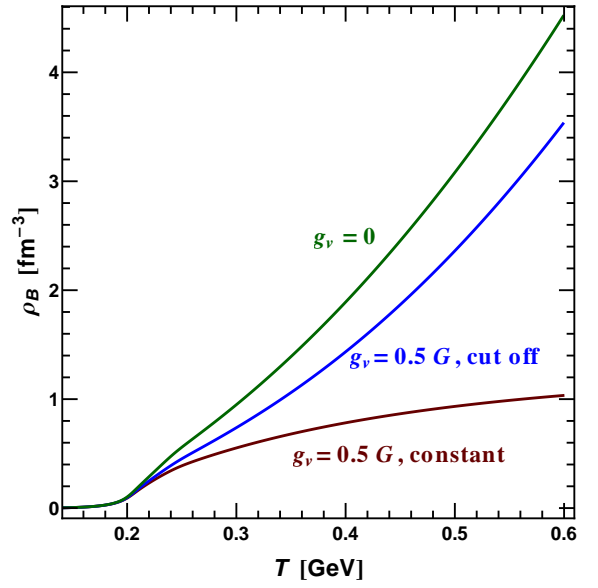


Fig. 7.4: Total baryon number density as a function of temperature at $\mu = 100$ MeV for $g_v = 0$, and $g_v = 0.5 G$ both with g_v constant as function of momentum (middle curve), and with g_v cut off for $p > \Lambda$ (bottom curve).

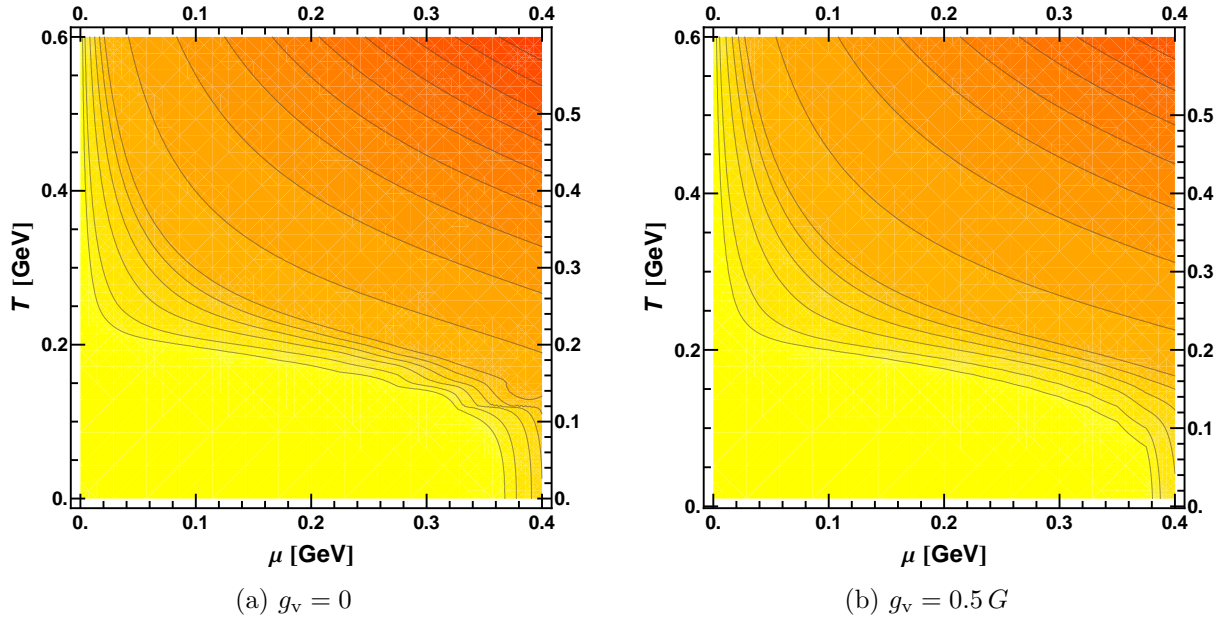


Fig. 7.5: Baryon density ρ_B as a function of T and μ for $g_v = 0.5 G$. Lighter color (yellow) signifies low density, darker color (red) higher density. The lines are lines of constant ρ_B . The same color coding is used for both plots.

In chapter 4 we have presented a consistent cutoff scheme that differs significantly from the most commonly applied schemes. It adheres strictly to the NJL precept of turning the interactions off for momenta larger than the cutoff. This applies also to the vector coupling strength g_v . The effect is briefly addressed by Fig. 7.4. It shows the total baryon number density as a function of the temperature at $\mu \equiv \mu_u = \mu_d = \mu_s = 100$ MeV for three different scenarios: 1) $g_v = 0$ (top curve), 2) $g_v = 0.5 G$ for $p \leq \Lambda$ and $g_v = 0$ for $p > \Lambda$ (middle curve) and 3) $g_v = 0.5 G$ for all momenta (bottom curve). In all cases we have set the other couplings to zero for $p > \Lambda$ so that the pure effect of the vector interaction and its coupling g_v is evident. Fig. 7.4 shows how strongly the picture changes by the consistent cutoff procedure. Even for $T \gtrsim T_c$, the behavior of the net quark density is notably different. The high temperature limit is completely off for the option of constant g_v , if we expect the particles to become asymptotically free. At high T and large μ , the abrupt change of $g_v \rightarrow 0$ at $p = \Lambda$ introduces some numerical intricacies in the determination of the density. Since that region is not of interest to us in this work, the issue is left to future work.

In the following, we study in detail the case of identical chemical potentials as a common option. We therefore dispense with the flavor indices and just use ρ_B as the baryon number density according to (7.2.22) and a single chemical potential $\mu = \mu_u = \mu_d = \mu_s$.

7.3 Baryon number density and chiral condensate

First we show in Fig. 7.5a the baryon number density ρ_B as a function of T and μ as it results from the model with $g_v = 0$, i. e. without vector interaction. The light colors around the origin denotes low density, the dark colors high density. Note that ρ_B increases asymmetrically in T and μ . This fact will become important later in section 7.6. Fig. 7.5b shows again ρ_B , but for $g_v = 0.5 G$. By comparison with Fig. 7.5a it is seen that with higher g_v the influence of the chemical potential on the density is increased with respect to the influence of the temperature. The color tones and curves of equal density in Fig. 7.5a and Fig. 7.5b correspond to each other. Slight irregularities Fig. 7.5a in the figure at large μ and low T are due to numerical issues of the interpolation around the first-order transition.

7.3.1 Baryon number density as a function of temperature

In this section we have a closer look at the baryon density ρ_B for different values of g_v as a function of temperature, especially regarding the high temperature limit. The results for ρ_B are presented in two different ways: first, normalized to the empirical nuclear matter saturation density $\rho_0 = 0.16 \text{ fm}^{-3}$. Second, normalized to the T - and μ -dependent density ρ_B^{free} of a free Fermi gas of massless quarks. The pressure of such a system [75] is given by

$$P_0(m=0) = N_c \left(\frac{7\pi^2 T^4}{180} + \frac{\mu^2 T^2}{6} + \frac{\mu^4}{12\pi^2} \right). \quad (7.3.1)$$

Using $\Omega' = -p$ with the pressure p and $\mu = \mu_u = \mu_d = \mu_s$, the quark density for each flavor is

$$\rho_{\text{quark}} = -\frac{\partial \Omega'}{\partial \mu} = \frac{\partial P_0}{\partial \mu}, \quad (7.3.2)$$

and therefore we have for the baryon density, $\rho_B = \frac{1}{3}\rho_{\text{quark}}$, with $N_f = N_c = 3$,

$$\rho_B^{\text{free}} = \frac{N_f}{3} \frac{\partial P_0}{\partial \mu} = \frac{\mu^3}{\pi^2} + \mu T^2. \quad (7.3.3)$$

We show both normalization variants for two fixed values of the chemical potential: $\mu = 1 \text{ MeV}$ and $\mu = 200 \text{ MeV}$, both below the chemical potentials at which a first-order transition is found².

First, we plot ρ_B/ρ_0 at $\mu = 1 \text{ MeV}$ in Fig. 7.6a and at $\mu = 200 \text{ MeV}$ in Fig. 7.6b for orientation. The large difference in scales between the two figures is simply due to the behavior of the free Fermi gas. This is proved by the next two diagrams.

Fig. 7.7a and Fig. 7.7b show, for the same cases as before, the baryon number density ρ_B normalized to the baryon density of free massless quarks ρ_B^{free} . The results for $\mu = 1 \text{ MeV}$ and $\mu = 200 \text{ MeV}$ are then almost identical for high T and show only small differences around $T \sim T_c$. With our new consistent cutoff scheme, the high temperature limit of the system at different chemical potentials is, correctly, the free Fermi gas scenario.

The stronger repulsive the vector interaction is, the more the increase of ρ_B towards this limit is suppressed. The suppression is sub-linear in g_v/G ; Fig. 7.8 shows ρ_B at $\mu = 1 \text{ MeV}$ for different values of g_v , normalized to the baryon density of a system without a vector interaction, i. e. with $g_v = 0$.

7.3.2 Baryon number density as a function of chemical potential

The next two figures show the baryon density as a function of the chemical potential μ for different values of the vector interaction coupling strength g_v at a fixed temperature of $T = 10 \text{ MeV}$. Fig. 7.9 presents ρ_B/ρ_0 , while Fig. 7.10 shows the baryon density normalized to the corresponding value for a free massless quark gas, cf. (7.3.3). In these figures we encounter for the first time the fact that for large enough g_v , the first-order transition in the phase diagram turns into a crossover even for $T \sim 0$. The next section will show that the discontinuities in the chiral condensates and the density interlocked.

The curves for $\rho_B/\rho_B^{\text{free}}$ in Fig. 7.10 do not increase towards $\rho_B/\rho_B^{\text{free}} = 1$ as in the case of Fig. 7.6, where we investigated the high T behavior. This is a consequence of the shifted chemical potential μ^r (7.2.14) and the fact that ρ_B increases faster with μ than with T (cf. Figs. 7.5a and 7.5b). At $\mu \gtrsim 450 \text{ MeV}$, cutoff effects start to play a role. Note that for large chemical potentials, the ground state is in any case expected to be given by color superconducting matter and not by asymptotically free quark-gluon matter, cf. chapter 2.

²We use $\mu = 1 \text{ MeV}$ instead of $\mu = 0$, because $\rho_q \equiv 0$ for $\mu = 0$.

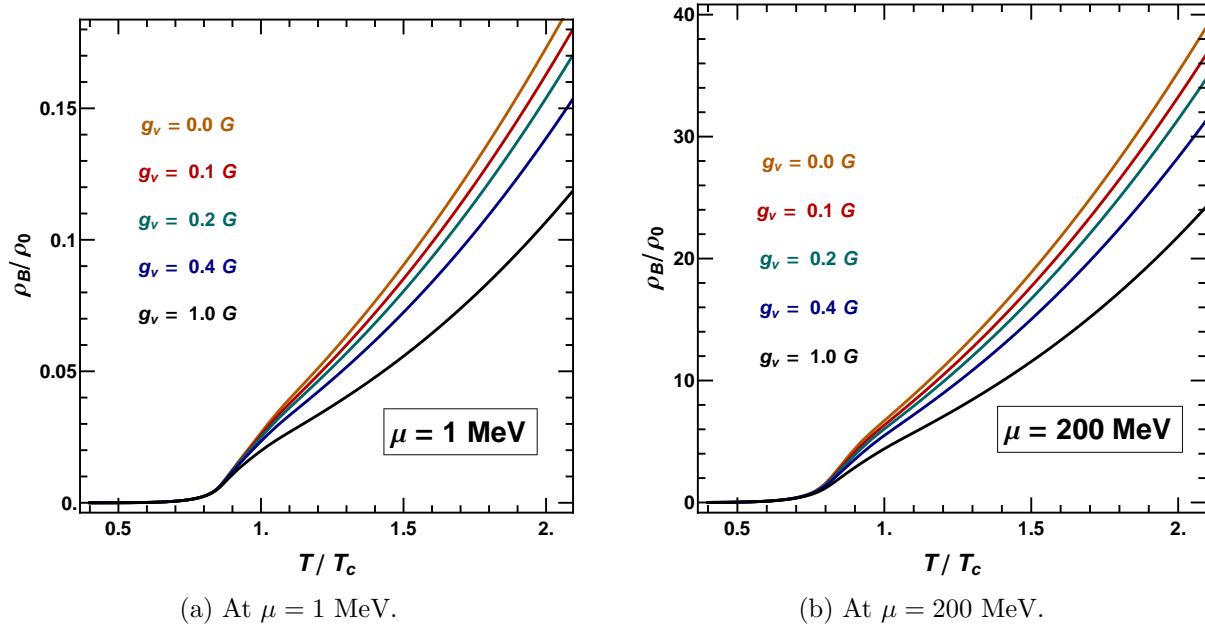


Fig. 7.6: Baryon density curves ρ_B/ρ_0 as a function of T/T_c for different values of the vector interaction coupling strength g_v . Curves are normalized to the empirical nuclear matter saturation density $\rho_0 = 0.16 \text{ fm}^{-3}$.

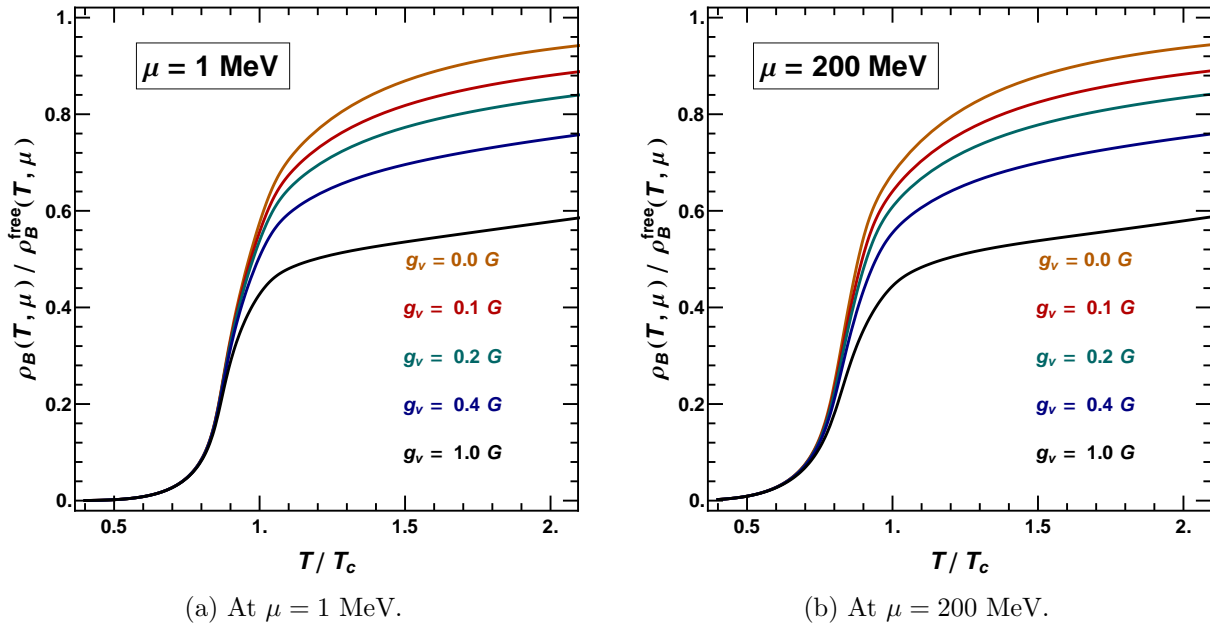


Fig. 7.7: Baryon density ρ_B normalized to the free massless baryon density ρ_B^{free} of (7.3.3) as a function of T/T_c for different values of the vector interaction coupling strength g_v at two different chemical potentials.

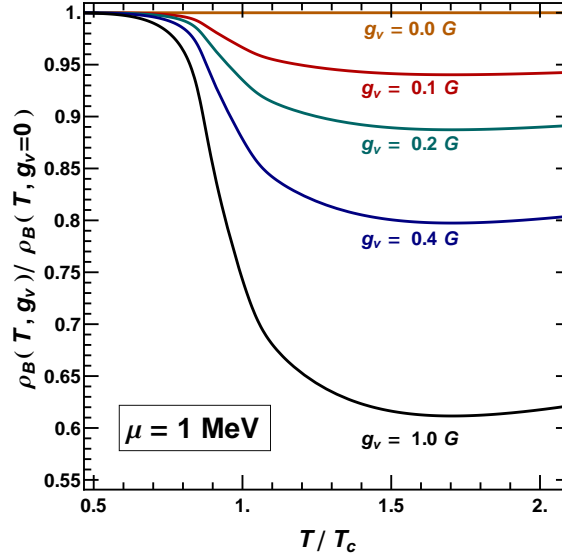


Fig. 7.8: Baryon density ρ_B normalized to the $g_v = 0$ curve as a function of T/T_c for different values of the vector interaction coupling strength g_v at the chemical potential of $\mu = 1$ MeV.

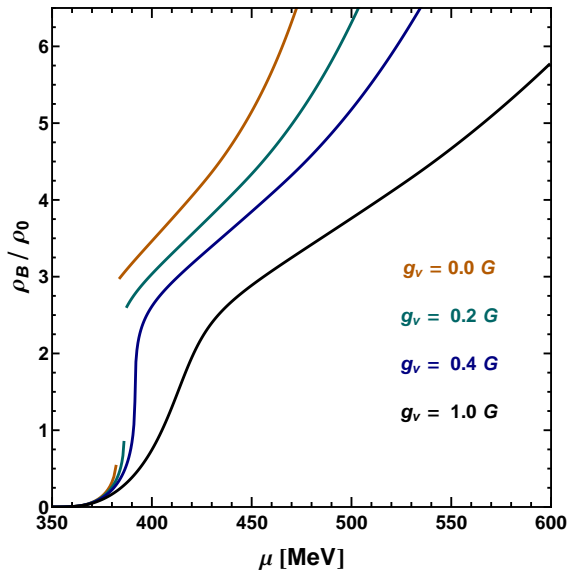


Fig. 7.9: Comparison of baryon density curves ρ_B/ρ_0 as a function of quark chemical potential μ at the temperature of $T = 10$ MeV for different values of the vector interaction coupling strength g_v , increasing from top to bottom.

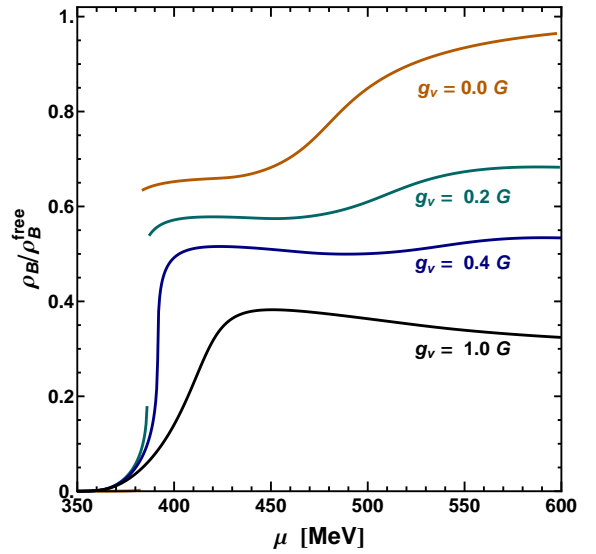


Fig. 7.10: Comparison of baryon density curves ρ_B normalized to the free baryon density ρ_B^{free} of eq. (7.3.3) as a function of μ at the temperature of $T = 10$ MeV for different values of the vector interaction coupling strength g_v , increasing from top to bottom.

7.3.3 Chiral condensates as functions of density

Next, we study the chiral condensate as a function of the baryon number density ρ_B for different choices of g_v at $T = 10$ MeV. Fig. 7.11a presents the chiral light quark condensate $\sigma_u(T)/\sigma_u(0)$ as a function of ρ_B for $g_v = 0.2G$, where it still undergoes a first-order phase transition. The dashed line is an extrapolation from the linear behavior at low ρ_B . Fig. 7.11b shows σ_u for $g_v = 0.66G$, where the transition has turned into a crossover. Plot points are $\Delta\mu = 1$ MeV

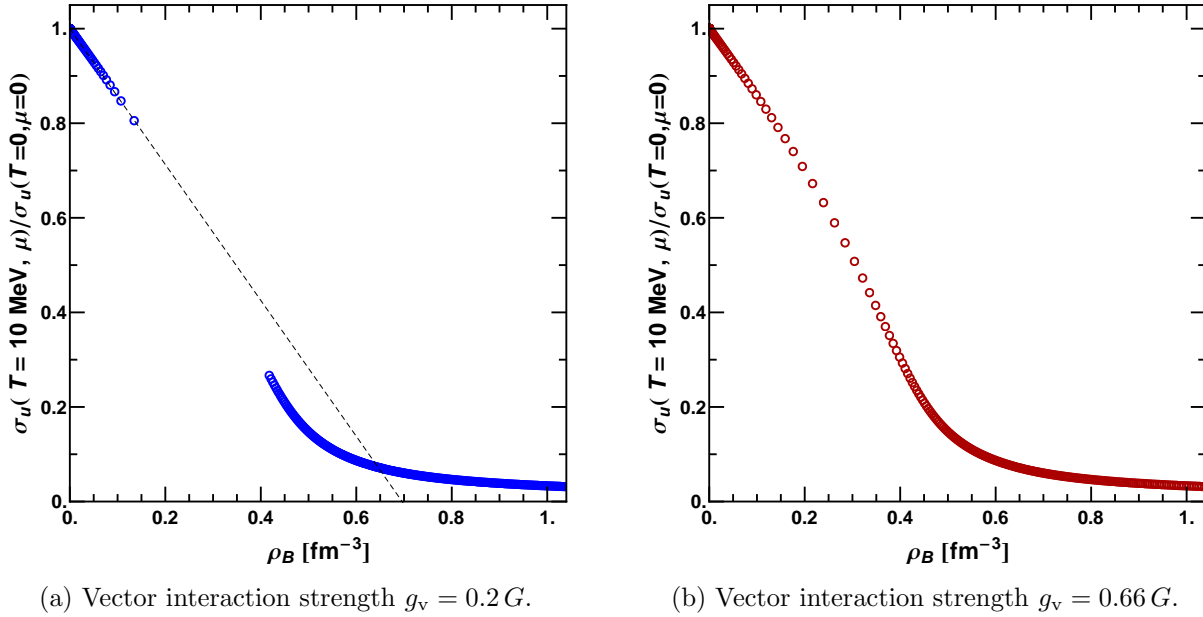


Fig. 7.11: Normalized light quark chiral condensate σ_u as a function of the baryon number density ρ_B at $T = 10$ MeV for different values of g_v .

apart from each other in terms of the chemical potential. The horizontal as well as vertical gap in Fig. 7.11a shows that the discontinuities in chiral condensate and the density are connected. This has been called a non-trivial finding of the PNJL model [52].

The curves from Fig. 7.11a and Fig. 7.11b are congruent with each other. We found that at any fixed temperature T , for all values of g_v , the curves of $\sigma_u(\mu)/\sigma_u(T=0, \mu=0)$ as functions of ρ_B are superimposable, at least for $\mu \leq \Lambda$. The only qualitative differences are the possible existence of a gap as in Fig. 7.11a, and its size. Both features are dependent on the combination of values of T and g_v . Quantitatively, for larger g_v , a smaller value of ρ_B is reached at $\mu_{\text{max}} = \Lambda$.

In Fig. 7.13 we show ρ_B as function of the normalized chiral condensate³, calculated with $g_v = 0.5 G$ at the temperatures $T = 0, 25 \text{ MeV}, \dots, 200 \text{ MeV}$. For $\mu \leq \Lambda$, all results for all values of g_v at a specific temperature T were congruent with the curve for that temperature T in this plot. The explanation is straight-forward: an increase in g_v delays the restoration of chiral symmetry in terms of μ . Fig. 7.12 demonstrates this for the same parameters as in Fig. 7.9. At the same time, it suppresses the baryon density ρ_B . These two effects are connected precisely in such a way that the curves of $\sigma_u(\rho_B)$ for fixed T are always congruent.

For $T \lesssim 200 \text{ MeV}$, we make an at first counter-intuitive observation: for a fixed baryon density, the chiral condensate becomes larger instead of melting. Only for $T \gtrsim 200 \text{ MeV}$, the expected reverse situation sets in at low ρ_B (lower right corner of Fig. 7.13). This effect is carried over into the QCD phase diagram in the T - ρ_B plane. Such a diagram is shown in section 7.6, where we also discuss the mechanism behind the effect.

7.4 Location of the critical point

We have already seen, e. g. in Fig. 7.12, that with increasing g_v , the transition order at a fixed temperature changes from first-order to a crossover. The systematics of this effect are best studied by plotting the trajectory of the critical point with varying g_v as in [52].

We present results with the ‘‘RKH’’ parameter set from [110] in Fig. 7.14. The critical point is pushed out of the phase diagram for $g_v \gtrsim 0.71 G$. This value is larger than the corresponding

³Note that for Fig. 7.13 we have flipped the axes with respect to Fig. 7.11 for easier plotting.

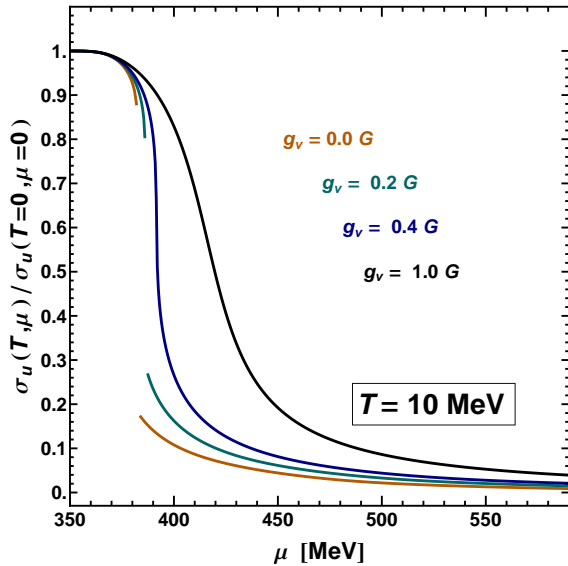


Fig. 7.12: Comparison of light quark chiral condensate σ_u normalized to the vacuum value as a function of μ at the temperature of $T = 10$ MeV for different values of the vector interaction coupling strength g_v , increasing from left to right.

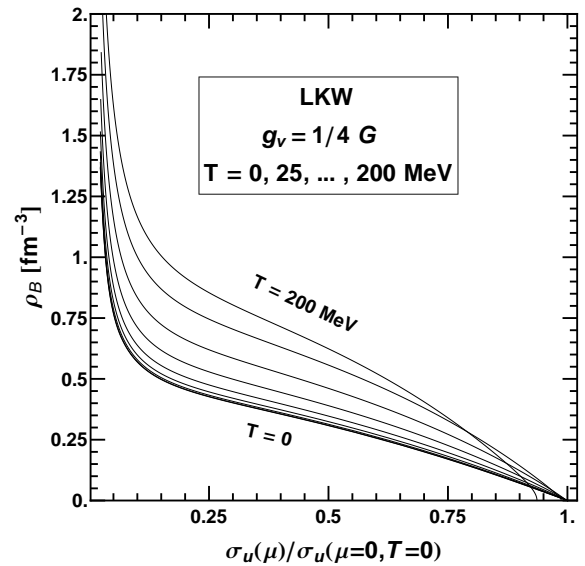


Fig. 7.13: Universal curves of the baryon density ρ_B as a function of the normalized chiral condensate, calculated with $g_v = 0.5 G$, at $T = 25, 50, \dots, 200$ MeV (from top to bottom).

value found in [52] by a factor of almost 2.

We therefore calculated the trajectory of the critical point also for other parameter sets in order to check their consistency. Fig. 7.15 presents results with the standard “LKW” parameter set of this chapter [92]. In this case, the critical point vanishes for $g_v \gtrsim 0.38 G$.

In [52], the “HK” parameter set from [63] was used, in addition to a “minimal” cutoff (see eq. (4.2.5) scheme and the simplified Polyakov loop effective potential shown in eq. (6.2.1). We have reproduced their results in the lower curve of Fig. 7.16. The upper curve shows results from our model setup, using the same “HK” parameter set. In both cases, the critical point vanishes for $g_v \gtrsim 0.41 G$.

For easier comparison, we collect the results for the trajectories of the critical point of these four scenarios. Fig. 7.17 shows the trajectories in the T - μ -plane. The “RKH” and the “LKW” curve at first seem to be very similar, while the “HK” results appear to be incompatible with them. It is instructive to study the relative change of the temperature of the critical point $T_{cp}(g_v) / T_{cp}(g_v = 0)$ as a function of g_v / G , as we have done in Fig. 7.18.

Here it becomes obvious that all parameter sets except the “RKH” set produce essentially equivalent results. The “critical” value g_v^c above which the phase transition is all crossover is consistently at about $g_v^c \approx 0.4 G$. The apparent differences in Fig. 7.17 are revealed to be mostly due to the different locations of the critical point in the $g_v = 0$ case. These results motivate our use of the “LKW” parameter set as a standard in this chapter.

Note that the critical value $g_v^c \approx 0.4 G$ is the low end of the range of likely physical values for g_v that we determined in 7.1.6. This is a first indication that the chiral phase transition in the QCD phase diagram is all crossover.

Next, we consider the termination point μ_t of the chiral first-order transition on the μ axis at $T \sim 0$. Fig. 7.19 shows that μ_t is quite robust under variation of g_v . Again, the “HK” and “LKW” parameter set results are consistent with each other, whereas the “RKH” curve is clearly separate. This underlines the reliability of the “LKW” and “HK” parameter set results for quantitative studies of vector interaction effects.

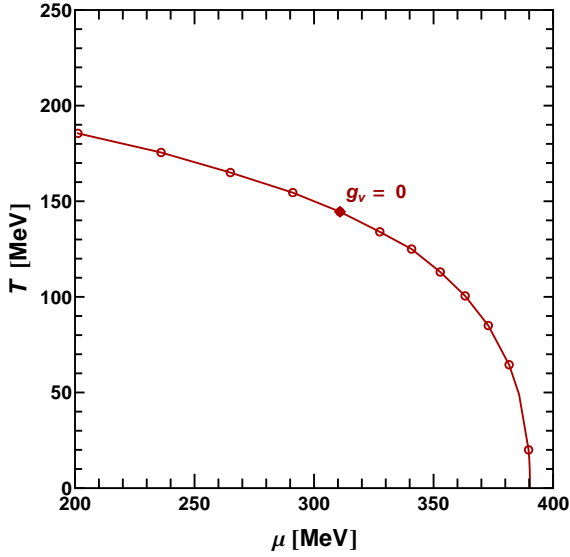


Fig. 7.14: Trajectory of the critical point in the phase diagram as a result of a change of the vector interaction strength g_v with our standard “RKH” parameter set. Points are $\Delta g_v = 0.1 G$ apart. The critical point disappears from the phase diagram for $g_v \gtrsim 0.71 G$.

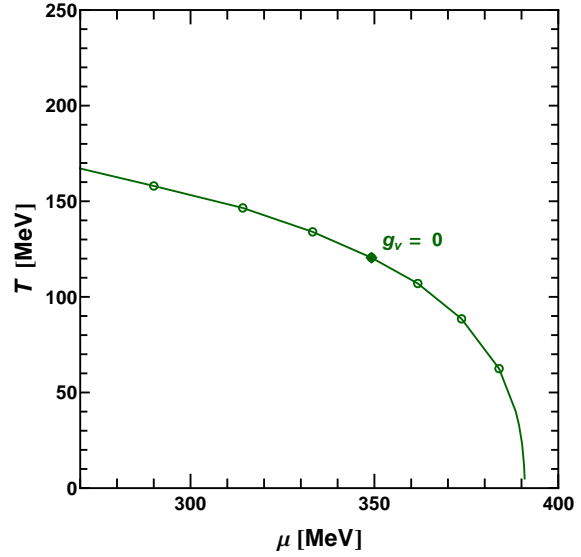


Fig. 7.15: Trajectory of the critical point in the phase diagram as a result of a change of the vector interaction strength g_v with the “LKW” parameter set. Points are $\Delta g_v = 0.1 G$ apart. The critical point disappears from the phase diagram for $g_v \gtrsim 0.38 G$.

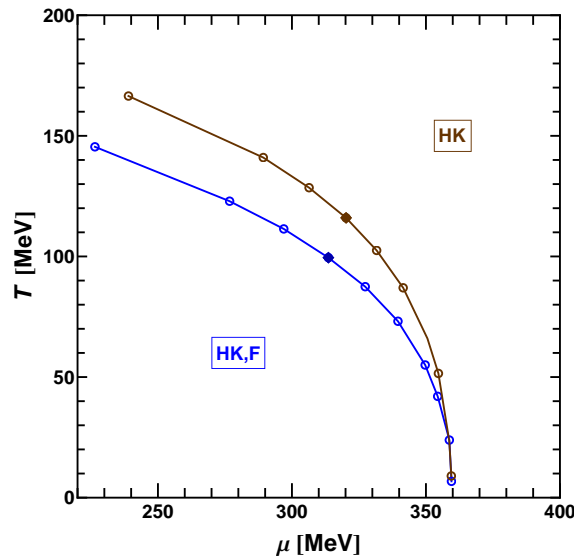


Fig. 7.16: Trajectory of the critical point in the phase diagram as a result of a change of the vector interaction strength g_v with “HK” parameter set from [63]. Lower, blue line (HK,F) shows results with cutoff procedure and Polyakov loop effective potential from [52]. Upper, brown line (HK) shows results with our standard choices. From left to right, the points denote in both cases $g_v/G = -0.2, -0.1, 0, 0.1, 0.2, 0.3, 0.35, 0.4$ and $g_v/G = 0.41$. The critical point disappears from the phase diagram for $g_v \gtrsim 0.41 G$.

7.5 First-order transition in the temperature–density plane

So far we have focused on the critical point itself. Fig. 7.20 shows the complete first-order transition lines starting at the critical point for three different combinations⁴ of values of the

⁴For easier comparison with results in chapter 5, we use the “RKH” parameter set for these exploratory studies.

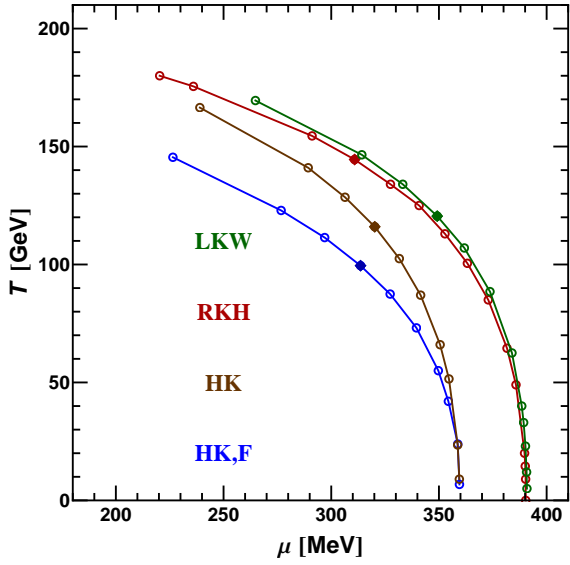


Fig. 7.17: Superposition of the critical point trajectories under a variation of g_v from Fig. 7.14, Fig. 7.16 and Fig. 7.15, using the parameter sets “RKH” [110], “LKW” [92] and “HK” [63], respectively. In the latter case, also the results with cutoff scheme and Polyakov loop effective potential from [52] have been added (HK,F).

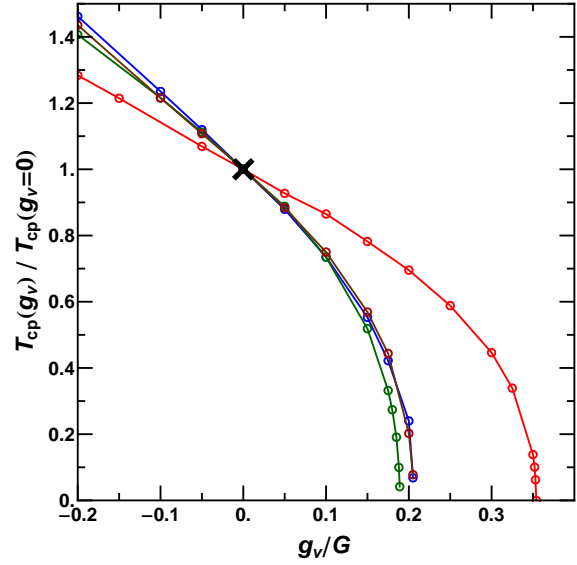


Fig. 7.18: Normalized temperature $T_{cp}(g_v) / T_{cp}(g_v=0)$ of the critical point as a function of g_v/G for parameters sets and with color coding the same as in Fig. 7.17. The detached curve to the right results from the RKH parameter set.

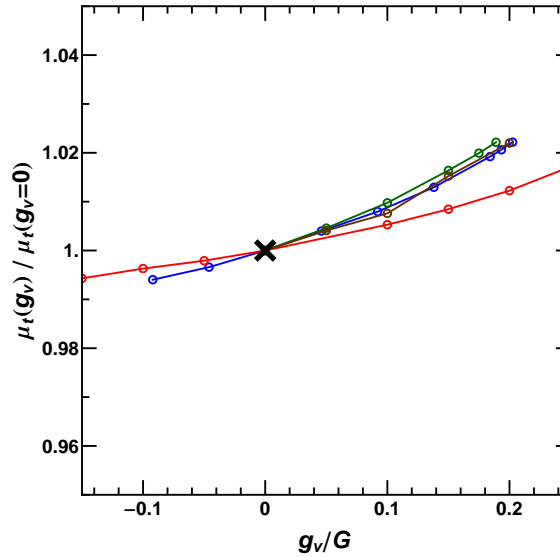


Fig. 7.19: Termination point chemical potential μ_t of the chiral first-order transition on the μ axis as a function of g_v/G . Color coding is the same as in Fig. 7.17. Detached curve is a result of the “RKH” parameter set.

KMT coupling strength K and g_v . The variation of these two input parameters results in considerable shifts of the location of the critical point.

To put constraints on the system, we use our knowledge of nuclear physics at low T and μ . The short black line labeled “NM” in Fig. 7.20 marks the nuclear matter liquid/gas transition with its critical point marked by a dot. The numerical values for this first-order transition stem

from an in-medium chiral perturbation calculation, which realistically uses nucleons as dynamic degrees of freedom [46]. Their results are calculated for symmetric nuclear matter with $\mu_u = \mu_d$ and $\mu_s = 0$, whereas we used $\mu_s = \mu_d = \mu_u$. However, Fig. 7.1 showed that strangeness has no influence on the chiral light quark transition in that area of the phase diagram. Results from both approaches are therefore well comparable. We find that the chiral transition for $g_v = 0$ and $K = 0.56 K_0$ overlaps unphysically with the nuclear matter phase transition, whereas the results for the other two scenarios in Fig. 7.20 seem to be allowed.

The complete situation is revealed only when we show the chiral first-order transition in the T – ρ_B plane in Fig. 7.21. As we saw in the previous sections of this chapter, the discontinuity in the chiral condensate is linked to the discontinuity in the baryon number density ρ_B . Plotted as a function of ρ_B , the chiral transition takes the form of a coexistence region. To the left of this bell-shaped region, chiral symmetry is broken, to its right it is restored⁵. Inside the “bell”, both types of matter coexist like in the water/vapor coexistence region in the p – V phase diagram of water.

In Fig. 7.21 we present the coexistence regions for the same parameter combinations as in Fig. 7.20. In the lower left, we have included the coexistence region for the nuclear matter phase transition [46] corresponding to the small “NM” line in Fig. 7.20. To the left of the bell, nuclear matter is in a gaseous, to its right in a liquid state. The coexistence region extends up to the empirical nuclear matter saturation density of $\rho_0 = 0.16 \text{ fm}^{-3}$. In contrast to the expectation from Fig. 7.20, *all* of the shown chiral coexistence regions overlap with the nuclear matter transition.

This would mean that even in well known nuclear matter systems there should be indications of restored chiral symmetry. This is not the case, therefore the overlap is unphysical. Comparing Fig. 7.17 and Fig. 7.18 sends an important message to model builders: the compatibility of a given QCD phase diagram result with nuclear matter constraints is not necessarily revealed by the T – μ plot. The T – ρ_B diagram can look decidedly different and should be used as the more relevant benchmark.

It is also seen that in the region of low density the chiral condensate from in-medium chiral perturbation theory [45] does not match well with the results of PNJL model calculations. For these reasons, in our studies of the chiral coexistence regions we put special emphasis on the question for which values of g_v and K the situation agrees with constraints from nuclear matter. In order to be compatible with known properties, the chiral coexistence region, if it exists, should be situated well above the nuclear saturation density, somewhere around twice or three times ρ_0 . In the following, we study locations and widths of the chiral coexistence regions as functions of either g_v or K . As we have seen some dependence on the parameter set in previous results, these studies are done for all the three different parameter sets introduced above.

The “RKH” set from [110] is treated in section 7.5.1. This is the set that was used throughout the previous chapters of this work so that comparisons are possible. Section 7.5.2 contains an analogous study for the “HK” parameter set [63]. Finally, the “LKW” set [92] is used in section 7.5.3. The discussion about the combined dependences of the coexistence region on g_v and K is found in section 7.5.4, where Fig. 7.28 summarizes the findings.

At low $T \sim 0$ the numerical cost of calculation is quite high. We therefore in all cases study the situation at $T = 10 \text{ MeV}$ as an excellent approximation⁶.

7.5.1 RKH parameter set

The coexistence region from the “RKH” parameter set at $g_v = 0$ has already been shown in Fig. 7.21. Fig. 7.22a shows the location and width of the chiral coexistence region at $T = 10 \text{ MeV}$ as a function of g_v/G . At the tip of the shape, to the right, the vector coupling g_v becomes so

⁵Explicit chiral symmetry breaking by the current quark masses is neglected in this discussion.

⁶The widths of the coexistence regions are therefore estimated conservatively.

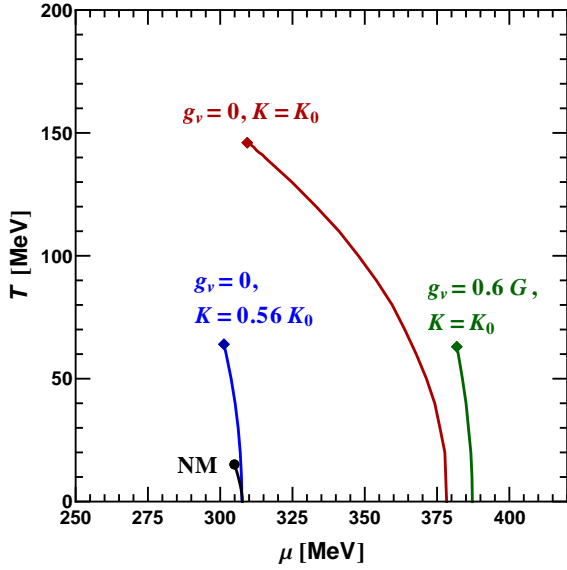


Fig. 7.20: Chiral first-order transition curve for three different scenarios with the RKH parameter set: standard scenario without vector interaction, i. e. $g_v = 0$ (red, center), scenario with $g_v = 0.6 G$ (green, right) and with $g_v = 0$ but $K = 0.56 K_0$ (blue, left). Small diamonds mark the respective critical points. In black at the bottom is the nuclear matter (NM) liquid/gas transition from [46] with the critical point marked by a dot.

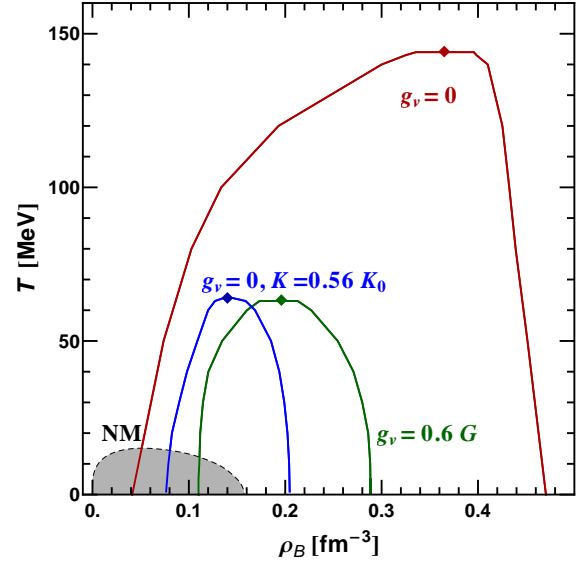


Fig. 7.21: Chiral coexistence regions (“bells”) for the three scenarios of Fig. 7.20. Small diamonds mark the respective critical points. The low gray region in the lower left is the nuclear matter (NM) result from [46].

large that the temperature of the critical point drops to 10 MeV. The critical point disappears from the phase diagram soon thereafter (cf. Fig. 7.14).

In the diagram we have also included the nuclear matter saturation density of $\rho_0 = 0.16 \text{ fm}^{-3}$ as a horizontal red line to help with the comparison. Remember that it also marks the high density boundary of the nuclear matter liquid/gas coexistence region according (Fig. 7.21). Evidently, the chiral coexistence “bell” simply shrinks as a function of g_v/G without moving away from ρ_0 . As long as there is a critical point in the phase diagram, the chiral coexistence region in this scenario will overlap with nuclear matter saturation density.

The possible reduction of K due to in-medium effects (cf. discussion in section 5.2) motivates the study shown in Fig. 7.22b. It is similar to Fig. 7.22a, but instead of g_v/G , the horizontal axis is now K/K_0 . The plot exhibits how the width of the coexistence bell systematically decreases with lowered K . For a given reduction of T_{cp} , the coexistence bell is consistently narrower if the reduction is done by lowering K , rather than by increasing g_v . An example was already seen in Fig. 7.21. Again, there is an overlap of the bell with ρ_0 for almost all values of K . In contrast to the change in g_v , the coexistence region also shifts slightly towards lower ρ_B so that it eventually even moves below ρ_0 .

7.5.2 HK parameter set

In this section we gather some interesting results calculated with the HK parameter set from [63]. Fig. 7.23 shows the chiral first-order coexistence region at $g_v = 0$ in the $T-\rho_B$ plane. Fig. 7.24a shows its width at $T = 10 \text{ MeV}$ for different choices of g_v/G ; it is the HK counterpart to

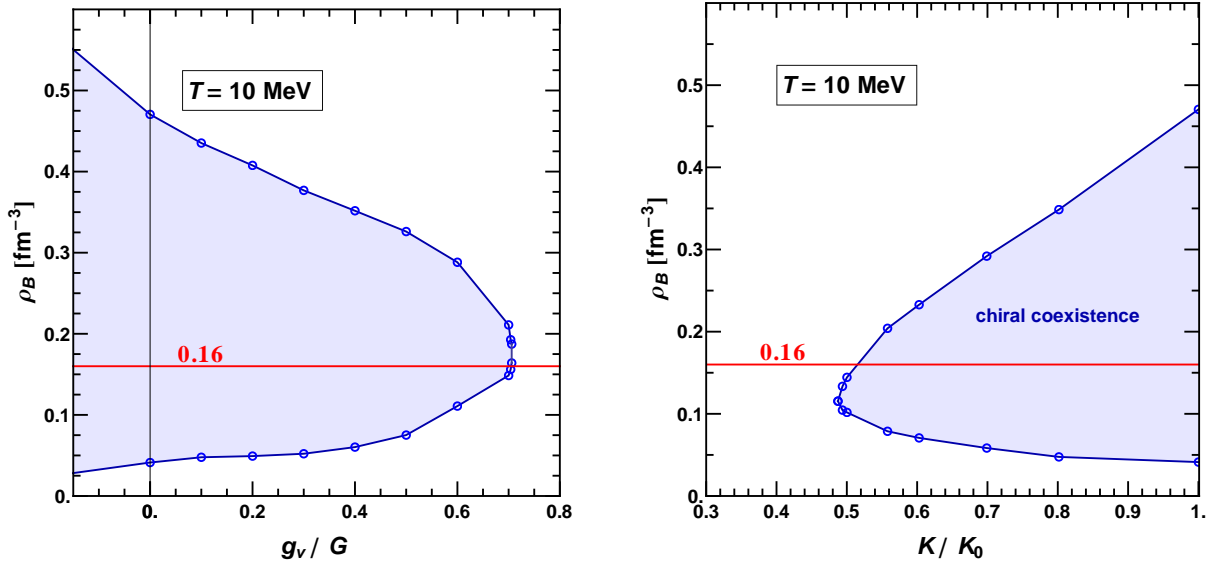
(a) Coexistence region as function of g_v/G .(b) Coexistence region as function of K/K_0 .

Fig. 7.22: Baryon density values within the first-order coexistence regions (colored blue) at $T = 10$ MeV, calculated with the “RKH” parameter set [110]. The red line marks empirical nuclear matter saturation density ρ_0 . The phase of broken chiral symmetry lies below the lower boundary of the shaded area, the phase with restored chiral symmetry above the upper boundary.

the RKH calculation in Fig. 7.22a. Fig. 7.24b shows the same quantity, but as a function of a change in K/K_0 , with $g_v = 0$ fixed. It corresponds to Fig. 7.22b from the “RKH” parameter set.

The large quantitative differences between the “RKH” and the “KH” set have already been discussed in section 7.4. Qualitatively, they are quite similar, including the tendency of the coexistence region to move below ρ_0 for small K .

7.5.3 LKW parameter set

This section shows results calculated with the “LKW” parameter set from [92]. The shown quantities are the same, and are presented in the same order, as in the previous section. Findings in section 7.4 already suggested that results from the “HK” and the “LKW” parameter sets might be generally similar.

From Fig. 7.26 we see that this is not always the case. In Fig. 7.26a location and width of the chiral coexistence region at $T = 10$ is presented as a function of g_v/G . In Fig. 7.26b, it is given as a function of K/K_0 . In both cases, there is a small parameter range where the complete coexistence region is clearly above $\rho_0 = 0.16 \text{ fm}^{-3}$. The largest difference is visible in Fig. 7.26b: the vanishing of the coexistence “bell” takes place at $\rho_B > \rho_0$. For the “RKH” parameter set (Fig. 7.22b) and the “HK” parameter set (Fig. 7.24b) it was the opposite.

It should be noted that the parameter ranges for which the existence of the first-order transition is compatible with nuclear matter constraints is very small.

7.5.4 Change of g_v for non-standard values of K

In the foregoing section, we have seen that with the “LKW” parameter set, there is a narrow range of g_v even for $K = K_0$ where the existence of a critical point is compatible with nuclear matter constraints, at least to the extent that the coexistence bells do not directly overlap. A

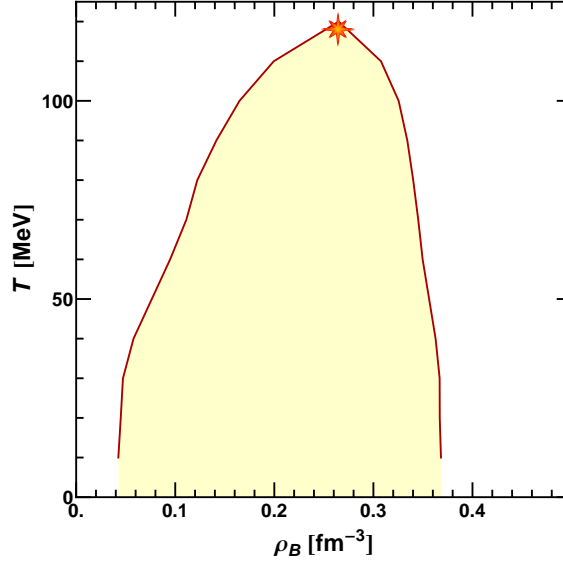
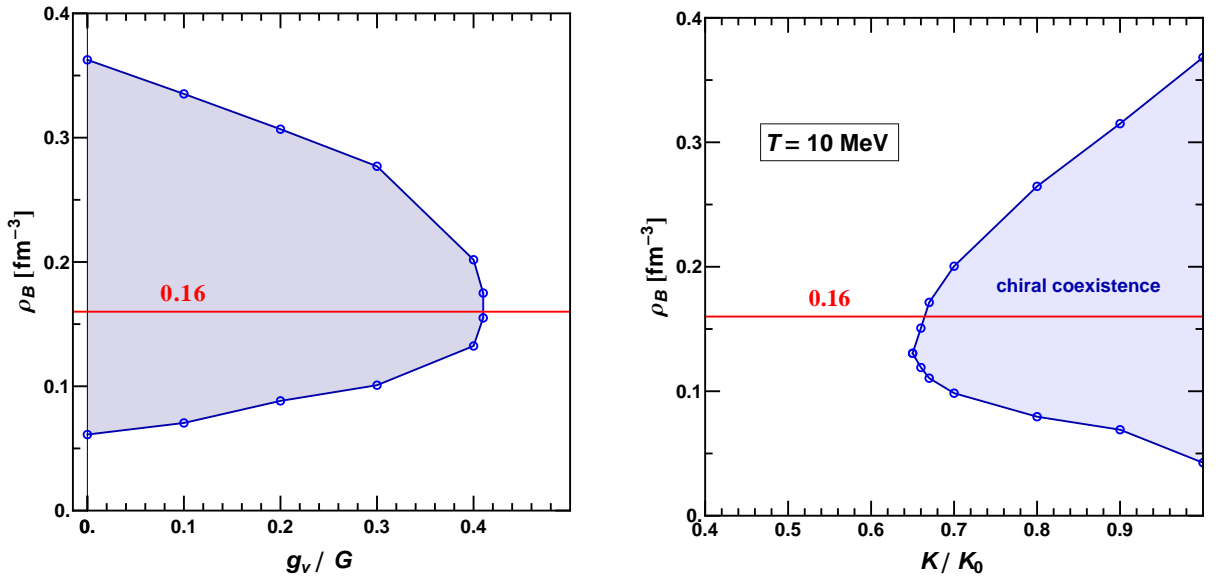


Fig. 7.23: Chiral first-order coexistence region in the T - ρ_B phase diagram, calculated without vector interaction ($g_v = 0$) for the “HK” parameter set [63]. The coexistence region is shaded, the region of broken chiral symmetry is situated to the left, chirally restored matter to the right.



(a) Coexistence region as function of g_v/G .

(b) Coexistence region as function of K/K_0 .

Fig. 7.24: Baryon density values within the first-order coexistence regions (colored blue) at $T = 10$ MeV, calculated with the “HK” parameter set [63]. Red line: nuclear matter saturation density ρ_0 . The phase of broken chiral symmetry lies below the lower boundary of the shaded area, the phase with restored chiral symmetry above the upper boundary.

similar range has been found for varying K at fixed $g_v = 0$. The next step is to combine these variations to determine the parameter “window” in which a critical point might be possible in this way.

Fig. 7.27 shows, as an example, results for the coexistence region at $K = 0.75 K_0$ in the LKW parameter set for different values of g_v/G . The parameter window for the critical point remains narrow, but is shifted to smaller values of g_v/G . In section Fig. 7.26a we saw that for

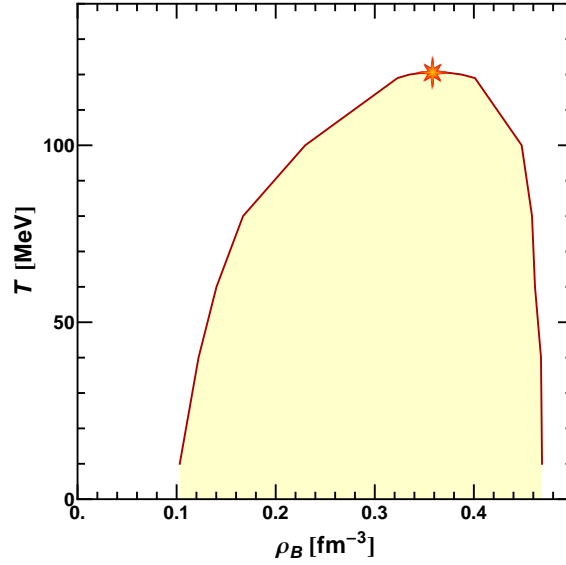
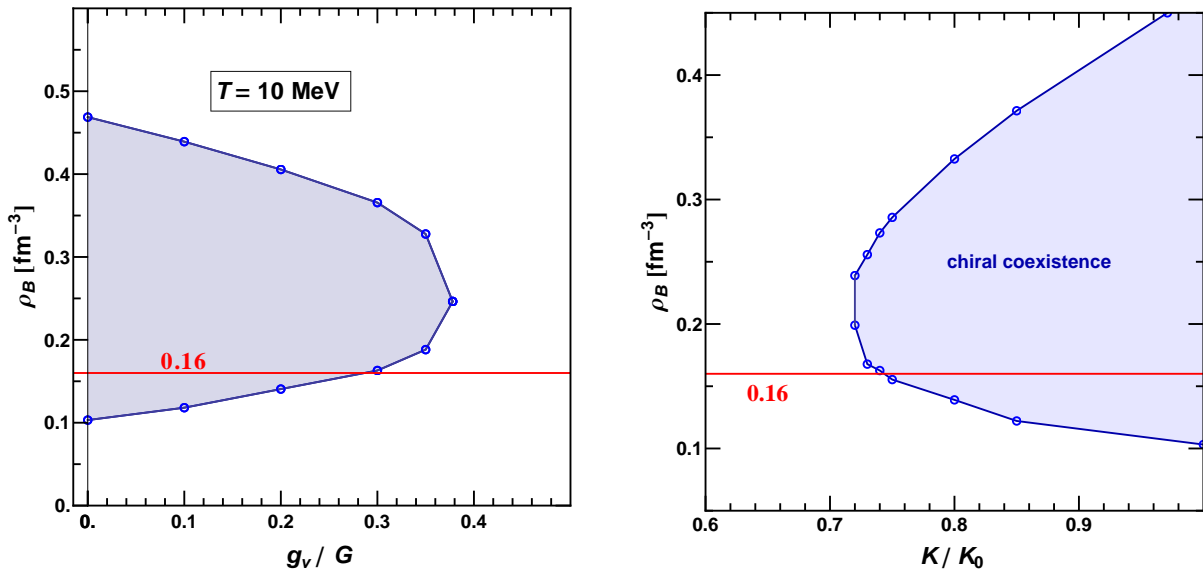


Fig. 7.25: Chiral first-order coexistence region in the T – ρ_B phase diagram, calculated without vector interaction ($g_v = 0$) for the “LKW” parameter set [92]. The coexistence region is shaded, the region of broken chiral symmetry is situated to the left, chirally restored matter to the right.



(a) Coexistence region as function of g_v/G .

(b) Coexistence region as function of K .

Fig. 7.26: Baryon density values within the first-order coexistence regions (colored blue) at $T = 10$ MeV, calculated with the “LKW” parameter set [92]. Red line: nuclear matter saturation density ρ_0 . The phase of broken chiral symmetry lies below the lower boundary of the shaded area, the phase with restored chiral symmetry above the upper boundary.

$K = K_0$ in the “LKW” set the window for the critical point was $0.29 G \leq g_v \leq 0.38 G$ with a width of $0.09 G$. For $K = 0.75 K_0$ we find the window $0.006 G \lesssim g_v \lesssim 0.056 G$ with the width of about $0.05 G$.

It is important to note that even though the chiral coexistence region has been shifted above ρ_0 , it is still very close to it. That such an effect would have gone unnoticed in the extensive study of nuclear matter is very unlikely.

Continuing along those lines, we show in Fig. 7.28 the g_v - K parameter plane. It displays which combinations of these two parameters would result in which of the two main scenarios:

1. the unphysical scenario where there is a first-order transition in the phase diagram (gray areas)
2. the scenario with a purely crossover chiral transition (white area above the solid line)

The light gray area just below the solid line is the band for which there is a small first-order transition line but where the coexistence region is slightly shifted away from the direct overlap with ρ_0 . Such an area was only found with the ‘‘LKW’’ parameter set.

Recall now our collection of likely values for g_v from sources outside of our model in section 7.1. We find that the low end of the range of values in (7.1.6) is consistently above the area in parameter space that results in a critical point. This is the case already for $K = K_0$ but even more so for $K < K_0$. Given the expected effective in-medium reduction of K (see section 5.2) and the tendency towards even higher g_v that we discussed around (7.1.6), the existence of a critical point in the phase diagram seems very unlikely.

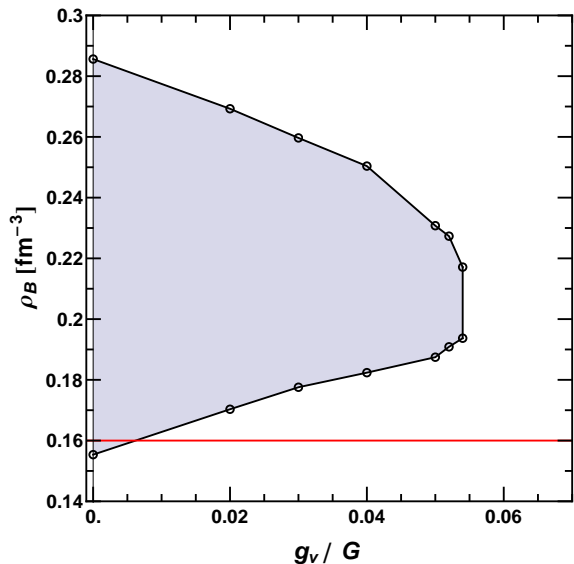


Fig. 7.27: Baryon density values within the first-order coexistence region (gray) at $T = 10$ MeV as a function of g_v/G with $K = 0.75 K_0$. Nuclear matter saturation density ρ_0 is added in red.

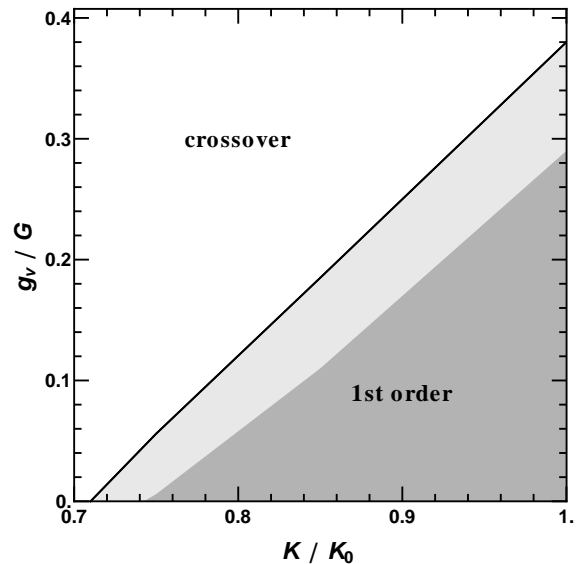


Fig. 7.28: Plot in the parameter space of g_v/G and K/K_0 , showing the boundaries between the two scenarios described in section 7.5.4 (see discussion there), calculated with the ‘‘LKW’’ parameter set at $T = 10$ MeV.

7.6 Phase diagram in the temperature–density plane

So far, we have only discussed the first-order phase transition. In this section, we show the complete chiral symmetry structure, including the crossover region, in the T - ρ_B plane. The Polyakov loop crossover plays no important role here and is therefore left out of the phase diagrams for the sake of clarity.

It is instructive to first have a look at the chiral limit case, where there is no explicit chiral symmetry breaking and there is a first-order phase transition all the way. In Fig. 7.29 we show the chiral first-order transition line of the chiral limit scenario in the T - μ plane as a basis for comparison. Fig. 7.30 then shows the corresponding plot for the T - ρ_B plane.

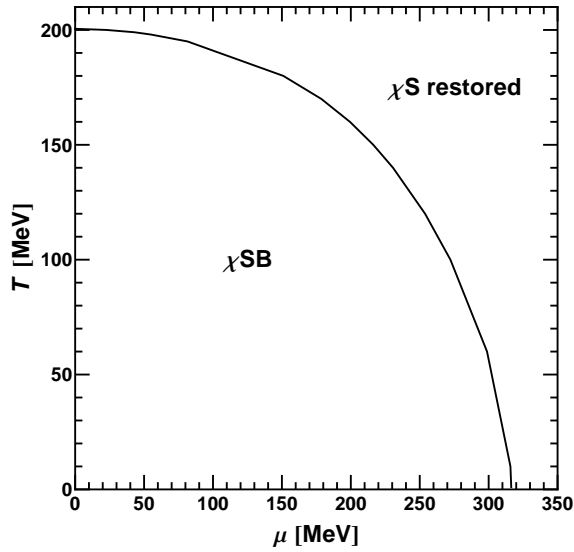


Fig. 7.29: Chiral first-order transition line in the T - μ plane in the chiral limit ($m_u = m_d = m_s = 0$). “ χ SB” denotes the phase with broken, “ χ S restored” the phase with restored chiral symmetry.

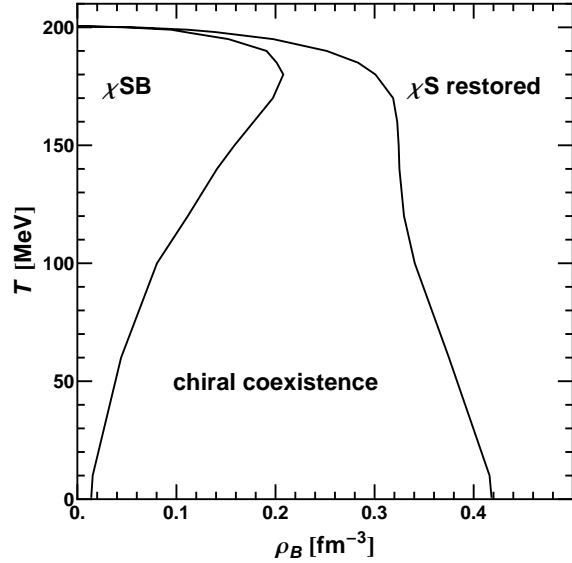


Fig. 7.30: Chiral first-order transition in the T - ρ_B plane in the chiral limit ($m_u = m_d = m_s = 0$). “ χ SB” denotes the phase with broken, “ χ S restored” the phase with restored chiral symmetry.

Next, Fig. 7.31 shows the phase diagram in the T - μ plane for three different choices of g_v/G in the “LKW” parameter set, two of them larger than the “critical” $g_v^c \approx 0.38 G$ that marks the disappearance of the critical point from the phase diagram. For the sake of lucidity, only the center lines of the transition bands are shown. As expected, there is little difference between the scenarios for small μ : the quark number density, and with it the influence of the vector interaction, is very low, even for temperatures around $T \sim 200$ MeV (see Fig. 7.6a and Fig. 7.6b). A pronounced difference between the scenarios is found in the curvature of the crossover transition lines that we have investigated in section 5.5. This motivates its study and comparison to lattice QCD results in section 7.7.

Translating the results of Fig. 7.31 for $g_v = 0.5 G$ and $g_v = G$ again into the T - ρ_B plane, we find that the two phase diagrams are identical within tolerances for the numerical methods. We explained this effect already in section 7.3.3. The result for $g_v = 0.5 G$ is shown in Fig. 7.32. In fact, the same shape is visible for *all* values of g_v , also those with $g_v < g_v^c$. The only difference is that the crossover curves in Fig. 7.32 are then overlapped at low T by the respective first-order chiral coexistence “bell”.

The T - ρ_B transition band exhibits a peculiar feature that we found already in section 7.3.3. A priori, one expects the chiral condensate to melt with increasing temperature: for higher temperatures T , the entropy density s in the free energy density

$$f = \epsilon - Ts \quad (7.6.1)$$

becomes important and pushes the system towards a state with higher symmetry, i. e. towards the restoration of chiral symmetry. However, when we look at physics at a fixed density, we must keep in mind that we will move along one of the lines of constant density in figures like Fig. 7.5a or Fig. 7.5b.

For a more detailed study, we have plotted two trajectories through the T - μ phase diagram for fixed densities through a background of the chiral condensate in Fig. 7.33. Dark gray signifies regions of large σ_u , light gray regions of small σ_u . The regions are chosen arbitrarily for instruc-

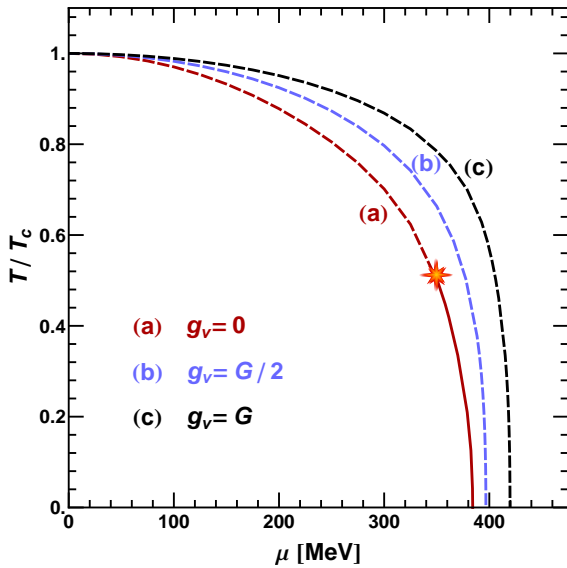


Fig. 7.31: Phase diagram in the T - μ plane for the “LKW” parameter set with $g_v = 0$, $g_v = 1/2 G$ and $g_v = G$. For the sake of lucidity, only the center lines of the transition bands are shown. Solid lines are first-order transitions, dashed lines crossovers.

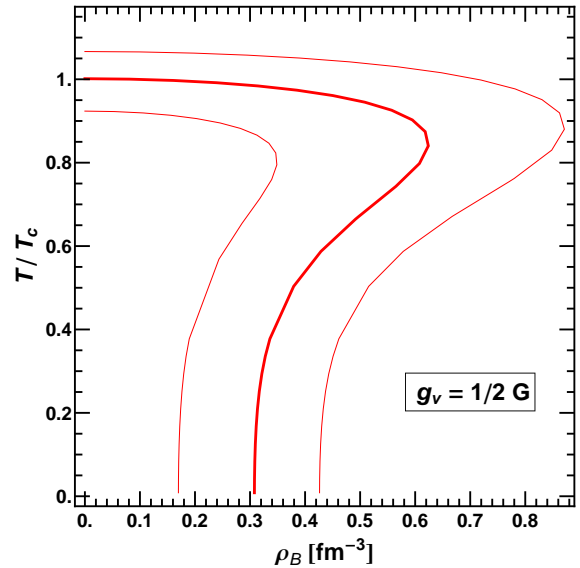


Fig. 7.32: Phase diagram in the T - ρ_B plane for the “LKW” parameter set with $g_v = 1/2 G$. Left-hand, center and right-hand line correspond to $\sigma_u(T, \mu) / \sigma_u(T = 0, \mu = 0) = 0.75, 0.5$ and 0.25 .

tive purposes and are not equidistant. The picture shows that for temperatures $T \lesssim 0.6 T_c$, a little increase in temperature is accompanied by a comparatively large⁷ decrease in μ . Therefore, in a certain temperature range, the lowering of μ increases σ_u more than the raising of T decreases it and the condensate increases with temperature instead of melting.

Let us follow in Fig. 7.34 the trajectory for a fixed density of $\rho \equiv 5\rho_0$, corresponding to the upper (red) trajectory in Fig. 7.33. It starts out coinciding with a curve of constant σ_u up to about $T \sim 0.2 T_c$, then curves towards higher values of σ_u . Only at about $T \sim 0.8 T_c$ it crosses the same curve again and moves towards higher values of σ_u . This behavior results in the counter-intuitive shape of the T - ρ phase diagram in Fig. 7.32. From a thermodynamics point of view, in

$$\Omega = -p = \epsilon - Ts - \mu\rho \quad (7.6.2)$$

the number density term $-\mu\rho$ acts in the same direction as the entropy (density) term $-Ts$: the phase with higher entropy is also the phase of higher quark number density, where the number of degrees of freedom is significantly larger. Fig. 7.34 shows the components of Ω , or $-p$, as a function of temperature at $g_v = 0.5 G$, again for $\rho_B \equiv 5\rho_0$. The $-\mu\rho$ term loses about as much in absolute value as the $-Ts$ term gains, until about $T \sim 0.65 T_c$. The combined weight of the two terms then starts growing, and it is in that temperature range that the curvature of the upper trajectory in Fig. 7.33 is reversed. From there on, the expected melting of the chiral condensate with increasing temperature is found.

We present here also the phase diagram for $g_v = G$ in the pressure-temperature plane for comparison to the $g_v = 0$ case given in Fig. 4.7, calculated with the “RKH” parameter set. The differing parameter sets have only some small quantitative effects.

⁷Note that the scale of the vertical axis in Fig. 7.33 is, with ~ 200 MeV, roughly half of that of the horizontal axis with 400 MeV.

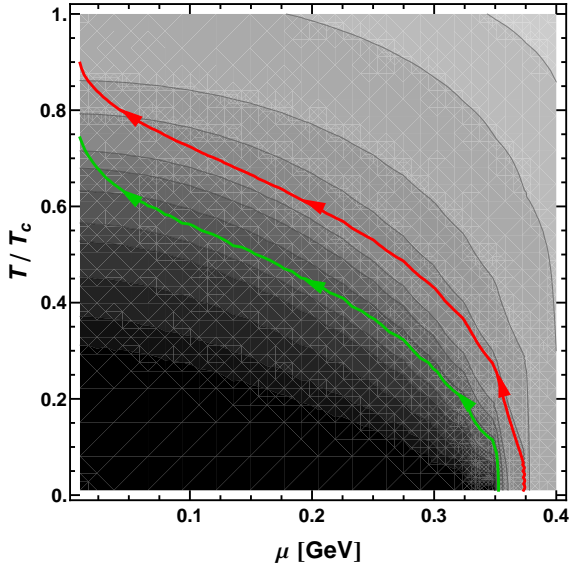


Fig. 7.33: Trajectory through the T - μ phase diagram for fixed density and increasing temperature with $g_v = 0.5G$. The background shading marks sections between (arbitrary) lines of constant light quark chiral condensate σ_u . Dark color symbolizes a strong condensate. The lower (green) trajectory is for a $\rho \equiv 0.5\rho_0$, the upper (red) curve for $\rho \equiv 5\rho_0$. Bumps in the lower right of the lines are interpolation artifacts and not actual results.

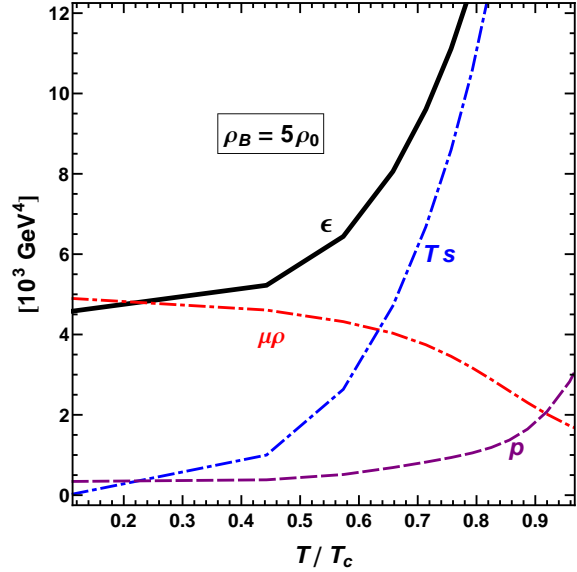


Fig. 7.34: Thermodynamic composition of Ω as a function of temperature for fixed $\rho = 5\rho_0$ with $g_v = 0.5G$, corresponding to the upper (red) trajectory in Fig. 7.33.

7.7 Transition line curvature as a function of g_v

In section 5.5 we already investigated the dependence of the curvature κ of the phase transition line close to $\mu = 0$ as a function of the KMT interaction strength K . It was found that the model results for the curvature were consistently too high in comparison with lattice QCD results. Fig. 7.31 has shown that varying g_v shifts the termination point of the transition on the μ axis, but not the termination point on the T axis. Consequently, increasing g_v reduces the curvature κ . The definition of κ is, again,

$$\frac{T_c(\mu)}{T_c(0)} = 1 - \kappa \left(\frac{\mu^2}{T_c^2} \right), \text{ or equivalently, } \kappa = -T_c \frac{dT_c(\mu)}{d\mu^2} \Big|_{\mu^2=0}. \quad (7.7.1)$$

Again, because of the smooth crossover transitions at $\mu = 0$, the κ points have error bars corresponding to the crossover bands. The result is shown in Fig. 7.36, where we also compare it to recent lattice QCD results [43, 72]. Only for $g_v \gtrsim 0.6G$ is the curvature compatible to the ranges given by the lattice groups. A strong coupling of $g_v \approx G$ yields almost perfect overlap with the more precise data of [72].

We had pointed out in section 5.2 that the KMT coupling strength K might depend on μ . In principle, this applies also to the four fermion coupling strength G . It could be argued that this would strongly affect κ , thus rendering the present discussion irrelevant. However, one should keep in mind that κ results from a leading (second) order expansion in μ/T . The μ dependence of e.g. the four point coupling G would therefore only play a role at higher orders [22].

The good agreement between lattice QCD results for κ and our result for $g_v \sim G$ points

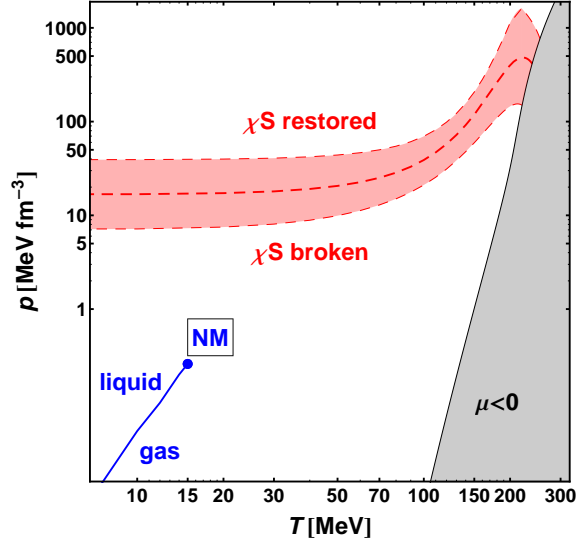


Fig. 7.35: Double-logarithmic phase diagram of QCD with pressure p and temperature T as external parameters. Calculated with the “LKW” parameter set and $g_v = G$. Chiral crossover band dashed, critical point denoted by a star. Results for the nuclear matter (NM) liquid/gas transition from [46]. See result for “RKH” parameter set and $g_v = 0$ in Fig. 4.7.

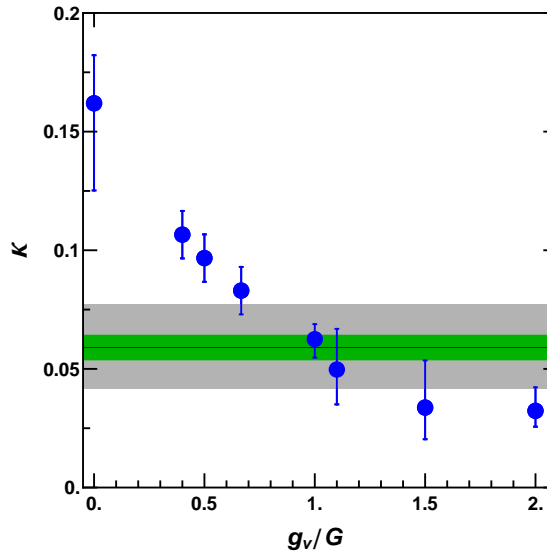


Fig. 7.36: Curvature κ of the crossover boundary near T_c as function of the vector coupling strength g_v . The dots are our calculations. Uncertainty measures attached to the dots give impression of the half width over which the crossover spreads. Upper horizontal line with narrow error band: (2+1)-flavor lattice QCD result of Ref. [72]; broad gray band: result of [43].

again to a likely large g_v in the physical scenario. This numerical value for g_v is not only within the range given in (7.1.6), but also very close to the value suggested by our parameter set, $g_v \sim 1.1G$, from [92]. The curvature of the phase transition line did not play any role in its determination.

7.8 Complete vector interaction

We turn now to the complete vector interaction,

$$\mathcal{L}_v^{\text{com}} = -\frac{g_v}{2} \sum_{a=0}^8 (\bar{\psi} \gamma_\mu \lambda^a \psi)^2. \quad (7.8.1)$$

The axial-vector term in (7.1.1) is omitted and left for future work. As in the previous section, we can restrict ourselves to the terms proportional to γ^0 . In addition, because of charge conservation (see section 3.3), we can drop the non-diagonal Gell-Mann matrices in flavor space and proceed with

$$\mathcal{L}_v^{\text{com}} = -\frac{g_v}{2} \left[(\bar{\psi} \gamma_\mu \lambda^0 \psi)^2 + (\bar{\psi} \gamma_\mu \lambda^3 \psi)^2 + (\bar{\psi} \gamma_\mu \lambda^8 \psi)^2 \right]. \quad (7.8.2)$$

Although seemingly more involved, the result is simpler than in the previous case. Using the same definitions as in (7.2.4), we arrive at

$$\mathcal{L}_v^{\text{com}} = -g_v \left[2(\rho_u \hat{n}_u + \rho_d \hat{n}_d + \rho_s \hat{n}_s) - (\rho_u^2 + \rho_d^2 + \rho_s^2) \right]. \quad (7.8.3)$$

The shifted effective thermodynamic potential is

$$\Omega'(T, V, \mu) = \Omega(T, V, \mu_q - 2g_v \rho_q) - g_v (\rho_u^2 + \rho_d^2 + \rho_s^2), \quad (7.8.4)$$

so that the chemical potential for each flavor is only directly connected to the quark number density *of that flavor*, in contrast to the reduced vector interaction in eq. (7.2.13).

7.8.1 Comparison between reduced and complete vector interaction

The “reduced” vector interaction (7.1.2) in the previous sections of this chapter is most commonly used in the literature. On the other hand, the “complete” vector interaction is certainly closer to physical reality. It is worthwhile investigating the differences between the two interactions. To this end, let us first compare the effective change in μ_u from eq. (7.2.18) and eq. (7.8.4): in the first case, μ_u is shifted by $-g_v \rho_{uds} = -g_v (\rho_u + \rho_d + \rho_s)$ and in the second case by $-2g_v \rho_u$. With isospin symmetry, we have $\rho_u = \rho_d$ so that the two shifts are exactly equal until the strange quark density ρ_s takes on a finite value.

From this it is already clear that the net strange quark density ρ_s plays the crucial role for the differences between the two interactions. For easier comparison, we define two effective vector coupling strengths for the reduced vector interaction, one for the light flavors ($\tilde{g}_{v,u}$) and one for the strange sector ($\tilde{g}_{v,s}$). The shift of the light quark chemical potential is then

$$\mu_u \rightarrow \mu'_u = \mu_u - g_v (\rho_u + \rho_d + \rho_s) = \mu_u - 2g_v \rho_u \left(1 + \frac{\rho_s}{2\rho_u} \right) = \mu_u - 2\tilde{g}_{v,u} \rho_u \quad (7.8.5)$$

and for the strange quark chemical potential as

$$\mu_s \rightarrow \mu'_s = \mu_s - g_v (\rho_u + \rho_d + \rho_s) = \mu_s - 2g_v \rho_s \left(1 + \frac{2\rho_u}{\rho_s} \right) = \mu_s - 2\tilde{g}_{v,s} \rho_s. \quad (7.8.6)$$

The definitions for the effective couplings are

$$\tilde{g}_{v,u} = g_v \left(1 + \frac{\rho_s}{2\rho_u} \right) \quad \text{and} \quad \tilde{g}_{v,s} = g_v \left(1 + \frac{2\rho_u}{\rho_s} \right). \quad (7.8.7)$$

From $\mu_u = \mu_d = \mu_s$ and the current quark mass relations $m_u = m_d$ and $m_u \ll m_s$ follow $\rho_u = \rho_d$ and $0 \leq \rho_s < \rho_u$ (see Fig. 7.37). This allows us to determine the bounds

$$g_v \leq \tilde{g}_{v,u} < \frac{3}{2} g_v \quad \text{and} \quad \frac{3}{2} g_v \leq \tilde{g}_{v,s}. \quad (7.8.8)$$

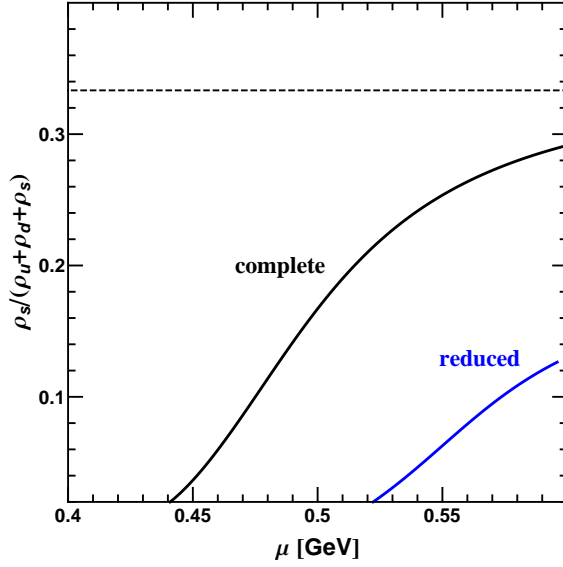


Fig. 7.37: Fraction of net strangeness with respect to the total density of all flavors as a function of $\mu \equiv \mu_u = \mu_d = \mu_s$ with $g_v = 0.5G$ and $T = 10$ MeV. The lower curve is for the reduced interaction (7.1.2), the upper curve for the complete vector interaction (7.1.1). The dashed line is the perturbative limit of $1/3$.

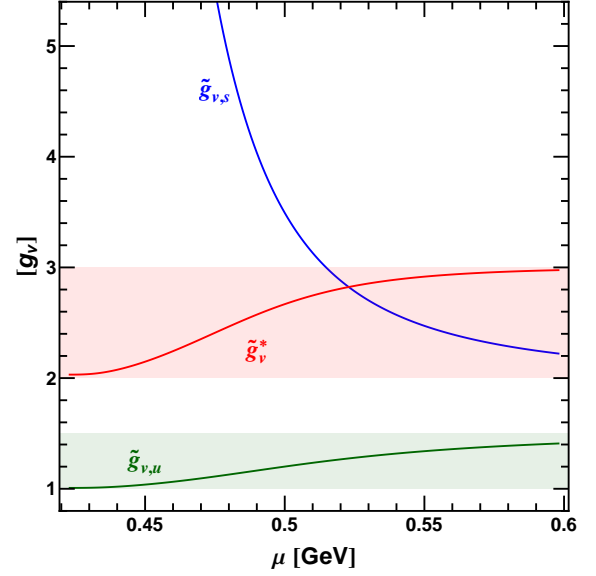


Fig. 7.38: Effective couplings as multiples of g_v at $T = 10$ MeV and $g_v = 0.5G$ for the reduced vector interaction, see eq.(7.8.7) and eq. (7.8.12). The shaded bands represent the maximum extent of $\tilde{g}_{v,u}$ and \tilde{g}_v^* for $\mu_u = \mu_d = \mu_s$.

Note that the effective couplings $\tilde{g}_{v,u}$ and $\tilde{g}_{v,s}$ in the reduced interaction are always stronger than their counterpart g_v in the complete interaction. In Fig. 7.38 they are plotted in terms of multiples of g_v and as functions of μ ; the shaded areas for $\tilde{g}_{v,u}$ and \tilde{g}_v^* (defined later in (7.8.12)) signify their respective range.

The analysis is not yet complete: the shifts in μ to lower values μ' result in decreased densities, so that a shift with the stronger effective coupling indeed suppresses the net quark densities more than a shift with just g_v . However, the term quadratic in the densities (condensation term) contributes with a negative sign to Ω and therefore acts towards an increase of the densities.

Setting again $\rho_d = \rho_u$ explicitly, we have for the reduced interaction

$$-\frac{g_v}{2}\rho_{uds}^2 = -\frac{g_v}{2}(2\rho_u + \rho_s)^2 = -g_v \left(2\rho_u^2 + 2\rho_u\rho_s + \frac{1}{2}\rho_s^2 \right) \quad (7.8.9)$$

and for the complete interaction for the same term

$$-g_v(2\rho_u^2 + \rho_s^2). \quad (7.8.10)$$

The two are equivalent as long as $\rho_s \approx 0$. Because of the larger current quark mass, the onset of ρ_s is delayed to large μ with respect to ρ_u and ρ_d (see e.g. Fig. 7.37 for $g_v = 0.5G$). If we focus on the transition pattern of the chiral light quark condensate as we did in the previous parts of this chapter, then the two vector interaction forms yield very similar results and our findings still hold. In the isospin symmetric scenario with zero net strangeness they are exactly identical.

To compare in terms of effective couplings, we rewrite the term (7.8.9) from the reduced interaction into a form similar to (7.8.10):

$$-g_v(2\rho_u + \rho_s)^2 = -g_v(2\rho_u^2 + \rho_s^2) + 2g_v(\rho_u^2 + 2\rho_u\rho_s) = -\tilde{g}_v^*(2\rho_u^2 + \rho_s^2) \quad (7.8.11)$$

with

$$\tilde{g}_v^* = g_v \left(1 + \frac{2\rho_u^2 + 4\rho_u\rho_s}{2\rho_u^2 + \rho_s^2} \right) \quad (7.8.12)$$

and

$$2g_v \leq \tilde{g}_v^* < 3g_v. \quad (7.8.13)$$

We have added \tilde{g}_v^* as a function of μ and a shaded band depicting its bounds to Fig. 7.38. For small $\mu \equiv \mu_u = \mu_d = \mu_s$ the relative strength of the strange quark density-increasing coupling \tilde{g}_v^* with respect to the density-decreasing coupling $\tilde{g}_{v,s}$ is much lower than in the case of the complete interaction, where they are identical. At around 520 MeV the ratio $\tilde{g}_{v,s}/\tilde{g}_v^*$ becomes of the order of 1. This is where, with the reduced vector interaction, the onset of strangeness is indeed found in this scenario of $T = 10$ MeV and $g_v = 0.5G$.

We show the total baryon number density (Fig. 7.39) and the strange quark chiral condensate σ_s (Fig. 7.40) as functions of $\mu_{ud} \equiv \mu_u = \mu_d$ at $T = 10$ MeV and with a vector interaction strength of $g_v = 0.5G$ for both vector interaction forms. In both cases we plot the curves for $\mu_s = \mu_{ud}$ as well as for $\mu_s = 0$. As has been discussed, for $\mu_s = 0$, where $\rho_s = 0$ follows, the two interactions are identical so that their curves coincide exactly (orange line lying on top of the blue line). The delayed onset of strangeness for the reduced vector interaction follows from our foregoing discussion. However, the chiral light quark crossover is still unaffected. This means that that our main results from the reduced interaction are valid even when using the complete interaction.

It is important to keep in mind that the statements regarding the relative abundance of flavors and, accordingly, of the “effective couplings” to compare the two interaction types, are only valid for either $\mu_u = \mu_d$ and $\mu_s = 0$ or $\mu_s = \mu_u = \mu_d$. In the next section, we will make use of the complete vector interaction formalism and study the effects of independent flavor-specific chemical potentials μ_u , μ_d and μ_s . The reduced interaction is less suited for this task, as the shifting of all the chemical potentials by the same term obfuscates the effects.

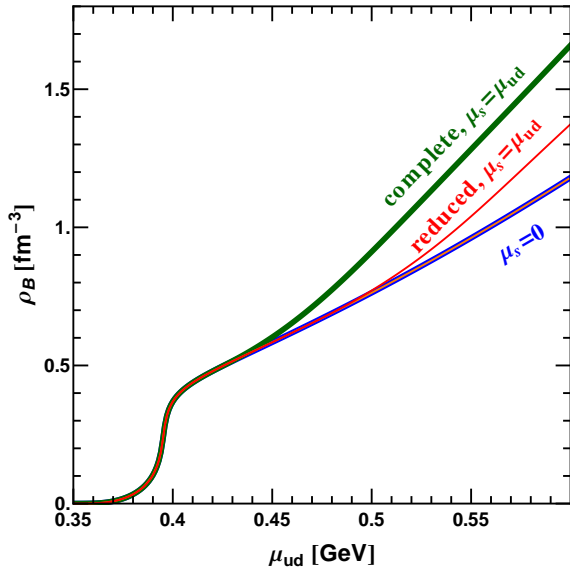


Fig. 7.39: Comparison of the total baryon number densities as a function of $\mu_{ud} \equiv \mu_u = \mu_d$ at $T = 10$ MeV and $g_v = 0.5G$ for $\mu_s = \mu_{ud}$ and $\mu_s = 0$, as well as for the reduced and the complete vector interaction in both cases.

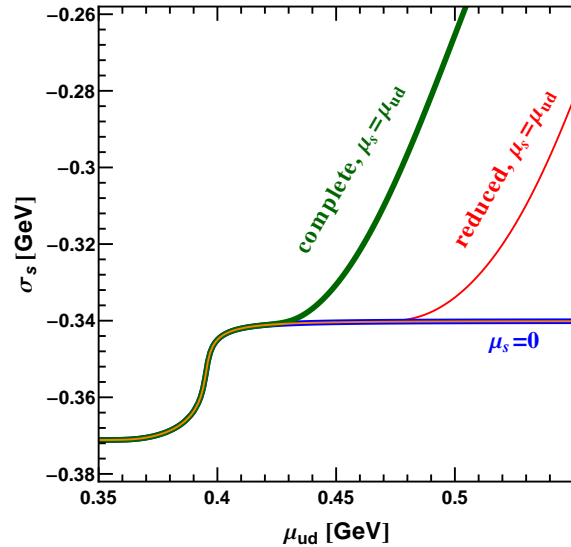


Fig. 7.40: Strange quark condensate σ_s in the same four scenarios as in Fig. 7.39. For vanishing strange quark chemical potential, σ_s does not die out.

7.8.2 Fixed density ratios

The matter mix that is usually studied in the three flavor QCD phase diagram with a single μ is neither symmetric in the three flavors, because of the differences in the current quark masses, nor is it purely composed of two flavors, see e. g. Fig. 7.37. By freeing the flavor chemical potentials from fixed ratios we can study different types of matter, for example pure neutron matter with $2\rho_u = \rho_d$ and $\rho_s = 0$ or actually flavor symmetric matter with $\rho_u = \rho_d = \rho_s$. In this section, we choose a different approach than before: instead of setting flavor-specific chemical potentials, we fix a relation between the three quark flavor *densities*. As a free parameter we use the down quark chemical potential μ_d , and by the fixed density ratio conditions we can then solve for μ_u and μ_s . We restrict ourselves to a few instructive studies with this setup, out of a large number of possible topics which we leave for future work.

So far in this chapter, we have stressed that the chiral light quark transition was unaffected by the different scenarios, i. e. $\mu_s = 0$ or $\mu_s = \mu_u = \mu_d$ and the usage of the reduced or the complete vector interaction. The reasons for this, discussed in the foregoing, boil down to the different strange quark mass and the resulting suppression of strangeness. Allowing independent variation of the flavor-chemical potentials changes the situation drastically: if $\mu_s \gtrsim \mu_u$, then ρ_s/ρ_u can become of the order of 1 or even larger.

In Fig. 7.41a and Fig. 7.41b we investigate the transition behavior of the light quark chiral condensate for different flavor density ratios. On the vertical axis is the strange quark fraction $\rho_s/(\rho_u + \rho_d + \rho_s)$. The horizontal axis shows the fraction of ρ_u/ρ_d . It can be easily converted into the often used asymmetry parameter δ by

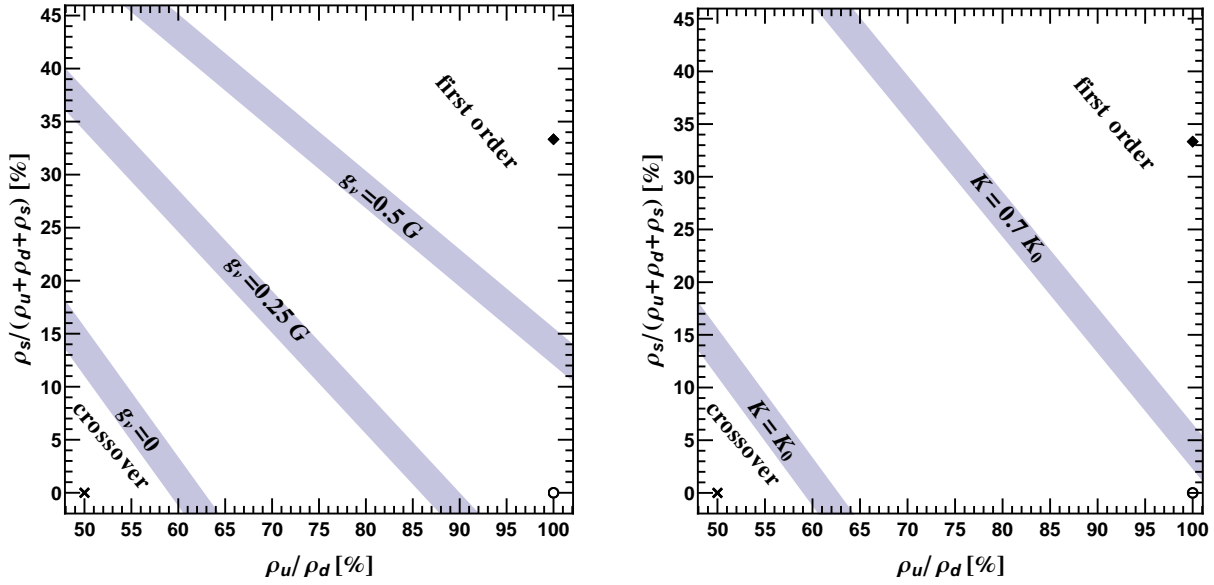
$$\delta = \frac{\rho_u - \rho_d}{\rho_u + \rho_d} = \frac{\rho_u/\rho_d - 1}{\rho_u/\rho_d + 1}. \quad (7.8.14)$$

On this plane, three distinct points are pointed out: a cross marks pure neutron matter with $\rho_s = 0$ and $\rho_d = 2\rho_u$. A diamond signifies totally flavor symmetric matter $\rho_u = \rho_d = \rho_s$. The empty circle marks symmetric nuclear matter with $\rho_u = \rho_d$ and $\rho_s = 0$. In the two plots, we draw, for different parameter choices, a boundary band between two areas: On the one hand, the area where the chiral light quark transition is first-order, starting from the top right corner. On the other hand, there is the area where the transition is a crossover, starting from the lower left corner. Within the bands the transitions are second order or very close to it from either side. In Fig. 7.41a, we vary g_v and depict how the boundary band moves from the lower left ($g_v = 0$) to the middle ($g_v = 0.25G$) and finally to the right ($g_v = 0.5G$). In Fig. 7.41b we do the same thing but instead of g_v we decrease the Kobayashi–Maskawa–’t Hooft interaction strength K from $K = K_0$ (lower left) to $K = 0.7K_0$ (top right).

There are a few interesting observations from the two figures:

1. Pure neutron matter will have a chiral crossover for all repulsive vector interactions and $K \leq K_0$. In [46] it was shown that pure neutron matter also undergoes a crossover from a gas to a liquid, as opposed to the first-order transition of symmetric nuclear matter. The phase diagram of pure neutron matter is then completely free of first-order transitions.
2. The explicit inclusion of strangeness in the system has an effect similar to the increasing of g_v or the decreasing of K . That it, for a given ratio of ρ_u/ρ_d , model builders can turn the transition into a crossover by a) increasing g_v , by b) decreasing K , or by c) adding some net strangeness to the system.

To explain this latter fact, we start with pure nuclear matter, symmetric or asymmetric. Remember that the increase in strange density and the strong decrease of the strange quark chiral condensate σ_s always coincide (see e. g. Figs. 7.39 and 7.40). Small values of ρ_s then in turn



(a) Left band marks the boundary between crossover and first-order transitions for $g_v = 0$. The middle band is the boundary for $g_v = 0.25 G$ and the right band for $g_v = 0.5 G$.

(b) Left band marks the boundary between crossover and first-order transitions for $K = K_0$. The right band is the boundary for $K = 0.7 K_0$.

Fig. 7.41: Transition type of the chiral light quark transition as a function of the strange quark fraction of the total density (vertical axis) and of the up-to-down quark ratio (horizontal axis) at $T = 10$ MeV. To the lower left of the bands is a crossover, to the upper right of the respective band the transition is first-order. A cross marks pure neutron, and a diamond totally flavor symmetric, and an empty circle symmetric nuclear matter. The left band marks the boundary between crossover and first-order transitions for $g_v = 0$.

mean large values of σ_s . The flavor mixing KMT interaction introduces an additional term to the effective mass of the light quark flavors,

$$M_u = m_u - \sigma_u + \frac{K}{2G^2} \sigma_d \sigma_s \quad \text{and} \quad M_d = m_d - \sigma_d + \frac{K}{2G^2} \sigma_s \sigma_u. \quad (7.8.15)$$

In the parameter sets we collected in section 3.4, $\frac{K}{2G^2}$ ranges between 0.45 GeV^{-1} (LKW) and 0.76 GeV^{-1} (RKH) with the HK value in between at 0.55 GeV^{-1} . For low μ_s , ρ_s is around -0.37 GeV and ρ_u and ρ_d range between 0 and about -0.3 GeV . In effect, then, the strange quark condensate contributes a term of around 30 MeV to the effective light quark mass, compared to the bare quark mass of the order of 5 MeV of the light flavors. An increased effective quark mass acts towards the reduction of the first-order transition line (see section 5.3). This is why the bands in Fig. 7.39 and Fig. 7.40 are oriented in such a way that scenarios with little net strangeness tend towards crossovers. Increasing net strangeness is equivalent to decreasing σ_s so that the system tends more towards a first-order transition.

It is important to remember these relations when one tries to use two flavor models to predict actual physical systems: in nature, the strange quark degree of freedom is always available. As a specific example, it is found that in a nonlocal two flavor model the value of g_v necessary to remove the first-order transition from the phase diagram completely is considerably higher than for three flavors [66]. Apart from other differences, this might be attributed to the fact that in the two flavor system there is no strong background strange quark condensate that contributes in smearing out the transition.

7.9 Summary

In this chapter we have investigated two types of vector interactions added to the PNJL Lagrangian: the “reduced” version (7.1.2) that is commonly used in the literature, and the “complete” version (7.8.1) that is closer to physical reality. An analysis in section 7.8.1 has shown that for most fields of interest, the two yield identical results. This changes drastically if systems with large net strangeness are studied (see section 7.8.2).

For the more common scenario with low ρ_s , we have found three main results:

First, the “RKH” parameter set from [110] that we have used through most of this work was seen to be not ideal for studies including the important vector interaction. More advisable is the usage of the “HK” parameter set from [63] or the “LKW” set from [92], which are largely compatible with one another, see discussion in section 7.4.

The second finding, in section 7.7, is that lattice QCD results for the curvature κ of the chiral crossover are well reproduced by a large vector coupling strength of $g_v \sim G$. This result, together with the observation that the first-order chiral coexistence region always overlaps with the nuclear matter coexistence region, points towards a large value of g_v in a realistic scenario.

Thirdly, in section 7.5.4, we have shown it to be very unlikely that there is a critical point in the QCD phase diagram. Reasonable values of g_v from a wide range of different approaches (see section 7.1), including our own determination of $g_v \sim G$ from the chiral crossover curvature κ , as well as the notion of a KMT strength probably reduced in-medium (section 5.2), put the “physical point” of the g_v - K plane in Fig. 7.28 far into the crossover region.

Chapter 8

Summary and outlook

8.1 Summary

In this thesis, we studied features of the QCD phase diagram using the Polyakov–Nambu–Jona-Lasinio (PNJL) model. This model is nonrenormalizable; as a consequence, a cutoff has to be applied in the thermodynamic potential. We implemented a physically consistent cutoff scheme in the scenario with $2 + 1$ flavors: for momenta larger than the cutoff scale Λ , the quarks propagate interaction-free in a background set by the Polyakov loop. The predominantly used “minimal” cutoff scheme was shown to be unphysical and the mechanism behind the inconsistencies explained. We demonstrated that the QCD phase diagram resulting from PNJL type models is strongly influenced by the choice of the cutoff scheme, even in a two-flavor scenario. Especially the degree of entanglement between chiral and Polyakov loop crossover was seen to be sensitive to it, which sheds new light on arguments based on this effect at finite μ .

Most of our results with this “soft” cutoff, e. g. for thermodynamic quantities or the “flavor-combined” chiral condensate Δ_{ls} (see def. (4.5.2)), as functions of T/T_c , agree very well with lattice QCD results. Where a discrepancy due to the recent calculation of better lattice QCD results was noted, e. g. regarding the slope of the Polyakov loop transition, we have investigated the systematics and pointed out how improvements could be made within the model.

A major focus was the Kobayashi-Maskawa-’t Hooft (KMT) coupling strength K that controls the axial $U(1)$ anomaly in the model. We explored its effect on the model for a large number of quantities such as the location of the critical point, the bending of the critical surface in the μ - m_u - m_s Columbia plot and the curvature of the chiral crossover line.

We then explored in considerable detail the effects of the inclusion of vector-type interactions in the model. Two different forms were used; a simple “reduced” ansatz that is found most commonly in the literature, and a more complete form with a complex flavor structure. We discussed differences between the two approaches and showed that for the purpose they are usually employed for, both are essentially equivalent. An important condition for this was the use of the same chemical potential for all quark flavors.

Finally, we used the quark flavor densities ρ_u , ρ_d and ρ_s independently as variables instead of the flavor-specific chemical potentials in order to discuss phase transitions at low T for different types of matter, e. g. pure neutron or symmetric nuclear matter.

8.2 Discussion

We have studied a large number of effects and hypotheses in this work, but we would like to emphasize again two primary results.

First, in chapter 5 we showed that the continuation of the $\mu = 0$ Columbia plot to finite chemical potentials is highly non-trivial. The strength K of the axial anomaly plays a crucial role, and the differences between scenarios with different K manifest themselves only for intermediate

values of $\mu \gtrsim 150$ MeV. This suggests that the curvature of the critical surface of Columbia plots, calculated with lattice QCD, might not be as useful a tool in the determination of the existence of a critical point as was expected: the observed structure at intermediate μ cannot be fully specified in terms of the curvature alone.

The second main result concerns the existence of the critical point. For a long time, it were chiral models like the (P)NJL model that predicted a first-order transition in the QCD phase diagram at low T , while lattice QCD calculations showed crossovers for $\mu/T \lesssim 1$. Recently, however, it has become increasingly doubtful if the existence of a first-order transition is compatible with all facts that are already known. We contribute arguments pointing strongly towards a phase diagram with a crossover for all T and μ .

Since we feel that this is the most important point of this work, we briefly recapitulate the line of thought. It is well known that in the T - ρ_B rendition of the phase diagram, the chiral coexistence “bell” appears as long as there is a first-order chiral transition present. The region of low T and $\rho_B \lesssim \rho_0 = 0.16 \text{ fm}^{-3}$, the empirically confirmed domain of nuclear matter, has been probed for decades in countless experiments with no indication of restored chiral symmetry effects. Therefore the separation of these two domains, described by different degrees of freedom, is a strong constraint on models. We systematically studied the location and width of the chiral coexistence region as functions of the KMT interaction strength K and the vector coupling strength g_v . It was found that the coexistence region, as long as it exists, is not clearly separated from the liquid/gas coexistence region of nuclear matter for any combination of these parameters. For two out of three studied NJL input parameter sets, the chiral coexistence “bell” always directly overlapped the density region dominated by nuclear dynamics – contrary to our empirical knowledge.

This observation was complemented by discussions of probable values for g_v and in-medium values of K (sections 5.2 and 7.1) based on a large number of independent sources. According to the current state of research, likely combinations of the values of K and g_v are far from those that produce a critical point in the phase diagram.

Our own determination of g_v is based on a fit of the chiral transition curvature κ (cf. section 5.5). A large value of $g_v \sim G$ was found to reproduce the small curvature found in lattice publications. This number is perfectly compatible with the results of the other sources. For a g_v of this magnitude, the existence of a critical point is almost impossible, regardless of other parameter choices.

8.3 Outlook

Throughout this work, the Kobayashi-Maskawa-’t Hooft interaction strength K and the strength g_v of the vector interaction played a prominent role. For K , at the moment only the vacuum value is known but not its dependence on temperature T and chemical potential μ which is expected to be considerable (see our discussion in section 5.2). A recent work based on instanton dynamics [37] suggests an expression for the instanton density and therefore K as a function of 4-momentum p as well as T and μ . It appears promising to start including such an ansatz in our framework.

In chapter 7, we discussed the vector interaction term in eq.(7.1.1) and used it in our calculations, while the axial-vector term was omitted. It is a logical next step to include this term in the model, especially since it could appear with a weight comparable to the vector term, see eqs.(7.1.4) and (7.1.5). Given the indications pointing towards a large value of g_v/G that we found, the influence of this term may be considerable. This is particularly interesting in the context of recent speculation about the formation of inhomogeneous chiral symmetry breaking phases [28] which might be suppressed by a repulsive axial-vector interaction.

We also mentioned that in the limit of very large chemical potentials, the ground state of QCD is given by color superconducting matter. Numerous studies with (P)NJL type models suggest

that some diquark condensate types form already close to the $T = 0$ termination point μ_t of the chiral transition line. It has also been shown that certain interaction forms including diquark degrees of freedom in the usual NJL Lagrangian can induce the appearance of a second critical point, realizing quark-hadron continuity at very low T . The study of vector type interactions in combination with that sort of ansatz is a natural extension of our discussion about the improbable existence of a critical point in the QCD phase diagram. An investigation of how our consistent cutoff scheme influences the found patterns – and the diquark phase structure in general – also promises to be a rewarding topic.

Finally, the extremely precise measurement [41] of the two-solar mass neutron star PSR-J1614-2230 has given new, strong constraints on the equation of state of neutron stars [64, 89, 88, 137], i. e. matter at low temperature and moderate density. This fact can be used to further limit the parameter space of our model, allowing for an ever more precise prediction of the structure of the QCD phase diagram [93, 66]. The elusive critical point is not yet completely ruled out – but its chances are dwindling.

Appendix A

Appendix

A.1 Intermediate calculations in the bosonization procedure

In this part of the appendix we derive some of the more technical relations used in section 3.3, where we discussed the three-flavor NJL bosonization formalism.

A.1.1 The Transformation of $\det J_{\pm}$

First, in this section we will prove that $\det J_{\pm}$ can be recast into eq. (3.3.5),

$$\det J_{\pm} = \left(\sqrt{\frac{2}{3}} \right)^3 (c_0^{\pm})^3 - \sqrt{\frac{2}{3}} \sum_{m=1}^8 c_0^{\pm} (c_m^{\pm})^2 + \frac{2}{3} \sum_{l,m,n=1}^8 d^{lmn} c_l^{\pm} c_m^{\pm} c_n^{\pm}. \quad (\text{A.1.1})$$

This is done using two auxiliary formulae: The formula already presented in eq. (3.3.4),

$$\det A = \frac{1}{6} (\text{tr}[A])^3 - \frac{1}{2} \text{tr}[A] \text{tr}[A^2] + \frac{1}{3} \text{tr}[A^3], \quad (\text{A.1.2})$$

is proven either explicitly or by the Newton-Girard formulae, which give relations between power sums (in this case, the traces of powers of the matrix A) and elementary symmetric polynomials (here the determinant of the matrix).

The second auxiliary formula is eq. (3.3.3),

$$c_a = \frac{1}{2} \text{tr}(\lambda^a J_{\pm}).$$

We go through the terms of eq. (A.1.2) with $A = J_{\pm}$ step by step:

$$\text{tr}[J_{\pm}] = \text{tr} \left[\sum_{a=0}^8 \lambda^a c_a^{\pm} \right] = \sum_{a=0}^8 c_a^{\pm} \text{tr}[\lambda^a] = c_0^{\pm} \text{tr}[\lambda^0] = \sqrt{6} c_0^{\pm}, \quad (\text{A.1.3})$$

because $\text{tr}[\lambda^m] = 0$, $m = 1, \dots, 8$ and by definition $\text{tr}[\lambda^0] = \sqrt{6}$. Similarly, with

$$\text{tr}[\lambda^a \lambda^b] = 2\delta_{ab}, \quad (\text{A.1.4})$$

we get

$$\text{tr}[J_{\pm}^2] = \text{tr} \left[\sum_{a,b=0}^8 \lambda^a c_a^{\pm} \lambda^b c_b^{\pm} \right] = \sum_{a,b=0}^8 c_a^{\pm} c_b^{\pm} \text{tr}[\lambda^a \lambda^b] = 2 \sum_{a=0}^8 (c_a^{\pm})^2. \quad (\text{A.1.5})$$

Finally, with careful counting of multiplicities of the terms and using the trace relations,

$$\begin{aligned}
\frac{1}{3}\text{tr}[J_{\pm}^3] &= \frac{1}{3} \sum_{a,b,d=0}^8 \text{tr}[\lambda^a \lambda^b \lambda^d] c_a^{\pm} c_b^{\pm} c_d^{\pm} \\
&= \frac{1}{3} \text{tr}[(\lambda^0)^3] (c_0^{\pm})^3 + 3 \cdot \frac{1}{3} \sum_{l,m=1}^8 \text{tr}[\lambda^0 \lambda^l \lambda^m] c_0^{\pm} c_l^{\pm} c_m^{\pm} + \frac{1}{3} \sum_{l,m,n=1}^8 \text{tr}[\lambda^l \lambda^m \lambda^n] c_l^{\pm} c_m^{\pm} c_n^{\pm} \\
&= \frac{1}{3} \cdot \sqrt{\frac{2}{3}}^3 \cdot 3 (c_0^{\pm})^3 + 2 \cdot \sqrt{\frac{2}{3}} \sum_{m=1}^8 c_0^{\pm} (c_m^{\pm})^2 + \frac{1}{3} \sum_{l,m,n=1}^8 \text{tr}[\lambda^l \lambda^m \lambda^n] c_l^{\pm} c_m^{\pm} c_n^{\pm} = \\
&= \sqrt{\frac{2}{3}}^3 (c_0^{\pm})^3 - 2 \sqrt{\frac{2}{3}} \sum_{m=1}^8 c_0^{\pm} (c_m^{\pm})^2 + \frac{1}{3} \sum_{l,m,n=1}^8 \text{tr}[\lambda^l \lambda^m \lambda^n] c_l^{\pm} c_m^{\pm} c_n^{\pm}, \tag{A.1.6}
\end{aligned}$$

so that

$$\begin{aligned}
\det J_{\pm} &= \frac{1}{6} (\text{tr}[J_{\pm}])^3 - \frac{1}{2} \text{tr}[J_{\pm}] \text{tr}[J_{\pm}^2] + \frac{1}{3} \text{tr}[J_{\pm}^3] = \\
&= \sqrt{\frac{2}{3}}^3 (c_0^{\pm})^3 - \sqrt{\frac{2}{3}} \sum_{m=1}^8 c_0^{\pm} (c_m^{\pm})^2 + \frac{1}{3} \sum_{l,m,n=1}^8 \text{tr}[\lambda^l \lambda^m \lambda^n] c_l^{\pm} c_m^{\pm} c_n^{\pm}. \tag{A.1.7}
\end{aligned}$$

From SU(3) group theory it is known that

$$[\lambda^a, \lambda^b] = 2i \sum_c f^{abc} \lambda^c, \tag{A.1.8}$$

$$\{\lambda^a, \lambda^b\} = \frac{4}{3} \delta^{ab} \mathbf{1} + 2 \sum_c d^{abc} \lambda^c, \tag{A.1.9}$$

where $[\lambda^a, \lambda^b]$ is the commutator and $\{\lambda^a, \lambda^b\}$ is the anticommutator. The quantities d^{abc} (f^{abc}) are the totally symmetric (antisymmetric) structure constants of SU(3). With these relations, we express

$$\lambda^a \lambda^b = \frac{1}{2} [\lambda^a, \lambda^b] + \frac{1}{2} \{\lambda^a, \lambda^b\} = i \sum_c f^{abc} \lambda^c + \frac{2}{3} \delta^{ab} \mathbf{1} + \sum_c d^{abc} \lambda^c. \tag{A.1.10}$$

Now we write a trace over three Gell-Mann matrices λ^a , $a = 1, \dots, 8$ as

$$\begin{aligned}
\text{tr}[\lambda^a \lambda^b \lambda^d] &= i \sum_c f^{abc} \text{tr}[\lambda^c \lambda^d] + \sum_c d^{abc} \text{tr}[\lambda^c \lambda^d] + \frac{2}{3} \text{tr}[\lambda^c] \delta^{ab} \\
&= 2i \sum_c f^{abc} \delta^{cd} + 2 \sum_c d^{abc} \delta^{cd} \\
&= 2i f^{abd} + 2 d^{abd}. \tag{A.1.11}
\end{aligned}$$

In the last term in eq. (A.1.7), we sum over all indices a, b, c . Since f^{abc} is totally antisymmetric, this term in (A.1.11) cancels out and only the totally symmetric term with the d^{abd} remains. In conclusion, inserting eq. (A.1.11) into eq. (A.1.7), we get

$$\det J_{\pm} = \sqrt{\frac{2}{3}}^3 (c_0^{\pm})^3 - \sqrt{\frac{2}{3}} \sum_{m=1}^8 c_0^{\pm} (c_m^{\pm})^2 + \frac{2}{3} \sum_{l,m,n=1}^8 d^{lmn} c_l^{\pm} c_m^{\pm} c_n^{\pm}. \tag{A.1.12}$$

A.1.2 Symmetry properties of products of Gell-Mann matrices

Eq. (3.3.29) in section 3.3 contained the expression $v_l v_m v_n d^{lmn}$, where the d^{lmn} are defined by equation (A.1.9) and the v_a by the relation (3.3.24). We stated there that we can write

$$v_l v_m v_n d^{lmn} \equiv d^{lmn} \quad (\text{A.1.13})$$

We will prove this relation in this short section. First, we take an arbitrary symmetric Gell-Mann matrix λ^S , i. e. $S \in \{1, 3, 4, 6, 8\}$ and another arbitrary, but antisymmetric, Gell-Mann matrix λ^A , i. e. $A \in \{2, 5, 7\}$. In component notation, for their anticommutator we find

$$\{\lambda^A, \lambda^S\}_{ik} = \sum_j (\lambda_{ij}^S \lambda_{jk}^A + \lambda_{ij}^A \lambda_{jk}^S) = \sum_j (\lambda_{ji}^S (-\lambda_{kj}^A) + (-\lambda_{ji}^A) (\lambda_{kj}^S)) = - \sum_j (\lambda_{kj}^A \lambda_{ji}^S + \lambda_{kj}^S \lambda_{ji}^A) \quad (\text{A.1.14})$$

which means that the anticommutator is antisymmetric:

$$\{\lambda^A, \lambda^S\} = - \{\lambda^A, \lambda^S\}^\top. \quad (\text{A.1.15})$$

Using eq. (A.1.9) and $\delta^{AS} \equiv 0$, we express it now as a sum over all Gell-Mann matrices λ^c with some coefficients,

$$\{\lambda^A, \lambda^S\} = 2 \sum_{A' \text{ asym.}} d^{ASA'} \lambda^{A'} + 2 \sum_{S' \text{ sym.}} d^{ASS'} \lambda^{S'}, \quad (\text{A.1.16})$$

where we have divided the whole set of Gell-Mann matrices again into symmetric and antisymmetric ones. Since the anticommutator on the left-hand side of this equation is an antisymmetric quantity, it cannot be composed of any symmetric Gell-Mann matrices. Therefore the second term on the right-hand side has to vanish:

$$d^{ASS'} \equiv 0 \quad (\text{A.1.17})$$

with $A' \in \{2, 5, 7\}$ and $S, S' \in \{1, 3, 4, 6, 8\}$. Next, because the d^{lmn} are totally symmetric, eq. (A.1.17) means that *every* d^{lmn} where exactly one index (l, m or n) corresponds to an antisymmetric matrix must vanish. The same reasoning can be applied to a combination of three antisymmetric matrices. We find that $\{\lambda^A, \lambda^{A'}\}$ with $A, A' \in \{2, 5, 7\}$ is symmetric and therefore, in a split-up like in eq. (A.1.16),

$$\{\lambda^A, \lambda^{A'}\} = 2 \sum_{A'' \text{ asym.}} d^{AA'A''} \lambda^{A''} + 2 \sum_{S \text{ sym.}} d^{AA'S} \lambda^S, \quad (\text{A.1.18})$$

the first term has to vanish. It follows that

$$d^{AA'A''} \equiv 0, \quad (\text{A.1.19})$$

for $A, A', A'' \in \{2, 5, 7\}$. We have then found that $d^{lmn} \equiv 0$ if *one* or *three* of the indices $l, m, n \in \{2, 5, 7\}$. Coming back to the definition of the v_a in eq. (3.3.24), it is evident that the expression $v_l v_m v_n$ can only take the value of -1 in exactly the same two cases. In all other cases, it is simply 1. In conclusion, we find that

$$v_l v_m v_n d^{lmn} \equiv d^{lmn} \quad (\text{A.1.20})$$

which was what we wanted to show.

a	b	c	$3\sqrt{3}A^{abc}$
0	0	0	$2\sqrt{2}$
0	8	8	$-\sqrt{2}$
8	8	8	-2
0	1	1	$-\sqrt{2}$
0	2	2	$-\sqrt{2}$
0	3	3	$-\sqrt{2}$
8	i	j	$2\delta_{ij}$

Table A.1: Non-vanishing entries of the $9 \times 9 \times 9$ matrix A^{abc} , $a, b, c = 0 \dots 8$, in def. (3.3.31).

A.2 Influence of parameters on the crossover bands

We collect here plots that show the dependence of location and width of the crossover bands at $\mu = 0$ as functions of the parameters of Polyakov loop effective potentials, as discussed in chapter 6. In the main text, we omitted them to keep the focus on more important points. However, a systematic collection is useful for comparing different Polyakov loop effective potentials.

The style of the plots is the same as in Fig. 6.16. In all cases, the upper, red band is the chiral crossover band, where the three lines mark $\sigma_u(T)/\sigma_u(0) = 0.25, 0.5$ and 0.75 from top to bottom. The lower, blue band marks the Polyakov loop crossover, with the three lines denoting $\Phi = 0.2, \Phi = 0.35$ and $\Phi = 0.5$, respectively.

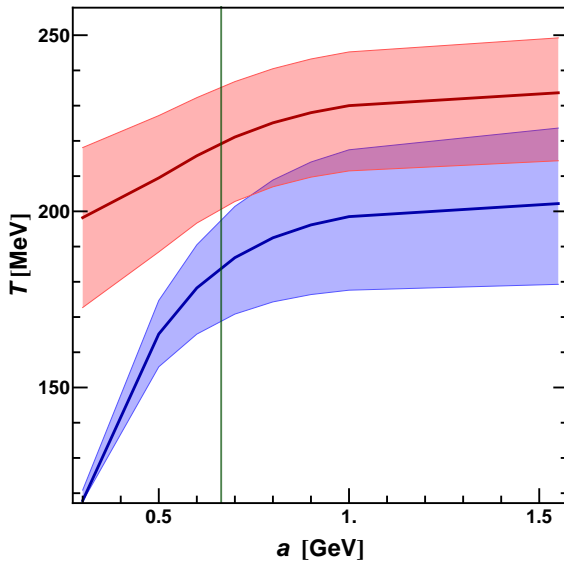


Fig. A.1: Transition bands as a function of a in potential ansatz (6.2.1). The vertical line denotes $a_0 = 664$ MeV as the choice of [52].

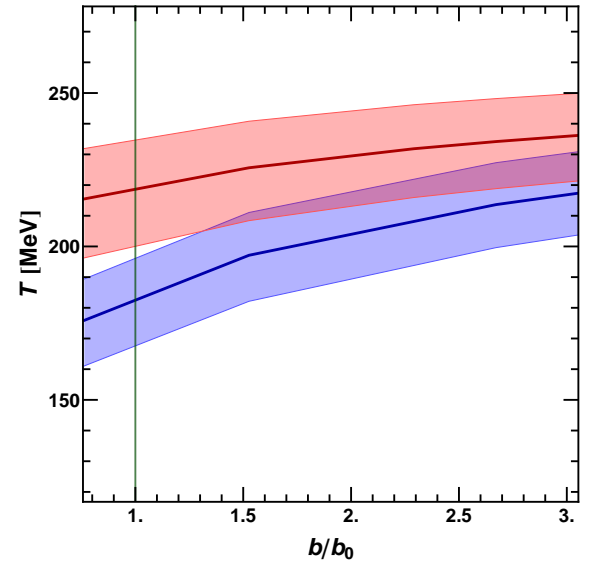


Fig. A.2: Transition bands as a function of b/b_0 in potential ansatz (6.2.1). The vertical line marks b_0 .

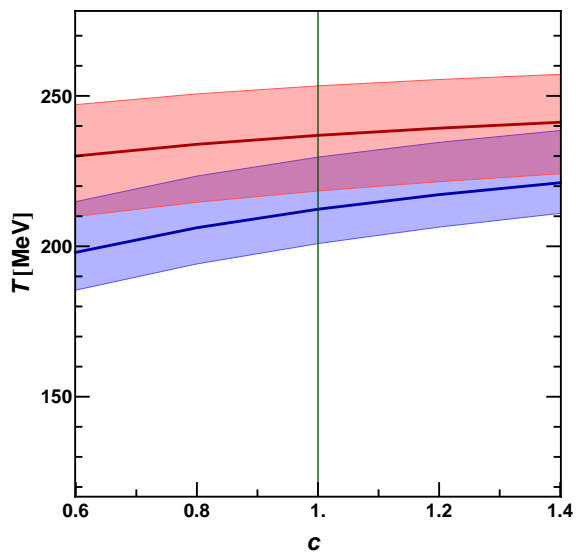


Fig. A.3: Transition bands as a function of c in (6.3.4).

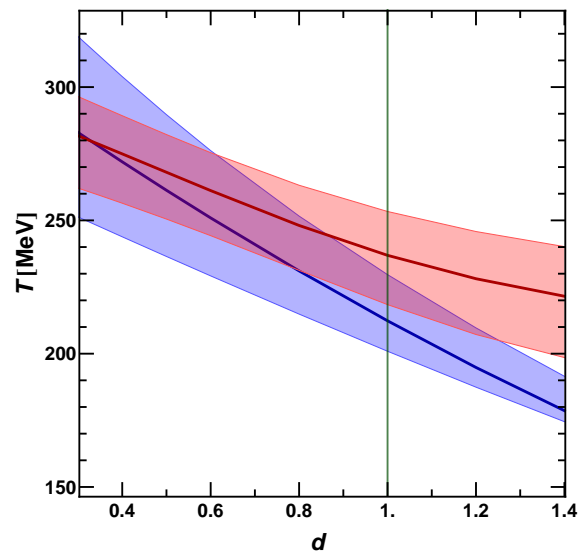


Fig. A.4: Transition bands as a function of d in (6.3.4).

Bibliography

- [1] S. L. Adler. Axial vector vertex in spinor electrodynamics. *Phys. Rev.*, 177:2426–2438, 1969.
- [2] M. Aggarwal et al. An experimental exploration of the QCD phase diagram: the search for the critical point and the onset of de-confinement. 2010.
- [3] M. G. Alford. Color superconductivity in ultra-dense quark matter. *PoS*, LAT2006:001, 2006.
- [4] M. G. Alford, K. Rajagopal, and F. Wilczek. Color flavor locking and chiral symmetry breaking in high density QCD. *Nucl.Phys.*, B537:443–458, 1999.
- [5] R. Alkofer and L. von Smekal. The infrared behavior of QCD Green’s functions: confinement, dynamical symmetry breaking, and hadrons as relativistic bound states. *Phys.Rept.*, 353:281, 2001.
- [6] A. Andronic, P. Braun-Munzinger, and J. Stachel. Thermal hadron production in relativistic nuclear collisions: the hadron mass spectrum, the horn, and the QCD phase transition. *Phys.Lett.*, B673:142–145, 2009.
- [7] M. Asakawa and K. Yazaki. Chiral restoration at finite density and temperature. *Nucl. Phys.*, A504:668–684, 1989.
- [8] J. Bardeen, L. N. Cooper, and J. R. Schrieffer. Microscopic theory of superconductivity. *Phys. Rev.*, 101:162–164, 1957.
- [9] A. Bazavov. Chiral transition temperature and aspects of deconfinement in 2+1 flavor QCD with the HISQ/tree action. *PoS*, LATTICE2011:182, 2011.
- [10] A. Bazavov, T. Bhattacharya, M. Cheng, C. DeTar, H. Ding, et al. The chiral and deconfinement aspects of the QCD transition. *Phys.Rev.*, D85:054503, 2012.
- [11] A. Bazavov et al. The chiral transition and $U(1)_A$ symmetry restoration from lattice QCD using domain wall fermions. 2012.
- [12] A. Bazavov and P. Petreczky. Taste symmetry and QCD thermodynamics with improved staggered fermions. *PoS*, LATTICE2010:169, 2010.
- [13] A. Bazavov and P. Petreczky. Study of chiral and deconfinement transition in lattice QCD with improved staggered actions. *J.Phys.G*, G38:124099, 2011.
- [14] F. Becattini, J. Manninen, and M. Gazdzicki. Energy and system size dependence of chemical freeze-out in relativistic nuclear collisions. *Phys.Rev.*, C73:044905, 2006.
- [15] J. S. Bell and R. Jackiw. A PCAC puzzle: $\pi^0 \rightarrow \gamma\gamma$ in the σ model. *Nuovo Cim.*, A60:47–61, 1969.

- [16] J. Beringer et al. Review of Particle Physics (RPP). *Phys.Rev.*, D86:010001, 2012.
- [17] S. Borsanyi, Y. Delgado, S. Durr, Z. Fodor, S. D. Katz, et al. QCD thermodynamics with dynamical overlap fermions. *Phys.Lett.*, B713:342–346, 2012.
- [18] S. Borsanyi, G. Endrodi, Z. Fodor, A. Jakovac, S. D. Katz, et al. The QCD equation of state with dynamical quarks. *JHEP*, 1011:077, 2010.
- [19] S. Borsanyi et al. Is there still any T_c mystery in lattice QCD? Results with physical masses in the continuum limit III. *JHEP*, 1009:073, 2010.
- [20] G. Boyd et al. Thermodynamics of SU(3) lattice gauge theory. *Nucl. Phys.*, B469:419–444, 1996.
- [21] N. Bratovic. Studies in a three-flavor PNJL model (Diploma Thesis). 2008.
- [22] N. M. Bratovic, T. Hatsuda, and W. Weise. Role of vector interaction and axial anomaly in the PNJL modeling of the QCD phase diagram. 2012.
- [23] J. Braun, H. Gies, and J. M. Pawłowski. Quark confinement from color confinement. *Phys.Lett.*, B684:262–267, 2010.
- [24] R. Brockmann, W. Weise, and E. Werner. Chiral symmetry breaking, confining potentials and the Goldstone pion. *Phys.Lett.*, B122:201–206, 1983.
- [25] F. R. Brown, F. P. Butler, H. Chen, N. H. Christ, Z.-h. Dong, et al. On the existence of a phase transition for QCD with three light quarks. *Phys.Rev.Lett.*, 65:2491–2494, 1990.
- [26] M. Buballa. NJL model analysis of quark matter at large density. *Phys.Rept.*, 407:205–376, 2005.
- [27] N. Cabibbo and G. Parisi. Exponential hadronic spectrum and quark liberation. *Phys.Lett.*, B59:67–69, 1975.
- [28] S. Carignano, D. Nickel, and M. Buballa. Influence of vector interaction and Polyakov loop dynamics on inhomogeneous chiral symmetry breaking phases. *Phys.Rev.*, D82:054009, 2010.
- [29] A. Casher. Chiral symmetry breaking in quark confining theories. *Phys. Lett.*, B83:395, 1979.
- [30] J.-W. Chen, K. Fukushima, H. Kohyama, K. Ohnishi, and U. Raha. $U_A(1)$ anomaly in hot and dense QCD and the critical surface. *Phys.Rev.*, D80:054012, 2009.
- [31] M. Cheng, N. H. Christ, M. Li, R. D. Mawhinney, D. Renfrew, et al. The finite temperature QCD using 2 + 1 flavors of domain wall fermions at $N_t = 8$. *Phys.Rev.*, D81:054510, 2010.
- [32] M. Cheng, S. Ejiri, P. Hegde, F. Karsch, O. Kaczmarek, et al. Equation of state for physical quark masses. *Phys.Rev.*, D81:054504, 2010.
- [33] M. Cheng et al. The QCD equation of state with almost physical quark masses. *Phys. Rev.*, D77:014511, 2008.
- [34] M. Cheng, P. Hengde, C. Jung, F. Karsch, O. Kaczmarek, et al. Baryon number, strangeness and electric charge fluctuations in QCD at high temperature. *Phys.Rev.*, D79:074505, 2009.
- [35] J. Cleymans, H. Oeschler, K. Redlich, and S. Wheaton. Comparison of chemical freeze-out criteria in heavy-ion collisions. *Phys. Rev.*, C73:034905, 2006.

- [36] G. Cossu, S. Aoki, S. Hashimoto, T. Kaneko, H. Matsufuru, et al. Topological susceptibility and axial symmetry at finite temperature. *PoS, LATTICE2011*:188, 2011.
- [37] M. Cristoforetti. Instanton fermionic zero mode at finite temperature and chemical potential. *Phys.Rev.*, D84:114016, 2011.
- [38] T. Csorgo, R. Vertesi, and J. Sziklai. Indirect observation of an in-medium η' mass reduction in $\sqrt{s_{NN}} = 200$ GeV Au+Au collisions. *Phys.Rev.Lett.*, 105:182301, 2010.
- [39] P. de Forcrand and O. Philipsen. The chiral critical line of $N_f = 2 + 1$ QCD at zero and non-zero baryon density. *JHEP*, 0701:077, 2007.
- [40] P. de Forcrand and O. Philipsen. Constraining the QCD phase diagram by tricritical lines at imaginary chemical potential. *Phys.Rev.Lett.*, 105:152001, 2010.
- [41] P. Demorest, T. Pennucci, S. Ransom, M. Roberts, and J. Hessels. Shapiro delay measurement of a two solar mass neutron star. *Nature*, 467:1081–1083, 2010.
- [42] G. Endrodi, Z. Fodor, S. Katz, and K. Szabo. The nature of the finite temperature QCD transition as a function of the quark masses. *PoS, LAT2007*:182, 2007.
- [43] G. Endrodi, Z. Fodor, S. Katz, and K. Szabo. The QCD phase diagram at nonzero quark density. *JHEP*, 1104:001, 2011.
- [44] L. Ferroni and V. Koch. Mean field approach to flavor susceptibilities with a vector interaction. *Phys.Rev.*, C83:045205, 2011.
- [45] S. Fiorilla, N. Kaiser, and W. Weise. Chiral nuclear thermodynamics. *Prog.Part.Nucl.Phys.*, 67:317–321, 2012.
- [46] S. Fiorilla, N. Kaiser, and W. Weise. Chiral thermodynamics of nuclear matter. *Nucl.Phys.*, A880:65–87, 2012.
- [47] C. S. Fischer. Infrared properties of QCD from Dyson-Schwinger equations. *J.Phys.*, G32:R253–R291, 2006.
- [48] S. Floerchinger and C. Wetterich. Chemical freeze-out in heavy ion collisions at large baryon densities. *Nucl. Phys. A 890-891*, 11, 2012.
- [49] H. Fujii and T. Sano. A chiral random matrix model with 2+1 flavors at finite temperature and density. *Phys. Rev.*, D81:037502, 2010.
- [50] K. Fukushima. Chiral effective model with the Polyakov loop. *Phys.Lett.*, B591:277–284, 2004.
- [51] K. Fukushima. Critical surface in hot and dense QCD with the vector interaction. *Phys.Rev.*, D78:114019, 2008.
- [52] K. Fukushima. Phase diagrams in the three-flavor Nambu-Jona-Lasinio model with the Polyakov loop. *Phys.Rev.*, D77:114028, 2008.
- [53] K. Fukushima. Phase diagram of hot and dense QCD constrained by the Statistical Model. *Phys.Lett.*, B695:387–391, 2011.
- [54] K. Fukushima and T. Hatsuda. The phase diagram of dense QCD. *Rept.Prog.Phys.*, 74:014001, 2011.
- [55] K. Fukushima and K. Kashiwa. Polyakov loop and QCD thermodynamics from the gluon and ghost propagators. 2012.

- [56] M. Gell-Mann, R. Oakes, and B. Renner. Behavior of current divergences under $SU_3 \times SU(3)$. *Phys.Rev.*, 175:2195–2199, 1968.
- [57] D. Gomez Dumm, A. Grunfeld, and N. Scoccola. Phase diagram of quark matter in nonlocal chiral models under color and electric charge neutrality conditions. *Braz.J.Phys.*, 37:526–531, 2007.
- [58] L. P. Gor’kov. On the energy spectrum of superconductors. *Sov. Phys. JETP*, 7:505–508, 1958.
- [59] D. Gross and F. Wilczek. Asymptotically free gauge theories. 1. *Phys.Rev.*, D8:3633–3652, 1973.
- [60] D. Gross and F. Wilczek. Ultraviolet behavior of nonabelian gauge theories. *Phys.Rev.Lett.*, 30:1343–1346, 1973.
- [61] D. J. Gross, R. D. Pisarski, and L. G. Yaffe. QCD and instantons at finite temperature. *Rev.Mod.Phys.*, 53:43, 1981.
- [62] R. Gupta. Introduction to lattice QCD: course. pages 83–219, 1997.
- [63] T. Hatsuda and T. Kunihiro. QCD phenomenology based on a chiral effective Lagrangian. *Phys. Rept.*, 247:221–367, 1994.
- [64] K. Hebeler, J. Lattimer, C. Pethick, and A. Schwenk. Constraints on neutron star radii based on chiral effective field theory interactions. *Phys.Rev.Lett.*, 105:161102, 2010.
- [65] T. Hell. *Modeling the thermodynamics of QCD*. Dissertation, Technische Universität München, München, 2010.
- [66] T. Hell, K. Kashiwa, and W. Weise. In preparation. 2012.
- [67] Hell, T. and Rößner, S. and Cristoforetti, M. and Weise, W. Thermodynamics of a three-flavor nonlocal Polyakov–Nambu–Jona-Lasinio model. *Phys. Rev.*, D81:074034, 2010.
- [68] Hell, T. and Rößner, Simon and Cristoforetti, M. and Weise, W. Dynamics and thermodynamics of a non-local PNJL model with running coupling. *Phys.Rev.*, D79:014022, 2009.
- [69] T. K. Herbst, J. M. Pawłowski, and B.-J. Schaefer. The phase structure of the Polyakov–quark-meson model beyond mean field. 2010.
- [70] J. Hubbard. Calculation of partition functions. *Phys. Rev. Lett.*, 3:77–78, 1959.
- [71] Y. Iwasaki, K. Kanaya, S. Kaya, S. Sakai, and T. Yoshie. QCD phase transition with strange quark in Wilson formalism for fermions. *Z.Phys.*, C71:343–346, 1996.
- [72] O. Kaczmarek, F. Karsch, E. Laermann, C. Miao, S. Mukherjee, et al. Phase boundary for the chiral transition in (2+1)-flavor QCD at small values of the chemical potential. *Phys.Rev.*, D83:014504, 2011.
- [73] O. Kaczmarek, F. Karsch, P. Petreczky, and F. Zantow. Heavy quark free energies, potentials and the renormalized Polyakov loop. *Nucl. Phys. Proc. Suppl.*, 129:560–562, 2004.
- [74] T. Kaneko et al. JLQCD’s dynamical overlap project. *PoS*, LAT2006:054, 2006.
- [75] J. Kapusta and C. Gale. Finite-temperature field theory: principles and applications. 2006.

- [76] J. I. Kapusta, D. Kharzeev, and L. D. McLerran. The return of the prodigal Goldstone boson. *Phys.Rev.*, D53:5028–5033, 1996.
- [77] V. Karnaukhov, H. Oeschler, S. Avdeyev, V. Rodionov, A. Simomenko, et al. Multifragmentation and nuclear phase transitions (liquid fog and liquid gas). *Nucl.Phys.*, A734:520–523, 2004.
- [78] V. Karnaukhov, H. Oeschler, A. Budzanowski, S. Avdeyev, A. Botvina, et al. Critical temperature for the nuclear liquid-gas phase transition (from multifragmentation and fission). *Phys.Atom.Nucl.*, 71:2067–2073, 2008.
- [79] K. Kashiwa, T. Hell, and W. Weise. Nonlocal Polyakov-Nambu-Jona-Lasinio model and imaginary chemical potential. *Phys.Rev.*, D84:056010, 2011.
- [80] B. Kerbikov and Y. Simonov. Path integral bosonization of three flavor quark dynamics. 1995.
- [81] S. Klevansky. The Nambu-Jona-Lasinio model of quantum chromodynamics. *Rev.Mod.Phys.*, 64:649–708, 1992.
- [82] S. Klimt, M. F. Lutz, U. Vogl, and W. Weise. Generalized SU(3) Nambu–Jona-Lasinio. Part 1. Mesonic modes. *Nucl.Phys.*, A516:429–468, 1990.
- [83] M. Kobayashi, H. Kondo, and T. Maskawa. Symmetry breaking of chiral $U(3) \otimes U(3)$ and $X \rightarrow \eta\pi\pi$ eta pi pi decay amplitude. *Prog.Theor.Phys.*, 49:634–639, 1973.
- [84] M. Kobayashi and T. Maskawa. Chiral symmetry and eta-x mixing. *Prog.Theor.Phys.*, 44:1422–1424, 1970.
- [85] K.-I. Kondo. Toward a first-principle derivation of confinement and chiral-symmetry-breaking crossover transitions in QCD. 2010.
- [86] Y. Kwon, S. H. Lee, K. Morita, and G. Wolf. Renewed look at η' in medium. *Phys.Rev.*, D86:034014, 2012.
- [87] E. Laermann and O. Philipsen. The status of lattice QCD at finite temperature. *Ann.Rev.Nucl.Part.Sci.*, 53:163–198, 2003.
- [88] J. M. Lattimer. Neutron star structure and the equation of state. *Prog.Theor.Phys.Suppl.*, 186:1–8, 2010.
- [89] J. M. Lattimer and M. Prakash. What a two solar mass neutron star really means. 2010.
- [90] O. Lourenco, M. Dutra, A. Delfino, and M. Malheiro. Hadron-quark phase transition in a hadronic and Polyakov–Nambu–Jona-Lasinio models perspective. *Phys.Rev.*, D84:125034, 2011.
- [91] O. Lourenco, M. Dutra, T. Frederico, A. Delfino, and M. Malheiro. Vector interaction strength in Polyakov-Nambu-Jona-Lasinio models from hadron-quark phase diagrams. *Phys.Rev.*, D85:097504, 2012.
- [92] M. Lutz, S. Klimt, and W. Weise. Meson properties at finite temperature and baryon density. *Nucl. Phys.*, A542:521–558, 1992.
- [93] K. Masuda, T. Hatsuda, and T. Takatsuka. Hadron-quark crossover and massive hybrid stars with strangeness. 2012.

- [94] L. D. McLerran and B. Svetitsky. A Monte Carlo study of SU(2) Yang-Mills theory at finite temperature. *Phys.Lett.*, B98:195, 1981.
- [95] L. D. McLerran and B. Svetitsky. Quark liberation at high temperature: a Monte Carlo study of SU(2) gauge theory. *Phys.Rev.*, D24:450, 1981.
- [96] P. N. Meisinger and M. C. Ogilvie. Coupling the deconfining and chiral transitions. *Nucl.Phys.Proc.Suppl.*, 47:519–522, 1996.
- [97] Y. Nambu. Quasiparticles and gauge invariance in the theory of superconductivity. *Phys.Rev.*, 117:648–663, 1960.
- [98] Y. Nambu and G. Jona-Lasinio. Dynamical model of elementary particles based on an analogy with superconductivity. I. *Phys. Rev.*, 122:345–358, 1961.
- [99] Y. Nambu and G. Jona-Lasinio. Dynamical model of elementary particles based on an analogy with superconductivity. II. *Phys. Rev.*, 124:246–254, 1961.
- [100] R. Narayanan and H. Neuberger. A construction of lattice chiral gauge theories. *Nucl.Phys.*, B443:305–385, 1995.
- [101] C. Nonaka and M. Asakawa. Hydrodynamical evolution near the QCD critical end point. *Phys.Rev.*, C71:044904, 2005.
- [102] G. Odyniec. Beam energy scan program at RHIC: experimental approach to the QCD phase diagram. *Phys.Atom.Nucl.*, 75:602–606, 2012.
- [103] G. Odyniec. Search for the critical point of the nuclear matter phase diagram. First results from the beam energy scan program at RHIC. *Acta Phys.Polon.*, B43:627–634, 2012.
- [104] J. Oppenheimer and G. Volkoff. On massive neutron cores. *Phys.Rev.*, 55:374–381, 1939.
- [105] J. M. Pawłowski. The QCD phase diagram: results and challenges. *AIP Conf.Proc.*, 1343:75–80, 2011.
- [106] O. Philipsen. Lattice QCD at finite temperature and density. *Eur.Phys.J.ST*, 152:29–60, 2007.
- [107] H. D. Politzer. Reliable perturbative results for strong interactions? *Phys.Rev.Lett.*, 30:1346–1349, 1973.
- [108] H. D. Politzer. Asymptotic freedom: an approach to strong interactions. *Phys.Rept.*, 14:129–180, 1974.
- [109] C. Ratti, M. A. Thaler, and W. Weise. Phases of QCD: lattice thermodynamics and a field theoretical model. *Phys.Rev.*, D73:014019, 2006.
- [110] P. Rehberg, S. Klevansky, and J. Hufner. Hadronization in the SU(3) Nambu–Jona-Lasinio model. *Phys.Rev.*, C53:410–429, 1996.
- [111] H. Reinhardt and R. Alkofer. Instanton induced flavor mixing in mesons. *Phys.Lett.*, B207:482–488, 1988.
- [112] A. Roberge and N. Weiss. Gauge theories with imaginary chemical potential and the phases of QCD. *Nucl.Phys.*, B275:734, 1986.
- [113] C. D. Roberts. Strong QCD and Dyson-Schwinger equations. 2012.

- [114] C. D. Roberts and S. M. Schmidt. Dyson-Schwinger equations: density, temperature and continuum strong QCD. *Prog.Part.Nucl.Phys.*, 45:S1–S103, 2000.
- [115] Rößner, Simon. *Phases of QCD*. Dissertation, Technische Universität München, München, 2009.
- [116] Rößner, Simon and Hell, T. and Ratti, C. and Weise, W. The chiral and deconfinement crossover transitions: PNJL model beyond mean field. *Nucl.Phys.*, A814:118–143, 2008.
- [117] Rößner, Simon and Ratti, Claudia and Weise, W. Polyakov loop, diquarks and the two-flavour phase diagram. *Phys.Rev.*, D75:034007, 2007.
- [118] A. Scarpettini, D. Gomez Dumm, and N. Scoccola. Light pseudoscalar mesons in a nonlocal SU(3) chiral quark model. *Phys.Rev.*, D69:114018, 2004.
- [119] B.-J. Schaefer, J. M. Pawłowski, and J. Wambach. The phase structure of the Polyakov–Quark-Meson model. *Phys. Rev.*, D76:074023, 2007.
- [120] B.-J. Schaefer, M. Wagner, and J. Wambach. Thermodynamics of (2+1)-flavor QCD: confronting models with lattice studies. *Phys.Rev.*, D81:074013, 2010.
- [121] Schäfer, Thomas and Shuryak, Edward V. Instantons in QCD. *Rev.Mod.Phys.*, 70:323–426, 1998.
- [122] M. Stephanov. QCD phase diagram: an overview. *PoS, LAT2006:024*, 2006.
- [123] R. L. Stratonovich. On a method of calculating quantum distribution functions. *Soviet Physics Doklady*, 2:416, July 1957.
- [124] e. 't Hooft, Gerard, e. Itzykson, C., e. Jaffe, A., e. Lehmann, H., e. Mitter, P.K., et al. Recent developments in gauge theories. Proceedings, Nato Advanced Study Institute, Cargese, France, August 26 - September 8, 1979. *NATO Adv.Study Inst.Ser.B Phys.*, 59:1–438, 1980.
- [125] G. 't Hooft. Symmetry breaking through Bell-Jackiw anomalies. *Phys.Rev.Lett.*, 37:8–11, 1976.
- [126] G. 't Hooft. How instantons solve the U(1) problem. *Phys.Rept.*, 142:357–387, 1986.
- [127] M. Thaler. Phases of QCD: lattice thermodynamics and quasiparticle approaches (Dissertation). 2006.
- [128] R. C. Tolman. Effect of inhomogeneity on cosmological models. *Proc.Nat.Acad.Sci.*, 20:169–176, 1934.
- [129] R. C. Tolman. Static solutions of Einstein's field equations for spheres of fluid. *Phys.Rev.*, 55:364–373, 1939.
- [130] G. Veneziano. U(1) without instantons. *Nucl.Phys.*, B159:213–224, 1979.
- [131] R. Vertesi, T. Csorgo, and J. Sziklai. Significant in-medium η' mass reduction in $\sqrt{s_{NN}} = 200$ GeV Au+Au collisions. *Nucl.Phys.*, A830:631C–632C, 2009.
- [132] R. Vertesi, T. Csorgo, and J. Sziklai. In-medium reduction of the η' mass in $\sqrt{s_{NN}} = 200$ GeV Au+Au collisions. *EPJ Web Conf.*, 13:04004, 2011.
- [133] R. Vertesi, T. Csorgo, and J. Sziklai. Significant in-medium η' mass reduction in $\sqrt{s_{NN}} = 200$ GeV Au+Au collisions at the BNL Relativistic Heavy Ion Collider. *Phys.Rev.*, C83:054903, 2011.

- [134] U. Vogl, M. F. Lutz, S. Klimt, and W. Weise. Generalized SU(3) Nambu–Jona-Lasinio model. Part 2. From current to constituent quarks. *Nucl.Phys.*, A516:469–495, 1990.
- [135] U. Vogl and W. Weise. The Nambu and Jona Lasinio model: its implications for hadrons and nuclei. *Prog.Part.Nucl.Phys.*, 27:195–272, 1991.
- [136] J. Wambach, K. Heckmann, and M. Buballa. Transport properties of strong-interaction matter. *AIP Conf.Proc.*, 1441:794–796, 2012.
- [137] W. Weise. Nuclear chiral dynamics and phases of QCD. *Prog.Part.Nucl.Phys.*, 67:299–311, 2012.
- [138] C. Wetterich. Exact evolution equation for the effective potential. *Phys.Lett.*, B301:90–94, 1993.
- [139] K. G. Wilson. Confinement of quarks. *Phys.Rev.*, D10:2445–2459, 1974.
- [140] E. Witten. Current algebra theorems for the U(1) Goldstone boson. *Nucl.Phys.*, B156:269, 1979.
- [141] K. Yagi, T. Hatsuda, and Y. Miake. Quark-gluon plasma: from big bang to little bang. *Camb.Monogr.Part.Phys.Nucl.Phys.Cosmol.*, 23:1–446, 2005.
- [142] Z. Zhang and T. Kunihiro. Vector interaction, charge neutrality and multiple chiral critical point structures. *Phys.Rev.*, D80:014015, 2009.
- [143] Z. Zhang and T. Kunihiro. Roles of axial anomaly on neutral quark matter with color superconducting phase. *Phys.Rev.*, D83:114003, 2011.

Acknowledgments

During my work on this thesis, I had the pleasure and the privilege to work with some of the smartest people that I will ever meet. I could not have asked for a better working environment than this friendly group with its diverse talents and easily sparked enthusiasm. Although everybody contributed in some way to the pleasant atmosphere and to the success of this project, I am grateful to a few people in particular:

First of all, I want to thank Prof. Dr. Wolfram Weise who gave me the opportunity to work on this thesis in his group and who supported me throughout all of my scientific career. Not only did I enjoy great freedom in my work but also had the chance to attend conferences, give talks and work with groups all over the globe. I don't think it is common that a supervisor is always available for a chat to his students, is so actively engaged in securing their well-being and even invites them into his home (on rainy days).

Prof. Dr. Tetsuo Hatsuda and his group are warmly thanked for their hospitality at RIKEN and the University of Tokyo and the friendly and open manner with which they welcomed me.

Prof. Dr. Norbert Kaiser deserves thanks for his almost constant availability and his mathematically precise yet beautifully intuitive explanations.

I am also grateful to Dr. Bertram Klein for frequent discussions, kind hospitality, meticulous editing and masterful dough-working.

Dr. Jeremy Holt was always busy with work, usually writing a new paper. But regardless of how much he had on his plate, he was never too busy to answer my questions regardless of their nature, nor to join me in whatever was planned for the weekend. Even if it was "Dakota". I am grateful to him for good advice on physics, life, music, and, most of all, for playing Chopin's *Fantasia Impromptu*.

I am also much indebted to Dr. Thomas Hell, who was in all situations ready to discuss physics and never failed to come up with a solution if possible and necessary. I appreciate his insights and help with calculations both numerical and analytical. Apart from that, I also profited from his adventurous spirit and organizing talent.

Alexander Laschka was always willing to listen to all problems personal and professional, but especially technical. I cannot count the times that he helped me fix a computer, mend a broken code or use some obscure piece of software that magically did whatever it was that I needed.

Robert Lang was a valuable source of good mathematics knowledge (and less good mathematics jokes) and always up for a physical puzzle or a controversial discussion.

Matthias Drews rekindled my interest in philosophy, both by being impressively well-read and by his sheer enthusiasm. I'm looking forward to keeping up the exchange.

The perpetually good-humoured Stefan Petschauer helped me tremendously with the intricacies of LaTeX and updated me on the latest developments in software and technology.

Pavel Springer introduced me to contemporary Russian literature and started to teach me some very effective ways of expressing anger or frustration in Russian.

I thank also my previous office mates, Bernhard Musch and Simon Rößner for taking me in and showing me the ropes. In addition, I am grateful to all other members of our group, both current and previous, permanent and temporary, for the frequent discussions, spare time activities and culinary excursions.

Finally, I am most indebted to my parents and my friends for their continuous support. Without them, this thesis would simply not have been possible.